Universität Stuttgart

Multiscale Modelling and Simulation of Metal Fatigue and its Applications

Von der Fakultät Energie-, Verfahrens- und Biotechnik der Universität Stuttgart

zur Erlangung der Würde eines Doktors der Ingenieurwissenschaften (**Dr.-Ing.**) genehmigte Abhandlung

Vorgelegt von

Marijo Mlikota

geboren in Konjic, Bosnien und Herzegowina

Tag der mündlichen Prüfung:
29. Juli 2020

Prüfungsvorsitzender:	Prof. Dr. K. Andreas Friedrich
Hauptberichter:	Prof. Dr. rer. nat. Dr. h. c. Siegfried Schmauder
Mitberichter:	Prof. dr. sc. Željko Božić

Institut für Materialprüfung, Werkstoffkunde und Festigkeitslehre (IMWF)
der Universität Stuttgart

Stuttgart, Deutschland
2019

LEGAL STATEMENT

I solemnly declare that I have produced this work all by myself. Ideas taken directly or indirectly from other sources are marked as such. This work has not been shown to any other board of examiners so far and has not been published yet. I am fully aware of moral and legal consequences of making a false declaration.

EHRENWÖRTLICHE ERKLÄRUNG

Hiermit erkläre ich, dass ich die vorliegende Arbeit selbstständig verfasst und keine anderen als die angegebenen Hilfsmittel genutzt habe. Alle wörtlich oder inhaltlich übernommenen Stellen habe ich als solche gekennzeichnet. Ich versichere außerdem, dass ich die vorliegende Arbeit keiner anderen Prüfungsbehörde vorgelegt habe und, dass die Arbeit bisher auch auf keine andere Weise veröffentlicht wurde. Ich bin mir der moralischen und gesetzlichen Konsequenzen einer falschen Aussage bewusst.

Stuttgart, den 10. Dezember 2019 Marijo Mlikota

Table of Contents

List of Abbreviations and Symbols

Abbreviation / Symbol	Description
a	Crack length (mm)
A	Dislocation distribution
AA	Aluminium alloy
a_f	Crack length at failure (mm)
a_{ini}	Initiation (transitional) crack length (mm)
a_0	Initial crack length (mm)
b	Burgers vector
BCC	Body-centred cubic
C	Paris law constant
CRSS	Critical resolved shear stress (MPa; N/mm^2)
CTOD	Crack tip opening displacement (mm)
C_{11}, C_{12}, C_{44}	Material elastic constants for cubic crystal symmetry (MPa)
d	Slip band length; grain size (mm)
D	Top-surface diameter of a cylindrical micropillar (mm)
D_i	Dislocation density
d_s	Length of a slip band segment (mm)
da/dN	Fatigue crack growth rate (mm/cycle)
DIC	Digital image correlation
E	Young's/elastic modulus (MPa)
e	Strain
EBSD	Electron back-scatter diffraction
EPFM	Elastic-plastic fracture mechanics
e-N	Strain-life
FCC	Face-centred cubic
FCGR	Fatigue crack growth rate (mm/cycle)
FEA	Finite element analysis
FEM	Finite element method
FM	Fracture mechanics
G	Shear modulus (MPa)
HCF	High-cycle fatigue
HCP	Hexagonal close-packed
HEA	High-enthalpy alloy
J_i	Crack initiation energy (N/mm)

Abbreviation / Symbol	Description
J_{Ic}	Fracture toughness (N/mm)
K_{Ic}	Fracture toughness (MPa√m)
L	Left
LCF	Low-cycle fatigue
LEFM	Linear-elastic fracture mechanics
m	Paris law constant
MD	Molecular dynamics
MMM	Multiscale materials modelling
MPT	Micropillar test
ms	Microstructure
N	Number of loading cycles, lifetime
N_c	Crack initiation cycles
N_f	Number of loading cycles to failure
N_g	Number of loading cycles for crack nucleation in a grain
N_{ini}	Number of loading cycles for fatigue crack initiation
N_{pro}	Number of loading cycles for fatigue crack propagation
N_s	Number of loading cycles for fatigue crack nucleation on a slip band segment
O/P	Output
PEEQ	Equivalent plastic strain
R	Right
R	Loading stress ratio
RdM	Rate-drop method
R_e	Elastic limit (yield stress/strength) (MPa)
RoM	Run-out method
RVE	Representative volume element
S	Loading stress level (MPa)
S_a	Stress amplitude (MPa)
S_e	Endurance limit (MPa)
S_{up}	Upper value of cyclic loading stress (MPa)
S_{low}	Lower value of cyclic loading stress (MPa)
S_u	Ultimate strength (MPa)
S-N	Strength-/stress-/fatigue life
SEM	Scanning electron microscopy
SP	Shot-peening
S12	Shear stress as software Abaqus output variable (MPa)
TM	Tanaka-Mura

Abbreviation / Symbol	Description
U	Self energy of dislocations (J; Nm)
U_i	Increment of the self-energy stored in the i^{th} stage of stress reversal (J)
VHCF	Very high-cycle fatigue
XFEM	Extended finite element method
W_c	Crack initiation energy (N/mm)
γ	Plastic displacement (mm)
υ	Poisson's ratio
τ_c	Critical Resolved Shear Stress (MPa)
τ_{dh}	Dislocation hardening stress (MPa)
τ_{gbs}	Grain boundary strengthening stress (MPa)
τ_{pbs}	Phase boundary strengthening stress (MPa)
τ_{ps}	Strengthening stress induced by particles (MPa)
τ_{ssh}	Solid solution hardening stress (MPa)
τ_0	Peierls-Nabarro stress (MPa)
τ_1	Maximum applied shear stress (MPa)
τ_2	Minimum applied shear stress (MPa)
τ^D	Dislocation stress (MPa)
Δa	Crack extension (mm)
Δa_{str}	Stretched zone (mm)
ΔCTOD	Crack tip opening displacement range (mm)
ΔJ	*J*-integral range (N/mm)
ΔK	Stress intensity factor range (MPa√m)
ΔK_{th}	Stress intensity factor threshold range (MPa√m)
ΔS	Stress range (MPa)
ΔU	Increment of the self-energy per half cycle (J)
$\Delta\gamma$	Plastic strain amplitude
$\Delta\tau$	Shear stress range (MPa)
$\Delta\tau_n$	Shear stress endurance limit (MPa)
$\Delta\overline{\tau}$	Average shear stress on a slip band (MPa)
$\Delta\overline{\tau}_s$	Average shear stress on a slip band segment (MPa)
2D	Two-dimensional
3D	Three-dimensional

1 Abstract

Multiscale materials modelling (MMM) has been recently growing and simultaneously becoming a significant tool for understanding complexities of contemporary materials as well as a valuable driver for their development. In view of that, this work presents a MMM approach based on the application of different numerical techniques for predicting the fatigue life of metallic materials.

The work contains several fatigue problems of metals where the modelling approach has been successfully applied, including its highlight, which is the virtual determination of the fatigue life (*S-N* or Wöhler) curve. The approach is realized by coupling the analysis of microscopic (crack initiation on the basis of the physically-based Tanaka-Mura model) and macroscopic (crack growth on the basis of classical Fracture Mechanics) fatigue behaviour, together with the molecular dynamics (MD) and experimentally-based input determination. Particular emphasis has been placed on the application of the modelling approach to demonstrate the importance of the parameter critical resolved shear stress (CRSS) for the fatigue performance of several metals. The discovered relation between endurance limit and the CRSS provides a facet of fatigue theory that is numerically predictive and which allows the selection of those types of materials, which are more fatigue resistant. In addition to the CRSS, factors such as grain size, mean stress, plasticity, residual stresses and others have been also investigated with the aim to identify their influence on the *S-N* curves as well as endurance limits of various metallic materials. Aside of that, it is now possible to estimate the length of the short crack at the initiation end by application of the physically-based micromechanical simulations what opens new doors to an easier detection of the critical crack lengths in practical applications, e.g. for component and plant inspection. The experimental determination of the Paris law constants is typically tedious and time consuming. The successful determination of these constants by using the present physically-based multiscale materials simulation approach provides, on the contrary, an efficient method to equip engineers with these highly relevant fatigue data.

As the results of this work demonstrate, the introduced MMM procedure for metal fatigue characterization plays an important role in the understanding of present days' complex and advanced materials. Apart from that, this physically-based MMM approach represents a breakthrough in the field of fatigue research and opens the door for fast and cost-effective development of virtual metallic materials for present and future fatigue applications, such as, e.g., for additive manufactured materials.

1.1 Outline

The present work is structured into 13 Chapters. After a summary and outline in Chapters 1 and 2, the technical part of the work begins from Chapter 3, which provides an introduction into the fatigue process happening under cyclic loading in metallic material systems; it ends with Chapters 6 and 7 where a summary of the research results obtained in this work and an outlook as well as details on applied tools are given, respectively. These tools are the finite element method (Section 7.1) and the Tanaka-Mura model (Section 7.2), which both together served as a foundation of this work.

Chapter 4 discusses the fatigue process in more details, providing the existing experimental, numerical and theoretical approaches to understand and handle the process under control. The concept of multiscale modelling and simulation of metal fatigue is introduced in Chapter 4, too.

Application examples of the multiscale fatigue simulation approach are the topic of Chapter 5. Among the important influencing factors like loading ratio, residual stresses, grain and notch radius size, plasticity and crack initiation energy, the analysis of the relevance of the CRSS stands out as the leading study of this work. In addition, the study on the component fatigue life determination has a high practical value. The results of these studies could be validated by experimentally obtained measurements. This validation reveals excellent qualitative as well as quantitative agreement as shown in, e.g., Section 5.2.3. The successful numerical determination of Paris law constants is a part of Chapter 5, too.

Furthermore, the results obtained in this work have been presented at international conferences and resulted in several journal publications, the list of which can be found in Chapter 8.1. Some of these results have been also incorporated in lectures for different study courses by Prof. Siegfried Schmauder at the University of Stuttgart.

The work is a continuation and significant extension of work done during the master's study, in which the author numerically examined the fatigue crack growth in plates subjected to cyclic tension load. More details on this pre-work can be found in [10O]. Aside of that, the author has supervised several student research projects (in German Studienarbeit), bachelor and master theses on the topic of fatigue during the working time at IMWF (see Section 8.3).

The work concludes with the lists of figures, tables and references, respectively, and with an acknowledgement and short biography of the author.

2 Zusammenfassung

Die Multiskalen-Materialmodellierung (MMM) ist in jüngster Zeit eingeführt worden und hat sich gleichzeitig zu einem wichtigen Instrument für das physikalische Verständnis der Komplexität des mechanischen Verhaltens aktueller Materialien sowie zu einer wertvollen Triebfeder für deren Entwicklung entfaltet. In Anbetracht dessen stellt diese Arbeit einen MMM-Ansatz vor, der auf der Anwendung verschiedener numerischer Techniken zur Vorhersage der Ermüdungslebensdauer metallischer Werkstoffe basiert.

Die Arbeit enthält darüber hinaus mehrere Ermüdungsprobleme von Metallen und Legierungen, bei denen der MMM-Ansatz erfolgreich angewandt wurde, einschließlich dem Höhepunkt, der die virtuelle Bestimmung der Ermüdungslebensdauer (*S-N* oder Wöhler-Kurve) ist. Der Ansatz wird durch Kopplung der Analyse von mikroskopischem (Rissinitiierung auf der Grundlage des physikalisch basierten Tanaka-Mura-Modells) und makroskopischem (Risswachstum auf der Basis klassischer Bruchmechanik) Ermüdungsverhalten realisiert, zusammen mit der Molekulardynamik (MD) und experimentell basierten Eingabeparametern. Besonderes Augenmerk wurde auf die Anwendung des Modellierungsansatzes gelegt, um die Bedeutung des Parameters kritischen Schubspannung (CRSS) für das Ermüdungsverhalten mehrerer Metalle zu demonstrieren. Die gefundene Beziehung zwischen der Dauerfestigkeit und der CRSS bietet einen neuen Aspekt der Ermüdungstheorie, der numerische Vorhersagen erlaubt und der ermöglicht, diejenigen Arten von Materialien auszuwählen, die ermüdungsbeständig sind. Neben der CRSS wurden auch Faktoren wie Korngröße, Mittelspannung, Plastizität, Eigenspannungen und andere Größen untersucht, um deren Einfluss auf die Wöhler-Kurven sowie die Dauerfestigkeit verschiedener metallischer Werkstoffe zu ermitteln. Daneben ist es jetzt möglich, die Länge des kurzen Risses zum Ende der Initiierungsphase durch die Simulationen abzuschätzen, was neue Türen für eine einfachere Erkennung der kritischen Risslängen öffnet. Die experimentelle Bestimmung der Parameter des Parisgesetzes ist typischerweise mühsam und zeitaufwendig. Die erfolgreiche Bestimmung dieser Parameter unter Verwendung des vorliegenden physikalisch basierten multiskaligen Simulationsansatzes bietet im Gegensatz dazu eine neue und effiziente Methode, um Berechnungsingenieure mit diesen hoch-relevanten Ermüdungsdaten zu versorgen.

Die Ergebnisse dieser Arbeit belegen, dass das eingeführte MMM-Verfahren zur numerischen Charakterisierung der Metallermüdung eine wichtige Rolle für das Verständnis der heutigen komplexen Werkstoffe spielt. Abgesehen davon stellt dieser physikalisch basierte MMM-Ansatz einen Durchbruch im Bereich der Ermüdungsforschung dar und öffnet die Tür für eine schnelle und kostengünstige virtuelle Entwicklung verbesserter und neuer Materialien für aktuelle und zukünftige Ermüdungsanwendungen, wie z. B. für additiv gefertigte Werkstoffe.

2.1 Gliederung

Die vorliegende Arbeit ist in 13 Kapitel gegliedert. Nach einer Zusammenfassung und Gliederung in den Kapiteln 1 und 2 beginnt der technische Teil der Arbeit mit Kapitel 3, welches eine Einführung in den Ermüdungsprozess bei zyklischer Belastung in metallischen Werkstoffsystemen enthält; er endet mit den Kapiteln 6 und 7, in denen eine Zusammenfassung der in dieser Arbeit erzielten Forschungsergebnisse und ein Ausblick sowie Einzelheiten zu den angewandten Werkzeugen gegeben werden. Diese Werkzeuge sind die Finite-Elemente-Methode (Abschnitt 7.1) und das Tanaka-Mura-Modell (Abschnitt 7.2), die beide zusammen als Grundlage dieser Arbeit dienten.

In Kapitel 4 wird der Ermüdungsprozess ausführlicher erörtert, wobei die vorhandenen experimentellen, numerischen und theoretischen Ansätze zum Verständnis und zur Steuerung des Prozesses erläutert werden. Das Konzept der Multiskalenmodellierung und -simulation der Metallermüdung wird ebenfalls in Kapitel 4 vorgestellt.

Anwendungsbeispiele für den Ansatz der Multiskalen-Ermüdungssimulation sind das Thema von Kapitel 5. Neben den wichtigen Einflussfaktoren wie Belastungsverhältnis, Eigenspannungen, Korn- und Kerbgröße, Plastizität und Bruchenergie hebt sich die Analyse der Bedeutung des Parameters CRSS als die Leitstudie dieser Arbeit ab. Darüber hinaus hat die Studie zur Bestimmung der Lebensdauer von Bauteilen einen hohen praktischen Wert. Die Ergebnisse dieser Studien konnten durch experimentell gewonnene Messungen validiert werden. Diese Validierung zeigt eine hervorragende qualitative und quantitative Übereinstimmung, wie z. B., in Abschnitt 5.2.3 gezeigt. Die erfolgreiche numerische Bestimmung der Parameter des Parisgesetzes ist ebenfalls Teil von Kapitel 5.

Darüber hinaus wurden die in dieser Arbeit erzielten Ergebnisse auf internationalen Konferenzen vorgestellt und führten zu einer Reihe von Veröffentlichungen in Fachzeitschriften, deren Liste in Kapitel 8.1 zu finden ist. Einige dieser Ergebnisse flossen auch in Vorlesungen für verschiedene Studiengänge von Prof. Siegfried Schmauder an der Universität Stuttgart ein.

Die Arbeit ist eine Fortsetzung und wesentliche Erweiterung der Arbeit, die während des Masterstudiums durchgeführt wurde, in dem der Autor das Ermüdungsrisswachstum von Platten, die einer zyklischen Beanspruchung ausgesetzt waren, numerisch untersuchte. Weitere Details zu dieser Vorarbeit sind in [10O] zu finden. Daneben betreute der Autor während des Arbeitszeitraums am IMWF mehrere studentische Studien- sowie Bachelor- und Masterarbeiten zum Thema Ermüdung (siehe Abschnitt 8.3).

Die Arbeit endet mit der Auflistung der Abbildungen, Tabellen und Zitate sowie einer Danksagung und Kurzbiografie des Autors.

3 Introduction and Motivation

It has been estimated that over 75% of the failure problems in engineering systems each year are due to fatigue [07L]. Fatigue damage has been recognized as a fracture phenomenon occurring after a large number of loading cycles where a single load of the same magnitude would do no harm to the mechanical structures [03S]. In 1903, Ewing and Hunfrey [03E] carried out microscopic investigations, which showed that fatigue crack nuclei in metallic materials appeared from slip bands. From then on, fatigue damage began to be considered as more of a material problem, i.e. to be material dependent.

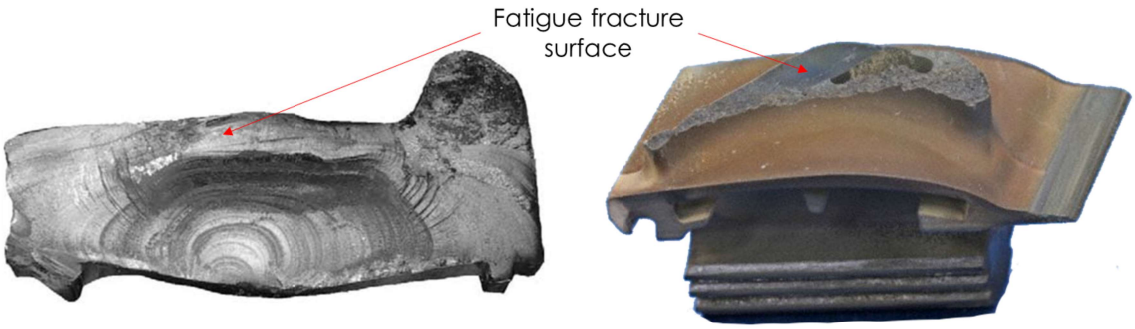

Figure 1: Left – Fatigue fracture surface of: Left – A broken train wheel [04E]; Right – The root of a fractured engine blade of Boeing 747-400 [12H].

Structural health monitoring and detection of fatigue failures are highly important for fitness and service assessment of structures. Failure of structures under fatigue loading can occur at load levels below the yield stress of the used material. Therefore, it is of special importance to be able to make predictions of life cycles until catastrophic fracture occurs. A well-known example of such catastrophic failure is the huge train accident in Eschede where one wheel of the train broke due to cyclic loading (Figure 1L) that has not been considered during construction [04E]. Another example in Figure 1R shows the root of a pressure turbine blade of the Boeing 747-400, that fractured as a result of the growth of a low stress/high cycle fatigue crack. Luckily, the aircraft flying from Sydney to Singapore landed safely and without casualties [12H].

However, not every single crack has to be critical immediately. Often structures can withstand cracks up to a certain crack length until unstable fracture occurs. In order to determine the point where the fatigue crack reaches its critical size, it is necessary to understand existing and develop new methods to estimate the total fatigue life.

4 Fatigue of Metals

Fatigue is one of the most important modes of failure in many mechanical components. Its significance lays in the fact that it may occur even if the stresses in a specific region are below the stresses, which that component could bear without any circumstances under static loading conditions. This kind of failure can be understood by a simple example. If one tries to break a thin wire made out of e.g. copper or aluminium by hands, this can be done in two ways. One way is to stretch it, shear it or bend it in one direction what would in most cases require a lots of effort. On the other hand, if one tries to bend it by a hogging-sagging method (i.e. cyclically), as illustrated in Figure 2, it would take considerable less time and effort to cause the breakage. This fact highlights the specificity and importance of the fatigue process.

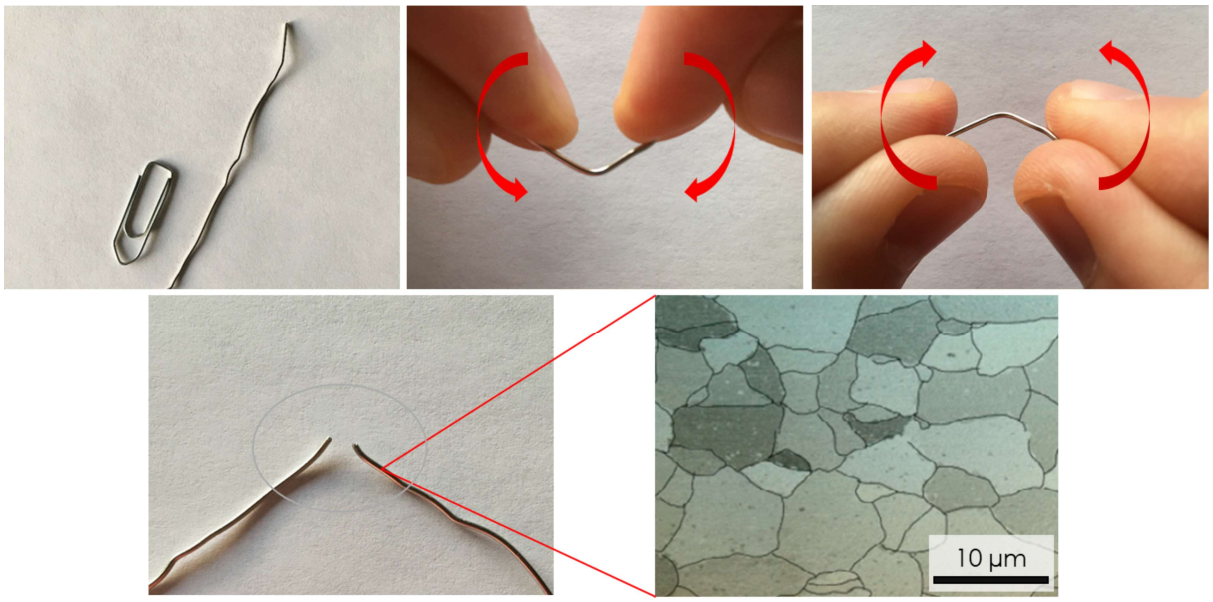

Figure 2: Braking aluminium wire by the hogging-sagging method and microstructure of an aluminium alloy (AA) [13N].

Extensive research studies have been carried out in the past decades, contributing to the understanding of mechanisms, which make fatigue damage in metallic materials so specific, as well as of its stages (short crack initiation and long crack growth). However, a complete understanding of this process is still missing due to numerous factors that affect its development. Generally speaking, these factors could belong to one of the following aspects: i) Surface effects like surface roughness, surface damage or various surface treatments; ii) Environmental effects like corrosion and temperature; iii) Geometrical effects like stress concentrations, and iv) Microstructural effects, such as grain size and shape, second phase particles, precipitation etc. [07L].

4.1 Factors Controlling Fatigue Damage of Metallic Materials

In order to address fatigue, it is necessary first to understand the mechanisms that facilitate crack initiation inside microstructures of metallic materials (bottom right image in Figure 2) [13S]. The microstructure, or in other words the crystalline structure, consists of grains (i.e. crystals) abutting one another. The lines between these grains are referred to as grain boundaries (Figure 2 – black lines in the bottom right image). In general, the size of the grains influences mechanical properties of alloys, i.e. the smaller the grains the better the properties – as more boundaries prevent the movement of dislocations in the microstructure (see Section 5.5 for more details). Through the use of powerful microscopy tools, it is possible to scan the microstructure of unloaded materials but also of the material that is stressed by outer loading and, furthermore, to superimpose resulting strain fields spatially distributed over the microstructure, as shown in Figure 4 [09T, 10D, 11F, 12A]. More precisely, digital image correlation (DIC) is the technique commonly used to analyse strain fields and strain localization on the surface of a specimen. Electron back-scatter diffraction (EBSD) scans are typically used in addition to DIC to realize the grain orientation and grain boundaries within the specimen's microstructure. Figure 4 illustrates an example of strain localization in a cut-out surface of a nickel-based superalloy [12A, 13S]. A specimen from the figure was loaded in one cycle consisting of forward uniaxial loading up to a strain of 2.2% and reverse unloading. During the cycle the recording of the microstructure from EBSD and the strain fields from DIC was performed. At the end of the cycle, the material retained deformed heterogeneously indicating by that the role of microstructure in strain localization.

As described earlier, fatigue is characterized by a series of such forward and reverse loadings, i.e. cycles. Over the course of accumulated cycles, it is expected that fatigue cracks will form in the vicinity of regions containing a large amount of strain accumulation. Strains in this case represent defects in the form of dislocations, which multiply and pile up over the area of slip bands. This behaviour results in an increase in the dislocation density [14R, 13S]. The slip bands, or lines, appear fine and

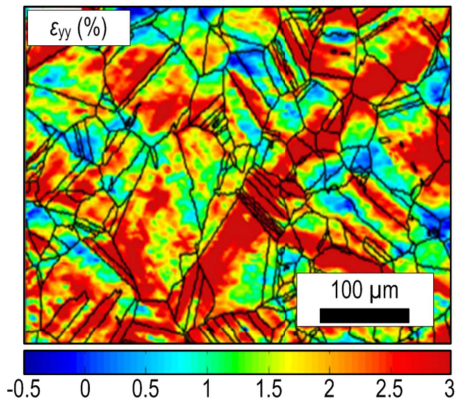

Figure 4: Strain fields measured experimentally from digital image correlation (DIC) after loading/unloading a sample in tension to 2.2% strain overlaid with the material's microstructure from electron back-scatter diffraction (EBSD) [12A].

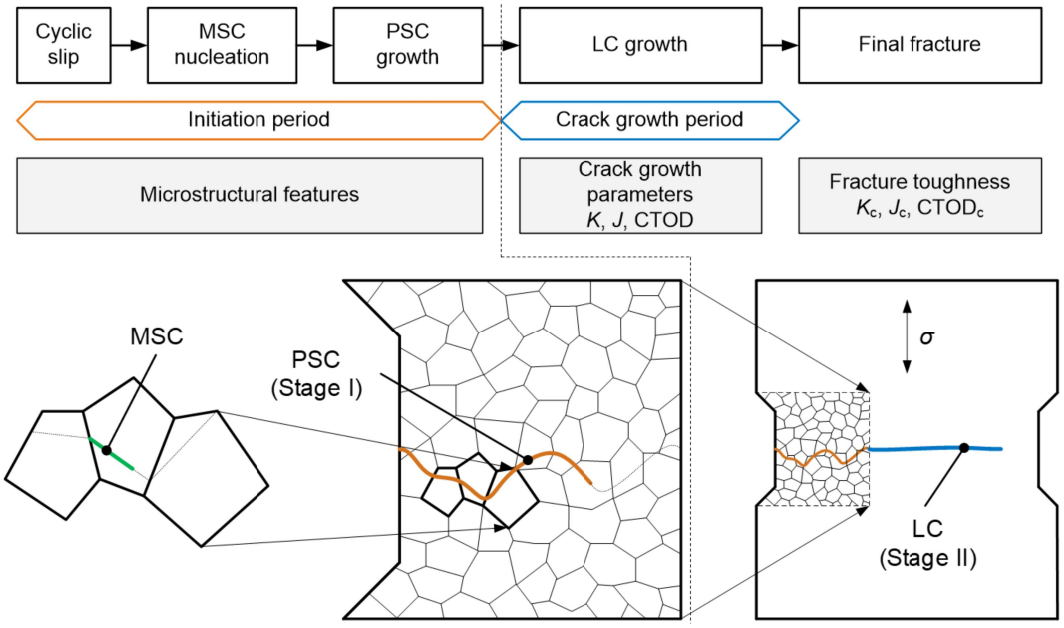

Figure 3: Stages of a fatigue crack during its growth and influencing factors [08S].

sharp in favourably oriented grains (crystals) within the microstructure, as depicted in Figure 4. Furthermore, as more cycles accumulate, more grains display signs of forming slip bands, the existing bands widen, and ultimately some of them nucleate fatigue cracks [03E]. In the course of further cyclic loading some of the formed cracks grow and link together forming in that way a dominant crack, which eventually can result in failure of a specimen or a component.

In general, the development of fatigue cracks can be divided into four stages [01K, 09A]:

- Nucleation due to cyclic slip and early growth of microstructurally short cracks (MSC in Figure 3; in further text: microcracks);
- Subsequent growth of physically short cracks (PSC in Figure 3; in further text: short cracks);
- Transition of the dominant short crack into relatively long crack (LC in Figure 3;) and its growth; and
- Final fracture.

In engineering applications, the first two stages are usually termed as the crack initiation period and long crack growth as crack propagation period (Figure 3). The initiation period generally accounts for most of the service life (up to 90%) [15M]. Figure 5 gives an example of a fatigue crack that initiated from a notch in a high-purity aluminium alloy (AA) [13N].

The number of slip systems in grains of metals is usually high. Under uniaxial cyclic loading, those systems that get activated and eventually form cracks are inclined approximately 45° to the direction of the applied outer loading. They can be recognized as planes with maximum shear stress. Once cracks have nucleated due to strain accumulation, i.e. cyclic slip, they grow on these slip planes in an early stage as microcracks. In this early stage, the microcracks are typically in the order of the

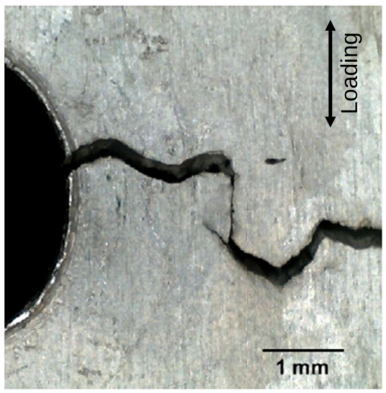

Figure 5: Crack growing from a circular notch of 4 mm diameter in a 1.41 mm grain size microstructure of an AA [13N].

material's grain size, or less, and nucleate all over critically stressed sections of the microstructure (bottom left image in Figure 3). In metals and alloys they nucleate and grow predominantly along crystallographic planes at erratic rate due to high effects of microstructural barriers such as grain boundaries (see Figure 6) or larger particles. Further, as some of the microcracks have grown through several grains they are considered to be short cracks (the length of short cracks is usually in the range from several grains up to 1 mm [84S]) (bottom middle image in Figure 3). Eventually, one short crack evolves into a dominant crack and upon reaching the end of the short crack regime where the microstructural influences become negligible and such a crack starts propagating in a continuous manner, i.e. it turns into a long crack (bottom right image in Figure 3). When the long crack has grown to such a size that the remaining ligament can no longer carry the applied load, the component fractures [01K]. The change from the short crack to the long crack regime is called the transition from Stage I (crystallographic growth) to Stage II (non-crystallographic growth) or transition from the crack initiation to the crack growth stage [80K].

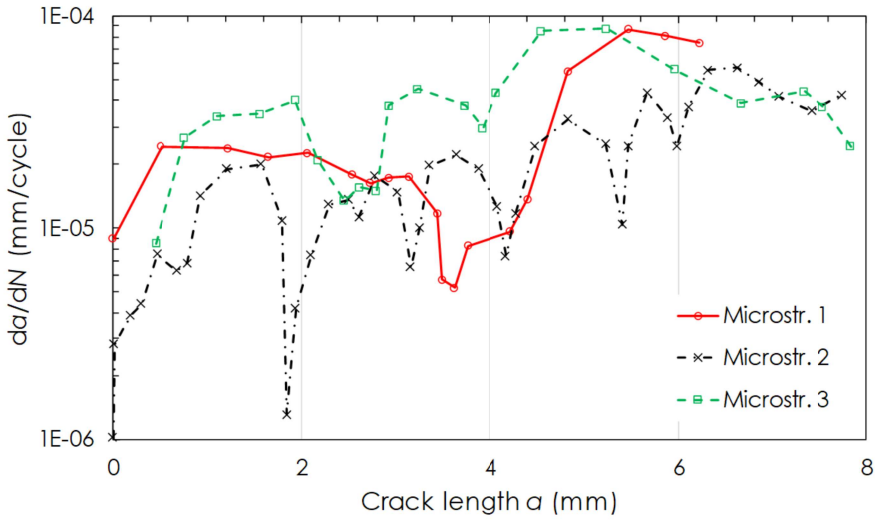

Figure 6: Experimentally observed crack growth rates (da/dN) vs. crack length for three different microstructures [13N].

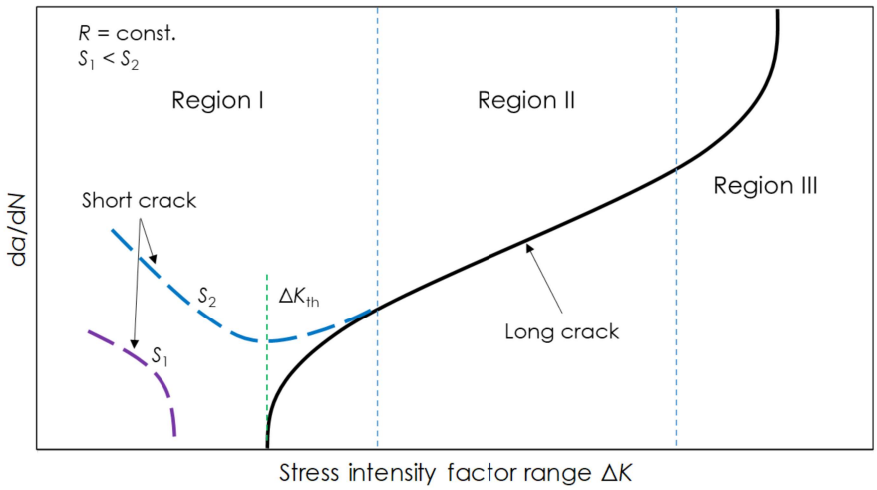

Figure 7: Typical fatigue crack growth behaviour for short and long cracks [99N].

In the long crack regime the fatigue crack growth rate (FCGR or da/dN) can be characterized by a dominant driving force named as stress intensity factor range (ΔK). A typical fatigue crack growth rate curve for the long crack, commonly called as da/dN versus ΔK curve, is illustrated in Figure 7. The curve is defined by three different regions – Region I, II and III [09B, 11B]. Region I, or already discussed Stage I, represents the early development of the fatigue crack where its growth rate is typically of the order 1E-12 mm/cycle or lower. This region is highly influenced by the crack growth threshold (ΔK_{th}) or the values of ΔK below which the requirements for the long fatigue crack growth are in practice not satisfied. Region II, or Stage II, represents the intermediate crack propagation zone where the crack propagates as long crack and where the length of the plastic zone ahead of the crack tip is large compared to the mean grain size, but still much smaller than the crack length. Region II is characterized by a linear relationship between log(da/dN) and log(ΔK), corresponding to stable crack growth. The crack growth rate is typically in the order of 1E-12 to 1E-09 mm/cycle. Region III represents the fatigue crack growth at very high rates – typically higher than 1E-09 mm/cycle – that is associated with unstable crack growth, which ends with final fracture. The corresponding stress level at the crack tip just prior to final fracture is very high and causes a large plastic zone in its vicinity [01K, 11B].

When compared to the long crack growth, short cracks usually exhibit a faster growth than predicted on the basis of the long crack methodology. They even grow below the threshold of stress intensity factor (ΔK_{th}) for long crack. The dashed blue lines lying to the left of the long crack curve giving quite high growth rates are given schematically in Figure 7. The fast growth rate of short cracks has often been attributed to reduced crack closure with respect to the long crack regime where the closure is caused by residual plastic deformation (i.e. plastic zone) left in the wake of an advancing crack [01K].

Another interesting observation with respect to the growth rate of short cracks is that it gradually decreases as approaching the long crack regime (blue dashed

lines in Figure 7). The explanation for this could be that with time, the number of grains that are favourable for cracking reduces. However, as the length of a dominant short crack increases, its data points eventually approach the long crack curve, being coincident with it, what represents the transition from Stage I to Stage II [80K]. The transition from short crack growth to long crack growth depends, however, on the magnitude of applied load (Figure 7). If the magnitude is insufficient, e.g. S_1, for the transition, the dominant short crack arrests.

Nowadays there are two common approaches used in experimental studies to evaluate fatigue damage in its early stages: The first one [06E, 14D, 14L] gives discontinuous evaluation of fatigue damage at the surface by scanning electron microscopy (SEM) in combination with EBSD. After certain numbers of cycles the specimens are periodically removed from the testing machine and the damage-affected areas are examined in a scanning electron microscope using electron channelling contrast and automated EBSD to evaluate short crack lengths and the crystallographic orientations of the grains involved.

The other approach is kind of novel [13N, 13L, 15L, 15N, 15O] providing in-situ simultaneous measurement of resonance frequency and crack growth by using optical and DIC techniques without the need to stop the tests. This technique allows an accurate relation between the two parameters to be established without the need for estimations or changes in the loading conditions during testing. These techniques allow the measurement of the crack length and growth as well as interactions of cracks with the microstructure, as depicted in Figure 6.

Figure 8 shows an example of a bicycle pedal crank, which failed under fatigue loading conditions. As depicted at the right side of the figure, the fatigue crack initiated at the location of the maximum tensile bending stress generated by the force on the pedal, close to the crank axle on the tensile side of the crank. After the initiation completion (Stage I), the crack propagated (Stage II, bright area on the right side of the fracture surface in the right image) slowly through the crank arm until the moment when the remaining ligament was not capable any more to bear the bending moment and the crank arm fractured rapidly (dark area on the left side of

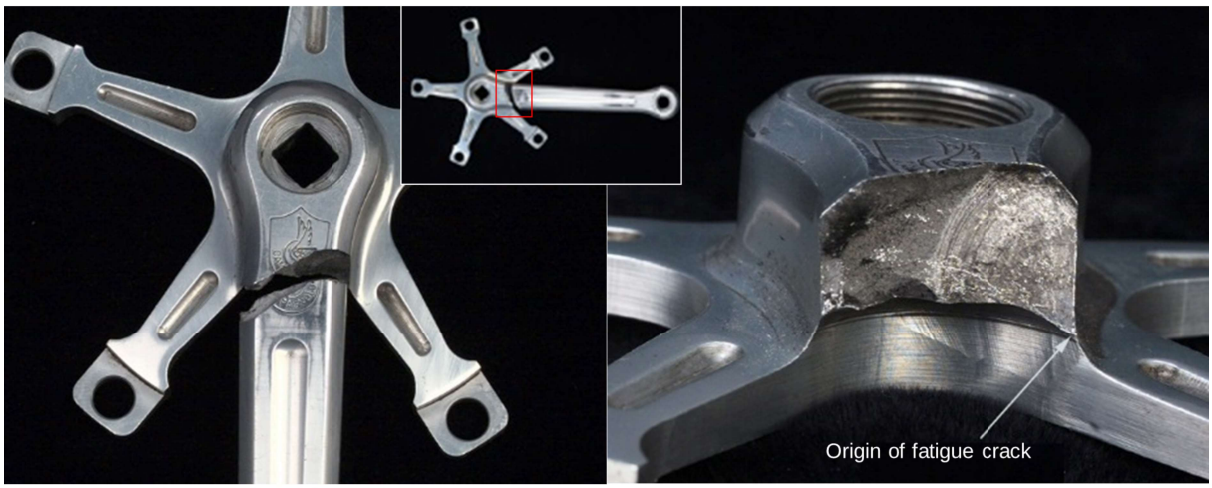

Figure 8: Fatigue failure in a bicycle pedal crank [05O].

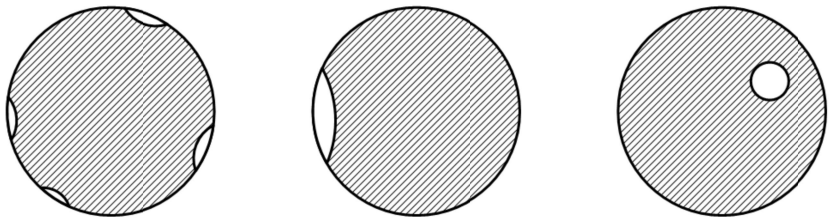

Figure 9: Difference in crack initiation site depending on the applied fatigue regime: Left – Low-cycle fatigue (LCF); Middle – High-cycle fatigue (HCF); Right – Very high-cycle fatigue (VHCF) [09E].

the fracture surface in the right image). The fatigue crack in this common component took a considerable time to nucleate from a machining mark and eventually to break apart. Such unfortunate incidents can be however prevented by periodic inspections or by predicting them by means of fatigue assessment methods [05O].

As visible in the upper crank example, fatigue crack nucleation does not invariably occur only at slip bands. Machining marks or second phase particles and inclusions in the microstructure are common crack nucleation sites, too. Crack nucleation sites also depend on the applied fatigue regime. At low-cycle fatigue (LCF; failure at around 1E04 cycles) and at high-cycle fatigue (HCF; failure at around 1E06 cycles), cracks usually nucleate at the surface or in the area close to the surface while in the very high-cycle fatigue (VHCF; failure at around 1E08 cycles) they nucleate inside the material, triggered by an inclusion or a void (see Figure 9) [09E].

4.2 Characterization of the Fatigue Process

The first reported method for characterizing the fatigue life emerged from the work of the German scientist August Wöhler [60W, 70W]. Wöhler developed curves known by his name, i.e. Wöhler curves, during the investigation of a train accident in Versailles, France, 1842, where the axle of the train locomotive failed on the railroad during the everyday service. As introduced already in Section 4.1 as a typical fatigue characteristics, this incident happened also under the repeated "low level" cyclic stress, which was lower than the ultimate strength and/or yield strength of the material used to manufacture the axle [16H]. Soon after, Wöhler introduced an apparatus for testing the railroad axles under repeated loads. This allowed him to plot the relationship between alternating/cyclic stress levels *S* and number of repeated cycles *N* to failure in controlled conditions. As Wöhler curves plot the relationship of *S* against *N*, they are often called simply as *S-N* curves.

Until the Versailles accident, engineers were confident about designing axles to withstand the static loads resulting from bearing a train during active and inactive service. They shared the opinion that an axle should carry the weight of a train without exception. However, the opinion has changed after the accident. For a majority of the investigators at that time, it seemed unpredictable when an axle might suddenly fail, as the concept of low level cyclic stresses, repeated over a long time, was relatively new and not well understood. This has changed after Wöhler intro-

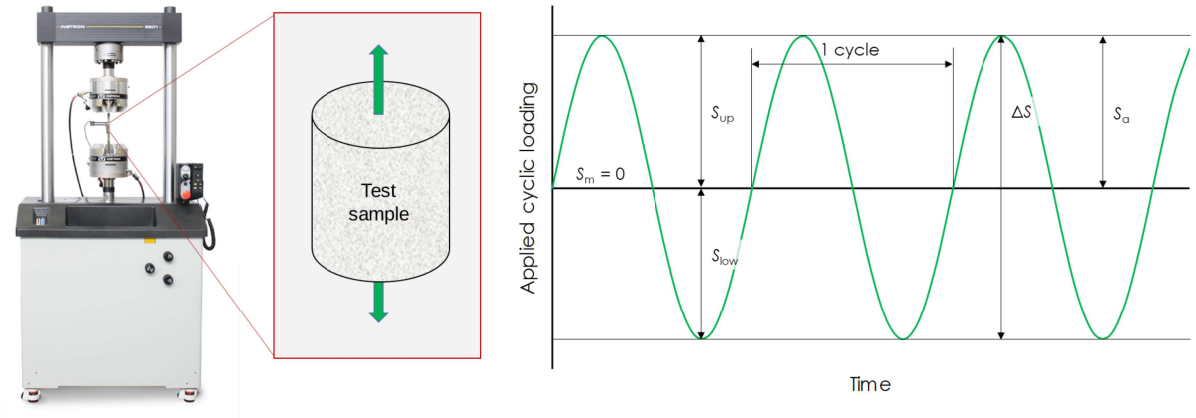

Figure 10: Left – Fatigue testing machine used to create fatigue life (S-N) curves for materials; Right – Fully reversed tension-compression loading, often referred to as a standard cyclic stress time history (S_m – mean stress, S_{up} – upper value of the applied stress range, S_{low} – lower stress value, ΔS – applied stress range, S_a – stress amplitude) [16H].

duced his fatigue life or *S-N* curves, what allowed the prediction of fatigue life in a relatively consistent manner. These curves are nowadays often produced by using fatigue testing machines. Namely, a test sample is placed into the machine and subjected to a cyclic (or alternating) stress time history (see Figure 10) until a crack or failure occurs. Several specimens need to be tested at different stress levels to create a complete *S-N* curve. Figure 11 gives an example of an *S-N* diagram with a curve derived from testing of metal specimens; typically, both the stress (*S*) and number of cycles (*N*) are displayed on logarithmic scales [16H].

In the case the stress cycles are completely reversed as shown in Figure 10, i.e. the mean stress S_m is zero and the loading ratio R (= S_{low} / S_{up}) is equal to –1, the ap-

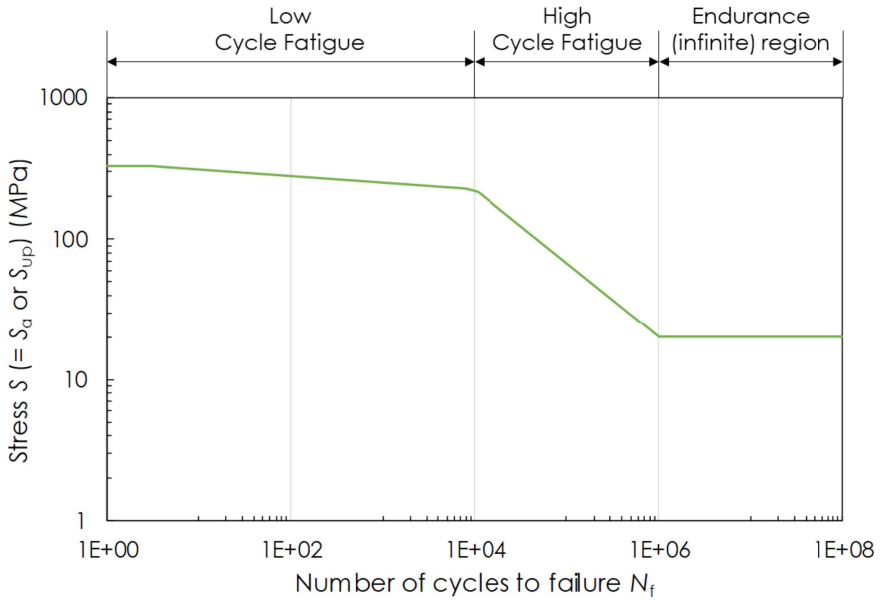

Figure 11: Schematic S-N curve for the standard loading case R = –1 (S_m = 0) showing that higher stress levels result in lower numbers of cycles to failure [16H]. The values of S_a and S_{up} (see y-axis) are equal for the loading ratio R = –1.

plied stress amplitude S_a is equal to the upper stress value S_{up} of the applied stress range ΔS and thus the stress (S) on the y-axis of the *S-N* diagram can be expressed in terms of any of those two stresses, as shown in Figure 11 ($S_a = S_{up}$). For this specific case, it is not required to put any additional information about the magnitude of S_m or R in the *S-N* diagram. In other words, if the *S-N* diagram does not contain any information about the S_m or R value, it means that they are equal to 0 and -1, respectively. However, the stress conditions in many practical cases often consist of an alternating stress and a superimposed tensile or compressive mean stress [18A]. In this case when $S_m \neq 0$ (i.e. $R \neq -1$) again both stresses, the S_a and S_{up}, can be used on the y-axis, however, the applied S_m or (more often) R value needs to be indicated in addition. It is noteworthy that both diagrams, the S_a-*N* and the S_{up}-*N* diagram, have similar relevance for the characterization of fatigue behaviour of technical materials due to the fact that one can be handily transformed into the other one, and vice versa. Therefore, the user is advised to apply that diagram, which better fits his/her current needs. The reader is advised to see Section 5.3 for more details on the difference between the two diagrams and on the effect of the mean stress on their *S-N* data. In further text the S_a-*N* diagrams are used as is done mostly in literature and theses diagrams are denoted simply as *S-N* diagrams. The current methods for determining the *S-N* curves is given in detail in ASTM Standards [ATM].

An *S-N* curve generally slopes downwards from the upper left to the lower right part of the *S-N* diagram. This indicates that high level stresses are accompanied with fewer number of cycles to failure compared to lower level stresses. Aside of that, an *S-N* curve falls typically into several different regions: a plastic region, an elastic (definite life) region and an infinite life region below the fatigue (endurance) limit, as shown in the left image of Figure 12 [16H].

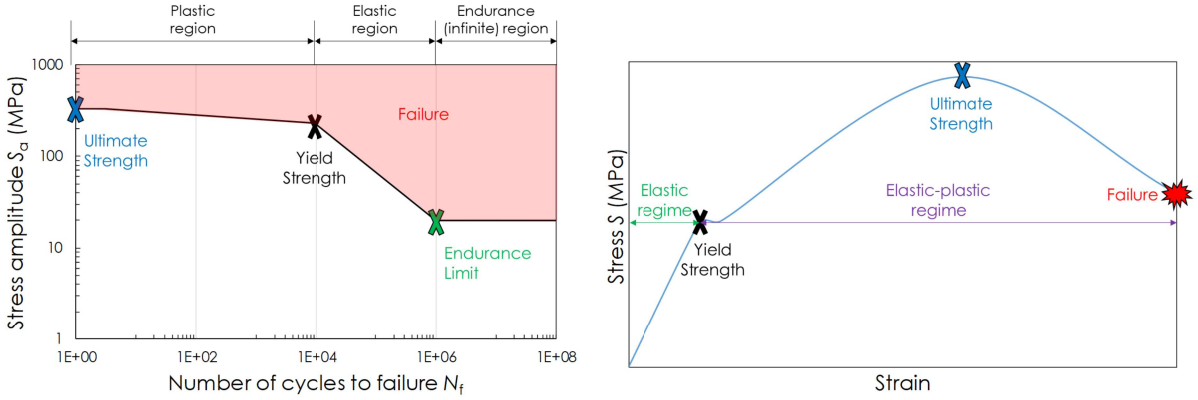

Figure 12: Left – Relevance of ultimate strength, yield strength and endurance limit for the S-N curve; Right – Ultimate strength and yield strength are determined by using static stress-strain tests (schematic curves) [16H].

There are three key values that separate these regions, as depicted in Figure 12:

- Ultimate strength (S_u): Stress level required to fail with one cycle
- Yield strength (R_e): Dividing stress between elastic and plastic region
- Endurance limit (S_e): Stress corresponding to the horizontal asymptote

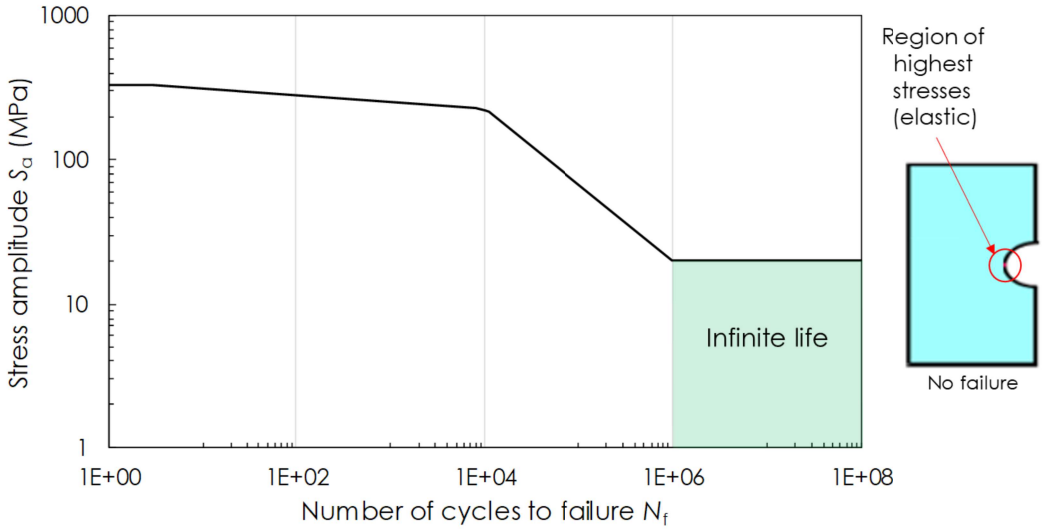

Figure 13: Left – Schematic S-N curve showing the infinite life region; Right – Specimen operating in the infinite life region [16H].

If the applied cyclic stresses are below a certain level, i.e. below the endurance limit (horizontal asymptote in Figure 13), an "infinite" number of cycles (green area in Figure 13) can be reached without causing a failure in a specimen or component. Tests are, however, not performed for an infinite number of cycles in real life experiments, but up to a few millions of cycles, typically up to 1E08 [16H]. The "infinite" needs to be taken with caution as failure at extremely high numbers of cycles has been recently detected in the case of VHCF [10C, 12W, 16T].

Table 1: Fatigue ratios for a number of materials in various crystal systems, data from [71G].

Lattice	Material	S_u (MPa)	S_e (MPa)	S_e/S_u
Body-centred cubic (BCC)	W	1,372	834	0.61
	Mo	696	500	0.72
	Ta	308	265	0.86
	Nb	294	225	0.77
	Fe (+0.2% Ti)	265	182	0.69
	Mild steel (0.13% C)	421	224	0.53
	AISI 4340 steel	1,103	482	0.44
Face-centred cubic (FCC)	Ni	303	108	0.36
	Cu	301	110	0.37
	Al	90	34	0.38
	AA 2024-T3	483	138	0.29
	AA 7075-T6	572	159	0.28
Hexagonal close-packed (HCP)	Ti	703	414	0.59
	Co (+0.5% Ti)	521	165	0.32
	Zn	145	26	0.18
	Mg	182	30	0.16

Critical components, like engine crankshafts and rods, are typically designed to operate in the infinite life region. In order to reach the infinite life of such components, all the imposed cyclic stress levels must be below the endurance limit. As ex-

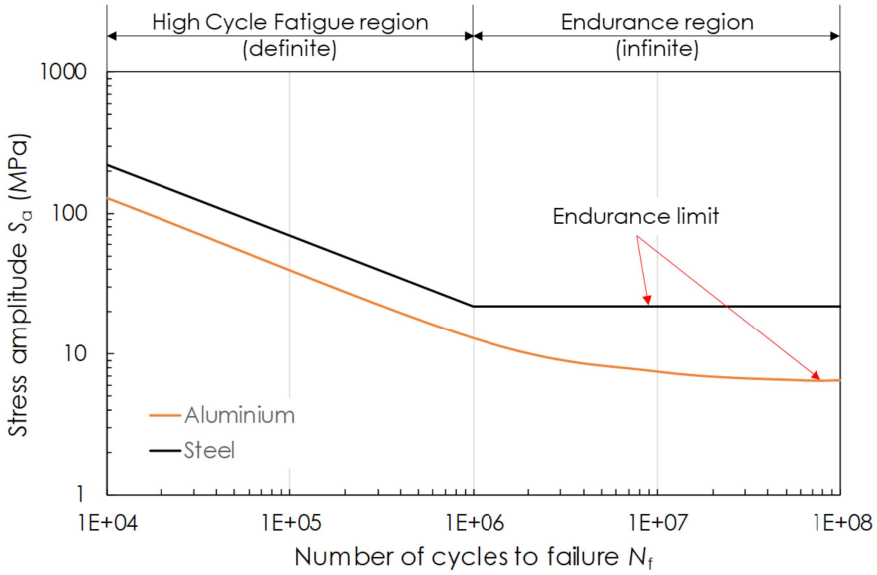

Figure 14: Non-well defined endurance limit of aluminium (orange) in contrast to the well defined limit of steel (black) [16H].

pected, different metals have different endurance limits; some typical values are shown in Table 1.

As Figure 14 depicts, many non-ferrous metals and alloys (e.g. aluminium, magnesium, and copper) do not show well-defined endurance limits, in contrast to ferrous alloys. More details on this topic can be found in Section 5.2.3.

In the elastic region (yellow area in Figure 15), stresses relate to strains in a linear manner, meaning that the material returns to its original shape and/or length upon application and removal of a cycle. This region is also known as the HCF region since a high number of stress cycles need to pass until the part fails [16H]. The relevant stress value in this region is the fatigue strength, which is the maximum stress a material can withstand repeatedly for a specified number of cycles without failure

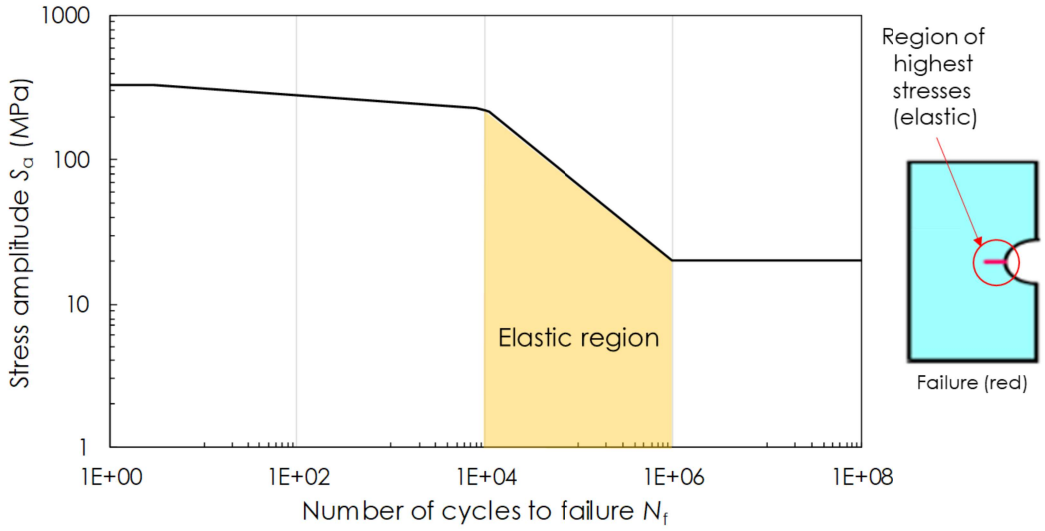

Figure 15: Left – Schematic S-N curve showing the elastic life region, characterized by definite life; Right – Specimen operating in the definite (elastic) life region [16H].

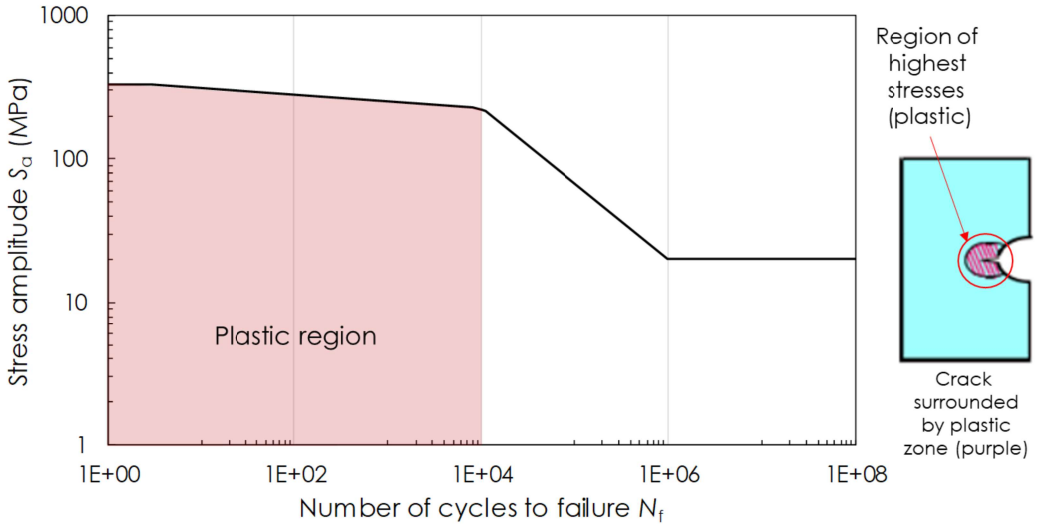

Figure 16: Left – Schematic S-N curve showing the plastic life region, characterized by definite life; Right – Specimen operating in the definite (plastic) life region [16H].

[18A]. Typical factors that influence the performance of a material in the elastic region are residual stresses (see Section 5.4) and geometric considerations like notches (see Section 5.6). Even though the region is named as elastic region, material plasticity might play a role, especially in the upper part, close to the plastic region. This aspect is a topic of a later study, presented in Section 5.7.

In the plastic region (red area in Figure 16), the material is exposed to high cyclic stress levels, leading to irreversible shape and/or geometry changes. This region is also known as the LCF region of the *S-N* curve (see [16Z]), where a low number of stress cycles (< 1E04), accompanied with a high amplitude, lead to failure [16H]. If possible, it is is recommended to avoid subjecting the material to cyclic stress levels that characterize the plastic region. Calculation of the fatigue life or damage in such a case is typically accomplished by using the strain-life approach, which provides *e-N* (strain versus number of cycles) curves as a result of analysis. A strain-life approach takes into account the order or sequence in which varied loads are applied [16H]. Typical components operating in the LCF region are reactor pressure vessels. Those components performing in the HCF region are vehicle door hinges and those in the so-called endurance limit region are gear wheels, crankshafts, or con-rods [18H].

Depending on the relevance, some materials have well-known *S-N* curves while some materials do not. When a new alloy is developed, the *S-N* curve may be completely unknown and, thus, testing is required to determine it. Conventionally, five different stress levels with three repetitions at each level are considered as the minimum when determining an *S-N* curve. With enough experiments, the *S-N* curve consists of a series of results (scatter) around the averaged curve [16H] (see an example in Figure 49). Often is complete fatigue life (N_f) divided into two stages in the *S-N* diagram, namely the number of cycles for fatigue crack initiation (N_{ini}), and for fatigue crack growth or propagation, (N_{pro}), respectively:

$$N_f = N_{ini} + N_{pro} \tag{4.1}$$

Such a representation of these fractions of fatigue life is known as the so-called French curve (Figure 17). As noted by various authors [79I, 00K, 09R, 15M] and in some standard text books [80K, 98S], the portion of the crack propagation period decreases continuously with the decrease of stress level, as visible from the figure. At the HCF region close to the endurance limit (horizontal asymptote), only a small fraction remains. In other words, fatigue crack initiation dominates the complete fatigue life in the HCF regime, especially at lower loading levels. In a study on a fatigued steel, Ibrahim and Miller [79I] also concluded that the size of the short (initiation) crack differs with fatigue life. The lengths of initiated microcracks in the investigated steel decreased with the increase of fatigue life. They lied in the range of a few hundreds of micrometres at higher stress levels and of a few micrometres at stress levels below the French curve [33F, 15M] (see Sections 4.3.4 and 5.1 for more details on the initiation crack length).

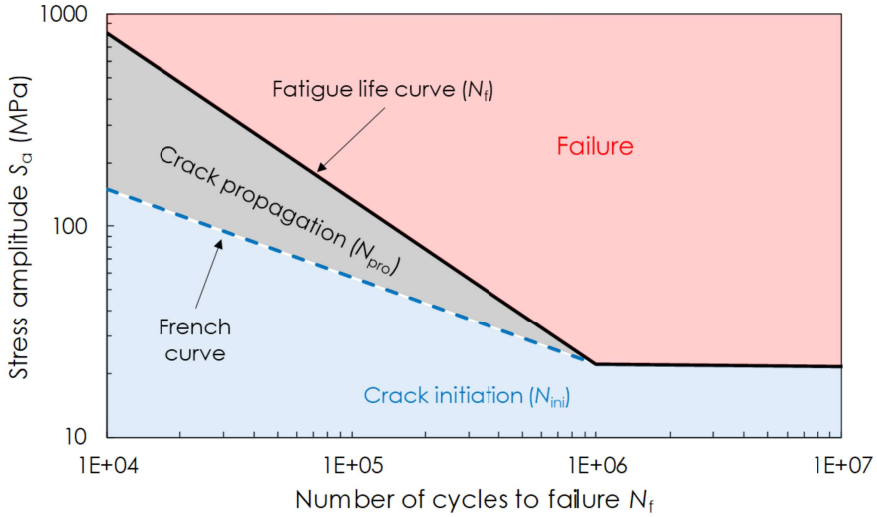

Figure 17: Comparison of Wöhler (fatigue or S-N) and French curve [15M].

To summarize, the different nature of the crack initiation and propagation stages gives rise to the importance of understanding the complete fatigue lifetime and also of being able to estimate the lifetime quantitatively. In connection with this, the application of numerical tools and a quantitative evaluation of the fatigue crack initiation and propagation processes by means of physically-based material and damage models, next to the experimental studies, are of high practical and economical interest. As indicated earlier, the tests should be ideally repeated many times and at many different stress levels to produce reliable *S-N* curve libraries, what can eventually be quite cost demanding. Therefore, it is advisable to apply numerical methods to support or completely replace the experimental efforts.

4.3 Multiscale Modelling and Simulation of Metal Fatigue

Structural health monitoring and detection of failures are highly important for fitness and service assessment of structures. Failure of structures under fatigue loading can occur at load levels below the yield stress of the used material. Therefore, it is of special importance to be able to make predictions of life cycles until catastrophic fracture occurs. On the other hand, not every single crack has to be critical immediately. Often structures can withstand cracks up to a certain crack length until unstable fracture occurs. In order to determine the point where crack growth becomes unstable, it is necessary to develop methods to describe crack growth numerically.

Computational modelling and simulation is the process of representing real world problems in mathematical terms in an attempt to find solutions to their associated complex systems. A formal model is an abstraction of the real world onto a mathematical/computational domain that highlights some key features while ignoring others that are assumed to be secondary. A numerical model should not be considered as representation of the truth, but instead as a statement of the current knowledge of the phenomenon under research. One of the main objectives of any model is to provide a predictive capability, that is, the possibility to make guesses in terms of plausible hypotheses related to the behaviour of the observed phenomenon in different scenarios that are of interest to experts [14P]. With high-speed calculators and the development of computational methods (e.g., finite element method – FEM), simulation has become the favourite design tool, allowing optimization of the investigated system. With mere experiments, it is nearly impossible to investigate the whole design space for understanding still unexplained mechanisms in order to mimic natural processes and make steps towards enhanced application of these mechanisms [15S].

In order to numerically analyse the total fatigue life of a structural component or a test specimen, from crack nucleation within a grain up to long crack propagation and final failure, a proper multiscale materials modelling (MMM) approach is required. Figure 18 shows a schematic description of scales that need to be considered, starting with nanoscale, going up to micro-/mesoscale and ending up with macroscale. The up-to-date nanoscale, i.e. atomistic, modelling techniques like ab-initio [14K, 15K, 16B] or molecular dynamics (MD) [05K, 10P, 11P] can provide relevant material parameters needed at higher scales of fatigue process modelling scheme. One such parameter is the critical resolved shear stress (CRSS) on the relevant, most active slip plane in a grain can be derived from MD simulations, e.g. by using the approach of Hummel [14B, 18B]. The CRSS can be used as the input parameter for the micromechanics-based model providing information on the number of loading cycles to nucleate a microcrack and subsequent growth of a short crack, or in other words comprising both, the number of cycles to initiate the short crack (Tanaka-Mura model [81T, 82T]). These initiation cycles are further transferred to the macroscale fatigue crack growth model based on power law equations (e.g. Paris

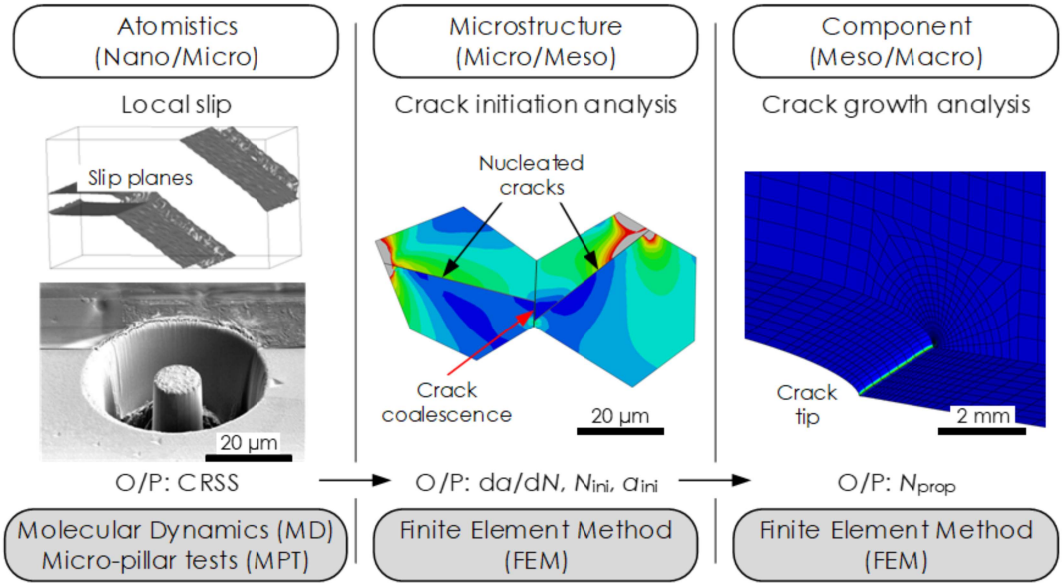

Figure 18: Multiscale materials modelling approach – Coupling of methodologies at the relevant scales, and accompanying outputs (O/P) (CRSS – critical resolved shear stress, da/dN – crack growth rate, N_{ini} – number of stress cycles for crack initiation, a_{ini} – initiation crack length, N_{pro} – number of stress cycles for crack propagation) [16J, 14B, 17L, 18L, ABQ].

law), by means of which then a total fatigue life up to final fracture can be assessed. By using the presented MMM workflow, the fatigue behaviour of a material can be simulated more or less independently of the experimental input, as already done in [14B, 17L, 17M, 17O, 18B, 18M, 18L].

Generally, polycrystalline materials in a microstructurally-based finite element analysis (FEA) are modelled as a two-dimensional (2D) or three-dimensional (3D) aggregate of grains (crystals) with a specified grain size. Material anisotropy can easily be introduced by assigning crystallographic orientations in a prescribed or random manner to each grain in the generated structure. After having modelled the microstructure in a proper way, a crack nucleation model can be used in combination with the FEM to simulate when a grain is likely to form a slip band and subsequently a crack. The driving force for nucleation depends on the orientation of each individual grain with respect to the applied loading and on their location with respect to global stress concentration. Once a crack forms in a grain, several growth scenarios should be considered. First, can the crack grow into the next grain? Can it coalesce with an existing crack in the neighbouring grain to form a longer crack? Under which conditions should the crack arrest at a grain boundary? When the crack growth is not affected by the microstructure any more and by that transforms into long crack? When will final failure occur? [96S] All these questions raise the importance of having comprehensive models (e.g. as given in Figure 18) to realize and quantify each of these scenarios.

Accordingly, the fatigue crack growth modelling procedure in the HCF regime should include the following steps [96S]:

- Microcrack nucleation within a grain;

- Coalescence of already existing microcracks and/or arrest at grain boundaries;
- Short crack or Stage I growth;
- Transition from Stage I to Stage II growth; and
- Long crack or Stage II growth.

Studies on the numerical determination of the CRSS on an atomistic scale are given later in Section 5.2.2, while the relevant crack growth modelling steps are discussed in the following sections.

4.3.1 Crack Nucleation within a Grain

Fatigue crack growth or propagation in engineering materials has been extensively studied for several decades. While the behaviour of the long crack can be quantified using the Paris law [63P] and its numerous modifications [80K, 88B], the growth behaviour of the short crack is still on its way of being completely understood in a qualitative as well as quantitative manner. Hence, using just the data of long cracks in fatigue lifetime calculations of specimens and components where the growth of short cracks represents a large proportion of the lifetime (more than 90% in HCF and VHCF), can lead to considerable overestimates in the fatigue lives. Some authors like Haddad et al. [79H] and Chapetti et al. [03H] proposed models based on linear-elastic fracture mechanics (LEFM) to describe the behaviour of short cracks. However, the disadvantage of these models is that they do not take into account microstructural features like grain size, microstructural texture, etc. A huge benefit of microstructurally enriched and physically-based numerical models is that they enable the growth behaviour of short cracks to become more and more quantitatively and qualitatively understood. Such models can be found in several papers like in [10M, 14C, 14T, 16D, 17G] etc.

A physical model based on dislocation theory of a double pile-up proposed by Tanaka and Mura in 1981 [81T, 82T] is often used to determine when a grain will develop a slip band and subsequently a crack [96S]. This model receives its popularity because it captures the essence of crack nucleation via dislocation slip and predicts the dependence of fatigue crack nucleation life on the cyclic plastic strain range $\Delta\overline{\tau}$, which agrees with the Coffin-Manson relationship [18W]. According to the Tanaka-Mura (TM) theory of fatigue crack nucleation, the forward and reverse plastic flows within slip bands under cyclic loading are caused by dislocations with different signs moving on two adjacent crystallographic planes. It is assumed that their movements are irreversible. Based on this model, the monotonic build-up of dislocations is systematically derived from the theory of (continuously distributed) dislocations. The number of loading cycles up to the nucleation of a crack about one grain diameter in length is reached when the self-strain energy of the accumulated dislocation dipoles reaches a critical value. The number of cycles required for microcrack nucleation (N_g) in a single grain (g) can be determined using the TM equation [81T, 82T]:

$$N_g = \frac{8GW_c}{(1-\upsilon)d(\Delta\bar{\tau} - 2CRSS)^2} \tag{4.2}$$

Equation (4.2) presumes that microcracks form along slip bands of grains, depending on the slip band length *d*, and average shear stress range on the slip band $\Delta\bar{\tau}$ [10G, 10N]. When Equation (4.2) is included in an FEA (see Appendix I, Section 7.1), the $\Delta\bar{\tau}$ is an input to it from the FEA and accordingly attains a key role in the simulation of the fatigue crack nucleation process. Other material constants, such as shear modulus *G*, crack initiation energy W_c, and Poisson's ratio υ, can be for most materials either found in literature or obtained experimentally, when required. The crack initiation energy is the value of the *J*-integral at the moment when the first crack nucleates inside a material; often given in literature as J_i [88R, 98D]. The CRSS is particularly interesting because it can be obtained by means of the lately popular micropillar test (MPT) [13B, 13O, 16O, 17P] or alternatively by MD simulations [14B], as already introduced in Section 4.3. The CRSS represents a critical value of the shear stress along the glide direction that must be overcome for the dislocation to move. If the resolved shear stress is lower than the CRSS, no dislocation movement is allowed and, consequently, no pile-up at the grain boundary is produced in the grain. The value of the CRSS depends on the mechanisms that rule the dislocation motion on the slip plane, including the interaction with obstacles such as dissolved atoms or fields of fine precipitates [59A, 08B]. More details on the CRSS and its importance in the fatigue performance of steels and other metals are given in Section 5.2. Furthermore, the theory behind the TM equation (Eq. 4.2), including the irreversible dislocation motion (Figure 19), is given in Appendix II (Section 7.2).

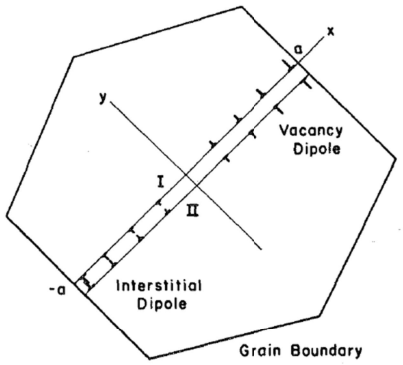

Figure 19: Dislocation motion in a most favourably oriented grain [81T].

Several authors [98H, 06B, 07G, 12B, 12N, 13G, 13K, 14B] used TM equation-based FEM models to simulate the Stage I crack growth process. Significant work was done by Jezernik et al. [10G, 10N] who introduced a numerical model for fatigue crack initiation in high strength martensitic structural steel S960QL based on the improved TM equation. In this work the TM equation has been implemented into the FEM-based software Abaqus, by a plug-in (written in Python programming language) that has been developed especially for handling microcrack nucleation and coalescence, i.e. crack initiation, inside a model containing the microstructure of a metallic material. Furthermore, an FEM model containing a microstructure (i.e. an aggregate of

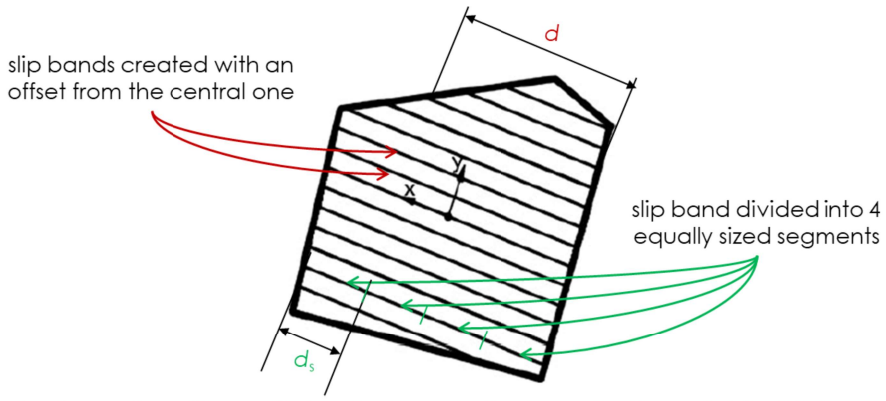

Figure 20: A single grain with multiple slip bands that are further divided into several equally sized segments. [10G, 10N]

grains) was enhanced in the way that each grain was filled in with multiple slip bands. The slip bands of a certain grain have the same orientation and are equi-distanced one from each other with an offset, as shown in Figure 20.

According to Figure 20, each slip band of each grain in a polycrystal is divided into equally-sized segments. This means that in each simulated sequence, solely one slip band segment of a particular grain gets cracked but also if a segment belonging to one grain cracks in one sequence, it can happen that in the succeeding sequence a segment belonging to another grain breaks [17L, 17M]. Segments belonging to different slip bands have accordingly different lengths. Consequently, the original equation, (Eq. 4.2), was adjusted by replacing the grain-breaking cycles, N_g, by segment-breaking cycles, N_s, and slip line length, d, by slip line segment length, d_s [10G, 10N]:

$$N_s = \frac{8GW_c}{(1-\upsilon)d_s[\Delta\bar{\tau}_s(1-R)-2CRSS]^2} \tag{4.3}$$

In the case of this modified Tanaka-Mura equation (in further text: TM equation/ model) the average shear stress range on the slip line segment $\Delta\bar{\tau}_s$, is an input from FEA. Additionally, the original equation was extended by a factor $(1 - R)$, taking into account the loading ratio sensitivity, R value [10N].

By decomposing Equation (4.3) with respect to its constitutive parameters, they can be divided into two groups. One group composes those parameters, which remain constant throughout the analysis. The non-varying parameters are material constants; namely the shear modulus G, the crack initiation energy W_c, Poisson's ratio υ, and the CRSS. The other group comprises parameters that vary from segment to segment. Those segment-specific parameters are the length d_s of a segment and the average shear stress $\Delta\bar{\tau}_s$ that acts along the segment. The d_s and $\Delta\bar{\tau}_s$ act accordingly as differentiating factors between the segments. As already hinted, the $\Delta\bar{\tau}_s$ is an input to Equation (4.3) from an FEM-based analysis and accordingly has one of the key roles in the simulation of the fatigue crack nucleation process. The variance of d_s is depicted and explained in Figure 20.

4.3.1. Crack Nucleation within a Grain

The following text explains, on the example of a single grain (see Figure 21), how the modified TM equation is implemented into FEM-based modelling. A single grain has been isolated from an aggregate of more grains and is used to explain the segmented cracking in more details. Generally, in the microstructural model consisting of an aggregate of grains, a crack can form on different slip band segments of the grains inside the model depending on the stress field inside and in the vicinity of the grains. The stress field in a grain is influenced by loading and boundary conditions (typically transferred from a global model), microstructural configuration (shape and orientation of each individual grain), material properties (e.g. elastic constants) and geometrical factors (e.g. presence of a notch and/or voids in the microstructure, as well as the presence of already formed cracks etc.). The slip band segment with highest stresses, i.e. the potentially weakest segment over which a first microcrack is expected to nucleate, is identified by using the Abaqus plug-in that incorporates the TM model, Equation (4.3) [10G, 10N]. Such a segment can be located in a grain lying at the surface or in a grain from the area close to the surface [03L, 14M] of a specimen/component operating under HCF regime conditions (see middle image in Figure 9). The criterion for the identification of the weakest segment says, according to the TM equation, that the absolute value of $\Delta\overline{\tau}_s$ has to be higher than two times the CRSS ($\Delta\overline{\tau}_s$ > 2CRSS). Namely, the denominator of the equation contains the factor ($\Delta\overline{\tau}_s$ – 2CRSS), which is the indirect explanation for the criterion: The slip band segment that fulfils the criterion and which, next to that, needs the lowest number of cycles to nucleate the crack according to the TM model gets cracked. The microstructural model is remeshed after introducing a newly nucleated crack and the process is repeated until the moment when there are no more segments favourable for cracking.

Figure 21 shows the formation of a crack throughout the whole grain together with accompanying stresses inside the grain, which eventually cause crack formation. The top left image in Figure 21 depicts the undamaged grain and the orange solid line shows that $\Delta\overline{\tau}_s$ varies inside of it. The reader can notice the presence of a stress concentration in the same image, visible by red and turquoise colours. These high stresses indicate the location where a slip band could be activated and, accordingly, where a crack could nucleate along the activated slip band. Upon activation of a particular slip band in a grain, new cracks can form in that grain only along the activated slip band. Furthermore, all segments of the activated slip band have the same length (d_s). In such an isolated case, the d_s can be grouped in the list of the constant parameters, while the $\Delta\overline{\tau}_s$ remains the only variable in Equation (4.3), i.e. the only differentiating factor between the segments. This means in particular that there can be more segments on the activated slip line that fulfil the stress criterion (i.e. $\Delta\overline{\tau}_s$ > 2CRSS, where 2CRSS is represented by the red dashed line in Figure 21). However, the sequence of breaking depends on the magnitude of $\Delta\overline{\tau}_s$. This means that the segment with the highest $\Delta\overline{\tau}_s$, and according to Equation (4.3), with the lowest number of cycles for the formation of a crack is the one which breaks first.

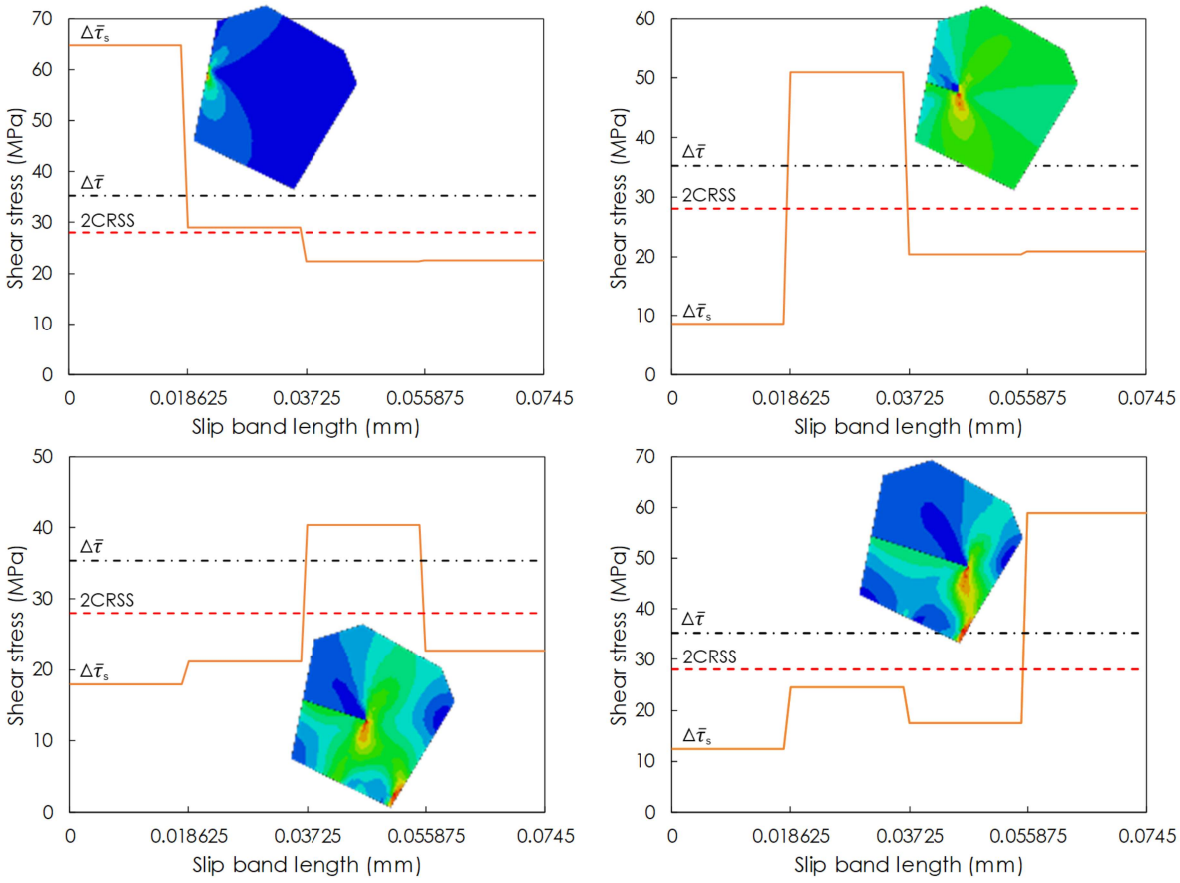

Figure 21: Segmental crack growth – Shear stress distribution along a cracked/uncracked slip band.

Upon nucleation of a first segmental crack in the microstructural model or, in this case, in the isolated grain (top right image, Figure 21), the cycles required to nucleate a new crack are again calculated for all slip line segments on the basis of the new stress field that is locally influenced by the newly nucleated crack. Stresses either relax (dark blue colour) or increase (red colour) in the neighbouring segment/ segments. The new stress field can also change the likelihood of some grains for the crack formation, in both directions. In the same manner as in the case of the undamaged microstructure, the next segment that is stressed beyond the 2CRSS and that needs a minimal number of cycles for crack nucleation is identified and a crack is introduced in the model. Figure 21 contains four simulation sequences where the stress range surpasses the criterion for the nucleation and accordingly the microcrack progresses through all segments and is finally formed along a whole slip band. The line representing an average shear stress along the whole slip band $\Delta\bar{\tau}$ (black dot-dashed line) shows the significance of using segmental cracking; Namely, in the non-segmental case, the crack would nucleate instantaneously throughout the whole grain as $\Delta\bar{\tau}$ is higher than the required threshold value (red dashed line) [10G, 10N]. In another non-segmental case, $\Delta\bar{\tau}$ might be just slightly lower than the 2CRSS leading to no crack nucleation. However, by applying the segmental growth in such a situation, there could exist a particular segment whose $\Delta\bar{\tau}_s$ is higher than the

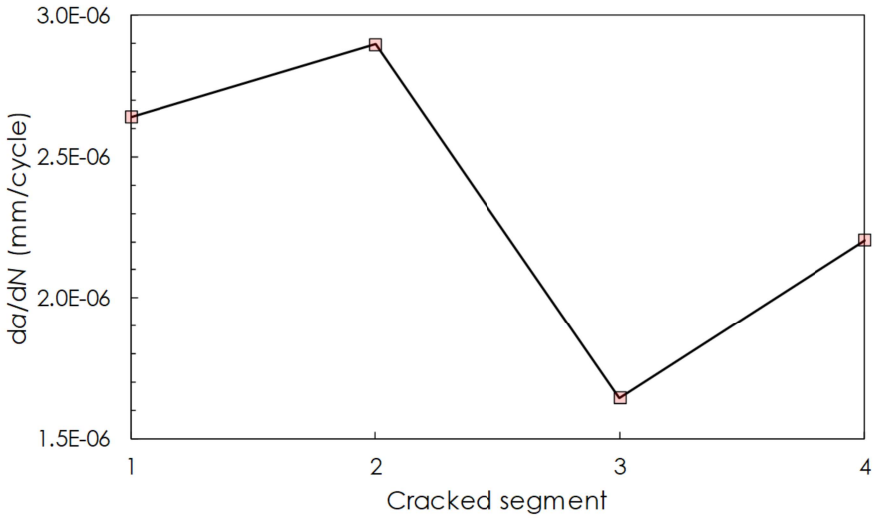

Figure 22: Segmental crack growth rate in a single grain.

2CRSS, what would trigger the nucleation of a crack on that segment of the slip band.

Each crack segment (i.e. microcrack) is formed in the grain model in a separate simulation run, i.e. sequence. Furthermore, after the crack condition has been satisfied in one simulation sequence, the model is updated with the latest crack and remeshed for the following sequence where the condition is applied again and a new weakest slip line segment is traced. The crack generation and remeshing process are done automatically by the Python-based Abaqus plug-in in every single sequence – by entering the Interaction (Seam Crack option) and Mesh module (Mesh option) of the software Abaqus. The simulation sequences run automatically one after the other, too.

Every segmental crack that forms in the micromodel on the basis of the TM equation (Eq. 4.3) possesses its length, da, and its formation lifetime, dN. The length da can be quantified using the Abaqus graphical interface or can be rather gathered from output data. By taking the measured da and the corresponding dN, one can derive the da/dN (fatigue crack growth rate) for each formed crack. Such a crack growth rate curve plotted as a function of the number of broken slip band segments can be seen in Figure 22 for the single-grain example discussed above. One can notice easily that the crack growth rate develops in an oscillating manner, similar as in Figure 6, which shows the da/dN of an aggregate of grains. The significance of this oscillating manner of the crack growth for the fatigue life prediction is discussed in more details in Section 4.3.4.

Since the Stage I of the fatigue crack growth, containing microcrack nucleation and subsequent short crack growth, is one highlight of this work, details about it are given in the following section.

4.3.2 Stage I Growth of Fatigue Crack

After the crack has formed in a single grain, as in Figure 21, however, this time in an aggregate of more grains, it has three available options to take; it can arrest at the grain boundaries, it can propagate into the neighbouring grain by triggering the nucleation of a new crack in that grain or it can coalesce with already existing crack in the neighbouring grain. Which option will be realized depends on the interaction between the crack and the affected grain boundary. Several authors [00Z, 03L, 03Q, 12M] performed experimental as well as numerical investigations on that interaction. In [00Z], Zhai et al. pointed out the twist and tilt angles (see Figure 23) of the crack-plane deflection at a grain boundary as the key factors that control the path and growth rate of a crack. A grain boundary with a large twist component could cause a short crack to arrest or branch. Ludwig et al. [03L] used Synchrotron Radiation X-ray microtomography to visualize and analyse simultaneously the 3D shape of crystallographic grains containing a short fatigue crack in a cast Al alloy. The 3D analysis of the crack with respect to the grain structure indicated that the passage of the crack into a new grain occurs preferentially from regions on the grain perimeter, where the growth can be accommodated by tilting of the crack plane. On the contrary, the crack has difficulties in entering a new grain from regions where twisting of the crack plane is required and tends to grow along the grain perimeter. Qiao et al. [03Q] reported that the twist misorientation across a high angle boundary has a more profound effect on cleavage fracture resistance than the tilt misorientation. Miao et al. [12M] performed investigations on a polycrystalline nickel-base superalloy and noted that most fatigue crack nucleation grains are located within grain clusters within which misorientations between grains are less than 20°.

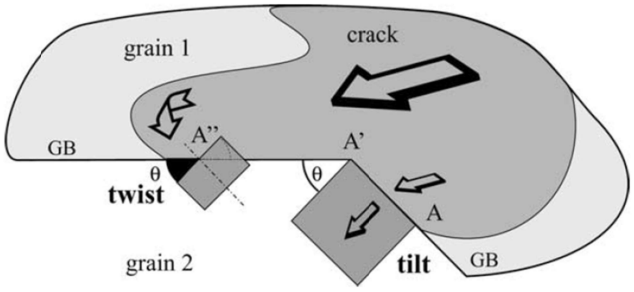

Figure 23: Crack growth across grain boundaries [03L].

Besides the aforementioned studies on roles of the tilt and twist angles in crack arrest/coalescence, Murakami and Endo [86M] have conducted extensive investigations on the threshold behaviour of short cracks. Their data suggest a threshold condition for coalescence that is determined by the grain size and endurance limit of the material:

$$\Delta K_{thgb} = Y \Delta \tau_n \sqrt{\pi d/2} \qquad (4.4)$$

where $\Delta\tau_n$ is the shear stress endurance limit, Y is a geometry factor and $d/2$ is the maximum distance along a single grain facet.

Similarly, it was reported in [96S] that two cracks in neighbouring grains in AISI 1045 medium carbon steel will coalesce when a threshold condition is satisfied and when the distance between their crack tips is less than some critical distance r, as shown in Figure 24. The maximum distance along a single grain facet r would be $d/2$ based on experimental observations of the cracking behaviour in this material. If these conditions are not satisfied, the crack arrests at the grain boundary.

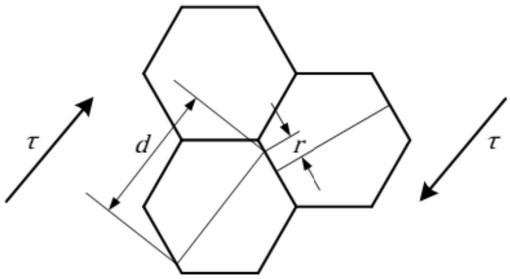

Figure 24: Crack coalescence [96S].

On the other hand, Jezernik et al. [10G, 10N] used a relatively straightforward criterion for the coalescence of transgranular cracks in the numerical simulation of crack initiation on the basis of the modified TM equation (Eq. 4.3). Namely, if two microcracks meet each other at the same grain boundary (red solid line in Figure 25) and if the average stress in between their tips surpasses the elastic limit R_e of the material (in this case pure iron with R_e = 260 MPa, grey area in Figure 25), a grain boundary crack is created on this line, effectively transforming the two transgranular microcracks into a single crack. The coalescence in such cases results in a significant stress relaxation, as visible in Figure 26. As indicated already, intergranular cracks along the grain boundaries occur in rare situations and only if two already nucleated transgranular cracks are located near the same grain boundary. The formation is simulated as being instantaneous and no cycles are prescribed to the event [18L]. Additionally, a crack on the grain boundary cannot be formed without the presence of at least one transgranular crack.

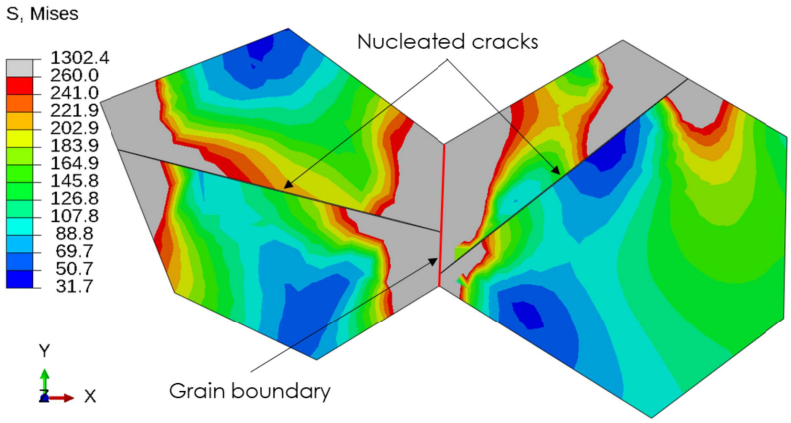

Figure 25: Transgranular cracks from neighbouring grains sharing the same grain boundary (red solid line).

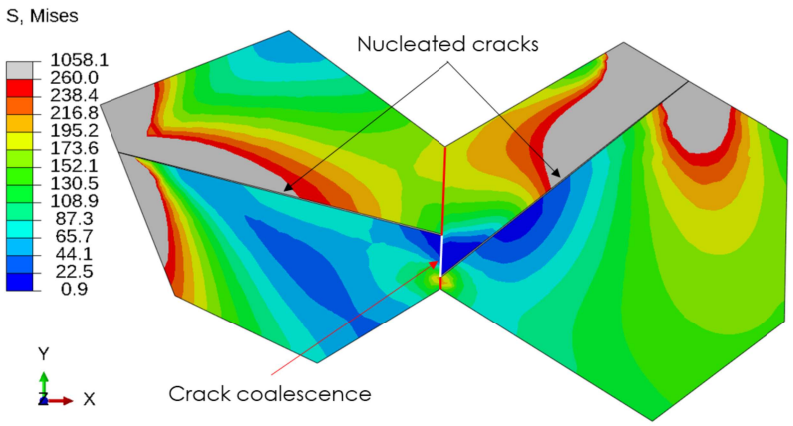

Figure 26: Simulation of crack coalescence.

By combining the nucleation within a single grain (see Section 4.3.1) with the above-described crack coalescence, the Stage I growth of the fatigue crack (i.e. initiation) modelling in an aggregate of grains (i.e. polycrystal) can be accomplished. In the following, an example of crack development in a polycrystalline model on the basis of the modified TM equation is given. Profound information on material properties, loading and boundary conditions are intentionally left out here since the sole purpose of the example is to present the methodology. Those details can be found in Section 5 where the methodology is applied to concrete cases.

The polycrystalline (microstructural) model is given in Figure 27. The microstructure of the model contains around 250 grains in total, with the average grain size of 60 µm. The size approximately corresponds to a grain size of high purity AA [15L].

Although looking like a 2D model, the microstructural model in Figure 27 is a 3D deformable shell model meshed with membrane elements with reduced integration (M3D4R). The model is created as a 3D representative volume element (RVE) where

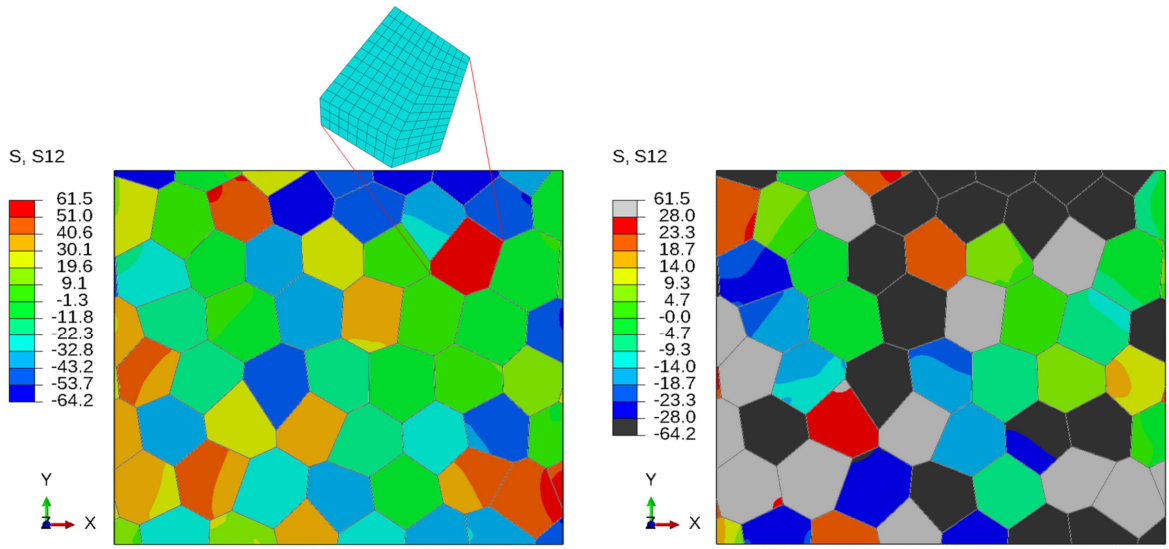

Figure 27: Shear stresses in a 3D deformable shell submodel under tension. Black and grey grains in the right image are favourable for cracking (S12 > 2CRSS).

grains have been generated by the Voronoi tessellation technique [07G] and are meshed with around 170,000 finite elements. According to Abaqus documentation [ABQ], general membrane elements are often used to represent thin components offering strength in the plane of the elements in solid structures, such as a reinforcing layer in a continuum. However, these elements have no bending stiffness, i.e. the stress being normal to the membrane surface (S33) is always zero for membrane elements [ABQ]. Accordingly, they can be used to model a layer of material inside a bulk, taking additionally the microstructure of the bulk into account. Additionally, software Abaqus uses a membrane section definition to define the section properties, including the thickness. The thickness of membranes can be defined as constant or as varying using a spatial distribution. In this specific case, the thickness of the 3D shell submodel is selected to be equal to the average grain size (60 μm), representing in that way a layer of grains in the XY plane, Figure 28. It is visible that each grain has its own local coordinate system.

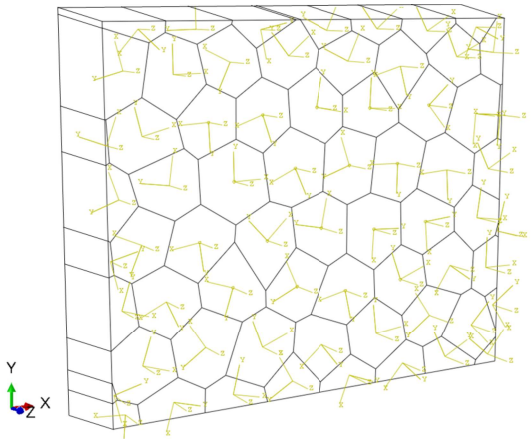

Figure 28: Columnar grains with the (shell) thickness in z-direction equal to the average grain size (in this case 60 μm).

The model has been subjected to an arbitrary loading, sufficiently high to trigger crack nucleation governed by the TM equation. Upon applying the loading, the shear stress distribution has been plotted in Figure 27, with an evident influence of the microstructure. Grey and black grains in the right image of Figure 27 are those where the condition for crack nucleation is satisfied according to the TM model, i.e. the absolute value of average shear stress in those grains is higher than two times the CRSS. In this example case, 2CRSS equals 28 MPa, as the typical value of the CRSS for high purity aluminium is 14 MPa [11N].

As aforementioned, the shear stresses differ from grain to grain as well as inside each individual grain on the segmental level. Based on that, the first microcrack is nucleated along the grain slip line segment with the shortest lifetime estimated using the TM equation. This means in particular that there can be more segments in the model that fulfil the stress criterion ($\Delta\overline{\tau}_s$ > 2CRSS), however, the sequence of breaking depends on the sequence of fulfilling the condition with respect to the lowest number of cycles for the formation of cracks. Aside of $\Delta\overline{\tau}_s$, the cycles are influenced by the segmental length d_s (see Eq. 4.3), which varies from grain to grain in the polycrys-

talline model. The $\Delta\overline{\tau}_s$ is an input to Equation (4.3) from the FEM analysis and accordingly has one of the key roles in the simulation of the fatigue crack initiation process.

Upon nucleation of a first segmental crack in the model, the cycles required to nucleate a new crack are again calculated for all grains and all slip line segments in the microstructure on the basis of the new stress field that is locally influenced by the newly nucleated crack. The new stress field can also change the likelihood of some grains for the crack formation, in both directions. In the same manner as in the case of the undamaged microstructure, the next segment that is stressed beyond the 2CRSS and that needs a minimal number of cycles for crack nucleation is identified and a crack is introduced in the RVE. Each microcrack is formed in the model in a separate simulation sequence. After the crack condition has been satisfied in one simulation sequence, the model gets updated with the latest crack and remeshed for the following sequence where the condition is applied again and a new weakest slip line segment is traced. The crack generation and remeshing process are done automatically by Python-based Abaqus plug-in in every single sequence – by entering the Interaction (Seam Crack option) and Mesh module (Mesh option) of Abaqus software. The simulation sequences run automatically one after the other, too. It is necessary to indicate that all slip planes of a predefined slip system in a grain are considered for crack nucleation until the moment when the weakest one becomes activated. All the remaining parallel slip planes of the grain are not further considered for cracking after the activation of the weakest slip plane. Nucleation of cracks in additional different slip systems remains one point for further development of the modelling scheme.

Figure 29 shows results of the crack development analysis for an arbitrary loading level and after several simulation sequences. The microstructural model contains nucleated cracks, which can be easily perceived with the help of von Mises stress distribution field. Figure 29 Left (L) contains also one isolated grain with a marked

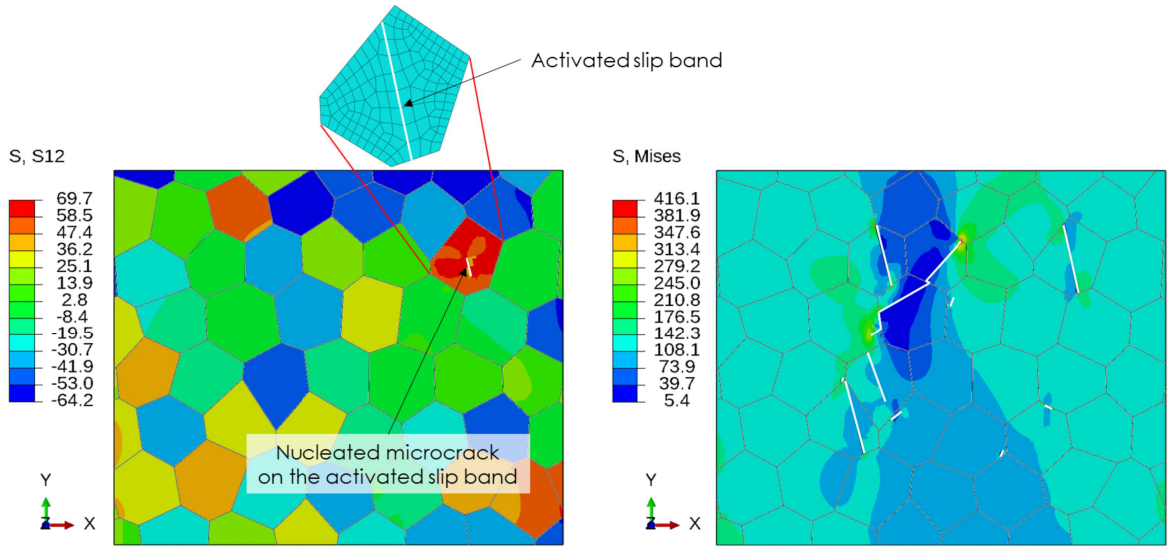

Figure 29: Left – The first fatigue microcrack in a micromodel; Right – Coalescence of existing microcracks in the micromodel.

(black solid line) slip band, which got activated in the first simulation sequence. Concerning the damage evolution, cracks tend to nucleate in the model in a scattered manner and in those grains that are favourably oriented. Under uniaxial loading the planes of cracks are typically inclined approximately 45° to the direction of the applied loading. Already nucleated crack segments tend to extend along the whole grain, causing local stress relaxation as well as concentrations at their tips and by that amplifying the likelihood for new crack formation in the vicinity. In the course of further sequences of simulating, cracks formed along these slip bands grow and link together – as in the example of Figure 29 Right (R).

As already mentioned, the TM model-based microcrack modelling considers just the transgranular cracking. Intergranular cracks along the grain boundaries occur in rare situations and only if two already nucleated transgranular cracks are located near the same grain boundary. In such cases, the yield stress is the cracking criterion and no cycles are prescribed to the event. The intergranular cracking is a topic of further development of the modelling approach.

It is necessary to indicate that the model has been loaded once in tension up to the maximum loading level, not cyclically as one could assume. The damage and resulting cycles to nucleate each individual crack evolve on the basis of the induced stress field inside the model and on the basis of the TM equation. Besides varying the maximum loading level, different loading ratios can be covered by the extension factor $(1 - R)$ in Equation (4.3) [10G, 10N]. More details about the loading ratio (R) influence are given in Section 5.3.

Since the microcrack nucleation and subsequent short crack growth, or Stage I, are the highlight of this work, details about the theory behind the TM model that is used to quantify them are provided in Appendix II (Section 7.2).

4.3.3 Shell Versus True 3D Modelling of Stage I

When comparing to 3D shell, the true 3D modelling of fatigue crack initiation processes inherently seems preferable, although the availability of a significant set of quantitative 3D microstructure data are often limited for a given material. For short cracks, very few studies in the literature [03L, 11R, 13R, 14M] have attempted to measure their 3D nature and the sequence of formation and propagation events. According to these studies, the crack initiation at the surface may sometimes correspond to subsurface crack initiation and growth to the surface, for example. Accordingly, there is a tremendous need for reliable experimental strategies that could continuously track 3D crack formation during the short crack growth rather than just relying on optical surface measurements [10M].

Nevertheless, there are studies dealing with true 3D crack modelling in the initiation stage. Huang et al. [07G] introduced a computer model based on a simplified 3D model of the microstructure, which is defined to simulate the inhomogeneous stress distribution and its influence on multi-crack initiation behaviour in a martensitic steel by using the TM model. Johnston et al. [06J] also performed 3D modelling of the crack initiation process, but based on a crystal plasticity modelling approach. Quey

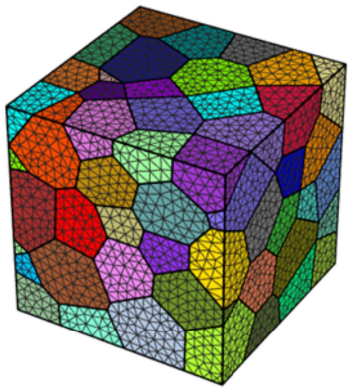

Figure 30: 3D mesh of a polycrystal morphology [11Q].

et al. [11Q] presented a methodology for the generation and meshing of large-scale 3D random polycrystals by using Voronoi tessellation (Figure 30).

If the case an engineer is looking at can be well represented by 2D or 3D shell analysis, it would generally be a good idea to start with such a relatively simple model – it may always be expanded to true 3D later, if needed to, but it can be much harder to wind a 3D model back to a 2D or 3D shell model. The benefit of this approach – start simple, add complexity as required – is that it provides the possibility to do numerous very fast "proving runs" with small simple models. More detailed models (if necessary) for final design checking can be created later if the simple approach has obvious weaknesses. Large complex models (especially 3D solid models) can be much harder to debug, and take much longer to run, than simple models. The 2D models as well as 3D shell models will generate sensible answers that can be used for "what if" scenarios, and to gain confidence about the results from the more complex models. Moreover, the 2D theory encompasses plane stress, plane strain, and axisymmetric theory, so one of these might be very useful even for a problem that is initially thought of as being a 3D problem. By using 3D shell models, a layer of grains in the microstructure can be reliably simulated, as shown in the studies of this work.

4.3.4 Transition from Stage I to Stage II

The change of the crack plane from active crystallographic plane to a non-crystallographic plane perpendicular to the external stress axis is called the transition from Stage I (crystallographic growth) to Stage II (non-crystallographic growth) or transition from crack initiation to crack growth stage, as depicted in Figure 3. This division between crack initiation and propagation is often difficult to quantify reliably. As broadly explained by using the French curve in Figure 17, at high cyclic loading levels, crack growth takes the larger part of fatigue life. The situation becomes more complex as the loading level decreases. The problem from the experimental point of view lies in the fundamental difficulty to precisely define the crack initiation stage. While the rate of crack growth can be measured accurately down to almost one atomic spacing per cycle, as has been done for many different materials and loading histories [79R], the reliable definition of the transition from crack initiation to crack

growth has always been difficult. The problem lies predominantly in the definition of the crack length at the transition from initiation to long crack growth. In this sense, Mughrabi [06M] proposed a possibility to define the initiation process in the way to include in it all stages of the cracking process until the crack has become large enough to describe its propagation by means of fracture mechanics (FM) [96L]. However, this definition may seem arbitrary, as stated by Mughrabi [15M].

The crack length a_{ini} at which the transition occurs depends mainly on the material and the stress level, but seldom exceeds a few tenths of a millimetre. In Stage II of fatigue crack growth, only one crack usually propagates while the remaining cracks usually retard by the end of Stage I. Stage I fatigue crack growth along slip bands is controlled by the shear component of the applied stress while non-crystallographic growth in Stage II is in turn controlled by the stress component normal to the crack growth direction [80K].

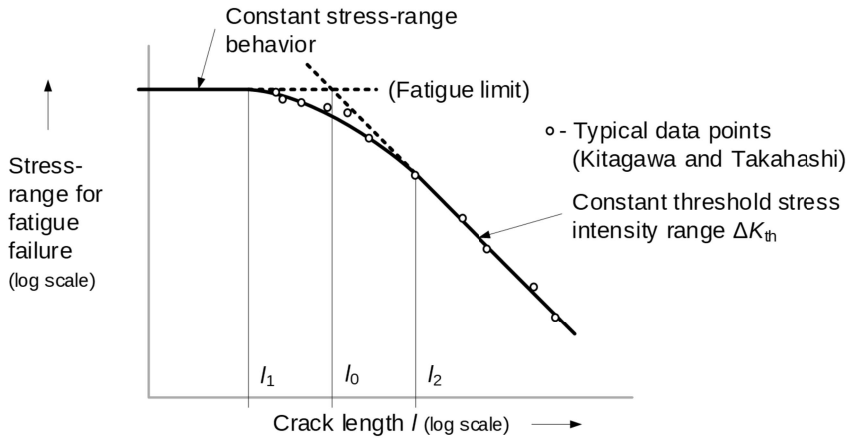

Figure 31: Kitagawa-Takahashi diagram showing limiting stress range for fatigue failure as a function of crack length [76K].

A useful way of determining the a_{ini} where the transition happens is by applying the Kitagawa–Takahashi diagram, which provides a plot of the stress-range necessary to cause fatigue failure versus crack length l, as shown in Figure 31. The Kitagawa-Takahashi diagram shows typical data obtained during short crack examinations that fall on a curve between the two straight-line regimes in such a way that it is possible to define two values of l, l_1 and l_2. These values represent the points of deviation from constant stress and constant stress intensity behaviour, respectively. Thus, cracks whose lengths lie between l_1 and l_2 can be expected to grow more quickly, and to have a lower value of ΔK_{th}, than cracks of length greater than l_2 [81Y]. The microstructural length l_1 has been observed to be either the average grain size or any microstructural barrier spacing, depending on the material microstructure, and below which the initial crack length has no effect on fatigue strength [81Y, 09A]. On the other hand, the point l_2 represents the crack length beyond which microstructural interactions no longer produce non-uniform effects on the crack growth rate. This leads to the conclusion that l_2 is the length which corresponds to a_{ini} [81Y]. Santus et al. [09A] investigated different steels and different titanium alloys

and observed that a good estimate of l_2 is: $l_2 = 10l_1$, what is also in agreement with Taylor and Knott [81Y].

Concerning the modelling example from Section 4.3.2, each microcrack or cracked segment that forms in the microstructural model on the basis of the TM equation possesses its length, d*a*, and its formation lifetime, d*N*, as explained in Section 4.3.1 on the example of a single grain. By taking the measured d*a* and the correlated d*N* one can evaluate the d*a*/d*N* for each simulation sequence. Such a crack growth rate curve in Stage I plotted as a function of the number of failed slip line segments can be seen in Figure 32L. It can be observed that the common crack growth rate is not a constant value, but develops in an oscillating manner (compare to Figure 6) and that it drops down after a certain time. Furthermore, a rough stabilization of the crack growth rate (after the green cross in Figure 32L) follows the drop [17O]. More details on crack development in the initiation stage are given in Section 5.1.

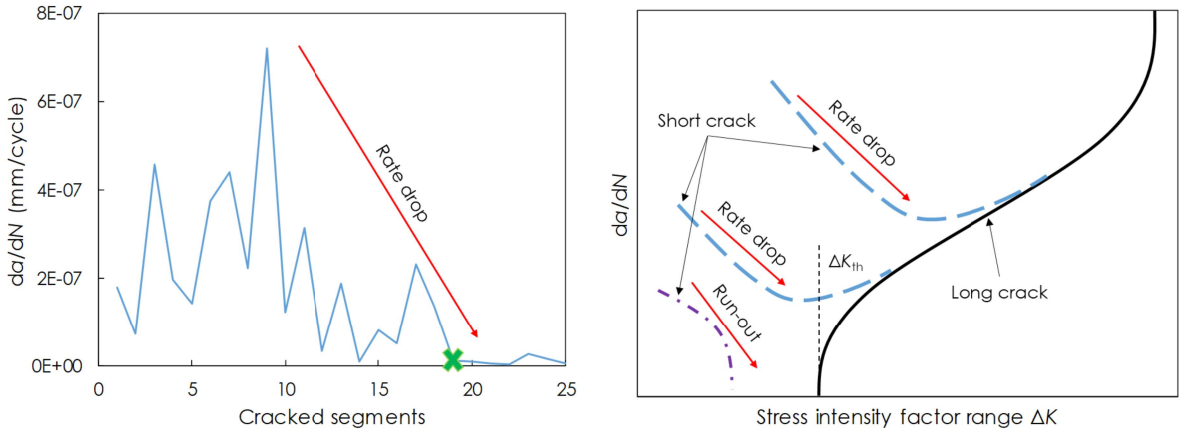

Figure 32: Left – Fatigue crack growth rate from simulations; Right – Fatigue crack growth rates from experiments for short and long cracks [99N], respectively.

A similar descending behaviour for the short crack growth was reported by Newman et al. [99N] and other researchers in [81Y, 83R, 84S] and is illustrated in Figure 32R, where the dashed and dot-dashed lines representing the growth of short cracks are lying to the left of the long crack curve (solid line). The (dot-)dashed lines give relatively high growth rates at Δ*K* values less than the long crack threshold (ΔK_{th}). For higher loading levels (blue dashed lines), the growth of the short cracks turn from descending into ascending trend and eventually approach the long crack regime, being coincident with it [14]. This is the point where the short crack transformed into the long one. This appearance has been used to derive a next methodology, besides the TK diagram, to estimate when the crack initiation process (Stage I) finishes and transition to the long crack growth regime (Stage II) takes place. Namely, as soon as the crack growth rate drops significantly as in Figure 32L, it is assumed that the crack exits the initiation stage and transits to the long crack growth regime. This methodology can be named as rate-drop method (in further text RdM). Generally, what happens in such cases is that the formation of microcracks in the microstructural model ceases after a certain number of sequences. The reason for this lies in

the fact that grains that are favourable for cracking on the basis of TM-based conditions fade out [16S]. Accordingly, the number of cycles for crack initiation can be estimated by summing the cycles required for all segmental cracks (N_s) that nucleated until the observed rate drop [17O, 18M, 18L]. This can be formulated by the following expression:

$$N_{ini} = f\left(\sum_{s=1}^{n} N_s, da/dN\right) \tag{4.5}$$

However, the dominant short crack does not always continue propagating as a long crack. Namely, in the case of a lower loading (purple dot-dashed lines in Figure 32R), the short crack may stop growing, i.e. it retards. Such situations are typically known as run-outs. The microstructurally-based crack initiation modelling approach coupled with the TM model is capable of simulating these scenarios, too. The loading cyclic stress level can be decreased incrementally until the point where just few or no cracks appear inside the microstructural model and where extreme cycles, accompanied with excessively low d*a*/d*N* magnitude, are reached for those few nucleated cracks. Besides these aspects characterizing crack development at low loading levels, the d*a*/d*N* does not show the typical decreasing characteristics. An example is given for a high purity AA in Figure 33 where an extremely large number of cycles as well as relatively low crack growth rates have been reached for only two nucleated cracks in the microstructural model. Such situations of the short crack retardation are considered as run-outs in the simulation analysis. This methodology of determining the run-outs can be named as run-out method (in further text RoM).

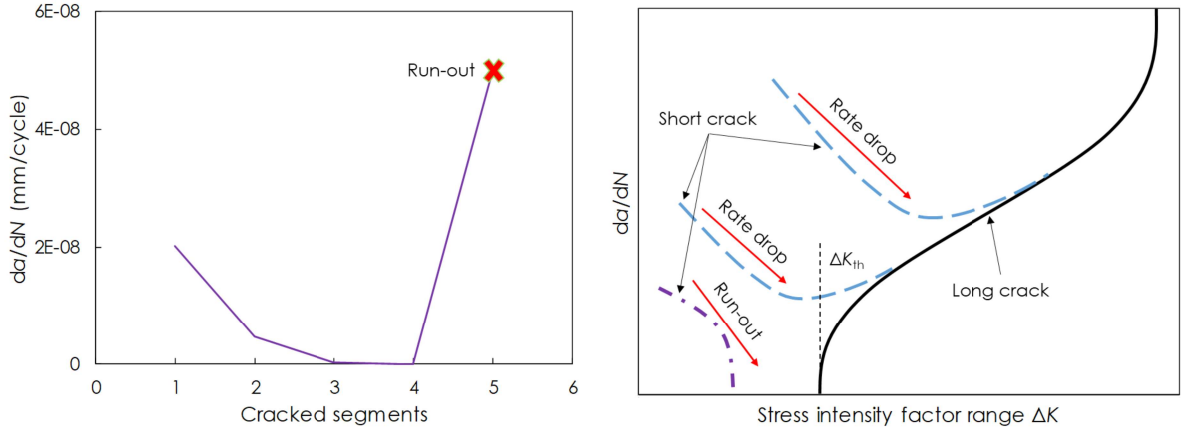

Figure 33: Left – Fatigue crack growth rate in the case of crack retardation; Right – Fatigue crack growth rates from experiments for short and long cracks, respectively.

To be able to simulate the complete fatigue life of a specimen or component, it is necessary to add the long crack growth cycles to the above-described crack initiation cycles. The modelling of the long crack growth and estimation of the cycles required for this type of fatigue crack to become unstable and causing thus the failure of the mechanical system, are discussed in the following section.

4.3.5 Stage II Growth

For most engineering alloys, the long fatigue crack growth rate in Region II of Figure 34, under a certain stress level, can be described accurately by the Paris law [63P], based on LEFM:

$$\frac{da}{dN} = C(\Delta K)^m \tag{4.6}$$

where d*a*/d*N* is the crack growth increment per cycle, Δ*K* is the range of stress intensity factor (Δ*K* = K_{max} – K_{min}), and *C* (intercept with the y-axis in Figure 34, red cross) and *m* (slope of the curve in Region II of Figure 34) are material constants that are deducted by fitting the experimental data or alternatively by using numerical methods [16S, 17M]. Numerically-based determination of Paris law constants *C* and *m* for carbon steel using the present multiscale fatigue simulation approach is explained in details in Mlikota et al. [17M] and in Section 5.11.

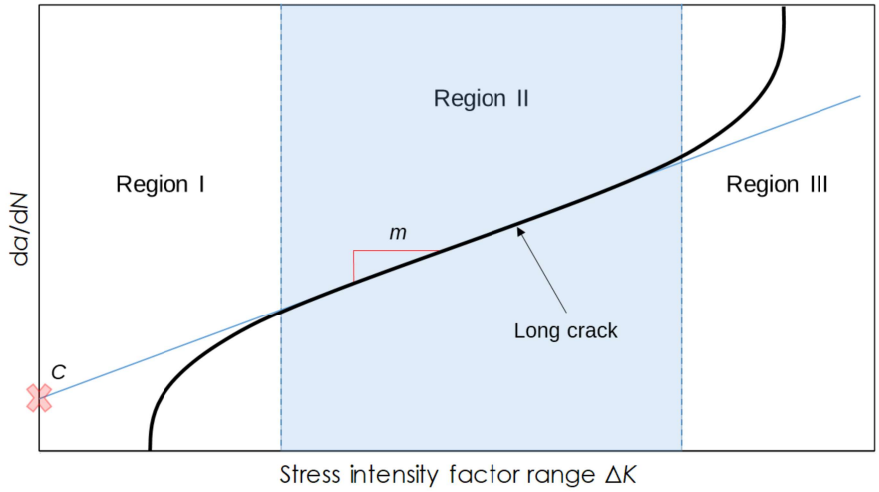

Figure 34: Fatigue crack growth rate of a long crack as function of the stress intensity factor range (ΔK) [11B].

Since the Paris equation (Eq. 4.6) covers only one *R* value, many generalizations of the equation are derived to allow for a unique set of material parameters to be taken into account. Several generalizations of the Paris law are available in literature, e.g. [97E]. The lines for different *R* values are often parallel, i.e. they have equal slope in Region II of the typical d*a*/d*N* versus Δ*K* curves (see Figure 34). Thus all these lines would have the same *m*-value (slope of the curve), but different *C*-values (intercept with the y-axis); the latter depending upon *R* as *C*(*R*). Hence, the following equation covers all *R* values:

$$\frac{da}{dN} = C(R)(\Delta K)^m \tag{4.7}$$

For many materials, the exact dependence of *C* and *R* can be described by means of the Walker or Forman equations [88B]. For example, the Forman equation is given as follows:

$$\frac{da}{dN}=\frac{C(\Delta K-\Delta K_{th})^m}{((1-R)K_{Ic}-\Delta K)} \tag{4.8}$$

where K_{Ic} is a critical level of ΔK, or the so-called fracture toughness, corresponding to unstable fracture. Other generalizations of the Paris law are designed, for example, to model the smooth transition at the near threshold condition. One popular modification introduced by Zheng and Hirt [83Z] assumes as an effective parameter the difference between the stress intensity factor range and the threshold stress intensity factor range:

$$\frac{da}{dN}=C(\Delta K-\Delta K_{th})^m \tag{4.9}$$

The N_{pro}, counted from the point of finished crack initiation up to the point of final failure, is determined from the crack length versus number or cycles, *a-N*, curve obtained by integrating the power-law equations from e.g. Equation (4.6) [88B]:

$$N(a)=\frac{1}{C}\int_{a_0}^{a_f}\frac{da}{(\Delta K)^m} \tag{4.10}$$

where a_0 is the initial crack length and a_f the crack length at failure. In addition to *a-N*, K_{Ic} is used to derive numerically the exact value of N_{pro}, meaning that $N_{pro} = f(N(a), K_{Ic})$. More details on this topic are given in Section 5.1, where a practical application of the present modelling approach is made for a specimen. Other authors [07H, 07F, 14E] applied crack propagation methods, like the virtual crack extension method, to simulate Stage II crack growth. It should be indicated that the Paris law and its modifications can only be used to calculate the endurance of structural components containing initial cracks.

The ranges of *J*-integral (ΔJ) and crack tip opening displacement ($\Delta\delta$, ΔCTOD) are widely used in elastic-plastic FM (EPFM); and their accurate estimation for postulated flaws under given load conditions is an important aspect of the use of EPFM in design [ABQ]. The domain integral method of Shih et al. (1986) provides a useful method for numerically evaluating contour integrals for the ΔJ and ΔK values. This method provides high accuracy with rather coarse models in two dimensions; in three dimensions, coarse meshes still give reasonably accurate values. It adds only a small increment to the cost of the stress analysis and can be specified easily. Abaqus [ABQ] offers the evaluation of these parameters for FM studies based on either the conventional FEM or the extended finite element method (XFEM). Contour integral evaluation is available in Abaqus for any loading (mechanical, thermal etc.) and for elastic, elastic-plastic, and viscoplastic (creep) behaviours, the latter two cases being based on the equivalent hypoelastic material concept. The evaluation of the contour integral in 3D cases is also often of interest. Figure 35 shows the finite element model of a 3D quarter model of the double-edged notch specimen meshed with one layer of C3D20 elements (second-order 20-node bricks) that is used for the calculation of FM parameters (*K*, *J* and δ) [ABQ].

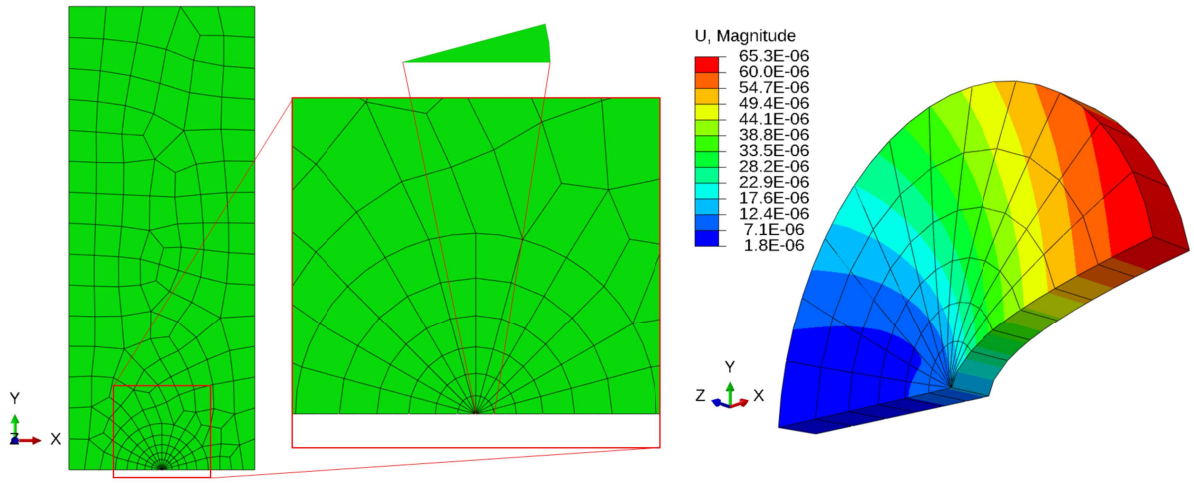

Figure 35: Finite element model of a three-dimensional quarter model of the double-edged notch specimen meshed with one layer of C3D20 elements. Displacement contours of the finite elements around the crack tip (isolated from the model) after application of an arbitrary external tensile load [ABQ].

One advantage of using second-order elements with the conventional FEM in LEFM is that they can be used to model the desired singularity at the crack tip. To obtain the singularity, the following conditions must be met [ABQ]:

- The elements around the crack tip must be focused on the crack tip. One edge of each element must be collapsed to zero length (as shown in Figure 35) so that the nodes of this zero length edge are located at the crack tip.
- The "midside" nodes of the edges radiating out from the crack tip of each of the elements attached to the crack tip must be placed at one-quarter of the distance from the crack tip to the other node of the edge.

Power-law models based on ΔK, ΔJ and $\Delta\delta$ have been used by the author in previous studies on fatigue crack growth [11B, 11C, 14B]. It has been shown in these studies that fatigue crack growth can be better described by using EPFM parameters ΔJ and $\Delta\delta$, when a large-scale plastic zone occurs in the vicinity of the crack tip. The models can be adapted for fatigue crack growth simulation in Stage II, up to fracture, which occurs as a final event in the total fatigue life of a specimen or component. It should be indicated that the Paris law and its modifications can only be used to calculate the endurance of structural components containing initial cracks (see Section 4.3.2). However, according to FM rules [88B], these initial cracks need, without exception, to be much larger than any possible short crack length that can be obtained from the microstructurally-based modelling approach (see Section 4.3.4).

Furthermore, the long crack modelling needs to be performed in accordance to standard procedures [88B]. A user needs to preselect few lengths for the long crack, for which he/she calculates ΔK. Eventually, the user determines cycles to failure by applying, for instance, Paris law. The only input that is needed from crack initiation modelling is the number of cycles spent for crack initiation. Nevertheless, this does not influence the final results. A first reason is that the long crack takes only a minor

part (up to around 20%) of the complete lifetime and the second reason is that long crack growth is not simulated explicitly (where an initial crack size would matter), but (as mentioned above) ΔK is calculated for preselected stationary long cracks.

Despite being standard, FM is a well-proven method and accordingly often employed for the characterization of long crack growth. Long crack modelling is widely used in the field of fatigue research and is accordingly well understood [18L].

4.3.6 Numerical Estimation of Fatigue Life (*S-N*, Wöhler) Curves

By applying the multiscale fatigue simulation approach (Section 4.3), the total fatigue life N (or N_f) for the cyclic stress levels S from the HCF region are obtained numerically by summing the number of cycles to initiate a fatigue crack N_{ini} (Section 4.3.4) and the number of cycles to propagate it N_{pro} (Section 4.3.5), representing that way one point in the *S-N* diagram; $N_f = N_{ini} + N_{pro}$. In the endurance (infinite) region, the N_f is equal to the run-out N_{ini} as the short cracks from this region do not transform into long cracks, i.e. they retard (see Section 4.2 and Figure 17 for more details). By performing this simulative approach for different stress levels, a complete fatigue life or *S-N* (*S-N*$_f$) curve can be determined, as schematically shown in Figure 36.

Furthermore, the white-filled points forming the slopes of the *S-N* curves in Figure 36 are determined by using the rate-drop method (RdM; see Section 5.1), while the red-filled points by using the run-out method (RoM; see Section 5.1). The transition between the white- and red-filled points represents the fatigue endurance limit (horizontal line).

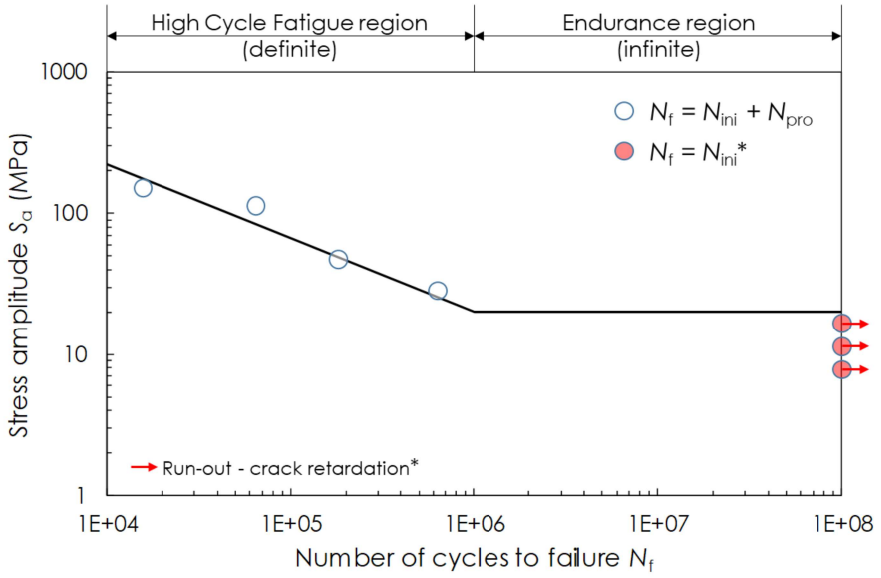

Figure 36: Schematic S-N curve showing difference between HCF and infinite region.

In connection with this, numerical investigations on complete fatigue lifetime including its keystone, the short fatigue crack growth, is of high practical interest and therefore, is the central topic of further studies.

5 Application of the Multiscale Fatigue Simulation Approach

This chapter deals with the initiation of a short crack and subsequent growth of the long crack in different metals under cyclic loading, concluding with the estimation of the complete lifetime represented by the fatigue life or *S-N* (Wöhler) curve (see Section 4.3.6). The finite element method (FEM) has been applied to calculate the non-uniform stress distribution in a micromodel containing the microstructure of a material. Simultaneously and in combination with the FEM results, the physically-based Tanaka-Mura (TM; Eq. 4.3, Section 4.3.1) model has been used to estimate the number of cycles needed for crack initiation in the microstructural model, as described in Section 4.3.4. The long crack growth is handled using standard fracture mechanics (FM). For more details on the introduced multiscale fatigue simulation approach see Section 4.3.5.

5.1 Determination of the Fatigue Life Curve for a Specimen

The purpose of this section is to put into use the modelling methods for the complete fatigue crack development and the estimation of accompanying life cycles, that have been discussed in details in the previous Section 4.3. An example based on a flat notched specimen and a vanadium-based microalloyed AISI 1141 steel reported in the work of Fatemi et al. [04F] has been examined for this purpose. The FEM-based model of the specimen (macro- or global model) is used for the assessment of the global output variables that are further transferred to a micromodel (microstructural model or submodel). The microstructural model is on the other hand used for the assessment of crack initiation process based on the TM equation. Additionally, the macromodel has been applied to calculate stress intensity factor range (ΔK) values, which are input to the evaluation of the long crack growth based on the Paris law [63P]. The exact geometry of Fatemi's specimen is shown in Figure 37. The relevant dimensions are 141.73 mm height (horizontal in Figure 37) and width of 63.50 mm, while the thickness is 2.54 mm and the notch radius 9.128 mm.

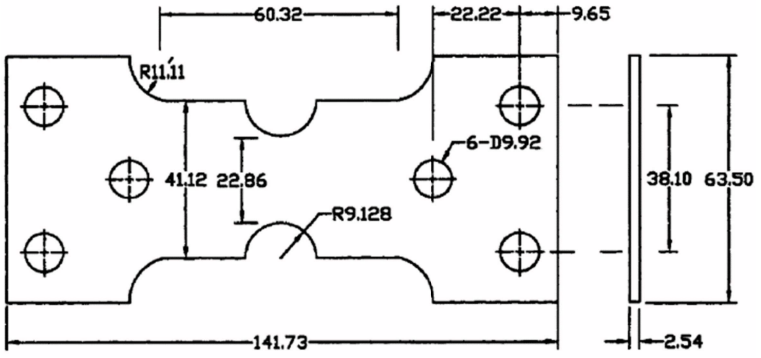

Figure 37: Geometry of Fatemi's specimen [04F].

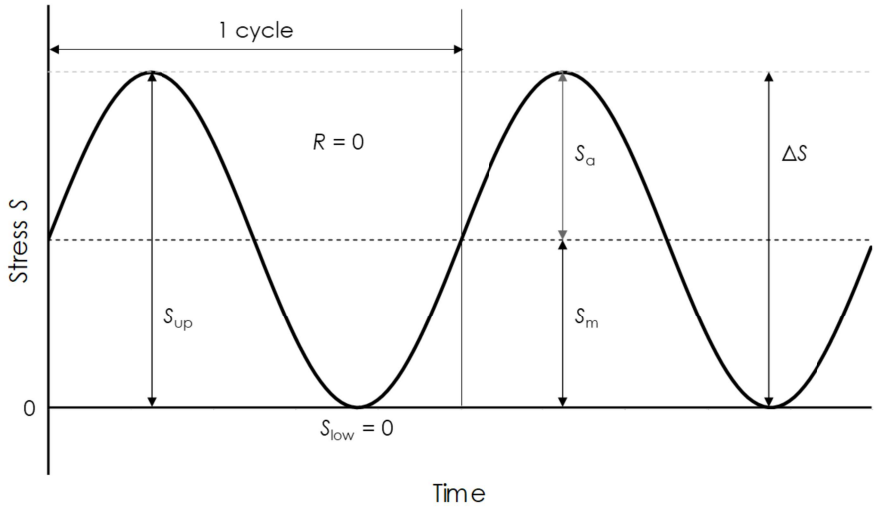

Figure 38: The stress-time trace applied in the present study: Pulsating stress between S_{up} and S_{low} = 0, where S_a = S_m = S_{up} / 2.

The specimen failed in experiments from Fatemi et al. [04F] under stress-controlled cyclic loading conditions, with the loading ratio R = 0, i.e. under pulsating loading stress between the upper stress of a loading cycle S_{up} and the lower stress of a loading cycle S_{low} = 0 (see Figure 38): the S_{up} values ranged from 130 to 256 MPa, and accordingly the stress amplitude S_a (= S_{up} / 2 = S_m in case of R = 0) from 65 to 128 MPa.

The reader is advised to see Section 5.3 for details on the difference between using the S_a and S_{up} values in fatigue applications and on the effect of the mean stress S_m on their magnitudes. In brief, the S_{up}-N diagram is suitable when it is needed to know if a cyclically investigated material operates in the HCF or in the LCF regime. On the other hand, the S_a-N diagram is preferable for the correct understanding of the effect of the mean stress (and R ratio).

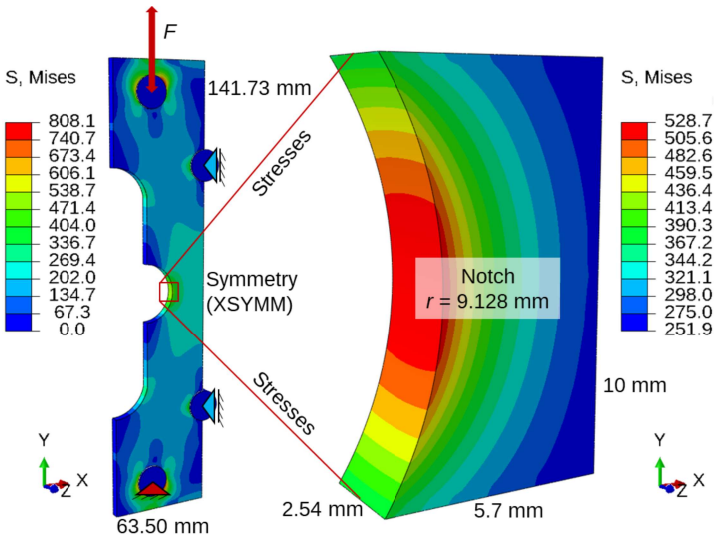

Figure 39: Left – 3D global model of the notched tensile specimen (half) at 112 MPa stress amplitude; Right – 3D submodel of the region at the notch ground.

The left image in Figure 39 shows the stressed three-dimensional (3D) model of the specimen; in this case a half of it due to applied symmetry boundary conditions in the direction of x-axis. The numerical model is created and analysed by using the FEM-based software Abaqus and is meshed with 25,752 linear hexahedral elements of type C3D8R, from the Abaqus element library [ABQ]. The critical (notch) site of the specimen – marked with a red square – that becomes vulnerable under cyclic loading is shown in Figure 39L.

The global 3D model (see Figure 39L) is subjected to a forward loading equal to the S_{up} magnitude (S_{up} = 130-256 MPa, same as in experiments of Fatemi et al. [04F]). As introduced previously, this global model served to provide boundary conditions for the microstructural model (Figure 40L), which is used for the crack initiation analysis based on the resulting stresses and on the Tanaka-Mura equation (Eq. 4.3). The transfer of the boundary conditions is accomplished by using a two-fold submodelling technique. Namely, in the first step, a 3D solid submodel is created at the location of interest (notch) with the aim to get more precise information about the accompanying stresses, as shown in Figure 39R. In the second step, the microstructural model (3D shell submodel) is embedded in the 3D solid submodel, where the displacements have been transferred over edges marked with numbers from 1 to 3 in Figure 40L. The submodelling technique can be generally used to drive a local part (submodel) by nodal results, such as displacements (node-based submodelling), or by the element stress results (surface-based submodelling) from the global model mesh [ABQ]. The reason that the microstructural shell model is driven in this study by the displacements of the 3D solid submodel is that the applied FEM software Abaqus allows the application of a stress-based submodelling only when solid-to-solid models are combined, as in the case of Figure 39.

The global model is loaded in a way to act in the high-cycle fatigue (HCF) regime. That is, the stresses in the notch region, where the two-fold connection between the global model and the submodels has been established, are generally kept below the elastic limit through the whole loading span (S_a = 65-128 MPa; see y-

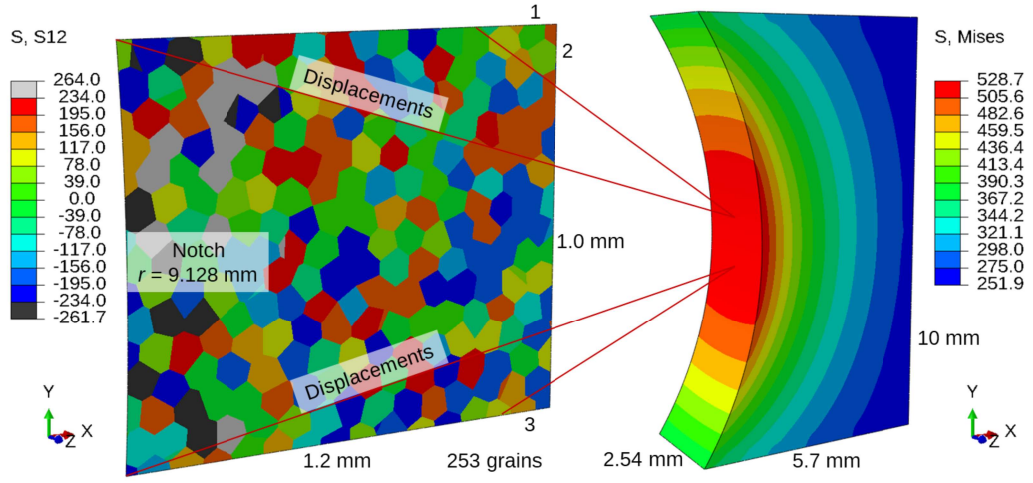

Figure 40: Left – Shear stress distribution in the 3D deformable shell submodel of AISI 1141 steel (microstructure 1) under 112 MPa loading level; Right – 3D submodel.

axis in Figure 49 showing the simulation-based *S-N* diagram for the steel AISI 1141). More precisely, the transferred displacements from the 3D submodel to the microstructural one did not generate stresses in it that are higher than the elastic limit, which is equal to 564 MPa for the steel AISI 1141.

The microstructure in the shell submodel is created on the basis of a microstructure of the steel AISI 1141 reported in the experimental study of Mirzazadeh and Plumtree [12P]. The model is created as a 3D representative volume element (RVE) generated by the Voronoi tessellation technique [07G]. The average grain size is estimated to be around 60 μm, and is accordingly applied during the modelling of the polycrystal. The submodel from Figure 40L contains 253 grains, which are meshed with 171,288 elements in total, giving a relatively fine mesh with approximately 677 elements per grain.

Although looking like a two-dimensional (2D) model, the microstructural model is a 3D deformable shell model meshed with membrane elements with reduced integration (M3D4R); reduced integration is often used as a means to avoid shear locking in thin shell structures [81T], such as the one investigated in this study. In addition and according to Abaqus documentation [ABQ], general membrane elements are often applied to represent thin stiffening components in solid structures, such as a reinforcing layer in a continuum. In this study, they are similarly used to model a layer of material inside a bulk, taking additionally the microstructure of the bulk into account. As further stated in [ABQ], general membrane elements should be used in 3D models in which the deformation of the structure can evolve in three dimensions, as in the present investigation.

Furthermore with regards to the microstructural model, the software Abaqus uses a membrane section definition to define the section properties, i.e. the thickness of a membrane model. In this specific case, the thickness of the 3D shell microstructural model is equal to the average grain size (60 μm), representing in that way a layer of grains in the XY plane (see Figure 28).

Concerning the material model definition, the pure isotropic elasticity with Young's modulus E = 200 GPa, shear modulus G = 78,125 MPa and Poisson's ratio υ = 0.3 [04F] is adopted in the 3D solid global mode and the 3D solid submodel while an elastic orthotropic material behaviour is assumed in the microstructural model. The components of the material stiffness matrix in elastic orthotropic description, i.e. the material elastic constants for cubic crystal symmetry are: $C_{11} = C_{22} = C_{33}$ = 255,682 MPa, $C_{12} = C_{13} = C_{23}$ = 99,432 MPa, $C_{44} = C_{55} = C_{66}$ = 78,125 MPa. The constants are calculated using the following equations: $C_{11} = E(1-\upsilon)/(1-\upsilon-\upsilon^2)$; $C_{12} = E\upsilon/(1-\upsilon-2\upsilon^2)$; $C_{44} = G$ [16R]. The material parameters of the TM model (Eq. 4.3), used in this study for the steel AISI 1141 are crack initiation energy (W_c) equal to 19 kJ/m^2 [88R] and the critical resolved shear stress (CRSS) equal to 117 MPa, which was determined by Hummel et al. [14B, 18B] by using molecular dynamics (MD) calculations.

Aside of the microstructure of the material, Figure 40L on page 53 shows the shear stress distribution – with an evident influence of the microstructure – that is obtained in the FEM-based analysis for the 128 MPa loading stress amplitude and which is the

input to the TM equation ($\Delta\overline{\tau}_s$ – average shear stress range on the slip line segment; see Eq. 4.3, Section4.3.1). Grey and black grains are those grains where the condition for crack nucleation is satisfied according to the TM model, saying that the absolute value of the average shear stress on a slip band segment has to be two times higher than the CRSS, i.e. 234 MPa in this case. It can be noticed that these grains, which are conditioned for cracking, are in close proximity of the notch. The model has been loaded in this study with five different S_a levels (see Figure 38), 75.5, 90, 100, 112 and 128 MPa, in accordance with the data available from the experimental study of Fatemi et al. [04F], and with additional stress amplitudes ranging between 75 and 65 MPa that served for the estimation of the endurance limit (see Table 3). The applied R is the same as in the study of Fatemi, i.e. R = 0, and is a direct input to the TM equation (see Section 5.3 for more details on the effect ot the R ratio).

An example of (damaged) model with a corresponding microstructure selected for the numerical analysis of the fatigue crack initiation lifetime of the specimen made of AISI 1141 steel is shown in Figure 41L. More precisely, Figure 41 shows results of the crack initiation analysis for the 128 MPa loading amplitude, i.e. it shows the moment when the initiation stage has been considered as being completed in terms of required cycles and when the crack should grow further as the long crack. The left image in Figure 41 depicts the microstructural containing nucleated segmental cracks, which can be easily perceived with the help of the grain boundaries and the von Mises stress distribution field. Concerning the damage evolution, cracks tend to nucleate in the model in a scattered manner and in those grains that are favourably oriented, and where the conditions for microcrack nucleation according to the TM equation are fulfilled (see Section 4.3.1 for more details). Already nucleated crack segments tend to elongate along the whole grain, causing local stress relaxation as well as concentrations at their tips and by that amplifying or decreasing the likelihood for new crack formation in the vicinity. At higher loading levels, some of the formed cracks grow and link together forming in that way a dominant crack, as in the case shown in Figure 41L.

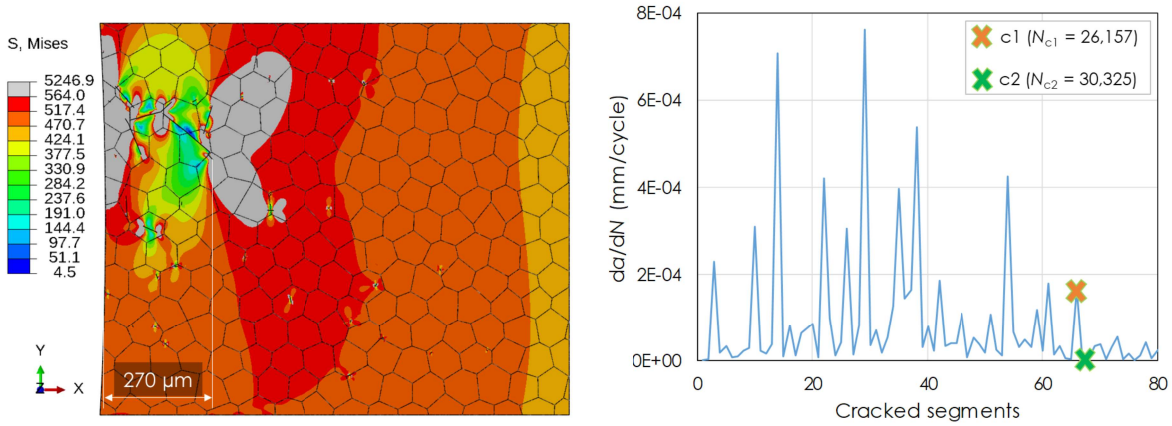

Figure 41: Left – Damaged microstructural model (128 MPa stress amplitude) and the estimated short crack length a_{ini} = 270 µm at the end of the initiation stage (Microstructure 2); Right – Accompanying fatigue crack growth rate.

It has been noticed by analysing the damaged models that stresses – even though defined in this study as purely elastic by the three elastic constants for cubic crystals, as described earlier – go beyond the theoretical elastic limit of the material (R_e = 564 MPa). This happens due to microstructural effects such as grain boundaries, grain shapes and orientations as well as due to formed cracks whose tips act as stress concentrators. The grey-coloured regions in Figure 41L represent stresses that surpass the elastic limit of the investigated AISI 1141 carbon steel and are created by using a user-defined option for plotting the output variable (von Mises stress) in Abaqus/Visualization module.

The image on the right of Figure 41 presents the accompanying crack growth rate and the cycles for the initiation completion that are estimated on the basis of the assumption that the short crack initiation finishes with the drop of the crack growth rate (see Section 4.3.4 for more details on the rate-drop method). This point is marked with a green cross and hereinafter referred to as c2. In this case, the number of cycles is equal to 30,325 (N_{c2}; see Table 2). In general, the number of cycles up to c2 (N_{c2}) equals the sum of cycles of all segmental cracks that nucleated until the observed crack growth rate drop. Aside of the cycles that are necessary for the short crack to initiate, it is also possible to roughly estimate the length of the most dominant crack. This crack can be also considered as the initiation crack length a_{ini}, or even the transitional crack length between Regions I and II (see Section 4.3.4) for higher loading levels. As it can be seen from Figure 41L, the length of the most dominant short crack equals roughly 270 µm, which enters into a range defining short cracks of ≤ 0.5-1 mm, as reported by Suresh and Ritchie [84S].

Table 2: Segmental cycles (N_s) for the stress amplitude level of 128 MPa.

Segment	N_s	Σ cycles
1	2,870	2,870
2	1,013	3,883
…	…	…
9	667	7,324
10	68	7,392
…	…	…
65	1,879	26,145
66 (c1)	12 ($N_{s,c1}$)	26,157 (N_{c1})
67 (c2)	4,168 ($N_{s,c2}$)	30,325 (N_{c2})
68	1,394	31,719
…	…	…

In the majority of cases, segmental cycles at c2 ($N_{s,c2}$) are typically at least three times higher than the average number of cycles needed for the nucleation of the first ten segments ($\overline{N}_{s,1\text{-}10}$) in a considered microstructure. In the case given in Figure 41 and tabulated in Table 2, the average of the first ten segments equals $\overline{N}_{s,1\text{-}10}$ = 739 cycles, what is 5.64 times less than 4,168 ($N_{s,c2}$) that are attributed to the segment cracking at c2. Furthermore, the number of cycles $N_{s,c2}$ accompanied to the segment that broke at c2 is typically much higher than the cycles of the previous segment ($N_{s,c1}$) and of all the preceding segments, as for example given in Table 2. The

complete number of cycles up to failure of this previous segment (N_{c1}) are marked with orange cross in Figure 41R and hereinafter this point is referred to as c1. Both points (c1 and c2) are considered in the estimation of the total number of cycles to initiate a short crack N_{ini}, i.e. they are averaged as shown in Table 3; $N_{ini} = (N_{c1} + N_{c2})/2$. This is done to reduce the relatively large deviation of c2 from the other values.

Table 3: Simulation-based crack initiation cycles N_{ini} for different loading levels; calculated by averaging N_{c1} and N_{c2} values of both investigated microstructures (ms1 and ms2). The green colour represents transition cases, while the red colour depicts run-outs.

S (MPa)	N_{c1} / ms1	N_{c2} / ms1	# of cracked segments at c2 / ms1	N_{c1} / ms2	N_{c2} / ms2	# of cracked segments at c2 / ms2	N_{ini} (cycles) averaged
128	51,912	55,034	103	26,157	30,325	67	40,857
112	91,667	101,726	54	27,478	34,009	26	63,720
100	107,883	134,131	31	63,179	78,602	27	95,949
90	297,240	384,876	22	110,853	141,365	22	233,584
75.5	574,959	1,605,591	7	204,662	349,758	8	683,743
75	10,476,408	16,504,438	8	246,201	370,581	7	6,899,407 *
72.5	33,118,944	33,553,719	5	436,802	864,971	7	16,993,609 *
70	275,380	911,586	3	3,884,775	9,944,255	8	2,753,982 *
67.5	479,919	2,453,766	3	2,862,187	2,872,130	6	2,417,001 *
65	1,046,427	23,948,429	3	1,245,818	360,668,973	5	96,727,412 *

** Run-outs (see red-filled squares in Figure 49).*

The methodology of initiation estimation can be further facilitated in the majority of cases by plotting the averaged fatigue crack growth rate (da/dN), as shown in Figure 42R, where every point is averaged with two preceding and two following neighbouring points. The derived average rate is smoother than the original one and allows easier detection of the drop (green square). However, the N_{ini} is estimated by considering the points c1 and c2 from the original da/dN diagram.

The ratio between the number of cycles at c2 and averaged cycles of the first ten segments ($N_{c2} > 3x\overline{N}_{s,1\text{-}10}$) as well as the smoothed da/dN rate are used as auxili-

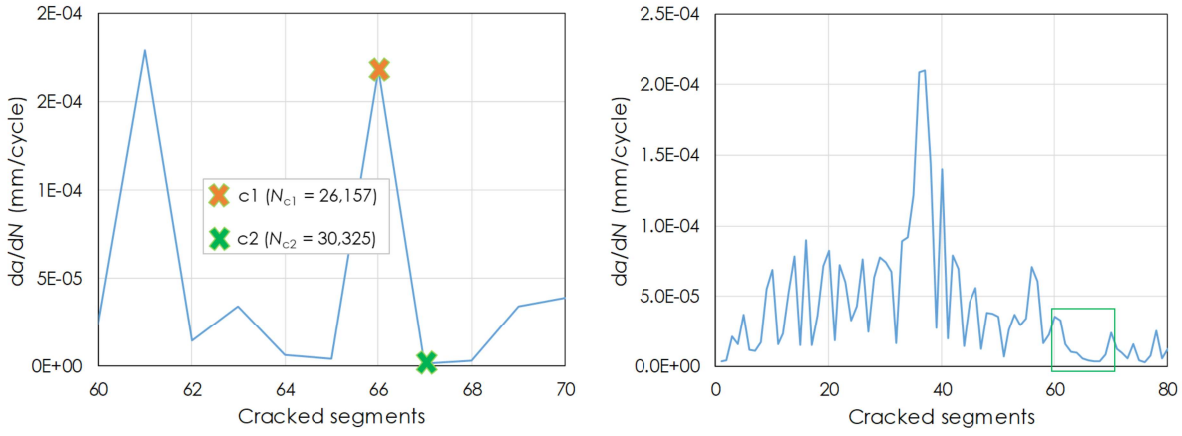

Figure 42: Left – Fatigue crack growth rate in the initiation completion stage; Right – Averaged fatigue crack growth rate.

ary criteria for the estimation of the initiation end, next to the rate-drop method (RdM).

The crack initiation analysis is performed for different loading levels and for two different microstructures (ms1 and ms2) with the same average grain size of 60 µm. Both microstructures are generated by using the Voronoi tessellation technique and have been assigned with the same material properties. The results for crack initiation for the two investigated microstructures are tabulated in Table 3. The final value of N_{ini} (last column in Table 3) is averaged between the microstructures ms1 and ms2, and their N_{c1} and N_{c2} values, what resulted e.g. for the amplitude level of 128 MPa in 40,857 cycles. It is assumed in all investigated cases above the endurance limit, as exemplarily shown in Figure 41L, that the damage in the microstructural model after the initiation completion is large enough to reach the transition to the long crack growth regime (see Figure 43). Therefore, the final N_{ini} value has been prescribed as a starting number in the long crack growth analysis, as shown later in Figure 48 and Table 5.

An interesting observation can be drawn from Table Table 3; namely, the number of cracked segments at point c2 decreases with the decrease of the loading stress amplitude. Furthermore, the development of cracks proceeds even after the estimated initiation based on the Rate-drop Method (RdM), as can be realized by the slightly fluctuating curve on the right hand side of the green cross in Figure 41R. Concerning colouring in Table Table 3, the green fields represent cycles determined by using the RdM while the red represent cycles determined by the run-out method (RoM). For more details on the RdM and RoM see Section 4.3.4.

In general, the RoM is used at lower stress amplitude levels in order to estimate the cases when the short crack arrests (run-out), i.e. it does not transform into a long one. Figure 44 shows a run-out example for the 70 MPa loading case where just three crack segments nucleated before the simulation has stopped, meaning that the crack retarded completely. Typically is point c2 in the run-out scenarios (red

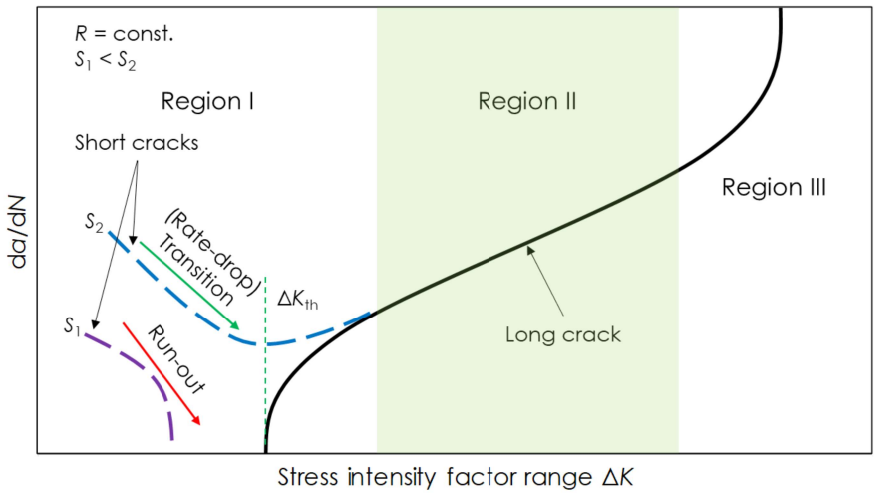

Figure 43: Loading level dependent transition from Region I into Region II (schematic representation) [99N].

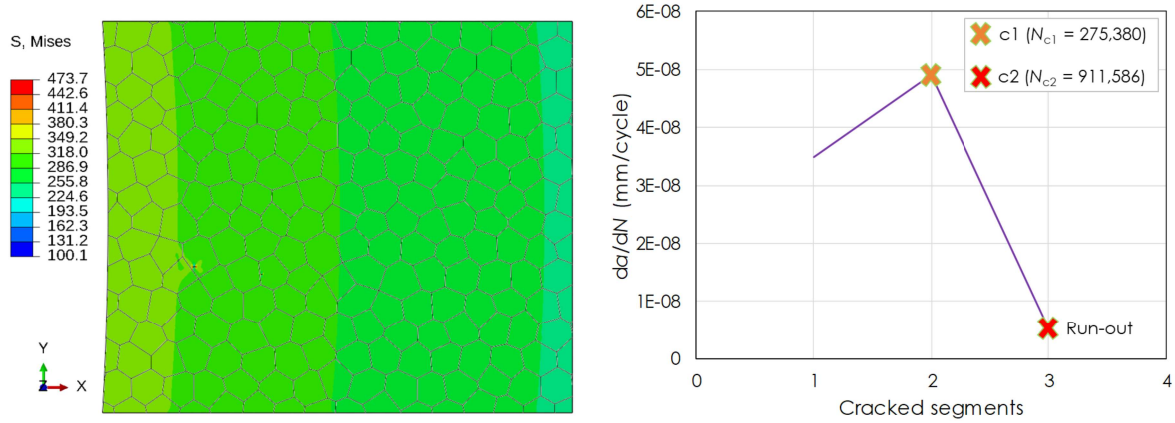

Figure 44: Left – Microstructural model in the endurance (infinite) region of the fatigue life containing only three broken segments (microstructure 1, 70 MPa amplitude level); Right – Fatigue crack growth rate characteristic for the endurance region (RdM used).

cross in Figure 44R) accompanied by less than ten cracked segments and by a very high number of cycles, as can be seen in the red fields of Table Table 3. Aside of that, the pronounced drop of the crack growth rate typical for higher loading stress levels does not show itself at the loading levels resulting in run-outs.

Another interesting observation can be made by plotting d*a*/d*N* versus the number of cracked segments curves of the investigated microstructures in a common diagram. Such a plot is obtained for different loading levels and is shown for microstructure designated as ms2 in Figure 45. What can be seen there, especially for lower loading levels (Figure 45L) is that d*a*/d*N* increases with increasing loading amplitude. Curves representing d*a*/d*N* for higher loading amplitudes at which short cracks satisfy conditions for the transition into the long crack (as suggested in Figure 43) do not differ from each other as clearly as those from Figure 45L due to higher number of cracked segments and stronger fluctuations of the curves, as can be seen from Figure 45R. Generally, these fluctuations in d*a*/d*N* are resulting from different lengths of each individual cracked segment (d*a*) and from different accompanying cycles (d*N*), which are estimated by using the Tanaka-Mura equation (Eq. 4.3); for more details on this topic, see Section 4.3.1.

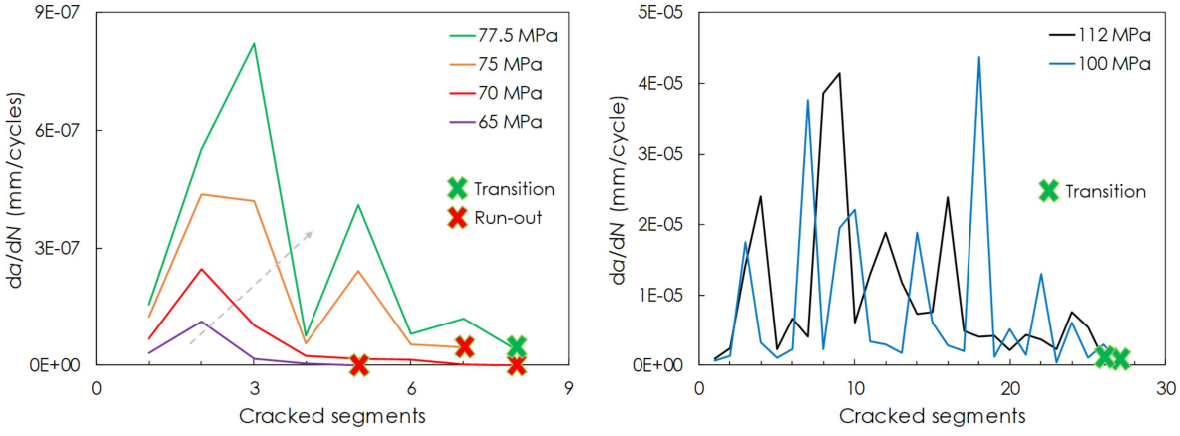

Figure 45: Crack growth rates at different loading levels (AISI 1141 steel).

Furthermore, a correlation can be recognized between Figure 45L and Figure 43 by comparing tendencies of da/dN curves in Region I. Namely, as the loading stress amplitude increases, the accompanying curves tend to move upwards and to the right. Eventually, at certain loading level the conditions for the transition from crack initiation stage are satisfied and the crack grows further in Region II as the long crack, as schematically shown in Figure 43. As depicted in Figure 45L, the lowest stress amplitude at which the short crack can grow further as a long one is equal to 77.5 MPa (green cross denotes the transition).

Figure 41 shows an example of the crack length at the end of the initiation stage a_{ini} (270 µm) at the loading amplitude of 128 MPa; in this case it is the transitional crack length, too. Similarly, the a_{ini} for the last run-out case from Figure 45L (75 MPa stress amplitude; red crosses denote the run-outs) of 191 µm is determined by summing the lengths of all nucleated micro-cracks before their arrest (run-out). The summation has been applied due to the absence of a dominant crack at this relatively low loading level. The ΔK value for this representative crack length – the last one before the transition starts taking place – of 9.39 MPa√m is calculated and can be considered as the simulation-based threshold ΔK value, i.e. ΔK_{th}, for the steel AISI 1141.

Furthermore, an example of the transition between Region I and Region II at the loading level of 90 MPa is shown in Figure 46. The fluctuating da/dN curve (as those in Figure 45) of the short crack at this loading level has been averaged (by using a polynomial function), scaled to fit the da/dN ranges of the da/dN versus ΔK diagram and visualized in Figure 46 by the blue dotted line. The da/dN value at the end of the initiation phase (see green crosses in Figure 45), i.e. at the moment of the transition, is indicated by the green cross, too, and by the green dashed horizontal line in Figure 46. Aside of that, the red horizontal line shows the highest growth rate of this short crack. Even thought the ΔK values on the x-axis of Figure 46 are often given in a logarithmic scale, this is avoided in the present case due to visualization reasons.

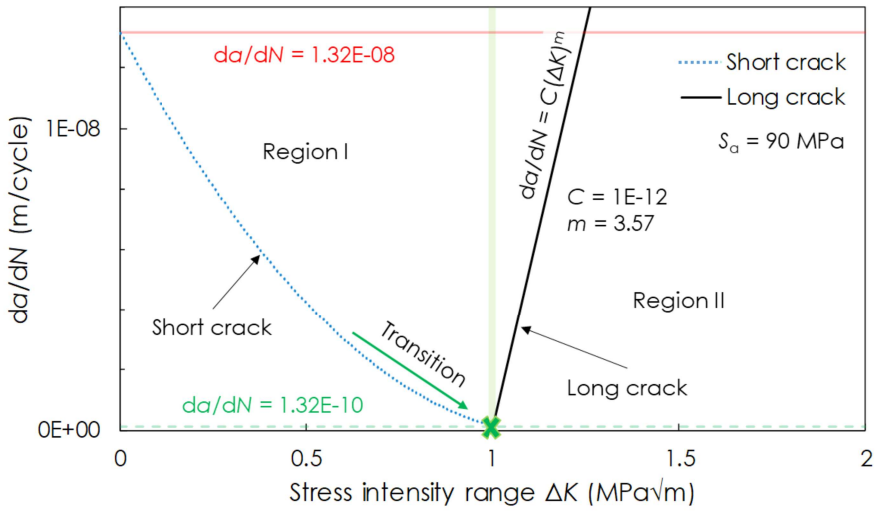

Figure 46: An example of the da/dN vs. ΔK diagram showing the transition between Region I and Region II at the amplitude level of 90 MPa (as schematically shown in Figure 43).

In order to characterize the long crack growth numerically, a 2D macromodel is created having the same geometry as the 3D solid model from Figure 39L. In addition, a special Abaqus technique termed as the seam crack is applied to this macromodel in order to represent the crack and eventually to determine the ΔK values. A seam defines an edge or a face that is originally closed but can open as a crack during an analysis [ABQ]. As in the case of the 3D solid model only one half of the specimen needs to be modelled, as shown in Figure 47L. The symmetry is realized by using boundary conditions on the vertical y-axis, with fix displacements in x-direction as well as rotations of any kind. The long crack growth analysis is performed by using classical linear-elastic fracture mechanics (LEFM), where ΔK values have been calculated for the S_a = 90-128 MPa loading span by means of Abaqus procedures.

Continuum plane stress 8-node elements with reduced integration (CPS8R) have been used to mesh the macromodel. In order to deal with the stress singularity at the crack tip in the case of ΔK values calculation, special elements have to be used that are able of handling the infinite stresses. This is done in Abaqus by collapsing one side of an 8-node isoparametric element in the way that all three nodes from that side have the same geometric location – in this case on the crack tip [ABQ] – as can be seen in Figure 47R. In addition, the middle nodes of the edges forming a newly created collapsed tip are moved to one fourth of the edges' length in the direction of the tip. Furthermore, the crack tip is modelled with a ring of collapsed quadrilateral elements.

Since a relatively small plastic zone at the crack tip is expected (see Figure 47), no plastic material data are necessary to be used. That is, the material behaviour is assumed to be purely linear elastic, as in the case of the 3D global model and the 3D submodel from Figure 39. The isotropic material data for the specimen made of AISI 1141 carbon steel are the same as those that have been used in the crack initiation modelling, E = 200 GPa, G = 78,125 MPa and υ = 0.3 [04F].

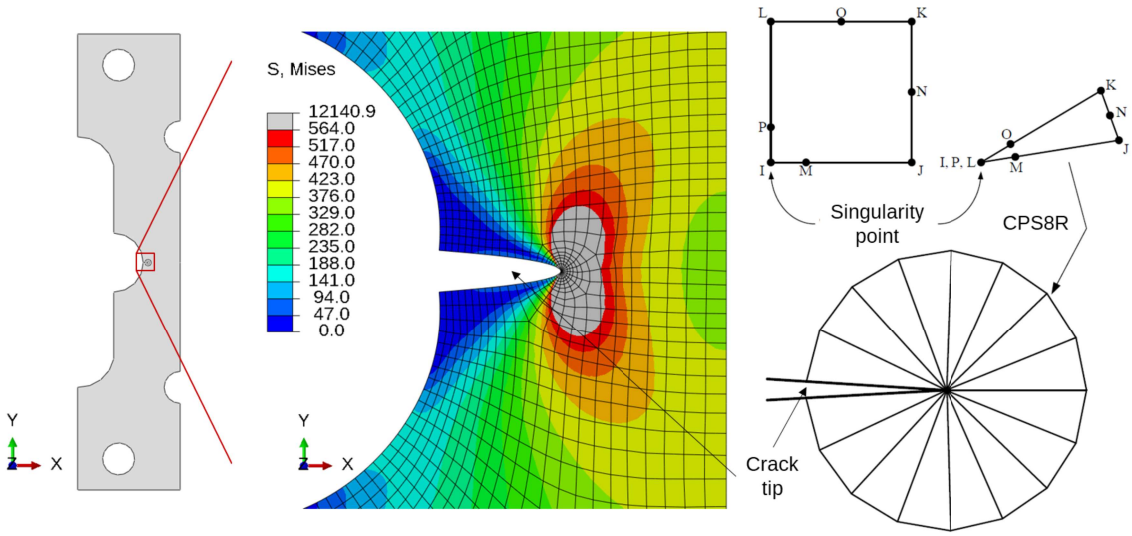

Figure 47: Left – Macromodel for calculation of the stress intensity factor range (ΔK); Right – The 5 mm long crack and collapsed elements at the crack tip (128 MPa amplitude level) [10O].

As aforementioned, the long crack growth analysis is performed solely for the transition cases marked with the green crosses in Figure 45 and in green in the last column of Table Table 3. The crack size where final failure occurs a_f depends on the loading stress level S and on the critical value of ΔK or fracture toughness K_{Ic} for the investigated steel AISI 1141; $a_f = f(S, K_{Ic})$. More precisely, the a_f values for different loading levels are estimated by integrating Paris law (Eq. 4.6, Section 4.3.5), which is based on S- and a-dependent ΔK values, and in combination with K_{Ic}, which is equal to 67 MPa√m for AISI 1141 carbon steel [96Y]. The Paris constants used for AISI 1141 carbon steel are m = 3.57 and C = 1E-12, according to Hui et al. [16I].

Table 4 exemplarily shows ΔK values calculated for different crack lengths under 128 MPa stress amplitude. According to the table (4), the modelled specimen failed at that loading level when the crack reached length a_f = 7.0 mm, i.e. when ΔK (66.58 MPa√m) magnitude reached K_{Ic} value ($\Delta K \approx K_{Ic}$, marked bold in the table). The same procedure has been performed for other stress amplitude levels.

Table 4: Calculated stress intensity factor range (ΔK) values for different crack lengths (a) at the 128 MPa loading level.

a (mm)	1.5	2.0	3.0	4.0	5.0	6.0	**7.0**	8.0	9.0	10.0
ΔK (MPa√m)	36.47	39.82	44.97	49.45	54.16	59.66	**66.58**	76.06	90.72	118.47

Since K_{Ic} has been reached at a crack length of 7 mm, according to Table 4, the number of cycles to propagate the crack up to failure N_f can be easily determined by drawing a vertical line from the point where the a-N curve – obtained by integrating Paris law and coloured in red in Figure 48 – intersects the magnitude of the crack length of 7 mm. Aside from that, Figure 48 contains the calculated number of cycles for both analyses, i.e. for short crack initiation (N_{ini}) and long crack growth (N_{pro}), including the overall lifetime (N_f). Namely, as already mentioned earlier in the text, the value N_{ini} for the 128 MPa loading stress amplitude is derived by averaging c1 and c2 values of two investigated microstructures (see Table 3), resulting in 40,857

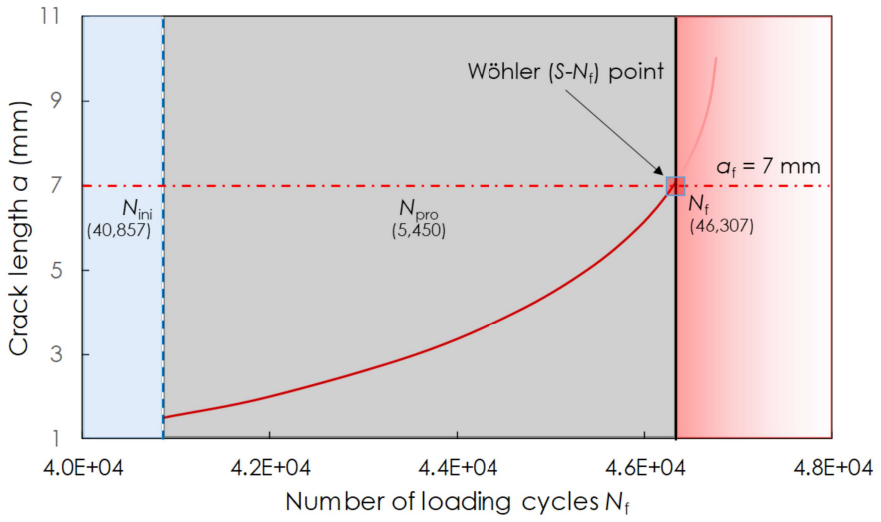

Figure 48: Dependence of the crack length on the loading cycles for the 128 MPa loading case.

cycles. These cycles have been prescribed as a starting number for the long crack growth. On the other hand, by applying the line intersection method based on a_f and described above, it has been estimated from Figure 48 that final failure occurs at N_f = 46,307 cycles. In the following step, the value N_{pro} has been obtained by subtracting the N_{ini} from the N_f what resulted in 5,450 cycles. The same procedure has been applied for other loading levels. A comparison of cycles spent for crack initiation and crack propagation, respectively, including the number of cycles at final failure, at different stress levels is presented in Table 5.

Table 5: Comparison between contributions of different fatigue life phases.

S_a (MPa)	N_{ini} (cycles)	N_{ini} (%)	N_{pro} (cycles)	N_{pro} (%)	N_f (cycles)
128	40,857	88	5,450	12	46,307
112	63,720	87	9,170	13	72,890
100	95,949	90	10,661	10	106,610
90	233,584	92	2,674	8	254,258
77.5 (S_e = 76)	683,743	100	0	0	683,743

Finally, the resulting N_f for all loading cases are presented in Figure 49 versus the accompanying stress level (S) in the form of an *S-N* curve. The variance (or scatter) of the slope-building crack initiation cycles from Table 3 (c1 and c2 for two different microstructures) is introduced by means of error bars (red horizontal lines).

Aside of the slope of the *S-N* curve, the modelling approach allows to determine the endurance limit S_e (in this case $S_{e,a}$), too, as visible from Figure 49. The determination of the endurance limit – the boundary between the definite life (slope of the *S-N* curve) and the infinite life (below the endurance limit) – has been accomplished by lowering the loading stress amplitude in a step-wise manner, starting from 75 MPa, until the point where no cracks have been observed inside the microstructural model or where extreme number of cycles (> 2E+06) for the formation of micro-

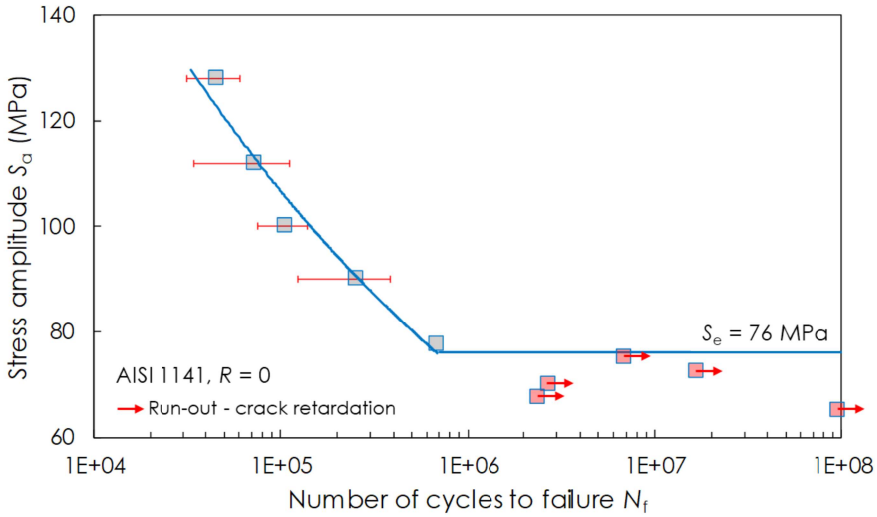

Figure 49: Simulation-based fatigue life (S-N) curves for the steel AISI 1141 [04F, 18M]. The run-out points are positioned horizontally at the number of cycles where no further failure occurs in the microstructure (see Table 3). These points are estimated based on the Run-out Method (RoM, see text above).

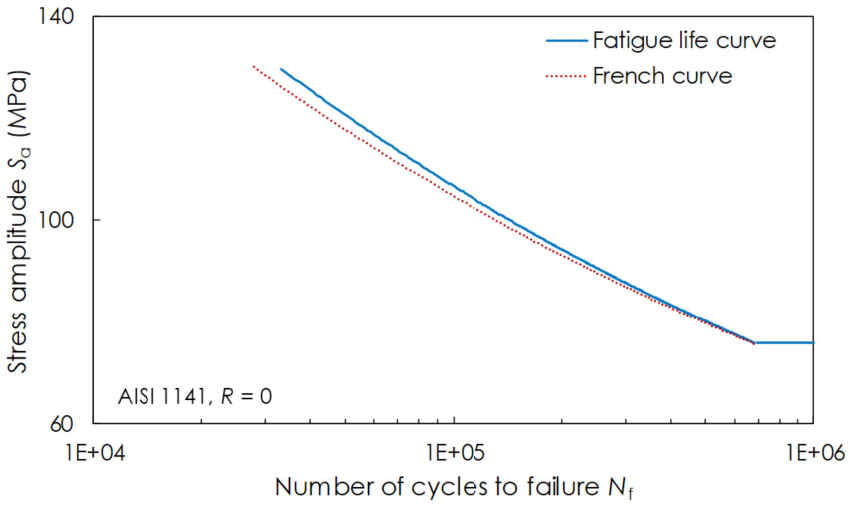

Figure 50: Comparison of the numerically determined French (crack initiation number of cycles) and Wöhler (complete number of cycles to failure) curves for the steel AISI 1141.

cracks have been reached. More precisely, the horizontal line denoting the S_e magnitude (see Figure 49, horizontal blue line) is drawn at the transition between the *S-N* points determined by applying the aforementioned RdM (grey-filled squares, i.e. transitional cases) and the RoM (red-filled squares, i.e. run-outs), respectively. The magnitude of the endurance limit (S_e) is estimated to be 76 MPa for the steel AISI 1141.

In addition, the number of cycles required for crack initiation (N_{ini}) have been plotted in the form of a French curve, as shown in Figure 50. This curve together with data from Table 5 confirm the statement from Section 4.2 that the initiation phase takes the majority of the fatigue life, especially in the region close to the endurance limit.

The two-scale approach used to produce the results from this study has already been reported by the author in [14B, 16S, 17L, 17M]. However, in [17O] the approach was applied for the first time to numerically construct the *S-N* curve in its whole extend, including the endurance limit; as shown in this study, too. Furthermore, a crack initiation criterion based on the crack growth rate drop is another novelty introduced here in [17O]. Similarly, this has been also reported later in [18M, 18L, 19M]. The results of the study presented in this section have been published in [18M].

To conclude, fatigue crack initiation and subsequent long crack growth in a polycrystalline material has been successfully simulated using the multiscale fatigue approach. The TM equation has been applied in the modelling of the crack initiation stage while the classical LEFM has been used for the long crack growth, up to final failure. By combining those two approaches, it is possible to construct the *S-N* curve numerically. However, an agreement could not be achieved by comparing the simulation-based *S-N* curve from Figure 49 and the experimentally obtained results of Fatemi et al. [04F], performed on the same specimen made of the same steel AISI 1141 and under the same loading conditions ($R = 0$). Namely, the experimentally de-

termined endurance limit (S_e) is equal to 155 MPa [04F], which is approximately two times higher than the calculated S_e value of 76 MPa. It needs to be remembered that these S_e values represent the stress amplitude of the applied cyclic stress range (S_a, see Figure 38) with the loading ratio R equal to 0. It is expected that a better agreement with the experimental results can be achieved by selecting another – considerably higher – magnitude of the CRSS. According to the TM model, the higher the CRSS, the better the durability of a material; or in other words, with higher values of the CRSS, the *S-N* curves shift upwards. More details on the influence of the CRSS follow in Section 5.2.

The CRSS of 117 MPa calculated by means of molecular dynamics for BCC α-iron by Hummel et al. [14B] is used in this study due to the lack of a more appropriate value for the steel AISI 1141. The reason to expect a higher CRSS magnitude – and by that a higher S_e value – for the used vanadium-based microalloyed steel AISI 1141 [04F] are its improved mechanical properties over conventional counterparts – and thus over iron – achieved by microstructural modifications, i.e. by the addition of small amounts of the microalloying element vanadium (V, 0.053 wt%) [96Y]. It is known that such alloying elements contribute to the strength in general, but also to the CRSS magnitude. Another reason to expect a higher CRSS is the relatively high elastic limit R_e of around 560 MPa for this steel. More details on the influence of alloying elements on the CRSS as well as on R_e can be found in Section 5.2.1. Aside of that, a repeated study on the same material and same specimen but with a higher CRSS value (232.5 MPa) is shown in Section 5.2.3. In this repeated study, a good agreement has been achieved by comparing the simulation-based S_e = 152 MPa and the experimentally obtained S_e = 155 MPa values [04F].

5.2 Determination of the CRSS and its Relevance in the Fatigue Process

This study can be considered as an extension of the previous one (see Section 5.1). It deals with the numerical estimation of the fatigue life represented in the form of stress- or strength-life (*S-N*, or Wöhler) curves of metals with different crystallographic structures, namely body-centred cubic (BCC) and face-centred cubic (FCC). Their life curves are determined by analysing the initiation of a short crack under the influence of the microstructure and the subsequent growth of the long crack, respectively, as discussed in previous sections. The long crack growth analysis is conducted using Paris law. The purpose of the study is to analyse the importance of the crystallographic and grain structure as well as the parameter CRSS on the shape and position of the fatigue life curve in the *S-N* diagram.

A scientific approach to the question of fatigue strength is to consider the effects of crystal structure on fatigue mechanisms [64F, 65F, 67B, 71G]. Researchers from the field of fatigue have long been aware of the ratio between endurance limit and ultimate ultimate strength, S_e/S_u. This ratio is also known as the fatigue ratio and is typically higher for ferrous materials (including steels), which are of the BCC type, than for

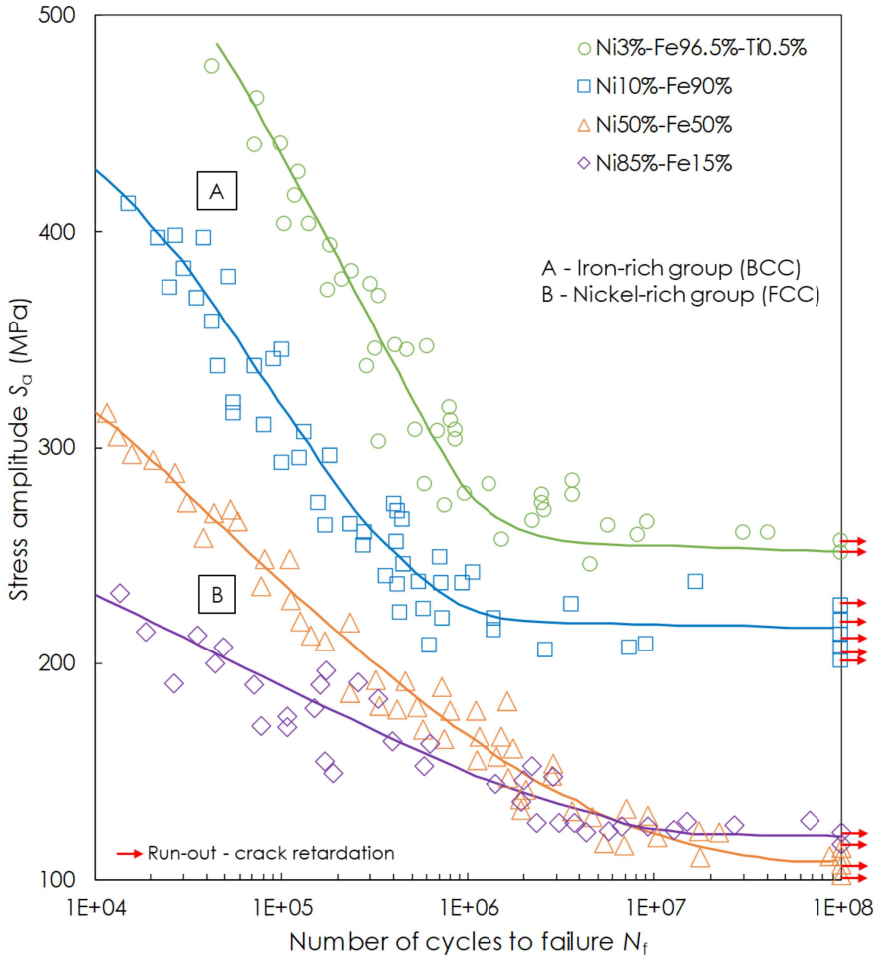

Figure 51: Comparison of S-N curves of iron-rich alloys, which are of the body-centred cubic (BCC) type, with nickel-rich alloys, which are face-centred cubic (FCC). These experimentally determined S-N curves illustrate the existence of definite endurance limits in BCC materials [64F, 71G].

non-ferrous materials, which are FCC. Table 1 shows the fatigue ratio S_e/S_u for a selection of technical materials. Furthermore, ferrous materials generally show a sharp "knee" in the *S-N* diagram at about 1E06 cycles, after which the strength-life curve increasingly flattens. The strength at this point is known as the endurance limit. Interestingly, most other materials exhibit a gradual flattening between 1E07 and 1E08 cycles (see Figure 14 and Figure 51). Although these effects have been explained by some researchers in terms of strain ageing and dislocation locking (see [71G]), there is also evidence that the crystal structures of the materials play an important role.

Ferro et al. [64F, 71G] examined two groups of iron-nickel alloys, which included an alloy with 96.5% iron and pure nickel. In these tests, the ferrous or iron-rich group (BCC) exhibited consistently higher fatigue strengths than the nickel-rich group (FCC), as well as showed a definite endurance limit at about 1E06 cycles in contrast to the FCC-based group. Figure 51 illustrates these effects. All materials had the same geometry, all had the same preparation process (annealing) and all have

been tested under the same cyclic conditions. More details on the preparation and fatigue experiments can be found in References [64F, 71G]. These same authors collected data on the fatigue ratio for a large number of pure materials with different crystal structures and concluded that the fatigue ratios of BCC materials are consistently higher than for FCC and HCP (hexagonal close-packed) materials [65F], as aforementioned as well as shown in Table 1 from Section 4.2. The comparisons are most meaningful for pure metals in which the effects of alloying, ageing, etc., are absent.

According to Grosskreutz [71G], there is certainly evidence that the crystal structure plays a contributory role on the height and appearance of the endurance limit under constant cyclic stress range. Besides the importance of the crystal structure, the aforementioned differences could be explained in terms of dislocation movement within the crystalline lattice of the grains. A question that can be posed is why should this influence exist. Since the reasons have not been proven, some general statements can be made. First, coherent slip leading to well-defined bands is not as likely in BCC structures simply because there are so many available slip systems, usually 24 to 36 compared to 12 in FCC structures and 3 to 6 in HCP materials, depending on the material (titanium is a special case, with 12 possible slip systems). Therefore, slip is well dispersed in BCC metals and slip band cracking is not as easily achieved. Furthermore, slip activity at a crack tip in BCC metals is not "exhausted" easily by hardening. Therefore, energy is consumed that might otherwise be available for crack extension. This capability to keep well-dispersed dislocation mobility, also in the case of extended fatigue cycling, is seemingly the most significant characteristic of the BCC system with respect to fatigue resistance. A second, assumingly related and thus equally relevant, reason for the superior performance of the BCC-based systems under fatigue conditions is the larger stress required to move dislocations. This stress is called the critical resolved shear stress (CRSS) which may be 100 times as large in BCC as in FCC structures. The yield stress of BCC metals is correspondingly higher, too. This fact, together with the work hardening rates, which are lower in BCC-based systems [65F], affects the endurance limit. Namely, BCC metals possess higher endurance limits than FCC metals, placing them for that reason closer to the ultimate strength.

Accordingly, the effects of crystal structure and the CRSS provide an interesting investigation site, which could eventually provide clues on the effective prediction of materials that are more fatigue resistant. Materials science and numerical methods are promising in combination that possesses capabilities to shed light on this not sufficiently resolved research topic. The aim of this section is to provide relevant information on the CRSS and to numerically investigate its importance in the fatigue performance of steels and other metals with different crystallographic structures.

5.2.1 Compression Testing of Small Pillars

A major interest in present-day materials science is to understand material deformation and failure mechanisms that are present in a vast number of applications and at different scales (predominantly at micro- and nanoscales). A method based on a new type of compression testing of pillars of the order of nano- and micrometer size has been developed and thereby opened a novel perspective on the investigation and measurement of the CRSS value for various materials. The method is becoming increasingly popular due to its cost-efficient and relatively simple procedure and the ability to analyse deformation mechanisms and material properties by focusing attention on a restricted material volume isolated from single crystals (see Figure 52). The experimental technique used to isolate these small-sized pillars is Focused Ion Beam (FIB) machining. Furthermore, the method of pillar compression testing enables the investigation of specific areas on the surface of a polycrystalline material, and thereby deeper insight into the underlying dislocation mechanisms that eventually contribute to the plastic flow resistance [15R].

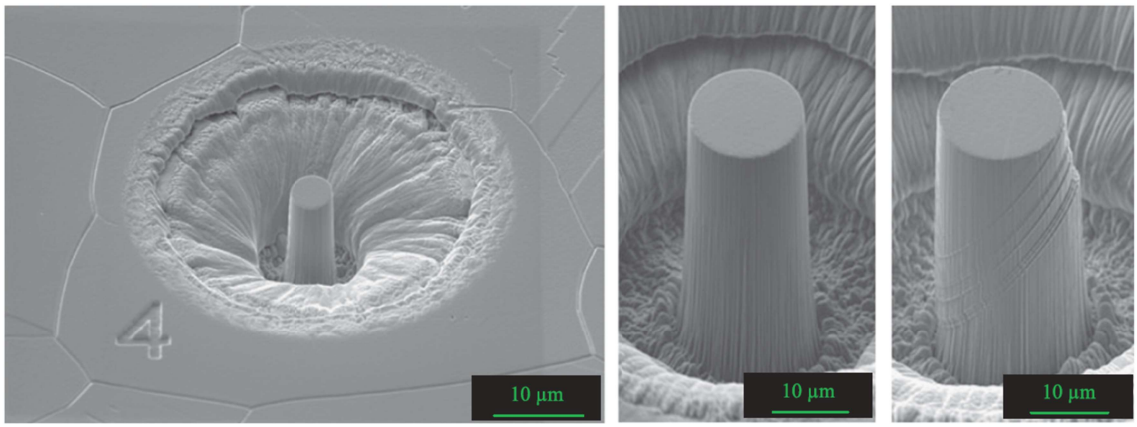

Figure 52: Example of a 10 μm pillar pillar cut within a large grain; Left – Pillar shown with respect to the grain boundaries; Middle – Zoomed view; Right – Deformed pillar after compression testing [13O].

The pioneering research in the field of pillar testing published by Uchic et al. [04U] in 2004 showed the example of cylindrical Ni micropillars, which at that time was an entirely new behavioural regime. Namely, the investigated pillar exhibited low hardening rates and discrete strain bursts (see Figure 53 for the two effects), and a power-law relationship between the CRSS and pillar diameter (*D*), or the so-called size effect (see Figure 54e) [11N]. It has been noted that the CRSS values of both FCC and BCC pillars decrease as the pillar size increases, conforming to inverse power-law scaling [04U, 11G, 16C]. Aside of already mentioned publications, a large number of other publications regarding small-scale plasticity are available today, some of them are [06D, 06K, 07C, 10J, 13B, 14G, 15C, 16A, 16J, 17P].

Figure 52 shows an example of a pillar cut within the austenitic grain (austenitic stainless steel AISI 316L), done by Monnet and Pouchon [13O]. After compression, the deformation markings visible as slip traces on the surface of investigated cyl-

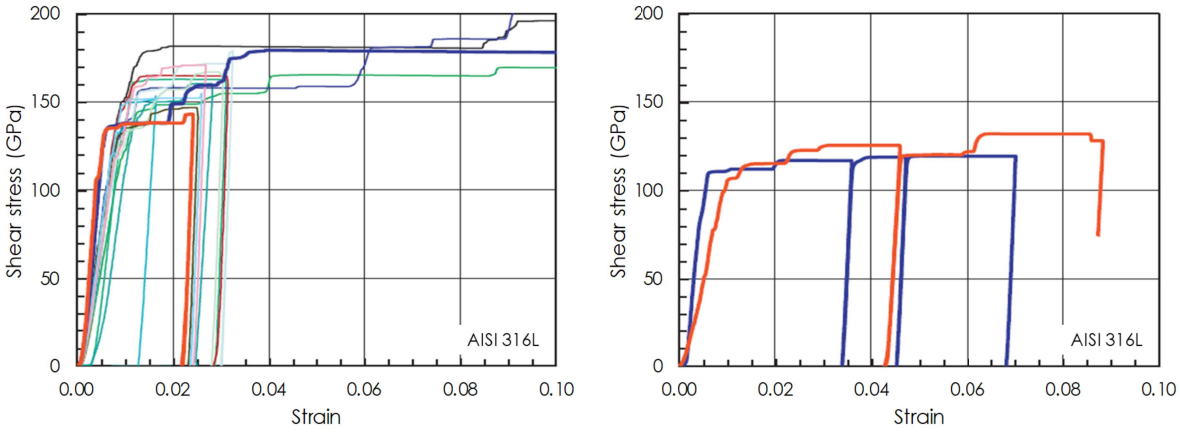

Figure 53: Resolved shear stress vs. strain curves of pillars made of AISI 316L austenitic stainless steel: Left – 5 µm pillar; Right – 15 µm pillar [13O].

indrical single-crystalline pillars indicate single slip mechanism, as Figure 52R depicts. Figure 53 gives resolved shear stress versus strain curves (deduced from the force versus displacement curves by using Schmid factors) of the pillars considered in their study. The strain bursts that emerge as flat regions have been observed as in the study of Uchic et al. [04U]. The first strain burst has been understood to be a product of the first motion of a dislocation while the succeeding strain bursts represent collective movements of dislocations in an avalanche-like manner [13O, 06D, 07C]. The small-scale yield (shear) stress, i.e. the CRSS, for pillars is determined as the stress at which the first strain burst occurs [16C].

A significant discrepancy in the value of the CRSS measured for the 5 µm pillars, 160 MPa (Figure 53L), is to be noted with respect to the larger 15 µm pillar, where the CRSS is equal to 110 MPa (Figure 53R). This confirms that the size effect is also present in AISI 316L steel. Another observation, from the same figures, that is in analogy to the general findings from the pillar compression testing are the fluctuations of the CRSS that decrease as the pillar size increases [13O].

Okamoto et al. [16O] investigated the behaviour of high-enthalpy alloy (HEA) CrMnFeCoNi-based pillars under similar compression tests. Figure 54b,c show cases where these researchers applied two different loading-axis orientations ([$\bar{1}$26] and [$\bar{1}$23], Figure 54a) in order to obtain stress-strain curves of micropillars. Values of the CRSS are calculated by using the small-scale yield stress magnitudes and the Schmid factors that correspond to the two investigated orientations (0.488 and 0.467 for [$\bar{1}$26] and [$\bar{1}$23], respectively) and are given in Figure 54e versus micropillar size. It follows from Figure 54e that the CRSS values for the two considered orientations match to each other over the whole range of investigated micropillar sizes. This undoubtedly indicates that the CRSS values for slip on the (111)[101] slip system are independent of crystal orientation. This was used by the authors [16O] to combine the data points from the two tests into one master curve, shown in Figure 54e by the red dashed line. Similar to what has been recognized in single crystalline micropillars of many other FCC and BCC metals [04U, 06D, 06K, 09C, 10J, 11G], the size effect has been also observed for the CrMnFeCoNi HEA.

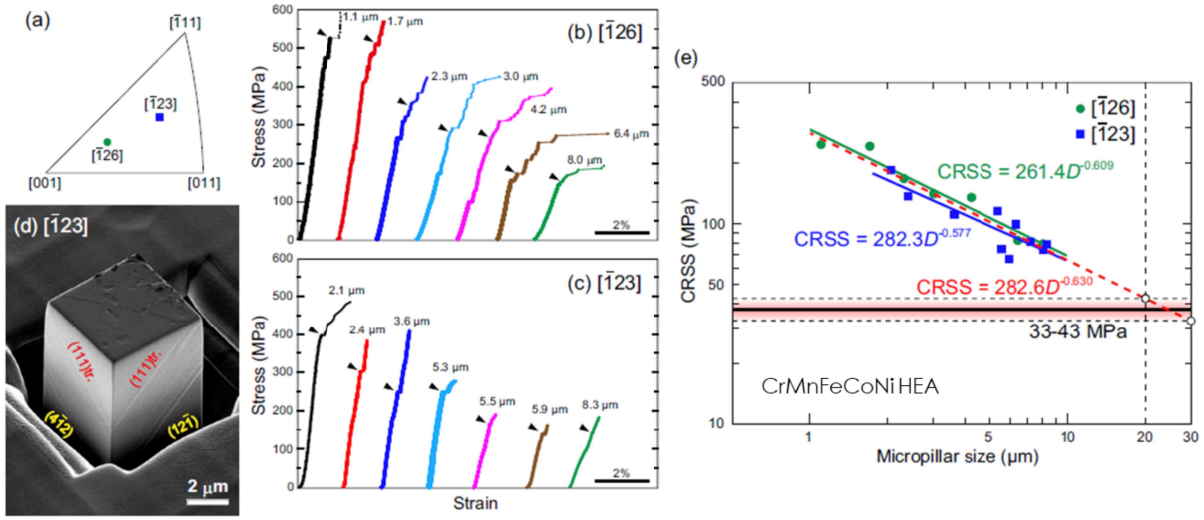

Figure 54: Compression tests of single-crystalline micropillars of the equiatomic CrMnFeCoNi HEA. (b,c) Selected stress-strain curves of single-crystalline micropillars with loading-axis orientations of (b) [$\bar{1}$26], and (c) [$\bar{1}$23], respectively; (d) Secondary-electron image taken in a scanning electron microscope showing {111} slip traces on the side surfaces of a deformed micropillar with [$\bar{1}$23] orientation; (e) Size dependence of the critical resolved shear stress (CRSS) for {111} <101> slip [16O].

A size effect or a power-law relationship between the CRSS and pillar diameter, invoked in the previous section, is known to affect two features of plastic deformation: (i) the CRSS becomes stochastic and increases with decreasing pillar dimension; (ii) the hardening rate decreases strongly in pillars of micron scale. However, concerning the CRSS, several studies have shown that the size effect vanishes beyond a given pillar size *D*. In pure nickel, *D* was found being close to 20 µm by Uchic et al. [04U] and 30 µm by Dimiduk et al. [05D]. In gold, the size effect seems to decrease strongly in pillars of sizes larger than 7 µm [05G]. However, in heterogeneous materials, such as Ni-based superalloys, the effect on the CRSS persists even in large pillars [04U, 12S, 13O]. However, as concluded by various researches [04U, 05D, 05G, 10J, 11N, 14O, 16O], this decrease of the CRSS continues until the micropillar size reaches a value of 20 to 30 µm, at which the estimated CRSS may be further taken, for e.g. FEM-based simulations, as the representative value of the bulk material. In other words, by extrapolating the micropillar data obeying the inverse power-law scaling to the critical pillar size, the bulk CRSS values can be estimated. Accordingly, the bulk CRSS value for the HEA is estimated in between 33 and 43 MPa (Figure 54e), what fits the range of determined values for pure FCC metals (e.g., ~14 MPa for Al [11N]).

The increased strength with reduced size follows a power law that explains the general relationship:

$$\tau_c = KD^{-n} \tag{5.1}$$

where τ_c is the CRSS, *D* is the top-surface diameter of a cylindrical pillar sample (see Figure 53), *K* is the power-law coefficient and *n* is the power-law exponent, i.e. the power-law slope [15R].

Despite being a matter of major discussions, it is generally agreed that the size effect is a consequence of the dislocation nucleation-governed plasticity, which is apparent from the higher stresses that arise during mechanical deformation of small-sized nanopillars. The explanation of the dislocation nucleation-governed plasticity can be found in its dependency on dislocation storage ability of FCC and BCC systems. Namely, dislocations moving inside the small-sized pillars are attracted to the free surface, and in order to sustain further deformation, new dislocations have to nucleate either inside the pillars or at their surface. This phenomenon especially concerns the strained FCC pillars deep in the sub-micron size region where they experience the so-called "hardening by dislocation starvation". In such cases, the pillars remain without dislocations, which vanish from the free surface at faster rates than they multiply inside the bulk [8, 20, 24]; and to nucleate new dislocations, higher stresses are required. According to experiments on FCC and BCC pillars [08G, 09C, 09S, 16A], the more pronounced size effect in FCC materials, with respect to BCC materials, is related to the lattice resistance to plastic flow, as aforementioned. A dislocation-starved condition is unlikely in the BCC system as a longer residence time is attributed to its dislocations, together with the ability to multiply new dislocations before the existing ones exit the pillar surface [16A]. On contrary, the longer residence time of dislocations in BCC systems might be an explanation for their higher strength at higher scales, what is also in accordance to the statement from Section 5.2 about higher values of the CRSS in the BCC systems and their superiority in fatigue performance with respect to FCC systems.

The plastic deformation of e.g. iron single crystals shows size dependent features that can be related to the underlying dislocation structure. In large single-crystal samples, the initial dislocation structure exists in a variety of configurations. The plastic flow initiates when the stress is high enough to move the first dislocations. The first dislocations can move over relatively large distances before interacting with other dislocations, so-called easy glide. The shear stress necessary to produce the easy glide is named as Peierls-Nabarro stress. The interactions between dislocations form barriers for further slip and cause work hardening of the crystal. In small single-crystal samples, the included dislocation structure is expected to vary between individual samples [08N]. When the first dislocations start to move, the movement is restricted by the nearby sample surface. The manufacturing process of the sample can truncate existing dislocations [07P, 07R] or possibly form new ones, e.g. from the FIB-induced deformation and damage process [07K]. Similarly as Kraft et al. in [10K], Rogne et al. [15R] summarized the plastic deformation into three regimes on the example of iron single crystals. The regimes are indicated in the upper part of Figure 55.

Regime 1 is the bulk-like regime, where the macroscopic stress–strain curves are relatively smooth. In this regime, the samples are typically a few microns or larger, up to the size of conventional samples for tension tests. The sample includes larger dislocation segments and parts of dislocation structures [08N]. When comparing the flow curves to mm-sized single-crystal samples, the flow stress is the highest in the μm-

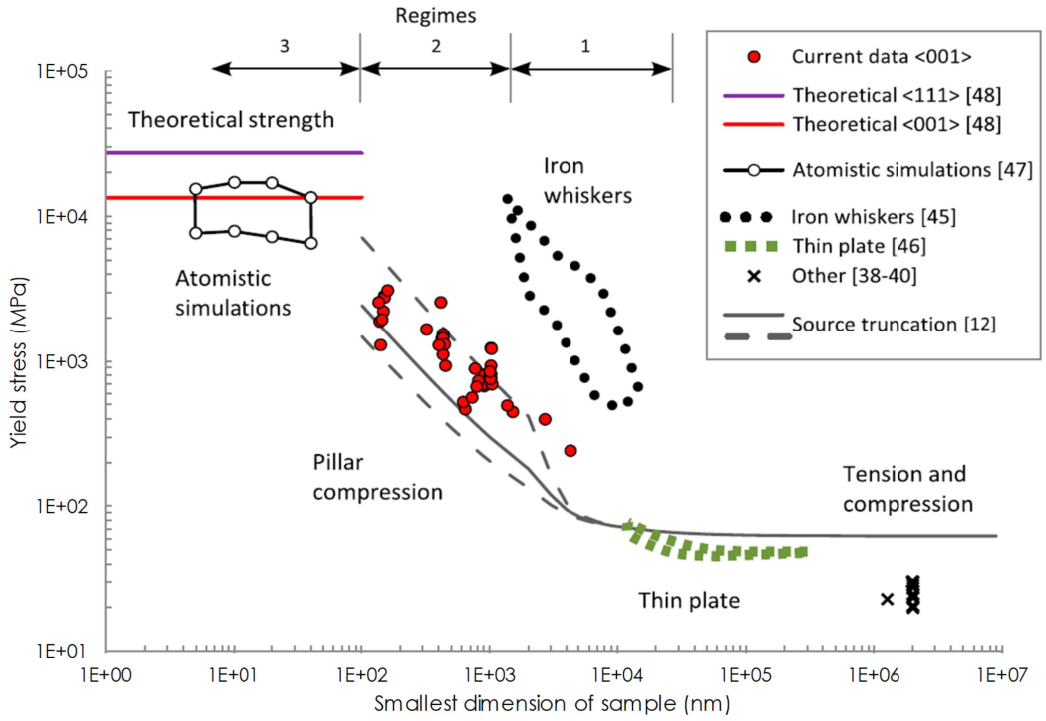

Figure 55: Yield stress of different sized single-crystal iron samples [04U, 05U, 07P, 09K, 09M, 09C, 09S, 09H, 10S, 15R].

sized samples and the work hardening is about equal [05D, 11T, 13T]. However, the limited volume constrains the dislocation movements and interactions and causes a strengthening effect [5].

Regime 2 is the intermediate regime for which the stress–strain curve presents irregular plastic flow with elastic segments and strain bursts (see Figures 53 and 54), for load-controlled experiments. Since the sample is smaller than the average distance between dislocations, it is likely that few and small dislocation segments are present in the sample. The truncated dislocation segments need a higher stress to operate in a stochastic way. The smaller the segment, or sample, the higher the stress necessary for deformation. Mobile dislocation segments may move to the free surface and annihilate [05G, 06G, 11K], or possibly multiply on the way [08C, 08G, 08W].

Regime 3 is the surface nucleation regime and has a plastic flow characterized by large elastic segments and abrupt strain bursts, where the stress is typically several GPa. The small volume makes it unlikely that dislocation segments from the initially annihilated dislocation structure exist in the sample. For plasticity to occur, dislocations have to propagate from surface irregularities introduced during the FIB fabrication [09H, 07K, 10L].

The experimental results obtained in micropillar tests (MPT) mainly fall under Regime 2, the intermediate regime.

Strengthening mechanisms in single-crystals, such as dislocation density (as explained in the text above in relation to the dislocation residence time) and solute atoms, directly influence the deformation behaviour in pillars, and thus the CRSS magnitude. An important strengthening source in industrial materials is solid solution

strengthening, or the alloy friction, that results from solute alloying elements, especially from substitutional elements, within the matrix. Furthermore, a significant content of added elements usually induces the formation of precipitates within the matrix of the host material, leading to another strengthening mechanism known as precipitation strengthening. In some industrial materials, like annealed AISI 316L-type austenitic stainless steel, no precipitation is observed, leaving the solid solution strengthening as the prevailing source to the strengthening process [13O].

The resistance for the dislocations to move through the crystal, or the CRSS (τ_c), is dictated by the present strengthening mechanisms in the crystal [15R]. To recall, the CRSS for compressive failure may have several components: The Peierls-Nabarro stress τ_0, the dislocation hardening τ_{dh}, the solid solution hardening τ_{ssh}, and the strengthening induced by particles τ_{ps}. Irrespective whether all or just particular strengthening components are present, linear superposition may be applied when calculating the CRSS (τ_c) [13O]:

$$\tau_c = \tau_0 + (\tau_{dh} + \tau_{ssh} + \tau_{ps}) \tag{5.2}$$

In the case of high purity materials, with zero initial dislocation density and with no added alloying elements, the CRSS comprises merely the Peierls-Nabarro stress τ_0, which is the minimum requirement for initial dislocation motion [13B].

Furthermore, the global yield stress R_e comprises the CRSS and further strengthening mechanisms that are present in bulk metals, namely the grain boundary strengthening τ_{gbs} and the phase boundary strengthening τ_{pbs}. Equation (5.3) summarizes all the mechanisms that contribute to the strength of metallic materials.

$$R_e = \tau_c + \tau_{gbs} + \tau_{pbs} = \tau_0 + \tau_{dh} + \tau_{ssh} + \tau_{ps} + \tau_{gbs} + \tau_{pbs} \tag{5.3}$$

An example of strengthening can be given with iron; The shear strength of large single-crystal samples, in mm size, can go below 10 MPa [63S, 83F, 15R] at room temperature in the case of high purity iron. Previous studies on iron with different impurity contents [66S, 15R] confirm the importance of interstitial solute atoms in the strengthening of crystals. In general, increased amounts of impurity elements lead to an increased shear strength in the crystal due to more resulting obstacles that hinder the gliding of dislocations. Based on these results, it has been estimated that the strengthening contribution of C and O is about 40 MPa; which is significantly higher than the 10 MPa for the high purity single-crystal iron. The strengthening from solute atoms and impurities is the same in different-sized pillars; and it should not be partially responsible for the size effect that is discussed in Section 5.2 [15R].

An interesting study was done by Guo et al. [14G] on the measurement of the CRSS for phases in a multiphase material. In their work, coupled with the electron back-scatter diffraction (EBSD) technique, micropillar compression was used to evaluate the CRSS of ferrite, which is BCC, and FCC austenite in a cast duplex stainless steel (Z3CN20-09M). Compression tests were carried out by compressing free-standing micropillars of ~5 μm diameter that were fabricated by FIB. The results reveal that BCC ferrite has a much higher strength than FCC austenite; while austenite pos-

sesses better ductility values than ferrite. The CRSS values are, quantified to be ~194 MPa and ~318 MPa for austenite and ferrite, respectively. Strengthening mechanisms can be regarded as responsible for the higher strength of ferrite. Firstly, solid solution strengthening is introduced by the higher alloying content of substitutional chromium in ferrite (26.74 wt.%) than in austenite (21.11 wt.%) [03C]. Although austenite contains a higher nickel content than ferrite, i.e. 9.14 wt.% in austenite compared to 5.18 wt.% in ferrite, it has been reported that the solid solution strengthening caused by chromium is higher than that of nickel [12R]. Secondly, as already stated in this section, the low mobility of screw dislocations in BCC crystals usually results in higher strengthening as well as a higher strain hardening rate through dislocation-dislocation interactions or kinetic pile-ups of the screw dislocations in an area close to the dislocation sources, which in turn leads to an enhanced strength of the ferrite phase [08G, 09S, 14G].

Quantification of the strengthening components is a challenging task but is also necessary for the understanding and eventual modelling of the mechanical behaviour of metals. For BCC and FCC materials, the slip event is usually activated in unique crystal systems when the applied stress is higher than their CRSS, which is associated with the intragranular crystal plasticity [14G]. Therefore, it is of great importance to be able to determine the CRSS of a phase or more different phases in metallic materials to understand the mechanical behaviour of their bulks and to further establish appropriate material and damage models (e.g. crystal plasticity theory and/or TM equation/model) for the simulation studies.

5.2.2 Atomistic Simulations

Atomistic methods, e.g. MD, are methods used to numerically simulate physical movements of atoms. In the most common version of MD, the trajectories of atoms are determined by numerically solving Newton's equations of motion for a system of interacting atoms, where forces between the atoms and potential energy are defined by molecular mechanics force fields. The method was originally conceived within theoretical physics in the late 1950s [59A, 64R] and, besides in materials sci-

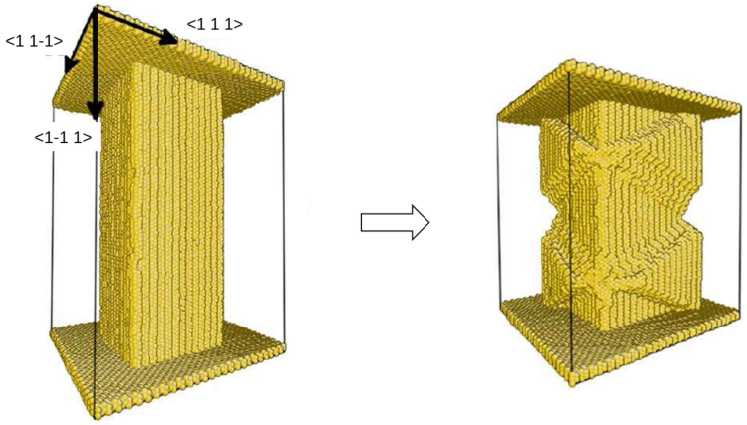

Figure 56: Left – Initial configuration of Cu nanopillar and compression plates; Right – Pillar following a compressive strain of 22% [14H].

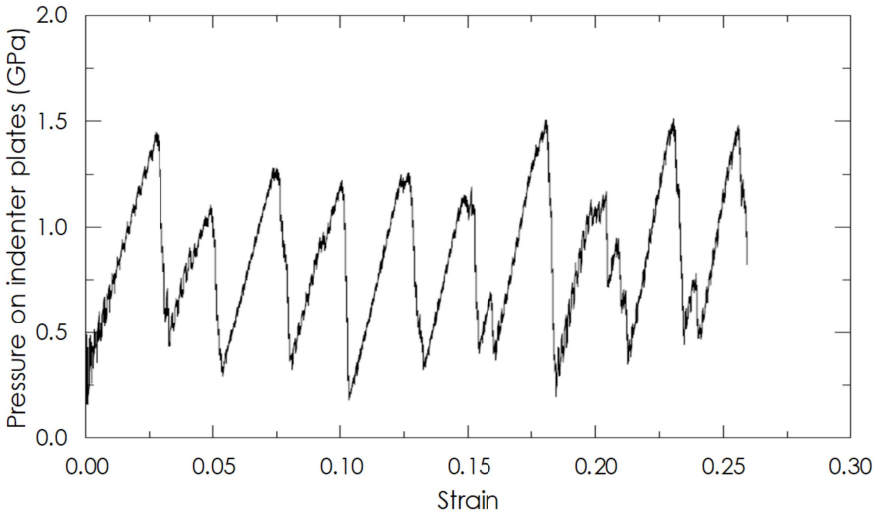

Figure 57: Plot of pressure acting on compression plates vs. strain for a pillar under compression [14H].

ence, is applied today also in chemistry, chemical physics and modeling of biomolecules. Many authors applied atomistic methods such as MD to calculate different strengthening mechanisms.

Healy [14H] carried out compression simulations on a Cu nanopillar. These simulations showed deformation mechanisms, which are likely to resemble those seen experimentally in plasticity of nanowires, nanopillars, and micropillars. The pillar with the side faces of 8 nm in width, 18 nm in length and containing around 100,000 atoms was placed in between two compression plates which consisted of constrained atoms. An image of the pillar prior to deformation and at a strain of 22% can be seen in Figure 56. The stress versus strain response on the indenter plate surfaces is characterised by increasing stress as the pillar is compressed followed by sudden decreases in the stress when a dislocation is generated and moves through the pillar. This can be seen in Figure 57.

Kositski et al. [17K] calculated the conditions for nucleating dislocations in α-iron (Fe) faceted nanowires under compression. In this configuration, dislocations were

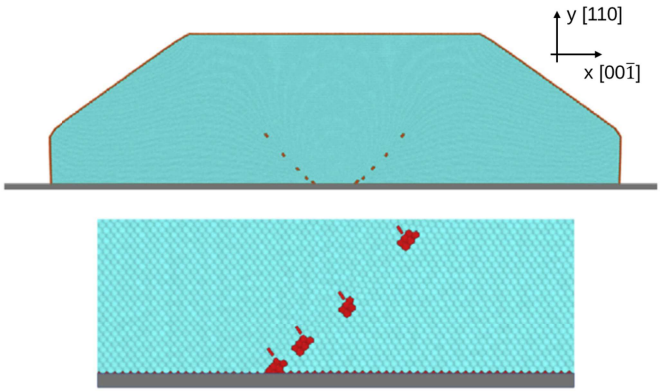

Figure 58: Top – 26.5 nm high α-Fe nanowire, on a rigid substrate, containing five dislocations (red atoms) that have been nucleated on each of the two slip planes; Bottom – The atomic structure with a pile-up showing four edge dislocations [17K]

nucleated at points of stress concentration but formed dislocation pile-ups (Figure 58), which contributed to strengthening [17K]. The cross-split mechanism was also identified with the observation that it occurs when the core of two opposite sign edge dislocation coalesce [17K].

In order to examine the effect of specimen size on the dislocation nucleation stresses, as well as on the stress needed for a cross-slip to occur, nanowires of various heights were constructed by Kositski et al. [17K]. The nucleation stresses at every nucleation event, as well as the stress needed for cross-slip for different heights of nanowires, are summarized in Figure 59. The extrapolation method for MPT discussed in the previous section (5.1) has not been applied for the numerical results from [17K] due to the fact that the stresses shown in Figure 59 are nucleation stresses and not the stresses required to move a dislocation.

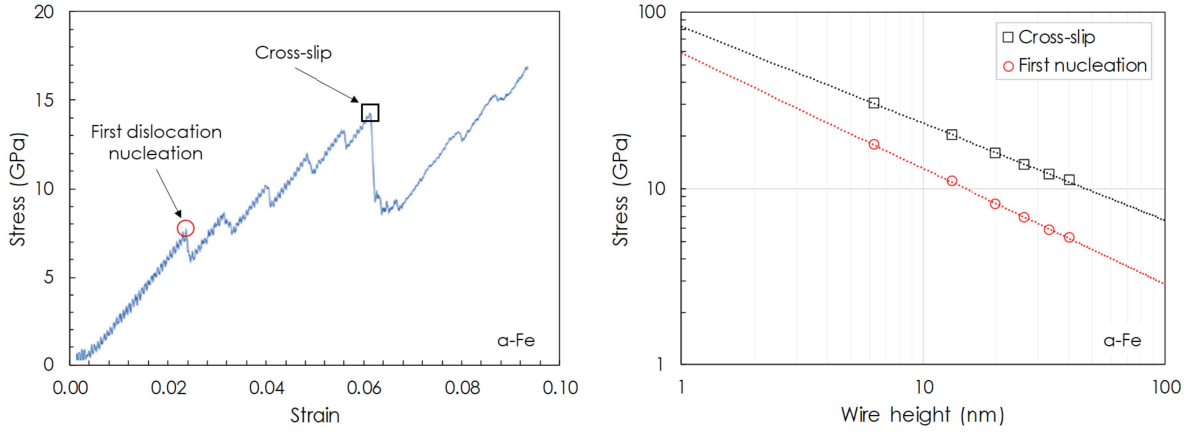

Figure 59: Left – Engineering stress vs. engineering strain calculated from compressing a 26.5 nm high nanowire; Right – Nucleation stresses (circles) and cross-slip critical stresses (squares) as a function of wire height [17K].

Similarly, Rogne et al. [15R] performed calculations of the theoretical tensile strength based on density functional theory calculations [03F], represented as upper strength limit in Figure 55 and plotted together with available data on single-crystal iron samples of various types. Here, the upper limit for loading along [0 0 1] was 12.7 GPa and along [1 1 1] was 27.3 GPa. As seen in the same figure, the strength levels from MD simulations were lower than the results for density functional theory calculations. Results from MD simulations of defect-free single-crystal iron nanopillars [12E] were different from the experiments, too. Three pillars of the same size, $D \approx 150$ nm, reached in experiments highest yield stresses between 2.7-3.1 GPa, as visible from Figure 55. This is about 45% lower than the values predicted from MD simulation of a pillar with the same loading direction and a diameter of 40 nm [12E]. An important difference, however, is that the MD pillar is initially defect free and that the deformation initiates when new dislocations nucleate from the surface of the pillar. The difference in yield stress between the experiments and MD simulation seems to be a consequence of the difference in the initial defect structure and the deformation mechanisms when plasticity starts. The atomistic simulations, with surface nucleated dislo-

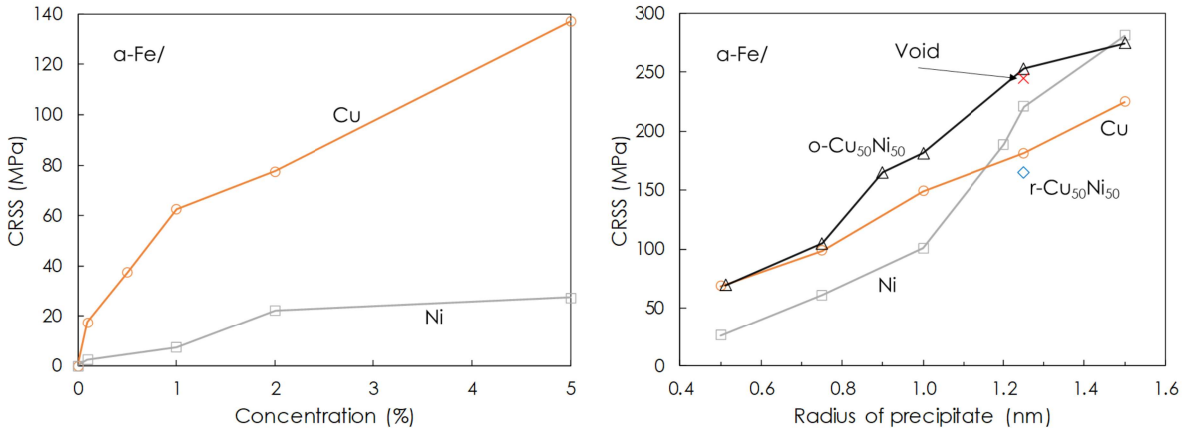

Figure 60: Left – CRSS of α-Fe in dependence of the concentration of dissolved Cu and Ni atoms [11S]; Right – CRSS for Cu, Ni and ordered CuNi (o) precipitates of different radii as well as for a randomly composed CuNi (r) precipitate and a void of radius 1.25 nm in α-Fe [05K].

cations, can be considered as an upper limit to the micropillar compression experiments [15R].

IMWF has a strong background concerning the usage of atomistic simulations [05K, 10P] on fundamental aspects of materials science, such as strengthening mechanisms and dislocation multiplication. In [11S], Schmauder and Kohler performed atomistic MD simulations of solid solution strengthening of α-iron by alloying it with substitutionally or interstitially dissolved atoms. Figure 60L shows the results for the strengthening, i.e. an observed increase in the CRSS with different concentrations of Cu and Ni atoms. In another paper, Kohler et al. [05K] performed MD simulations of the interaction of edge dislocations with precipitates in α-Fe in order to determine the CRSS for various morphologies of precipitates: pure copper and nickel precipitates, ordered and unordered copper/nickel precipitates, copper and nickel precipitates with substitutional iron atoms etc. The values of the CRSS values for these precipitates for typical dislocation-based glide planes are plotted in Figure 60R. Furthermore, Hummel [14B] performed MD simulations of cyclic deformation of the α-Fe system (Figure 61) in order to determine the CRSS magnitude.

The results from the study illustrate the development of the system from reversible plastic deformation to irreversible plastic deformation including dislocation nucle-

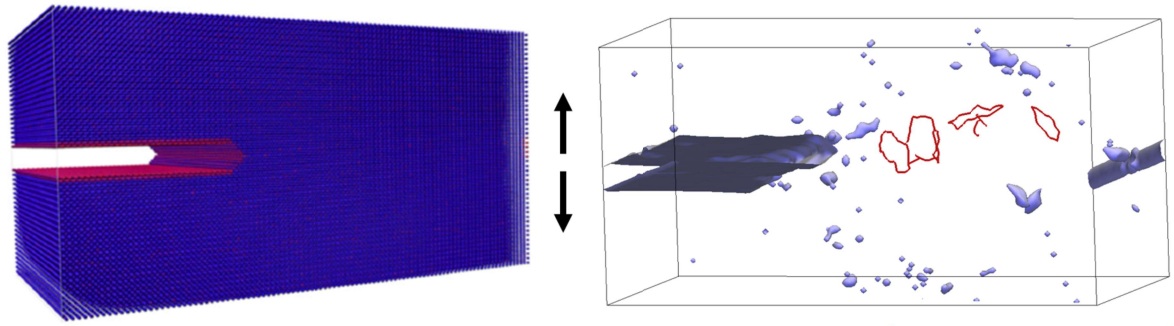

Figure 61: Left – BCC α-iron cuboid with dimensions of 286 x 143 x 143 Å³ and with a 15 x 90 Å² notch on a (110) plane (486,000 atoms); Right – Nucleated dislocations that remain in the system even when the applied stress has been removed after a few loading cycles [14B].

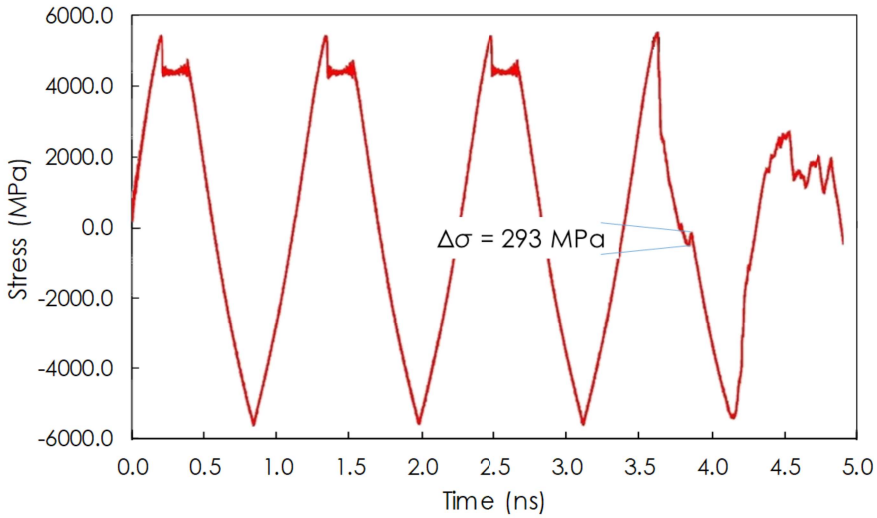

Figure 62: Stress in the loading direction vs. time (ns) during cyclic loading of the notched α-iron cuboid [14B].

ation, propagation, back-propagation and multiplication. The typical glide planes appearing under cyclic loading are plotted in Figure 61R. In these simulations, the intention was to force dislocation nucleation and to study such naturally formed dislocations as a realistic basis for dislocation movement analyses rather than to use artificially implanted dislocations in the model.

Further, dislocation nucleation takes place as the irreversible deformation begins. The small spikes in the stress-time curve are identified (see Figure 62) as single dislocation movement. The height of the spike, which is related to the CRSS to move a dislocation, is calculated to a value of 117 MPa, which is in very good agreement with an experimental value of 108 MPa that has been used for microscale modelling of fatigue by different authors [98H, 10G, 10N, 12N]. The 117 MPa value was used in the study on AISI 1141 steel from Section 5.1 as well as on Fe 99.9% from Section 5.2.3.

This value representing principally the stress required to move a dislocation through a perfect lattice with zero initial dislocation density and with no added alloying elements is also known as the Peierls-Nabarro stress (τ_0). As already mentioned in Section 5.2.1, the CRSS comprises merely the Peierls-Nabarro stress in the case of such a high purity material. In the presence of additional strengthening mechanisms in single-crystals of metallic materials, the linear superposition (Eq. 5.2) may be applied to calculate the overall CRSS (τ_c). A nice example of Fe-Cu steel for which the superpositioning principal can be applied is given in [04T]. By knowing the concentration of solute Cu (1.5 mass% [04T]), the diagram from Figure 60L [11S] can be used to estimate the solid solution hardening (τ_{ssh}). On the other hand, Cu clusters of around 0.9 nm size were observed in this steel, too. Here the diagram from Figure 60R [05K] can be used to estimate the strengthening induced by these clusters (τ_{ps}). By assuming a zero initial dislocation density, the CRSS for this specific case is estimated:

CRSS = $\tau_0 + (\tau_{dh} + \tau_{ssh} + \tau_{ps})$ = 117 + (0 + 70 + 125) = 312 MPa

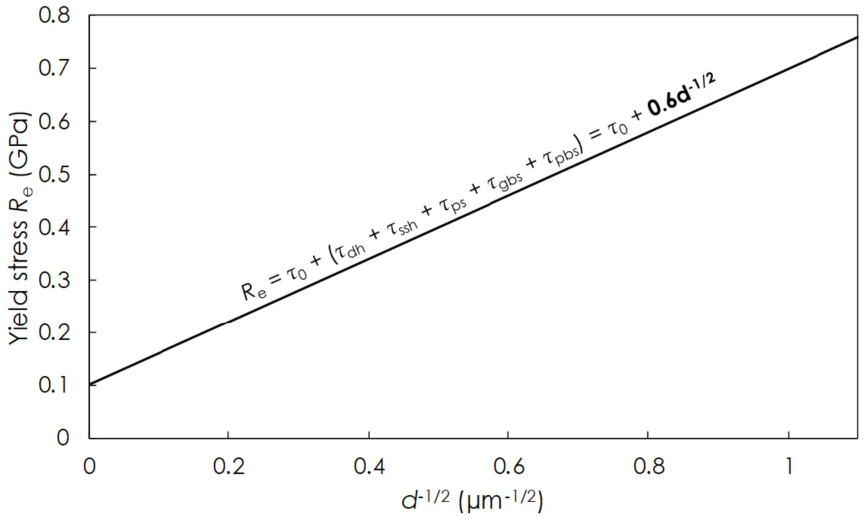

Figure 63: Hall-Petch relationship for steels [08E, 18Y]; R_e – yield stress, τ_0 – Peierls-Nabarro stress, τ_{dh} – dislocation hardening stress, τ_{ssh} – solid solution hardening stress, τ_{ps} – particle strengthening stress, τ_{gbs} – grain boundary strengthening stress, τ_{pbs} – phase boundary strengthening stress.

Furthermore, the global yield stress (R_e) can be calculated by adding the strengthening mechanisms that are present in the bulk material to the known CRSS magnitude (see Eq. 5.3). The grain boundary strengthening (τ_{gbs}) can be determined from the Hall-Petch relationship for steels (see Figure 63) by knowing the average grain size, which is equal to 1 μm for the considered Fe-Cu steel [04T]. The other strengthening mechanism contributing to R_e is the phase boundary strengthening (τ_{pbs}), and is equal to zero since the Fe-Cu steel contains a full ferritic microstructure. Accordingly, R_e is calculated for this steel:

R_e = CRSS + (τ_{gbs} + τ_{pbs}) = 312 + (405 + 0) = 717 MPa

Finally, the global dislocation density introduced by cold-working can be used to estimate the dynamic dislocation hardening (τ_{ddh}), which builds the tensile strength (S_u) together with the known R_e magnitude. According to Tanaka et al. [18Y], S_u for a grain size of 1 μm for the considered Fe-Cu steel [04T] is estimated:

$S_U = R_e + (\tau_{ddh}) = 717 + 623 = 1340$ MPa

The obtained S_u values fits quite well to the range of 1180-1350 MPa, reported by Takaki et al. [04T] for steels alloyed by Cu, what indicates that the superpositioning principle can be applied when the individual strengthening contributions for a specific metal are known.

5.2.3 The CRSS and its Effect on the Fatigue Life Curve

In order to numerically analyse the total fatigue life of structures, i.e. structural components or a specimen, from the moment when the first microcrack nucleates within a grain up to the moment when the dominant crack evolves into a critical one leading to final failure, a multiscale fatigue simulation approach can be applied, similar as done as in the case of AISI 1141-based specimen from the previous section (5.1).

5.2.3. The CRSS and its Effect on the Fatigue Life Curve

Figure 18 on page 30 shows a scheme of scales that need to be considered, starting with the nanoscale, going up to micro-/mesoscales and ending up with the macroscale. The up-to-date nanoscale, i.e. atomistic, simulation techniques like ab-initio [14K, 15K, 16B] or molecular dynamics (MD) [05K, 10P, 11P] can provide the relevant material parameters needed at higher length scales of fatigue modelling and simulation scheme. One of these parameters is the critical resolved shear stress (CRSS) on the most active slip plane in a grain, that can be derived from MD simulations, e.g. by using the approach of Hummel et al. [14B, 18B]. Other methods for the derivation of the CRSS is micropillar testing (MPT), as discussed above. The CRSS is used as the input parameter for the micromechanics-based model (see Section 4.3.1) providing information on the number of loading cycles to nucleate a microcrack and subsequent growth of a short crack inside the microstructure (see Sections 4.3.2 and 4.3.4) of an investigated material. These initiation cycles are further transferred to the macroscale fatigue crack growth model based on power law equations (e.g., Paris law), which are finally used to estimate the total fatigue life, up to final fracture. By using the presented modelling workflow, the fatigue of metals can be simulated more or less independently of the experimental input [14B, 17L, 17M, 17O, 18B, 18M, 18L]. As stated in previous sections, the TM parameter CRSS is a threshold value of the shear stress along the glide direction that a dislocation needs to surpass in order to start moving. If the resolved shear stress is lower than the CRSS, no dislocation is moving on the glide plane and, consequently, no pile-up takes place at the grain boundary.

In order to approach the question of fatigue strength in a proper way, it is interesting from the scientific point of view to consider effects of the crystal structure on fatigue mechanisms. Besides the importance of the crystal structure, an assumption for the reason of superior fatigue behaviour of BCC metals, in terms of higher endurance limits, is generally the higher stress needed to move dislocations through their system, i.e. a higher CRSS. It is thus worthwhile to analyse numerically the fatigue life curves of materials with different CRSS values, but also by having their crystal structures in view.

Table 6: Critical resolved shear stress (CRSS) values for different materials.

Material	Crystal structure	CRSS (MPa)	Method	Source
AISI 304 (X5CrNi18-10)	FCC	160	MPT	Monnet and Pouchon [13M]
AISI 1141 (40Mn2S12)	BCC	117	MD	Hummel et al. [14B, 18B]
Fe 99.9%	BCC	35	MPT	Rogne and Thaulow [15R]
AA 1050 (Al 99.5%)	FCC	14	MPT	Jennings et al. [10J]

The purpose of this section is therefore to present the derivation of the CRSS parameter for materials of interest by using different methods of determination (MPT and MD simulations) and its implementation in numerical analyses for fatigue initiation life determination, based on the TM model. To meet the purpose, four materials are selected and are tabulated in Table 6.

Aside of the AISI 1141 steel with BCC crystal structure that was analysed in the previous section (5.1), three additional materials taken into account are FCC austenitic stainless steel AISI 304, high purity iron (Fe 99.9%) that is BCC and a high purity aluminium alloy (AA) 1050 with an FCC structure. To remind the reader, as it has long been known that ferrous materials (BCC) typically show a sharp "knee" (endurance limit) in the *S-N* diagram at about 1E06 cycles, while most other metals (FCC) exhibit a gradual flattening between 1E07 and 1E08 cycles (see Figures 14 and 51). This is a strong reason to pay attention to the crystal structure in the numerical estimation of the fatigue life curves of materials with different magnitudes of the CRSS. Their life curves are determined by analysing the initiation of a short crack. Micromodels containing microstructures of the materials are set up by using the FEM and are applied in combination with the TM equation in order to estimate the number of cycles needed for crack initiation. The long crack growth has not been simulated in this section for materials AISI 304, Fe 99.9% and AA 1050 since it has been shown in previous section (5.1) that the initiation phase takes the majority of the fatigue life, especially in the region close to the endurance limit.

Values of the CRSS from Table 6 are estimated by using methods presented in Sections 5.2.1 and 5.2.2. Namely, the CRSS of 160 MPa for AISI 304 steel is taken from the MPT performed by Monnet and Pouchon [13O]. The 117 MPa high CRSS is taken from the study of Hummel et al. on α-Fe [14B, 18B] performed by using the MD method. This value has been applied for AISI 1141 steel in the numerical determination of its fatigue life curve in Section 5.1. To quantify the size-strengthening effect

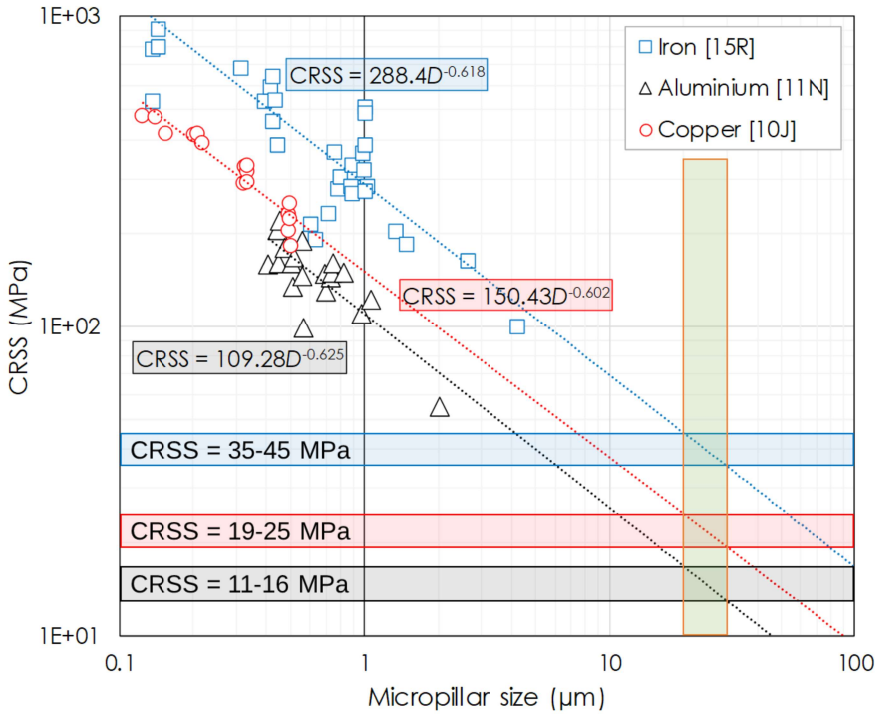

Figure 64: CRSS of iron [15R], copper [10J] and aluminium [11N], respectively, as a function of pillar diameter. Plots of data for different materials show the power law relationship, i.e. the size effect, between pillar diameter and CRSS [18L].

and to determine the CRSS of 99.9% pure iron, the experimental data from Reference [15R] were plotted and extrapolated, as introduced in Reference [16O] (see Figure 54e), as a function of pillar diameter in the double logarithmic plot in Figure 64. The CRSS is estimated to be 35-45 MPa for this material by applying the aforementioned extrapolation methodology, as explained in Section 5.2.1 in detail. Another example is given in Figure 64 where the data for high purity aluminium from [11N] were plotted and extrapolated as a function of pillar diameter. Here the values of CRSS are estimated to be 11-16 MPa. A third example found in literature is for copper [10J], with an estimated CRSS of 19-25 MPa. The data for copper are given for comparison reasons, but have not been considered in this numerical study. It is worth noting the observation that the power-law slopes of all three investigated metals (BCC iron and FCC aluminium and copper) are in the same range, namely −0.618 for pure iron, −0.602 for copper and −0.625 for aluminium. Furthermore, the slope of a BCC HEA from the study of Okamoto et al. [16O] is given as −0.63.

A notched specimen from the experimental study of Fatemi et al. [04F] is analysed in this study by using the above presented multiscale approach for fatigue life prediction. Figure 39L contains the 3D model of the specimen in a stressed state that was applied for FCC-based AISI 111 steel in Section 5.1 and for the three additional metals from Table 6 in this study, however with different material properties (see Table 7). Details about the specimen are provided in Section 5.1. The specimen fractured in experiments from Fatemi et al. [04F] under stress-controlled cyclic conditions with the R = 0, i.e. under repeated tensile stress loading, which is employed in this study, too.

The ranges of applied stress amplitude levels vary from material to material and are discussed in the following text. Furthermore, the global models of the considered metals serve to provide boundary conditions (in this case displacements) to the microstructural submodels, which are located at the notch ground of the global models and are used for the crack initiation analysis (see Figures 40 and 65). Similar as in the study on steel AISI 1141 (Figure 40), an intermediate submodel has been used to obtain more precise stresses in this critical region. The microstructures of all the investigated materials, i.e. their grains, are created by using a Voronoi tessellation technique. The average sizes of grains of the considered materials are shown in Table 7. Figure 65 shows exemplarily the microstructural submodel of AISI 304 steel in the stressed state (110 MPa amplitude level).

Table 7: Input data for the considered materials.

Material	E (GPa)	G [1] (MPa)	υ [1] -	C_{11} (MPa)	C_{12} (MPa)	C_{44} (MPa)	W_c [1] (N/mm)	d [1] (µm)
AISI 304	188	79,000	0.26	233,026	80,820	79,000	69	~30
AISI 1141	200	78,125	0.28	255,682	99,432	78,125	19	~60
Fe 99.9%	205	81,000	0.28	262,073	101,918	81,000	19	~65
AA 1050	72	26,000	0.33	106,678	52,543	26,000	11	~65

[1] *TM model parameters.*

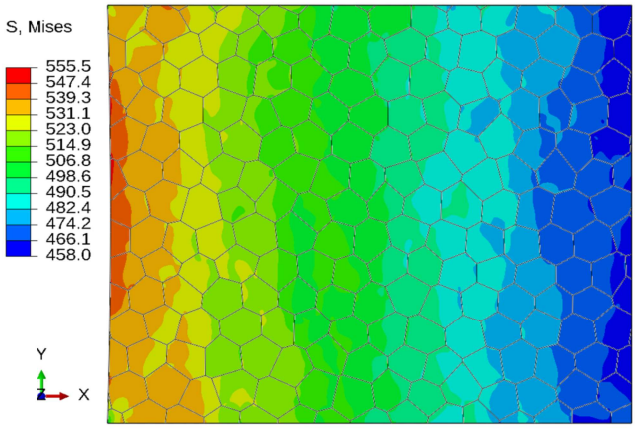

Figure 65: An undamaged microstructure of AISI 304 under 110 MPa amplitude level (microstructure 1).

As already mentioned, Table 7 contains simulation-relevant material properties; namely, the Young's modulus *E*, the shear modulus *G*, the Poisson's ratio υ, the three elastic constants C_{11}, C_{12} and C_{44}, the crack initiation energy W_c, and the average grain size *d* for all materials considered in this study. The length of slip band segment d_s, which is an input to the TM equation (Eq. 4.3), is calculated from the grain size *d* as recommended in [10G, 10N], i.e. $d_s = d/4$. The constitutive laws of the materials are purely linear elastic, defined by using orthotropic elasticity [ABQ], i.e. the three elastic constants.

Figure 66 shows an example of damaged microstructural model of Fe 99.9% after the analysis has been performed. The model contains visible microcracks, which have been introduced by applying the TM equation for the crack nucleation phase in the FEM-based analysis. A damaged state in the figure represents the end of the crack initiation stage, under a 37.5 MPa amplitude level. The method for the estimation of the moment when crack initiation (N_{ini}) is accomplished is well-documented in Section 4.3.4. An example is given in Figure 67, where the d*a*/d*N* estimated for the

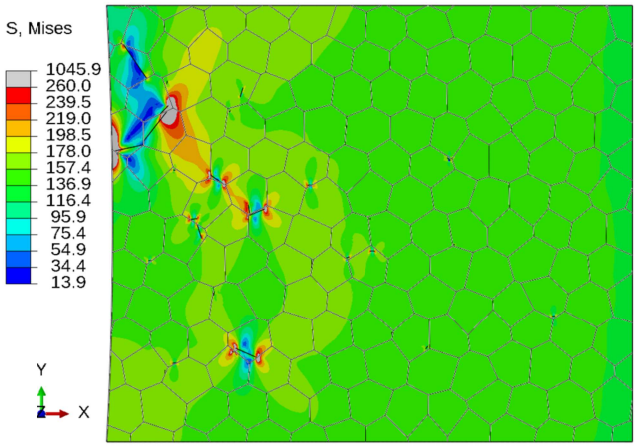

Figure 66: Damaged microstructural model (microstructure 1) of Fe 99.9% at the end of the crack initiation stage, under 37.5 MPa amplitude level (R = 0).

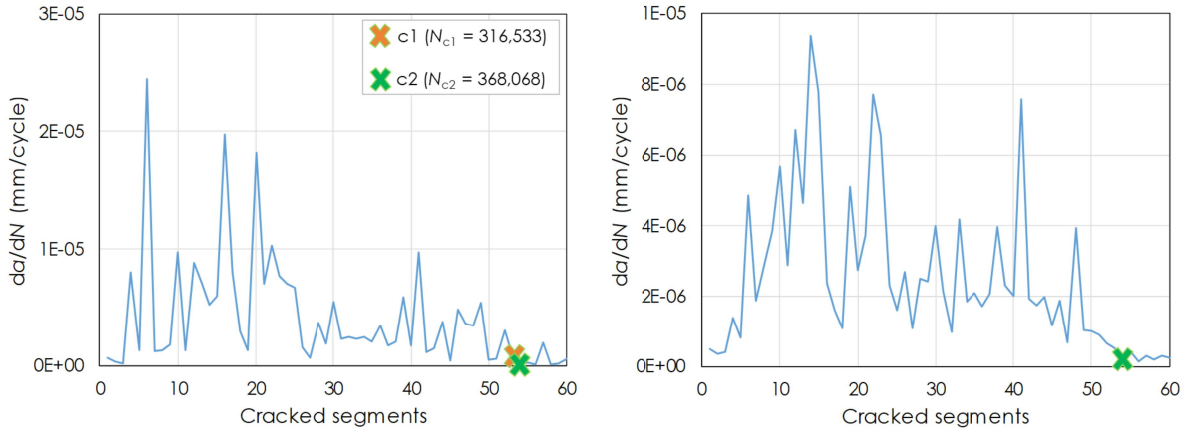

Figure 67: Left – Fatigue crack growth rate of Fe 99.9% until the end of the crack initiation stage; Right – Averaged fatigue crack growth rate of Fe 99.9%, where every da/dN point from the left graph is averaged with two preceding and two following neighbouring points.

damaged model from Figure 66 (Fe 99.9%) is plotted in relation to the number of nucleated microcracks, i.e. number of developed crack segments.

It can be observed in the present as well as in previous studies [17L, 17M, 17O, 18M, 18L] that the rate drops down and stabilizes after a certain time. The methodology of initiation estimation in this study is facilitated by plotting the averaged d*a*/d*N* (Figure 67R), where every d*a*/d*N* point is averaged with two preceding and two following neighbouring points. This d*a*/d*N* plot is smoother than the original plot and allows an easier detection of the drop. For more details on averaging d*a*/d*N*, the reader is advised to see Section 5.1. The number of cycles for the crack initiation phase is estimated by summing all the cycles spent for nucleation of individual segmental cracks that occurred in the microstructural model until the observed rate drop of the original d*a*/d*N* curve, Figure 67L. Generally, when combined together, the initiation and the succeeding FM-based long crack growth (see References [17M, 18M, 10G, 10N] for more details) allow the estimation of the specimen's complete fatigue life. The combined results are typically given as the finite life region (slope region) of the *S-N* diagram (see Section 4.3.6).

With the decrease of the loading stress level, the finite life region comprises more and more of just the crack initiation stage and eventually transforms into an infinite life region, as reported by Mughrabi [15M]. The aforementioned knee in the diagram, which also represents the fatigue endurance limit, can be typically recognized as the transition point between definite life (slope in the typical *S-N* curve) and infinite life (below the endurance limit). Thus, the endurance limit can be determined by solely calculating the initiation number of cycles as the transition of a short crack into the long crack does not take place in the endurance limit region [15M]. Accordingly, the loading level can be decreased incrementally in the microstructure-based crack initiation modelling approach, until the point where just few or no cracks appear inside the microstructural model and where extreme cycles are reached for those few nucleated cracks. An example is given for AA 1050 in Figure 68 where a large number of cycles as well as relatively low crack growth rates have

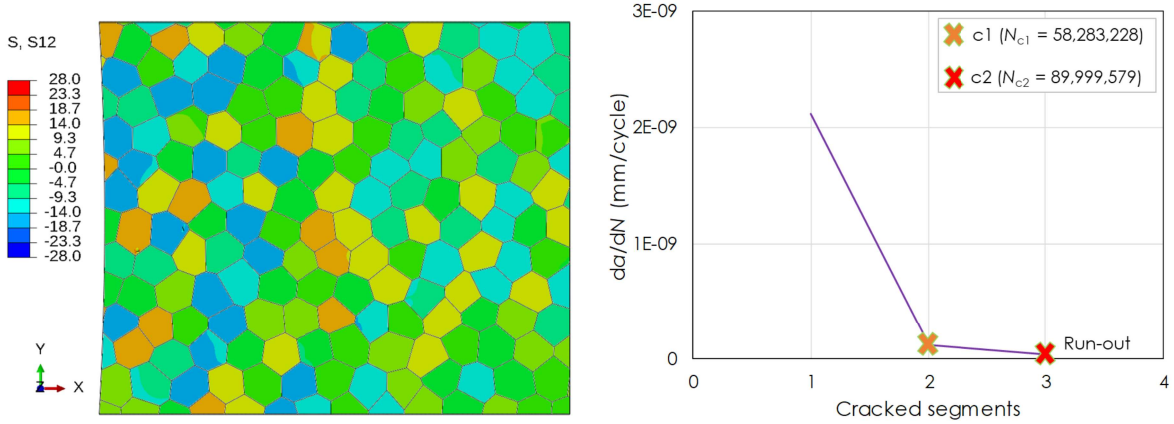

Figure 68: Left – Shear stresses in a damaged microstructural model of the AA 1050; Right - Fatigue crack growth rate of the AA 1050 at the end of the crack initiation stage (run-out), under a 7.5 MPa stress amplitude.

been reached for only two nucleated cracks in the microstructural model. Such situations of short crack retardation are considered as run-outs in the simulation analysis.

Figure 69 comprises results of crack initiation and long crack growth for AISI 1141 and of crack initiation for AISI 304, Fe 99.9% and AA 1050 in the form of fatigue life curves. Symbols in Figure 69 represent averaged results from two different microstructures analysed per material in the initiation analyses.

Figure 47 gives the global model of the notched tensile specimen (half) that has been applied for the long crack modelling and simulation in AISI 1141 by using the ΔK-based Paris law [63P]. As aforementioned, the long crack growth has not been simulated in this section for materials AISI 304, Fe 99.9% and AA 1050.

The magnitudes of the fatigue endurance limits (S_e) of the investigated materials have been extracted from the numerically obtained *S-N* diagram, tabulated and compared with the experimental values in Table 8. As reported by several researchers, the CRSS may be up to 100 times as large in BCC steels as in metals with FCC crystal structures. However, after a detailed survey, it has been observed that there exist also certain FCC steels, which have an unusually high CRSS (e.g. austenitic stainless steel AISI 304 with a 160 MPa high CRSS). Besides that, BCC metals typically show the "knee" and, on the other hand, certain FCC metals with a low CRSS show no sharp "knee" in the *S-N* diagram. Fatigue life curves in Figure 69 illustrate, however, the existence of definite endurance limits in both the BCC (AISI 1141) and the FCC steels (AISI 304). According to these numerical observations, the magnitude of the CRSS is directly responsible for the magnitude of the definite endurance limit (S_e). From the microstructure- and TM equation-based modelling point of view and from the resulting fatigue life curves in Figure 69, the following explanations for this recognition are listed:

- The transition from infinite life (below the endurance limit) to definite life (slope in the typical *S-N* curve) takes place when a sufficient number of microcracks develop in the material microstructure (typically >10). The cracking condition

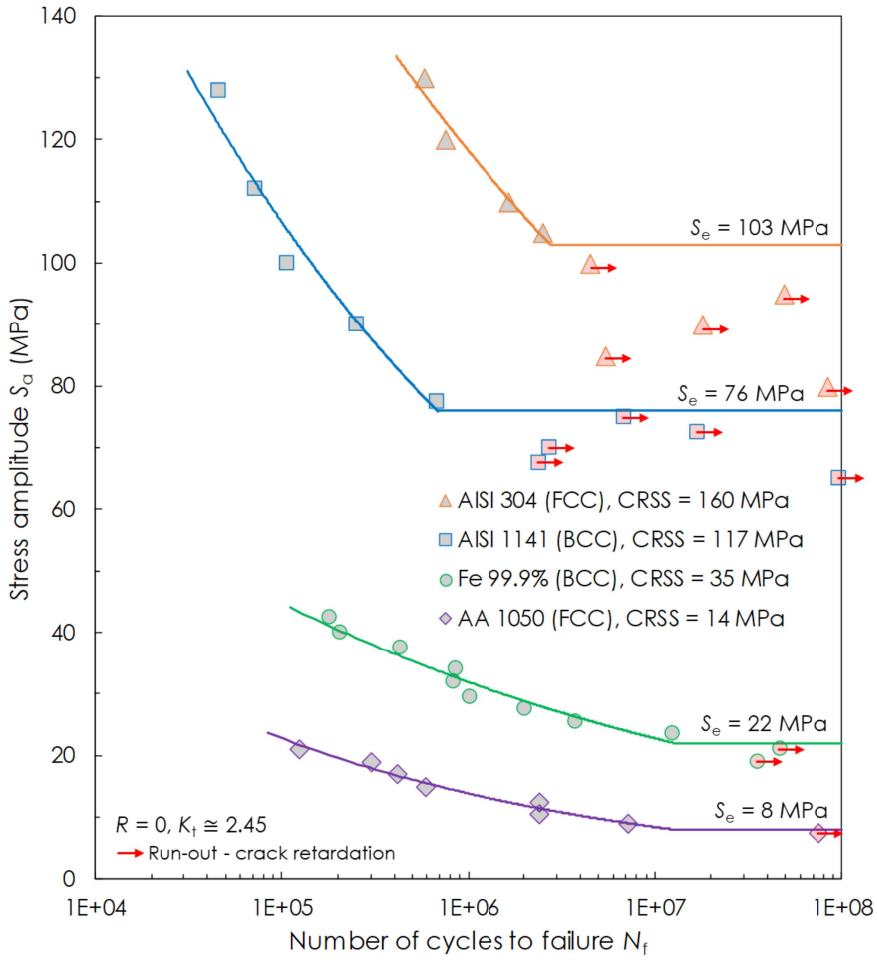

Figure 69: Simulation-based S-N curves, which illustrate the existence of definite endurance limits (S_e) in BCC and FCC materials depending on the magnitudes of the CRSS [18L].

according to the TM equation says that the absolute magnitude of average shear stress on a grain slip band has to be higher than two times the CRSS.

- The higher the CRSS magnitude of the metal of interest, the higher the loading stress level needed to accomplish the transition from infinite to definite life, as shown in Figure 69. In other words, the higher the CRSS magnitude, the higher the accompanying fatigue endurance limit. Despite having different crystal structures, FCC austenitic stainless steel AISI 304 and BBC vanadium-based microalloyed forging steel AISI 1141 are accompanied by relatively high CRSS values (160 MPa [13M] and 117 MPa [14B], respectively) and as a result endurance limits at considerably high positions in the *S-N* diagram, Figure 69.
- In the case of very high CRSS values, the stresses within the microstructural model are at a relatively high level at the moment of transition from infinite life to definite life, resulting in a high number of grains that are favourable for cracking. The higher the number of grains favourable for cracking after the transition from infinite life to definite life, the steeper the slope of the finite life region in the *S-N* diagram.

- The study showed that the crystallographic structure is not the predominant factor that determines the shape and position of a fatigue life curve in the *S-N* diagram, but it is rather the CRSS magnitude. Namely, the higher the CRSS of a certain material, the higher is the curve position is in the diagram, and the more pronounced is the transition between the definite and the infinite life region. Despite being an FCC material, the austenitic stainless steel AISI 304 shows an untypically high S_e of 103 MPa, which is higher than the estimated S_e of the BCC vanadium-based microalloyed forging steel AISI 1141 (76 MPa, see Section 5.1). The remaining two investigated metals, the BCC-based pure iron (Fe 99.9%) and the FCC-based high purity aluminium (Al 99.5%) possess, according to this numerical study, relatively low endurance limits, i.e. 22 and 8 MPa, respectively.

The simulation-based magnitudes of S_e, determined for a loading ratio $R = 0$ and a stress concentration factor $K_t \cong 2.45$, are summarized in Table 8 (see fourth column) and depicted in Figure 69 as well as published in [18L]. Furthermore, these values from the fourth column of Table 8 have been converted to the case of an unnotched sample ($K_t = 1$) with purely alternating stress ($R = -1$) in order to compare them with the experimental S_e values; see fifth and sixth columns, respectively. For more details on how to determine S_e values for $R = -1$ and $K_t = 1$, see Sections 5.3 and 5.6, respectively. It is necessary to remind the reader that these S_e values represent the allowable stress amplitude of the applied cyclic stress range S_α (see Figure 38; $R = 0$).

Table 8: Simulation-based endurance limits (S_e) from [18L] of the investigated materials in comparison with experimental values (S_e values are expressed in terms of nominal stress amplitude S_α). For details on how to determine S_e values for loading ratio $R = -1$ and stress concentration $K_t = 1$ (axial loading), see Sections 5.3 and 5.6, respectively. Values of K_t are determined from the numerical model of the notched sheet sample from Section 5.1 and vary between each material slightly due to different material properties defining their stress-strain responses. $K_t = 2.45$ is the average value for the investigated materials.

Material	Lattice	CRSS (MPa)	S_e (MPa) / Sim. $R = 0$, $K_t \cong 2.45$	S_e (MPa) / Sim. $R = -1$, $K_t = 1$	S_e (MPa) / Exp. $R = -1$, $K_t = 1$	S_U (MPa)
AISI 304	FCC	160 [13M]	103	303.7	325 [11A]	574 [85K]
AISI 1141	BCC	117 [14B]	76	190.7	450 [04F]	875 [04F]
Fe 99.9%	BCC	35 [15R]	22	49.7	222 [11L]	414 [11D]
AA 1050	FCC	14 [10J]	8	19.5	29 [20M]	110 [15L]

As visible from Table 8, the numerical study provides relatively good agreement of the calculated S_e values with the experimentally determined S_e values of some investigated materials (AISI 304 and AA 1050). This observation refers firstly to AISI 304 steel for which the numerically determined S_e value of 303.7 MPa is perfectly fitting the experimental value of 325 MPa that can be found in literature [11A]. A relatively good agreement, however with a slight underestimation, has been achieved for AA 1050 (19.5 MPa versus 29 MPa [20M]). An exception is the value determined for the steel AISI 1141 of 190.7 MPa, which is considerably lower than the experimental counterpart (450 MPa [04F]). The reason for this mismatch is elaborated in detail in

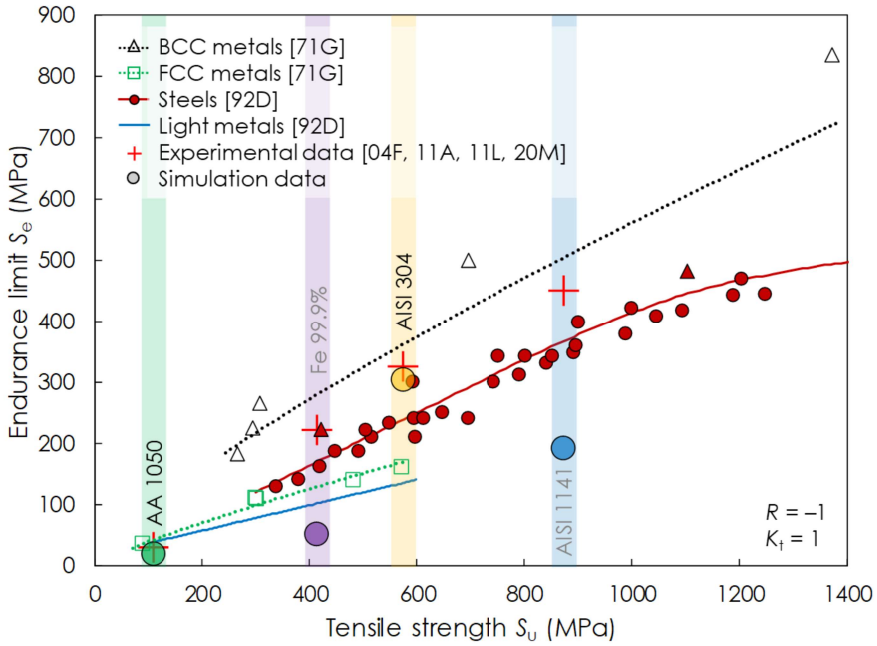

Figure 70: Relation between S_e and S_u values for various metals. The translations of an S_e value for a specific R ratio (in this case R = –1) and for a specific stress concentration factor (in this case K_t = 1) are discussed in Section 5.3 and Section 5.6, respectively.

Section 5.1. Another divergence from the values that can be found in literature is seen for Fe 99.9%; the numerically obtained S_e of 49.7 MPa is considerably lower than the experimental value of 222 MPa, reported in [11L]. Here the CRSS magnitude can be considered as a reason for the discrepancy, same as in the case of AISI 1141. Namely, the CRSS of 35 MPa extracted from MPT of Rogne and Thaulow [15R] and used in the study is considerably lower than the MD-based CRSS of 117 MPa of Hummel et al. [14B] for BCC α-iron.

Interestingly, when these four simulation-based S_e values of the investigated metals are plotted versus their S_U values (see Table 8), again a similar observation from Figure 70 follows; namely, the S_e-S_U points of AA 1050 (green circle) and AISI 304 (golden circle) – agreeing well with the S_e experiments in Table 8 – fall into the range of points characteristic for their groups of materials, i.e. to light metals and steels, respectively. On the other hand, the S_e-S_U points of the two other metals – Fe 99.9% (purple circle) and AISI 1141 (blue circle in Figure 70) – deviate considerably from the data representing steels and BCC metals, the same as they deviate from the experimental S_e values in Table 8 (see red crosses in Figure 70). This observation suggests that the S_e values and by that the CRSS values, too, of the last two metals might be too low. It is necessary to point out once again that simulation-based S_e values for the standard loading case characterized by loading ratio $R = -1$ and stress concentration factor $K_t = 1$ (Figure 70) are obtained from the S_e values characteristic for $R = 0$ and $K_t \cong 2.45$ (direct results from the simulations) by using an approach taking into account mean stress and/or loading ratio (see Section 5.3) in combination with the notch sensitivity approach (see Section 5.6).

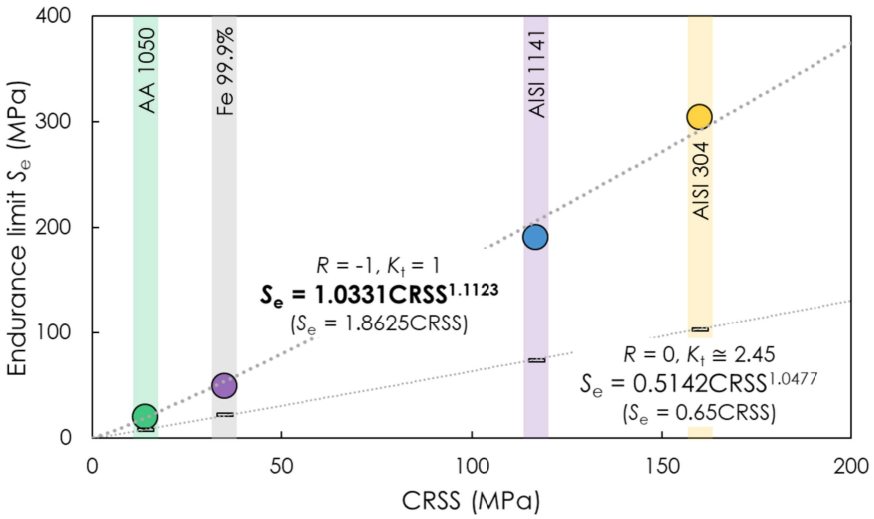

Figure 71: Relation between the S_e (= $S_{e,a}$) values of the investigated metals and their CRSS values.

Furthermore, when the numerically determined S_e values of the four investigated metals are plotted with respect to their prescribed CRSS magnitudes (see Table 8), an interesting relation can be observed, as shown in Figure 71.

Namely, the S_e values and the CRSS values relate to each other in an almost linear manner; despite considering incorrect CRSS values in some cases (AISI 1141 and Fe 99.9%). This relation can be expressed by a power-law:

$$S_e = m_0 CRSS^s \tag{5.4}$$

where m_0 is the intercept with the y-axis in Figure 71 and s the slope of the grey dotted line. According to the power-law approximation, m_0 = 0.5142 and s = 1.0477 for a loading ratio R = 0 and an average stress concentration factor K_t ≅ 2.45 (see Section 5.6 for more details). Interestingly, the slope factor s is approximately equal to 1 in this case. The S_e-CRSS relation can also be expressed by using a linear function, as S_e = 0.65CRSS for these specific R (= 0) and K_t (≅ 2.45) values. However, the power-law approximation is preferably used due to higher accuracy, while the linear relationship is simpler and easier to use in practice. It is noteworthy that the parameters m_0 and s of Equation (5.4) are dependent on the R ratio, K_t, etc. For the standard loading case (R = −1 and K_t = 1), m_0 = 1.0331 and s = 1.1123, while the slope of the linear function is equal to 1.8625 (see Section 5.3 for more details).

Even though based purely on the simulation results and just partly validated, the S_e-CRSS relation (Eq. 5.4) can be used as valuable tool in the next step to shed some light on the cases in Table 8 (Fe 99.9% and AISI 1141) where discrepancies with respect to the experimental results have been observed. A rather straightforward case to clarify is the one of Fe 99.9%, where by using the CRSS = 117 MPa of Hummel et al. [14B] for BCC α-Fe directly in the S_e-CRSS relation, an endurance limit of 75.5 MPa is obtained. To prove the validity from the numerical side, an additional simulation with the CRSS value of 117 MPa was performed, resulting in an S_e value of 74 MPa, which matches well the experimental S_e = 222 MPa [11L] when translated to the case char-

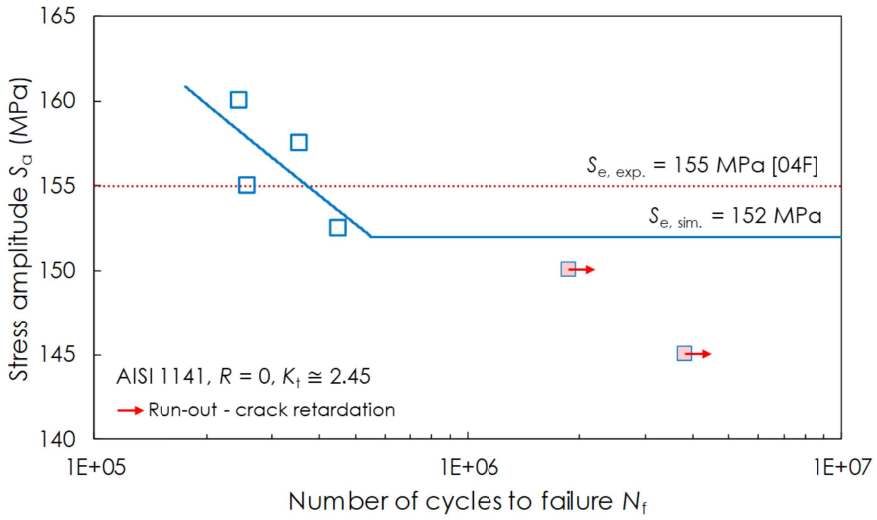

Figure 72: Comparison between simulation and experimental fatigue life (S-N) curves for AISI 1141 steel [04F].

acterized by $R = -1$ and $K_t = 1$ (200 MPa; see Table 9 as well as Sections 5.3 and 5.6 for more details). This could be a confirmation that the initially used and MPT-based CRSS of just 35 MPa [15R] is too low. The other case of AISI 1141 can be approached from another side; namely, by knowing the target S_e = 155 MPa from the experimental study of Fatemi et al. [04F], an estimation of the necessary CRSS to reach this S_e value by using the multiscale fatigue simulation approach can be done by means of the S_e-CRSS relation, e.g. CRSS = $\sqrt[s]{(S_e / m_0)}$ = $\sqrt[1.0477]{(155 / 0.5142)}$ = 232.5 MPa. To validate this estimation, is was necessary to perform additional simulations by taking all the input parameters the same as in the study on AISI 1141 from Section 5.1 and just by replacing the previous CRSS value of 117 MPa [14B] with the new S_e-CRSS relation-based value of 232.5 MPa. Finally, the resulting failure cycles are presented in

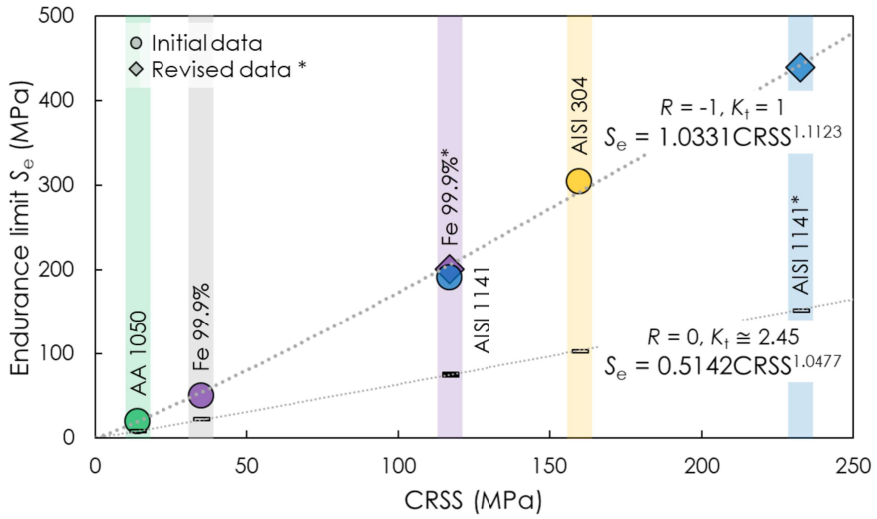

*Figure 73: Relation between S_e (= $S_{e,a}$) values of the investigated metals and their CRSS values (revised with the new results for the Fe 99.9% and for the steel AISI 1141, marked with *). For comparison with experiments, see Figure 74.*

Figure 72 versus the applied amplitude levels (S_a = 140-165 MPa; R = 0) and, at the same place, compared with the experimental result. These results (Figure 72) confirm the estimation of the CRSS magnitude of 232.5 MPa for the steel AISI 1141 – by using the S_e-CRSS relation – as being correct; the numerically obtained value S_e = 152 MPa is slightly lower than the experimentally derived value S_e = 155 MPa [04F] (= 450 MPa for R = −1 and K_t = 1; see Table 9), what is an acceptable deviation of 2% only.

*Table 9: Simulation-based S_e values of the investigated materials (revised with the new results for the steel AISI 1141 and for the Fe 99.9%, marked with *) in comparison with experimental values.*

Material	S_u (MPA)	CRSS (MPa)	S_e (MPa) / Sim. R = 0, $K_t \cong$ 2.45	S_e (MPa) / Sim. R = −1, K_t = 1	S_e (MPa) / Exp. R = −1, K_t = 1
AISI 304	574 [85K]	160 [13M]	103	303.7	325 [11A]
AISI 1141*	875 [04F]	232.5 (Eq. 5.4)	152	438.5	450 [04F]
AISI 1141	875 [04F]	117 [14B]	76	190.7	450 [04F]
Fe 99.9%*	414 [11D]	117 [14B]	74	200	222 [11L]
Fe 99.9%	414 [11D]	35 [15R]	22	49.7	222 [11L]
AA 1050	110 [15L]	14 [10J]	8	19.5	29 [20M]

Moreover, Table 8 and Figure 71 can now be revised with the new results for the steel AISI 1141 and for the Fe 99.9% (marked with *) in Table 9 and Figure 73. These results are published in [20L].

It is important to note that no matter the CRSS values are correct (i.e. validated by a correct resulting S_e value of an investigated existing material) or incorrect, there is always a linear relation (see Eq. 5.4) between the used CRSS values and numerically obtained S_e values, as can be seen in Figures 71 and 73. In addition, and in contrast to the initial data from Figure 70, the S_e-S_u points of the two revised metals – Fe

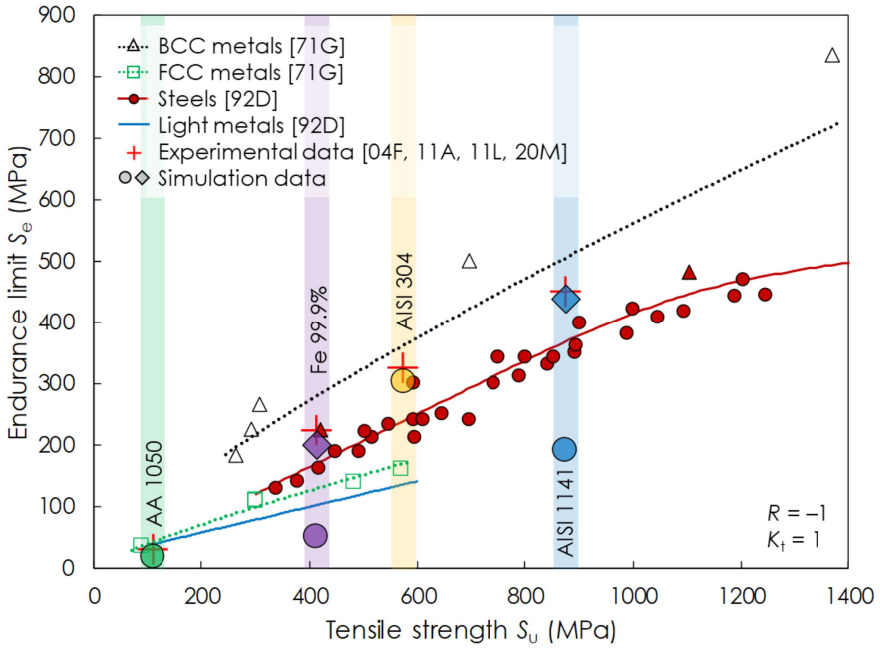

*Figure 74: Relation between S_e and S_u values for various metals (revised with the new results for Fe 99.9% and for the steel AISI 1141, marked with *).*

99.9% (purple diamond in Figure 74) and AISI 1141 (blue diamond in Figure 74) – agree well with the experimental values for these metals (see red crosses in Figure 74) as well as fall into the acceptable range of points characteristic for steels and BCC metals. This suggests that the revised S_e values of these two metals should be correct – as well as the accompanying CRSS values – similar to those of AA 1050 (green circle in Figure 74) and AISI 304 (golden circle in Figure 74), which were already considered as being correct in the initial study (see Figure 70).

It follows from these observations that the S_e-CRSS relation (Eq. 5.4) introduces a valuable new description of fatigue strength relations to material properties and a new perspective on the overall understanding of the fatigue process, especially when considering contemporary relations where S_e is being related to, e.g., the tensile strength S_u in a non-unique manner (see Figure 70 and/or 74). Accordingly, it seems to be more logical to relate S_e to CRSS due to the scattering of S_u that is depending on the strain hardening (i.e. cold-working) of the material after substantial plastic deformation has occurred [08S]; in addition to other strengthening mechanisms like grain boundary strengthening and phase boundary strengthening, which on the other hand have no influence on the CRSS (see Section 5.2.1 for more details). The scattered positions of S_e values for the four investigated metals in Figure 74 are especially eye-catching when compared to their linear distribution in Figure 73.

Furthermore, by having the S_e-CRSS relation (see Eq. 5.4) at disposal, it is quite handy to calculate the S_e value for any material with available CRSS data, and the other way around if the S_e value is known and the CRSS is required; CRSS = $\sqrt[s]{(S_e / m_0)}$. Namely, the S_e values of technical materials are far more accessible than the CRSS values; which have relative recently gained more attention in the materials research community. The pioneering research in the field of CRSS determination by using the

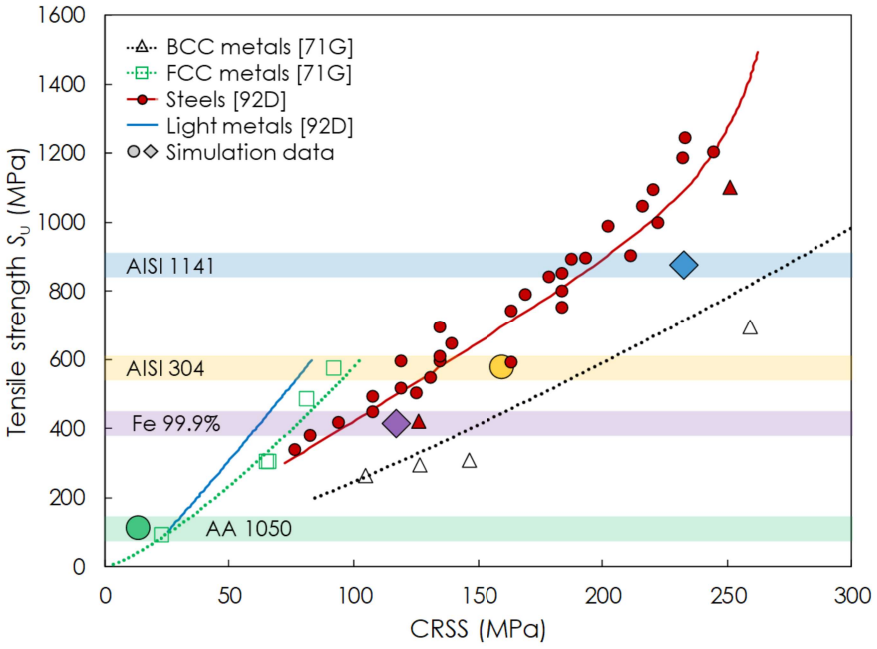

Figure 75: Relation between S_u and CRSS values for various metals.

micropillar testing was published only in 2004 by Uchic et al. [04U] (see Section 5.2.1 for more details). An example of a relatively vast amount of available S_e data (and accompanying S_U data) is given in Figure 74. By using the discovered S_e-CRSS relation in this case, the CRSS data set can be calculated for the groups of metals with FCC and BCC (as well as HCP) crystal lattice, respectively, from the figure and eventually plotted against the accompanying S_U data (see x-axis of Figure 70), as shown in Figure 75. In comparison to the S_e, the S_U values are even more accessible in materials databases (see, e.g. [98B]), meaning that by using the newly derived S_U-CRSS diagram it is now possible to roughly estimate the CRSS value of almost any metallic material; and by that the S_e value, too.

Another big benefit of having the S_U-CRSS diagram is possibility to check whether a certain S_U-CRSS data point (see Table 9) of a material considered in the multiscale fatigue simulations is fitting the range of S_U-CRSS data for its group of metals (see, e.g., yellow circle representing the steel AISI 304 in Figure 75). The same checking procedure can be performed for a data point consisting of the simulation-based S_e and available S_U values by using the existing S_e-S_U diagram (see again yellow circle representing the steel AISI 304 in Figure 74).

As aforementioned, the relations between, for example, the S_U and the CRSS values from Figure 75 can be approximated by a linear or a power law, which can be later on used to estimate one of the values if the other one is known. Similarly, the approximation functions can be derived for other relations like R_e-S_U [20M, 98B] or S_e-S_U (see Figure 70), too. Figure 76 comprises these relations between the four fatigue-relevant material parameters, expressed in terms of both the linear (for fast estimation) and the power law (for more precise estimation), for two also technically-relevant groups of metals, i.e. BCC and FCC metals. It is necessary to point out that the S_e parameter in Figure 76 represents the standard loading case characterized by fully

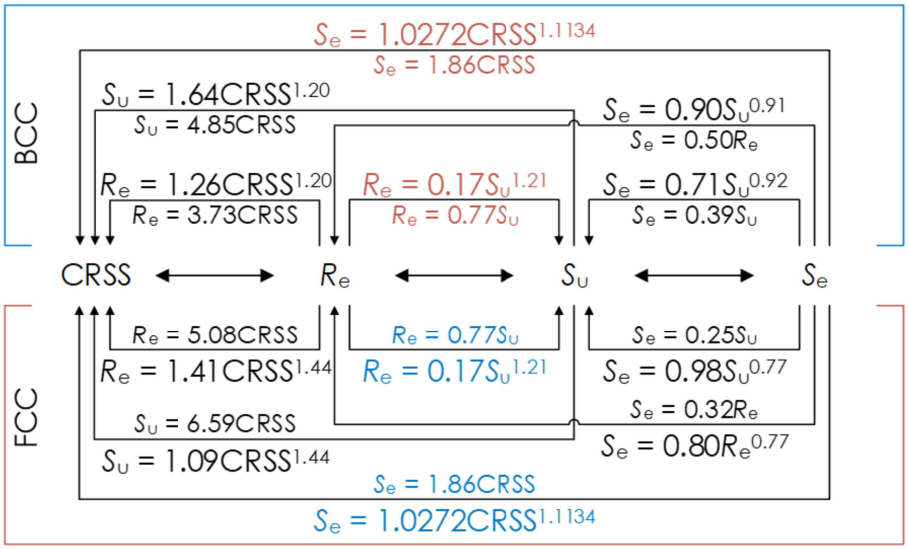

Figure 76: Relations between four fatigue-relevant material parameters expressed in terms of linear and power functions; CRSS – critical resolved shear stress, R_e – yield stress, S_U – ultimate tensile strength, S_e – fatigue endurance limit (for loading ratio R = –1 and stress concentration factor K_t = 1).

reversed tension-compression (loading ratio R = –1) and the stress concentration factor K_t = 1.

Furthermore, these relations can be used to get a clue on the mutual influence of the considered parameters. For this purpose, the stress-strain diagrams are used, as shown in Figure 77. Figure 77L shows the normalized stress versus strain diagram, where the stress components are normalized by the S_U value (golden diamond symbol), which was in addition taken as the same for both considered groups of the materials, BCC (blue full line) and FCC (red full line). It is visible from the diagram that BCC and FCC materials with a hypothetically same S_U magnitude would also have the same approximate R_e magnitude (golden square in Figure 77L), however, the BCC metal would have a higher accompanying CRSS value (blue circle in Figure 77L) and an accordingly higher S_e value (blue dashed horizontal line). Similar was done in Figure 77R, where the CRSS was taken as a normalization parameter (golden circle). In this case, the resulting S_e values are the same for equal CRSS values (see Eq. 5.4) for both the BCC and FCC metals (golden horizontal dashed line in Figure 77R). The R_e and S_U values are, however, higher for FCC metals in such a case. These observations bring new insights into these relations, as in the past only the relation between the S_e and S_U values was widely known (see Figure 70). It is noteworthy that the strains on the x-axes of both diagrams of Figure 77 are arbitrarily chosen since the stress-strain curves represent no specific BCC or FCC metal, but rather general cases.

On the other hand, Figure 78 shows a typical case, showing higher values of all the four technically-relevant material parameters in the case of BCC metals.

To conclude, the presented analysis yields a groundbreaking view on the importance of the parameter CRSS for the estimation of the fatigue strength of different groups of metallic materials. The newly discovered linear relation between the S_e and the CRSS values provides a facet of fatigue theory, which is numerically predictive and which allows the selection of those types of materials that are fatigue resistant. Furthermore, if proven with additional simulation as well as experimental studies,

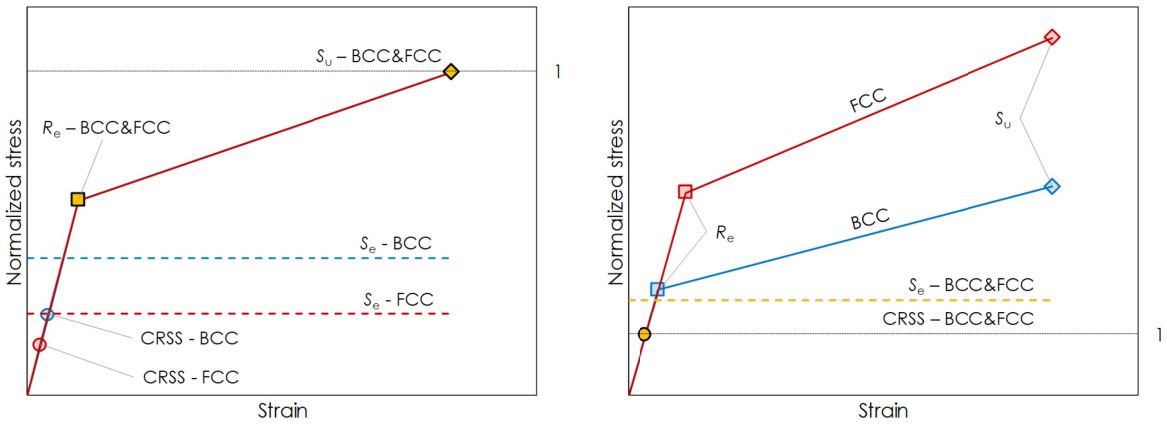

Figure 77: Relations between the four fatigue-relevant material parameters for BCC and FCC metals, expressed in terms of: Left – Stress-strain curves, where the stress is normalized by S_U: Right – Stress-strain curves, where the stress is normalized by the CRSS.

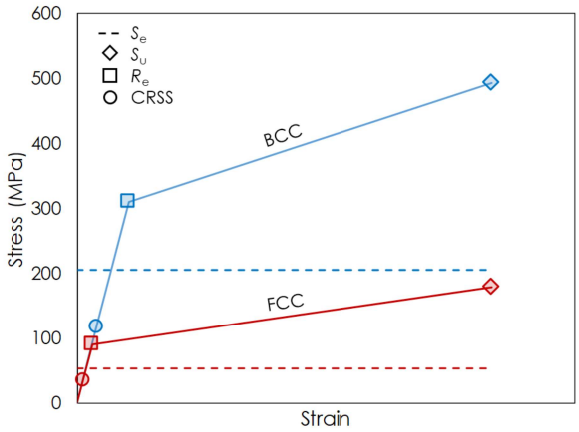

Figure 78: Typical relations between the four fatigue-relevant material parameters for BCC and FCC metals.

the S_e-CRSS relation can be used to estimate the S_e values of various metallic materials just by knowing their CRSS values.

It is noteworthy that the parameters m_0 and s of Equation (5.4) are dependent on the R ratio (see Section 5.3), the stress concentration factor K_t (Section 5.6), etc. A quantification of the possible dependencies require, however, additional numerical studies.

5.3 Effect of Mean Stress on Fatigue Behaviour of Metallic Materials

The cyclic loading in real-life applications typically involves changeable amplitudes and loading stress ratios (R), what results in changeable mean stress (S_m), too [16Y]. For the reminder, R is defined as usual as the lower value of the applied cyclic stress S_{low} (see Figure 79L) divided by the upper value S_{up} in a cyclic loading pattern, i.e. $R = S_{low} / S_{up}$ [16H]. On the other hand, the mean stress can be also determined as follows: $S_m = (S_{up} + S_{low}) / 2$. The two fatigue influencing factors (R and S_m) are directly related to each other by the following expression: $S_m = S_{up} (1 + R) / 2$. This means that an increase of one of these factors automatically results in the increase of the other factor, too, and the other way around. Accordingly, the effect of one factor on the fatigue behaviour of metallic materials implies the effect of the other factor in the same manner. When conducting tests intended for the development of a component, R values (i.e. S_m values) are typically selected in the way to represent the stress state that is present in the component while in operation. For example, many components of aerospace systems are tested under an R value equal to 0.1, what ensures a tension-tension loading pattern (see Figure 79L) on the component. Generally, fatigue tests in controlled experimental conditions are performed under various R values, typically ranging from –1 to 0.5 [16H]. Consideration of the effects of cyclic loading in terms of stress variance is a basic requirement for adequate fatigue life predictions [16Y].

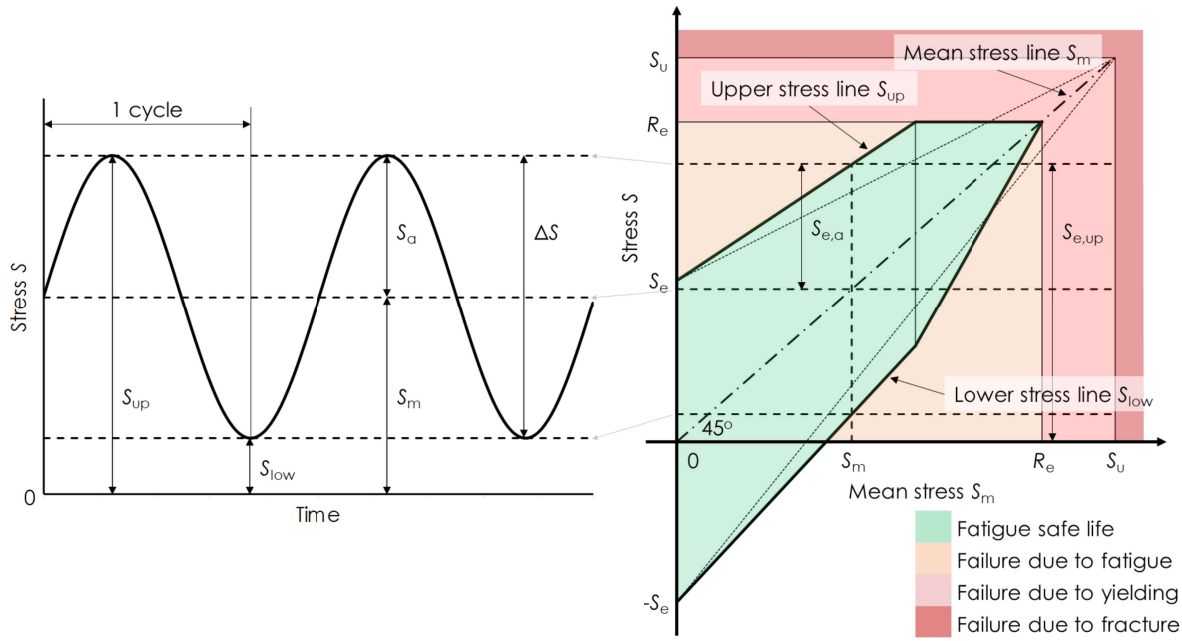

Figure 79: Left – Fluctuating tensile stress ($0 < R < 1$, $S_m > 0$); Right – Smith diagram showing the influence of the mean stress on the fatigue life; the higher the mean stress, the narrower the green (fatigue-tolerant) area [08S, 15B].

For example, Wu [96W] conducted fatigue tests on titanium alloy Ti-6Al-4V and aluminium alloy AA 2024-T3 with the aim to investigate the influence of *R* ratio on the fatigue performance of these two materials. Both materials have been tested under three different *R* values (–1, 0.1 and 0.5). As visible in Figure 80 [96W], there is an obvious effect of *R* ratio on crack growth rate (d*a*/d*N*). Namely, by increasing the magnitude of *R*, d*a*/d*N* is enhanced under a given stress intensity factor (Δ*K*) range [16Y].

Figure 81, on the other hand, shows experimentally obtained *S-N* curves of Ti-6Al-4V and AA 2024-T3 [09G], again both tested under three different *R* values of –1, 0.1 and 0.5. Generally, it can be concluded from these results that the *S-N* curves shift downwards in the *S-N* diagram with increasing *R* (and increasing S_m value) when the

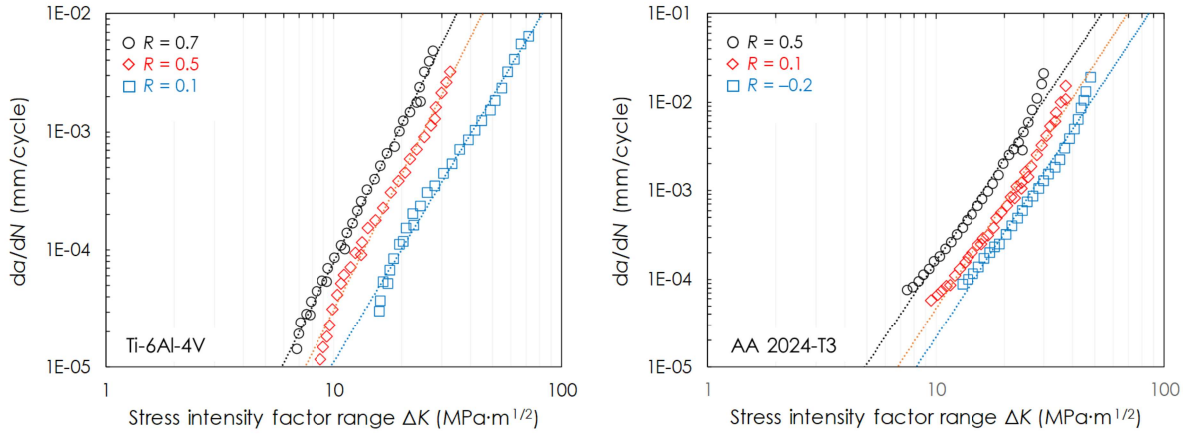

Figure 80: Experimental results of the fatigue crack growth rate of: Left – Ti-6Al-4V; Right – AA 2024-T3 [96W, 16Y].

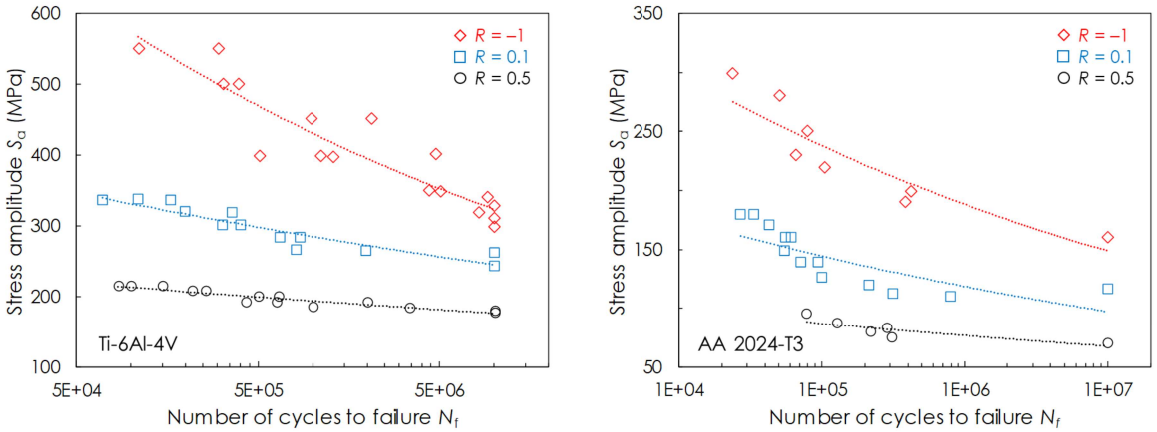

Figure 81: Experimental results of the S–N curves of: Left – Ti-6Al-4V; Right – AA 2024-T3 [09G, 16Y].

applied stress is expressed in terms of the allowable stress amplitude S_a (= ΔS / 2 = (S_{up} – S_{low}) / 2; see Figure 79L). In other words, this means that higher R values result in lower endurance limits (S_e) when they are expressed in terms of S_a. According to the test results of Ghidini and Donne [09G], S_e magnitudes of the Ti-6Al-4V alloy (Figure 81L) for the three R levels are 345 MPa (R = –1), 252 MPa (R = 0.1) and 178 MPa (R = 0.5) [16Y].

Furthermore, Mayer et al. [13M] investigated the fatigue performance of AA 2024-T351 (T351 – Solution heat treatment and cold working by stretching) at the same R values (–1, 0.1 and 0.5) as in the tests of Zhang et al. [16Y]. Figure 82 shows S-N data from these tests given in two different forms. In Figure 82L, the S-N curves are presented in relation to S_a. In this case, the curves shift downwards with increasing R values, as already shown in Figure 81. On contrary, as depicted in Figure 82R, the S-N curves shift upwards with increasing R values when presented in relation to S_{up} [13M].

Such a tendency in the S_a-N diagrams, as well as the opposite tendency in the S_{up}-N diagrams, can be understood with the help of the Smith diagram (sometimes called in English literature the modified Goodman diagram or the Goodman-Smith diagram [14J, 08S, 15B]), which is shown in Figure 79R. Namely, according to this

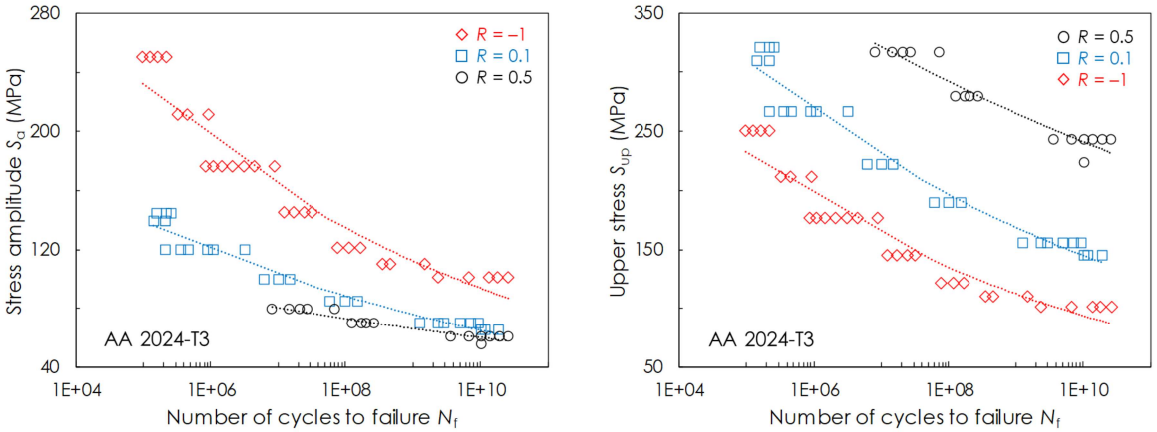

Figure 82: Fatigue lifetimes of AA 2024-T351 at different load ratios presented: Left – Vs. the cyclic stress amplitude S_a; Right – Vs. the upper stress of a load cycle S_{up} [13M].

practically relevant diagram [14J, 08S, 15B], higher R values (i.e. higher S_m values; increase to the right over the x-axis) result in lower allowable stress amplitudes ($S_{e,a}$, or simply S_e) in the fatigue safe life region (green area in Figure 79R). This means that the decrease of the fatigue life is conforming with the decrease of the $S_{e,a}$. On contrary, higher R values result in higher allowable upper stresses of the loading cycle ($S_{e,up}$), which is represented by the upper boundary of the fatigue safe life region.

In the ultimate case in the Smith diagram denoting failure due to fracture (dark red area in Figure 79R), the S_m, S_{up} and S_{low} magnitudes equal each other and reach the tensile strength S_u, the R ratio becomes equal to 1 (= S_{low}/ S_{up}) and the S_a becomes zero, meaning that the loading turns from cyclic into static.

It is noteworthy that both diagrams, the S_a-N (and $S_{e,a}$) and the S_{up}-N diagram (and $S_{e,up}$), have similar relevance for the characterization of fatigue behaviour of technical materials due to the fact that one can be handily transformed into another one, and vice versa (see Eq. 5.6). Therefore, the user is advised to apply that diagram, which better fits his/her current needs. One application where the S_{up}-N diagram is preferable is when it is needed to know if a cyclically investigated material operates in the HCF or in the LCF regime. Namely, the material operates in the HCF regime as long as the applied S_{up} value is below the yield stress (R_e) of that material. As soon as the S_{up} surpassed the R_e values, the materials enters the LCF regime. However, for the correct understanding of the effect of the mean stress (S_m; and R ratio), the S_a-N diagram is better reflecting the reality since it is evident from the Smith diagram that the decrease of the fatigue life (see narrowing of the fatigue safe region in Figure 79R) is conforming with the decrease of the allowable S_a (i.e. $S_{e,a}$) and not the increase of the allowable S_{up} (i.e. $S_{e,up}$) magnitude.

As already introduced in Section 4.3.1, the R value is taken into account in the TM equation (Eqs. 4.3 and 5.5; R marked in red) in the relation to the average shear stress range on the slip line segment $\Delta\bar{\tau}_s$.

$$N_s = \frac{8GW_c}{(1-\upsilon)d_s[\Delta\bar{\tau}_s(1-R)-2CRSS]^2} \tag{5.5}$$

According to Equation (5.5), the R level tunes the magnitude of the average shear stress on a slip band segment $\Delta\bar{\tau}_s$. Since this part of the equation, $\Delta\bar{\tau}_s(1 - R)$, is placed in the denominator, it influences the resulting segmental cycles (N_s) in a reverse manner. Namely, by considering the boundary situations, e.g. when R is equal to –1 (fully reversed loading), $\Delta\bar{\tau}_s$ gets multiplied by the factor of two, what leads to a minimum N_s. In the other boundary situation where R is equal to 1 (static loading case), this factor becomes zero leading to infinite N_s. The third interesting situation is when R equals 0 (repeated tensile loading) and where the prefactor $(1 - R)$ becomes equal to 1. To conclude, as R increases, the multiplication factor $(1 - R)$ of the TM equation decreases and, as a result, the segmental cycles increase as well as the complete initiation duration does (see Eq. 5.5), what is in agreement with the experimental observations when the S_{up}-N diagrams is applied (see, e.g., Figure 82R). This implies that the $\Delta\bar{\tau}_s$ values from the TM equation are resulting from the applied

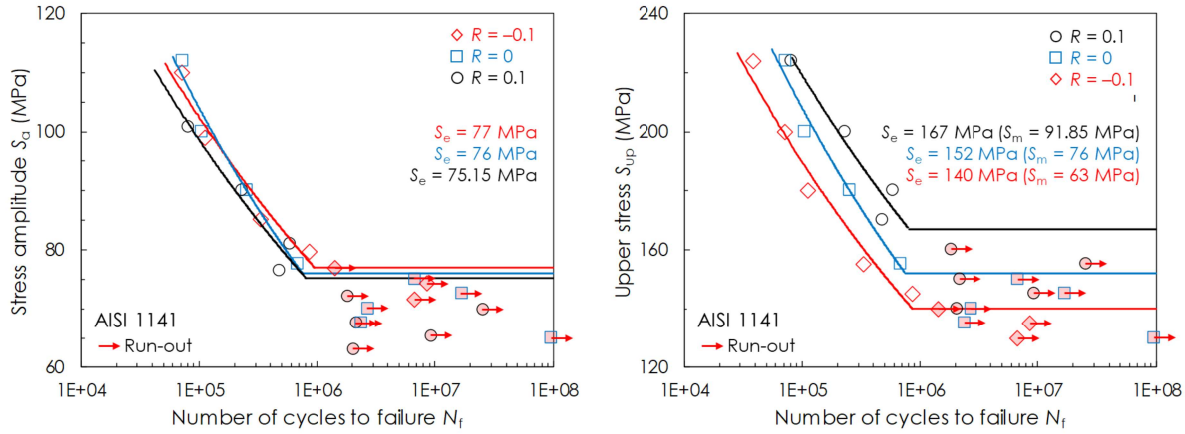

Figure 83: Influence of the load ratio R on simulation-based S-N curves presented: Left – Vs. S_a magnitude; Right – Vs. S_{up} magnitude. (The validation of the fatigue life curve for the R = 0 case is discussed in Sections 5.1 and 5.2.3)

S_{up}, and not from the S_a values. Accordingly, the S_{up} has been used in all previous and all following simulation studies to impose the loading to the investigated numerical models.

Similarly as in the experimental investigation, a numerical study by using the multiscale fatigue simulation approach (see Section 4.3) based on the TM equation has been performed under consideration of different *R* values. Simulation results for *R* = 0 (see Section 5.1) and for two additional arbitrarily chosen *R* values of 0.1 and –0.1 are given in Figure 83 in the form of S_a-*N* and S_{up}-*N* curves. The model and the material properties of Fatemi's specimen made of AISI 1141 steel have been taken from Section 5.1 (see there for more details). The long crack growth has been managed with the help of Forman power law (Eq. 4.8, Section 4.3.5), which accounts for the *R* value.

It is visible from Figure 83 that the simulation-based analysis obeys qualitatively the rules observed in the experiments, i.e. higher *R* values shift the fatigue life curves upwards in the S_{up}-*N* diagram, and downwards in the S_a-*N* diagram. The validation of the fatigue life curve for the *R* = 0 case is discussed in Sections 5.1 and 5.2.3, while the other two *R* values were chosen arbitrarily and thus could be validated just qualitatively as aforementioned.

The diagrams from from Figure 83 contain the estimated endurance limits (S_e) for different *R* values. If there is a need to convert the S_e values expressed in terms of the allowable stress amplitude ($S_{e,a}$) to the values expressed in terms of the upper value of the applied stress range ($S_{e,up}$) for a given *R* ratio and/or S_m value, and vice versa, this can be easily done by using the following expression:

$$S_{e,up} = \frac{2\,S_{e,a}}{1-R} = S_{e,a} + S_m \qquad (5.6)$$

An example can be given for the lowest endurance limit $S_{e,up}$ = 140 MPa from Figure 83L, which is accompanied with *R* = –0.1, i.e. with $S_m = S_{e,up}\,(1 + R) / 2$ = 63 MPa. The converted $S_{e,a}$ based on Equation (5.6) equals 77 MPa (see Figure 83L).

Furthermore, any endurance limit for a non-zero mean stress ($S_m \neq 0$, i.e. $R \neq -1$) can be translated to the zero S_m case ($R = -1$; often referred to as the standard case), where $S_{e,up}$ equals $S_{e,a}$ (see the Smith diagram in Figure 79R), as follows [19S]:

$$S_e = \frac{S_{e,a}}{\sqrt{1-\frac{S_m}{S_u}}} = \frac{S_{e,up}}{2\sqrt{1-\frac{S_m}{S_u}}} \qquad (5.7)$$

Here an example can be also given for the $S_{e,up}$ = 140 MPa case from Figure 83L, which is accompanied with the S_m = 63 MPa and with the tensile strength S_u = 875 MPa [04F]. The translated zero mean stress S_e based on Equation (5.7) equals 72.6 MPa.

Table 10: Simulation-based S_e values for different R and K_t cases.

	#2	#3	#4	#5	#6	#7	#8
Material	$S_{e,a}$ / Sim. (MPa) (R = 0, K_t = 2.36)	K_{fat} (see S. 5.6)	$S_{e,a}$ (MPa) (R = 0, K_t = 1)	S_m (= $S_{e,a}$) (MPa) (R = 0, K_t = 1)	S_u (MPa)	S_e / Eq. 5.7 (MPa) (R = -1, K_t = 1)	CRSS (MPa)
AISI 304	103	2.2699	233.80	233.80	574 [85K]	303.7	160 [13M]
AISI 1141	152	2.2510	342.15	342.15	875 [04F]	438.4	232.5 (Eq. 5.4)
Fe 99.9%	74	2.1280	157.47	157.47	414 [11D]	200.0	117 [14B]
AA 1050	8	2.2264	17.80	17.80	110 [15L]	19.4	14 [10J]

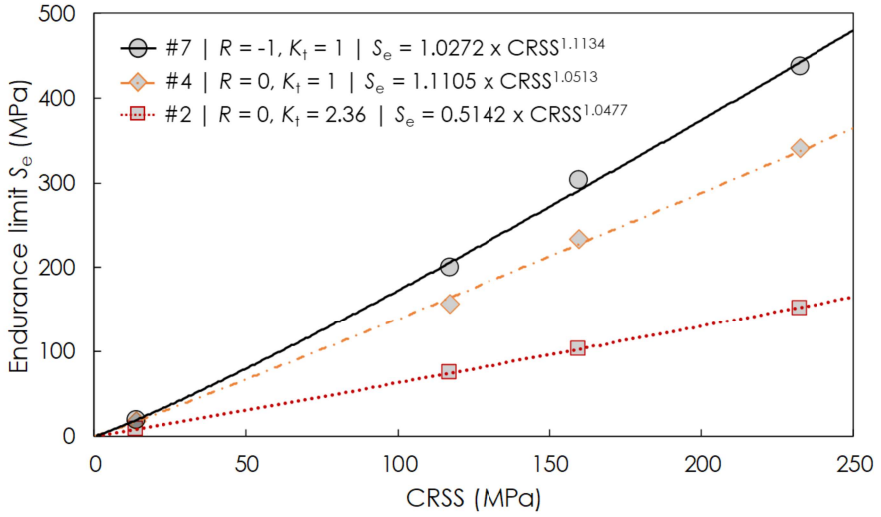

Figure 84: Relation between S_e and CRSS values for the standard case $R = -1$, $K_t = 1$ and comparison with the cases $R = 0$, $K_t = 2.36$ (see Section 5.2.3) and $R = 0$, $K_t = 1$ (see Section 5.6). Hashtags denote the numbers of the columns from Table 10.

By having the means of calculating the S_e values for the standard case characterized by fully reversed tension-compression loading ($R = -1$, $S_m = 0$) in the form of Equation (5.7), it is possible to derive the S_e-CRSS relation ($S_e = m_0 \times CRSS^s$, see Eq. 5.4) for this specific cyclic loading case. Firstly, the derivation of the S_e-CRSS relation for the $R = 0$ loading case (and for the stress concentration factor K_t = 2.36 [04F]) is discussed in details in Section 5.2.3. Table Table 10 contains the simulation-based $S_{e,a}$ values for four metals investigated in that same section (see 2nd column). The 3rd

column of Table Table 10 contains the fatigue stress concentration factors K_{fat} of the four investigated metals (see Section 5.6 for more details on the determination of the K_{fat} values), which are used to calculate the $S_{e,a}$ values from the 4th column (for R = 0 and K_t = 1) by multiplying the $S_{e,a}$ values from the 2nd column (for R = 0 and K_t = 2.36). Finally, the S_e values for R = –1 and K_t = 1 (7th column) are determined by means of Equation (5.7) and plotted against the CRSS values (from the 8th column) in Figure 84. The parameters m_0 and s of the S_e-CRSS relation for this standard case are equal to 1.0272 and 1.1134, respectively (see full black line in Figure 84). For the reminder, the $S_{e,a}$ and $S_{e,up}$ values are equal to each other for R = –1, i.e. simply S_e can be used for this case (see the 7th column of Table Table 10). Aside of that, the $S_{e,a}$ values for any R value are denoted in further text simply as S_e, with the addition of the applied R ratio.

The S_e-CRSS relation for the standard zero mean stress case (S_e = 1.0272 x CRSS$^{1.1134}$, see #7 in Figure 84) allows the determination of the endurance limit (S_e) of any metal with known CRSS value, and later the recalculation of it for a specific R ratio and for a specific stress concentration factor (K_t), in the opposite direction to the one explained in the previous paragraph.

By knowing the S_e value for the standard zero mean stress case (7th column of Table Table 10) and the S_e value for a non-zero mean stress case (see the 4th column of Table Table 10 for the $S_{e,a}$ values and the 5th column for the accompanying S_m values, respectively) as well as by knowing the tensile properties of a metal (the elastic limit R_e and the tensile strength S_u), it is possible to draw its Smith diagram [19S]. Figure 85 shows an example of such a diagram for the aluminium alloy AA 1050. Since the cyclic stress conditions in many practical cases often consist of a stress amplitude and a superimposed tensile or compressive mean stress, the Smith diagram allows

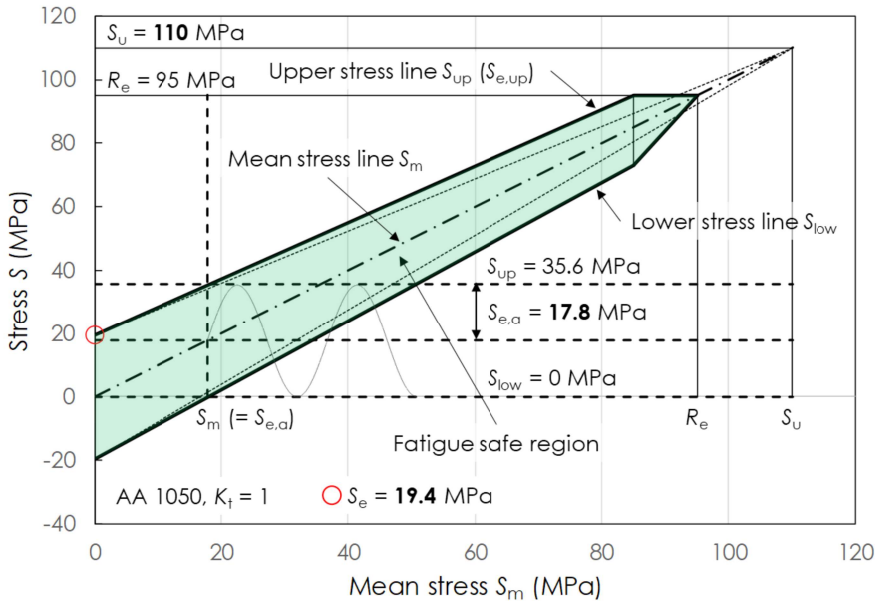

Figure 85: The Smith diagram for the aluminium alloy AA 1050 created by using the $S_{e,a}$ (4th column), S_u (6th column), and S_e (7th column) values from Table 10.

for an easy verification if the combination of the two stresses (S_a and S_m) falls in the fatigue safe region (see Figure 85).

To conclude, this study shows that the multiscale fatigue simulation approach is capable of properly taking into account the mean stress and/or the *R* ratio, as well as the stress concentration factor K_t (see Section 5.6 for more details), which are high practically relevant influencing factors during the designing of structural components.

5.4 Influence of Local Residual Stresses on the Fatigue Life Curve

This section is devoted to the investigation of the influence of local residual stresses on the fatigue life curve of AISI 1141 steel. It has been long known that local residual stresses at the surface of a material can contribute to its durability (compressive residual stresses) or, in contrast, can harm the structure (tensile residual stresses), depending on the nature of these residual stresses. A common treatment technique named as shot-peening (SP), where the surface of a structures is shot by small hard particle, is often used to introduce compressive residual stresses on the surface and, to a certain degree, in the depth of the material of the structure. These compressive stresses introduced by SP have beneficial effects on the overall fatigue life. The SP technique is visualised in Figure 86.

Rios et al. [95R] confirmed in their experimental study a basic 'engineering' rule of SP, saying that it affects fatigue crack behaviour by delaying fatigue failure and by increasing the fatigue endurance limit. Fractographic studies [01Z, 02T, 07J] showed that the formation of fatigue cracks in shot-peened specimens starts deeper in the material because of the induced stresses, what is the opposite scenario to non–shot-peened specimens where microcracks typically nucleate at the surface in the HCF regime [12P]. Accordingly, nucleation of fatigue cracks in subsurface layers of shot-

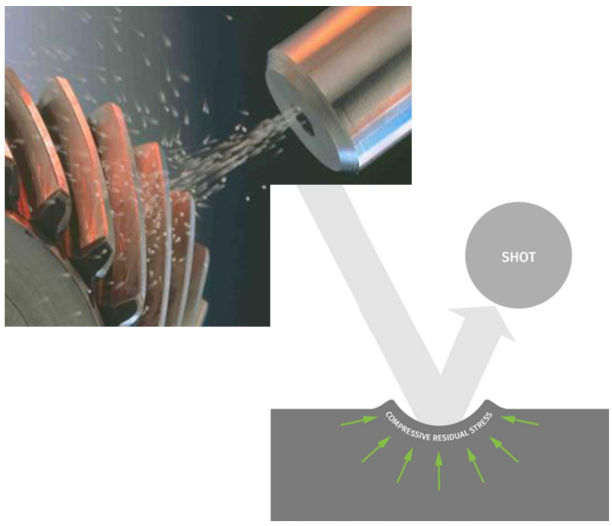

Figure 86: Shot-peening (SP) technique and its effect on the surface of a structural material [18T, 19P].

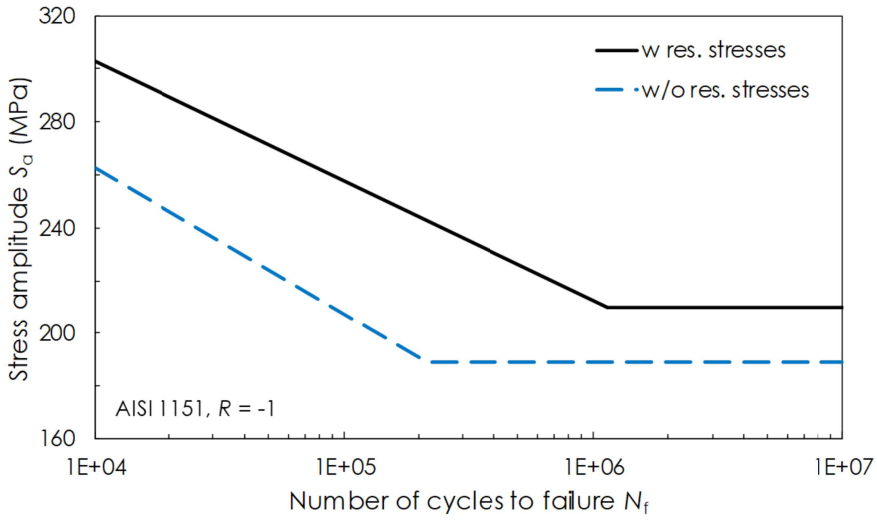

Figure 87: Experimental S-N curves for shot-peened (red solid line) and non–shot-peened (black dashed line) specimens made of AISI 1151 steel [12P] demonstrating the influence of compressive residual stresses.

peened specimens results in the reduction of the density of surface microcracks [12P, 95R]. This mechanism of shifting the fatigue cracks to the subsurface layers additionally minimizes the usually detrimental effect of surface roughness, which is typically high in the shot-peened structures. The increased surface roughness is influenced by the hardness of the surface and the size of the shots, although according to [95F] the former seems to be more dominant.

Figure 87 shows results of a study where the fatigue performance of the shot-peened, quenched and tempered AISI 1151 steel has been enhanced in comparison to the same but intact material [12P]. Further, Figure 88 gives an example of compressive residual stresses' profile on the surface of S355 structural steel [17W]. The shape of the curve shows a typical distribution of these stresses; i.e. they have their minimum close to the surface of the material, which is followed by an increase with the distance from the surface until eventual dissipation. Such a compressive stress

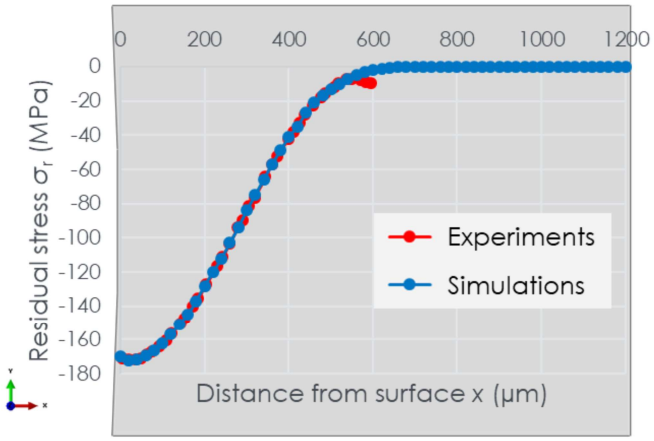

Figure 88: Profile of the applied compressive residual stresses based on the experimental results from [17W].

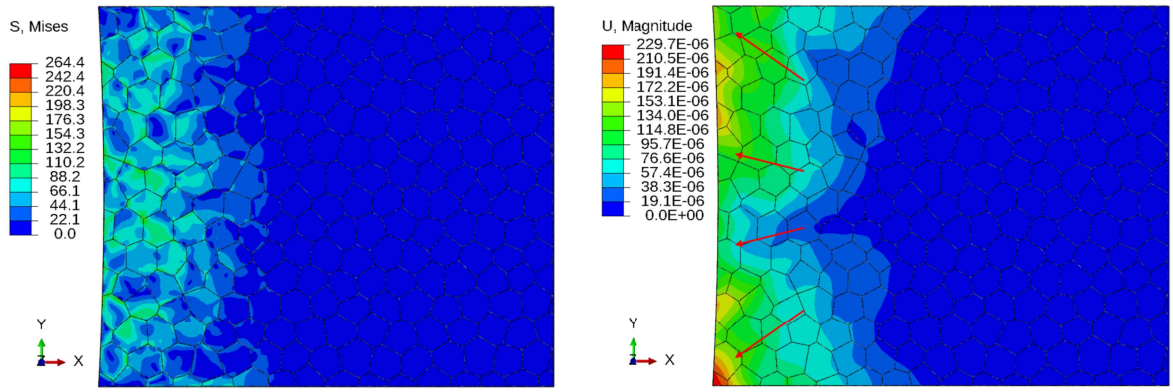

Figure 89: Left – von Mises stresses in AISI 1141 steel resulting from the implied compressive residual stresses (microstructure 1); Right – Displacements resulting from the applied compressive residual stresses (one forward loading applied).

profile was applied in the microstructural model of Fatemi's specimen made of AISI 1141 steel previously investigated in Section 5.1 (more details on model and material properties can be found there). Figure 88 depicts the profile applied into the model, and additionally, compares it with the profile reported by Wang et al. [17W].

Figure 89L shows von Mises stresses resulting solely from the implied compressive residual stresses. On the other side, Figure 89R depicts resulting displacements in the surface area of the model. Concerning the modelling of the compressive stresses, the profile from Figure 88 has been applied using Abaqus subroutine SIGINI.

During the loading of the microstructural model by an external stress (transferred from the global model using the submodelling technique, see Section 5.1 for more details), the compressive residual stresses are superimposed upon them, as done in most of the analyses to date [63F, 95R]. Figure 90 shows the comparison of the microstructural model with the stresses resulting solely from the outer loading versus the microstructural model where the compressive residual stresses are acting together with the externally induced stresses. It is visible that the residual stresses (Figure 90R) modify the relatively uniform stress (von Mises) distribution present in Figure 90L and by that apparently relocate the potential sites for microcrack nucleation.

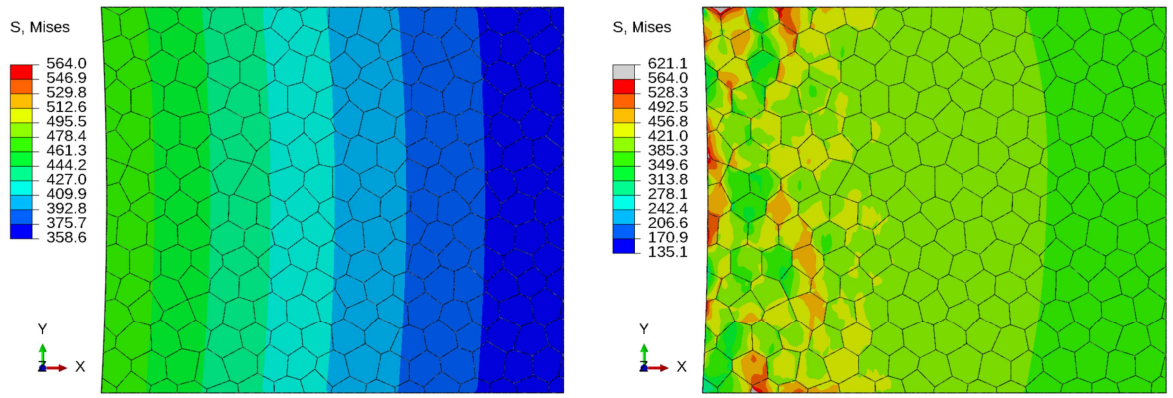

Figure 90: von Mises stresses in the microstructural model of AISI 1141 steel (microstructure 1) resulting from: Left – A stress amplitude of 100 MPa; Right – Compressive residual stresses acting together with the externally induced stresses (one forward loading applied).

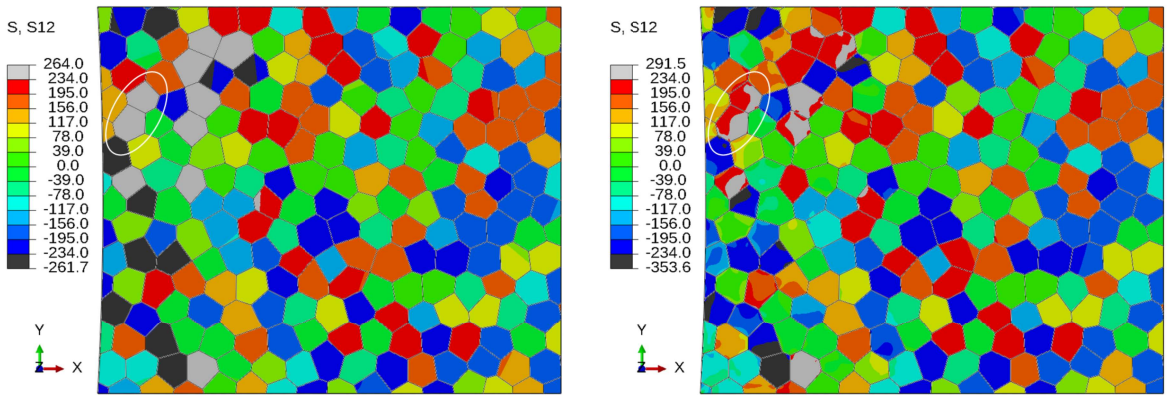

Figure 91: Shear stresses in the microstructural model of AISI 1141 steel (microstructure 2) resulting from: Left – A stress amplitude of 112 MPa; Right – Compressive residual stresses acting together with the externally induced stresses.

From the crack initiation modelling point of view, it is interesting to compare shear stresses in the models without and with induced residual stresses. The shear stresses obtained from the FEM analysis are of particular relevance as they are connected to the TM equation (see Eq. 4.3, Section 4.3.1) in the form of an average shear stress range on the slip line segment $\Delta\overline{\tau}_s$. Figure 91R of the microstructural model acting under the combined stresses indicates changes in the distribution of this fatigue modelling-relevant variable shear stress (designated by S12 in the figure).

Namely, grey and black areas in both images of Figure 91 represent grains (or portions of grains) where absolute values of the shear stress are higher than the 2CRSS, meaning that the condition for the crack nucleation criterion is fulfilled (see Section 4.3.1 for more details). By isolating an arbitrary set of nucleation-favourable grains with a sphere, it is visible by observing the grey areas that the residual stresses (Figure 91R) reduce those areas and by that the likelihood of the grains to form a fatigue crack, too (Figure 91L).

In the following step, the crack initiation analysis has been performed with the model exposed to the superimposed stresses (Figure 91R) and compared with the

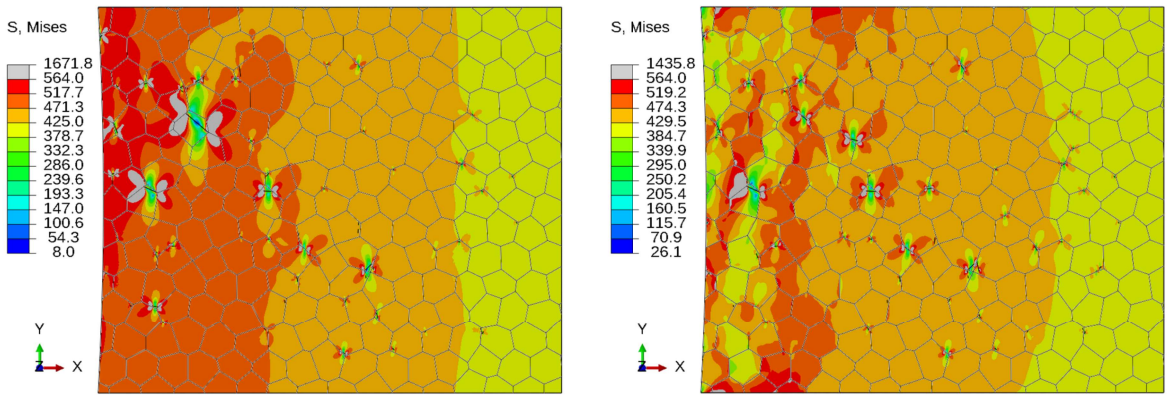

Figure 92: Damage in the microstructural model of AISI 1141 steel (microstructure 2) caused by: Left – A stress amplitude of 112 MPa (101 nucleated cracks, 344,317 cycles); Right – Combined influence of compressive residual stresses and externally induced stresses by an amplitude of 112 MPa (101 nucleated cracks, 527,539 loading cycles).

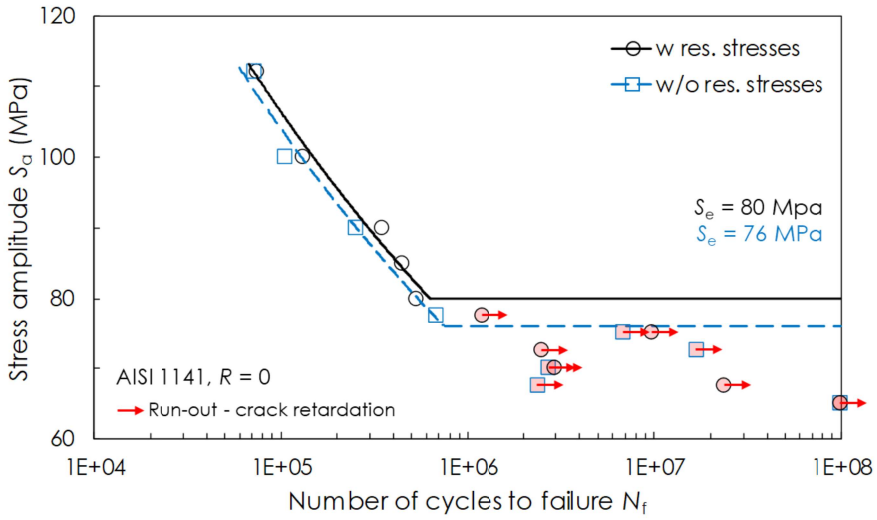

Figure 93: S-N curves of AISI 1141 steel showing the influence of compressive residual stresses. (The validation of the blue curve without residual stresses is discussed in Section 5.2.3)

results from Section 5.1 where solely outer loading has been considered. The procedures of modelling the crack initiation and evaluating the accompanying life cycles are the same as in all previous sections.

Figure 92 shows exemplarily the results of both analyses performed under 100 MPa outer loading. Aside of the reduction of the area containing crack nucleation-favourable grains, the residual stresses move to a certain degree the crack nucleation sites from the surface to the subsurface regions (Figure 92R), when compared to the pure outer loading case (Figure 92L). This coincides with the aforementioned experimental observations [12P, 95R].

Eventually, by plotting the fatigue life curve, of e.g. shot-peened specimen in Figure 93, and comparing it with the non-shot-peened specimen, it is apparent that the analysis provides qualitative agreement with the experimental observations, i.e. that the compressive residual stresses enhance the fatigue life of the investigated structure. Namely, the definite life portion of the fatigue life curve (the slope) of such a structure is shifted to the right in the *S-N* diagram for the selected compressive residual stresses' profile, while the infinite portion of the curve (endurance limit S_e) is shifted upwards, from 76 MPa (see Section 5.1) to 80 MPa.

5.5 Influence of the Grain Size on the Fatigue Life Curve

Experimental tests demonstrate that there is a sharp drop in resistance to fatigue fracture with the increase of the grain size. This is a known effect proven decades ago, e.g. by Clemens et al. [79C] in 1979, where the grain size of annealed AISI 316LVM (X2CrNiMo18-15-3) stainless steel has been increased from 75 to 150 µm. It has been also shown that plastic strains associated with fatigue cycling increase with increasing grain size. There are vast numbers of other publications, like [65K, 65Y, 79C, 85B, 08K, 14S], which argue or give experimental evidence for other specific

metallic materials where a reduced fatigue performance is related to a coarse grain size [79C]. The size of the grains determines mechanical properties of alloys, i.e. the smaller the grains the better the properties – as more boundaries prevent movement of dislocations in the microstructure. To achieve reduced a grain size, alloying elements such as iridium or ruthenium may be added to alloys in some cases. These elements are called grain refiners.

Kanemaru et al. [08K] demonstrated the difference between fine-grained (~6.5 µm) and coarse-grained (~20 µm) commercial carbon steel by means of *S-N* diagram (Figure 94). According to this study, the resistance to crack initiation becomes increased by refining the grain size. An interesting study was performed by Sharifi et al. [14S] where the effect of ferrite grain size on the fatigue properties of dual phase steels was investigated. Figure 94R shows the relationship between the endurance limit (at 1E07 cycles) and ferrite grain size in dual phase steels with a constant 25% volume fraction of martensite. According to the results, the endurance limit increased through decreasing the grain size of ferrite from 74.3 µm to 9.3 µm. Aside of that, it can be observed that the endurance limit varied linearly [14S].

Accordingly, a numerical study on the influence of grain size on the fatigue lifetime has been performed by using the fatigue modelling approach as introduced in Section 5.1. The specimen and the material are the same as in the previous study from Section 5.1, i.e. the specimen geometry is taken from the experimental study of Fatemi et al. [04F], as well as the material AISI 1141 steel. The reference microstructure (60 µm grain size) in the submodel is created on the basis of a typical etched microstructure of AISI 1141 from the study of Mirzazadeh and Plumtree [12P] (see Section 5.1). The model was created in the previous study as a 3D shell RVE, generated by the Voronoi tessellation technique and comprises 253 grains. The reference grain size of 60 µm has been slightly decreased in an additionally created microstructural model to 50 µm (313 grains in total) in order to capture the general grain size effect on the fatigue crack initiation stage. Figure 95 shows the reference and the additionally created microstructural models.

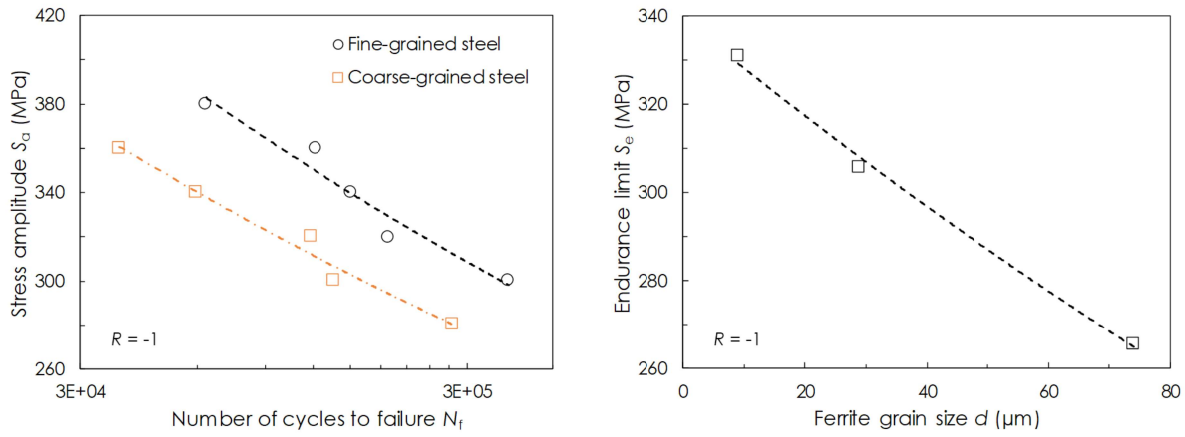

Figure 94: Left – Experimental S-N curves showing the influence of the grain size in commercial carbon steel [08K]; Right – The endurance limit variation with the grain size of ferrite in dual phase steels [14S].

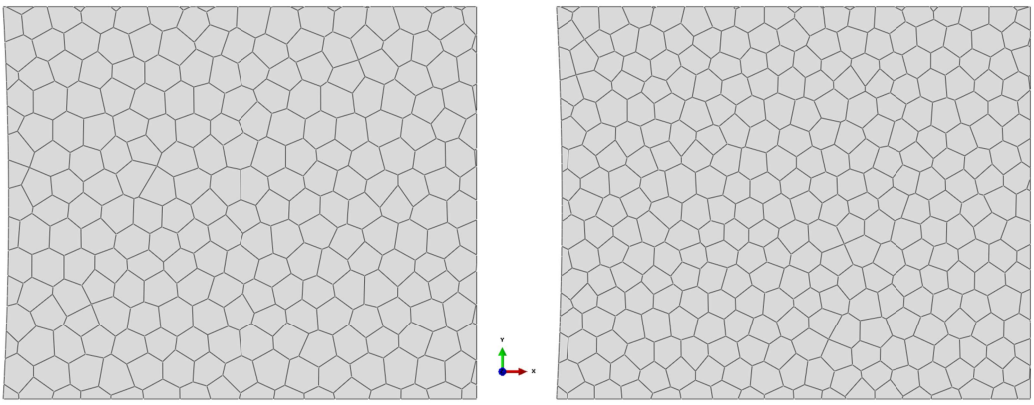

Figure 95: Microstructural models of AISI 1141 steel with: Left – 60 µm grain size and 253 grains; Right – 50 µm grain size and 313 grains in total.

As visible from Figure 96, the results from the numerical study are in accordance to the experimental observations showing that the finer the grain size, the higher the initiation cycles and accordingly the complete fatigue life. i.e. the fatigue life curve shifts to the right and upwards in the *S-N* diagram. The endurance limit has been increased from 76 MPa (60 µm grain size; see Section 5.1) to 78.5 MPa (50 µm grain size).

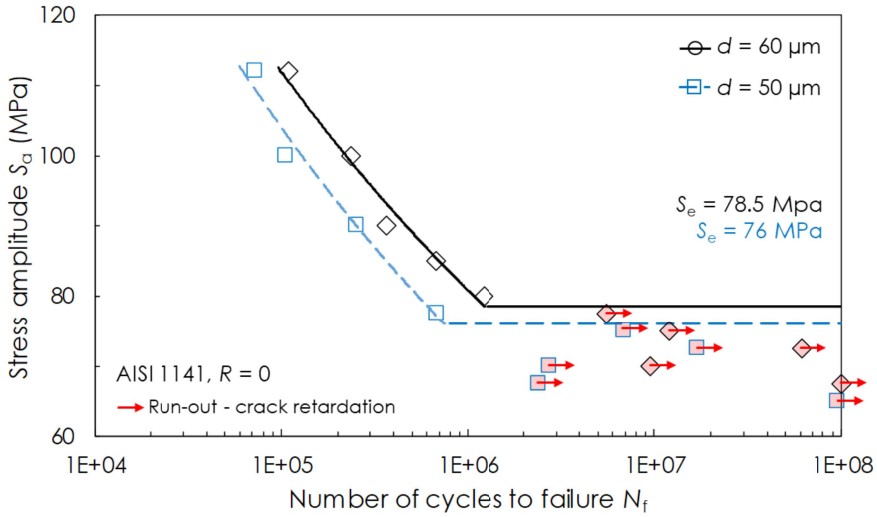

Figure 96: Influence of the grain size on S-N curves of AISI 1141 steel. (The validation for the case d = 60 µm is discussed in Section 5.2.3)

Aside of the experimental studies that show the decreasing fatigue resistance with the increasing grain size, the expectations to obtain the same trend in the numerical studies has been based on the TM equation. Namely, the grain size, or actually the slip band length, *d* is a part of the equation's denominator, meaning that the estimated cycles N_{ini} should increase by decreasing the *d* if all other factors of the equations are kept constant.

5.6 Influence of Notch Radius on the Fatigue Life Curve

Numerous researchers [03M, 03R, 04F, 08M, 13C] reported the influence of notch size on the *S–N* curve, as Lorenzino et al. [15L] did for aluminium AA 1050. As expected, an increase in the size of the notch radius resulted in an evident decrease in fatigue resistance of this material. The data displayed in Figure 97 correspond to the case of 3.46 mm grain size, but a similar trend has been observed for the other investigated grain sizes, although a stronger decrease in fatigue resistance has been observed for finer grains [15L].

In order to investigate the influence of notch radius using the advanced fatigue modelling approach introduced in this work, the model that was used in previous studies has been modified, as depicted in Figure 98. The notch radius of the modified numerical model has been arbitrarily selected to be 0.25 mm, what is considerably smaller than the radius of the original model of 9.128 mm (see Section 5.1). The difference of the radii is expected to ensure a difference in the fatigue life curves. The basic dimensions of the specimen are the same as in previous studies, i.e. the global model in Figure 98L is based on the specimen from the experimental study of Fatemi et al. [04F], while the considered material is the AA 1050, which has been already introduced, together with the simulation-relevant parameters, in Section 5.2.3. The average grain size in both cases is 60 µm.

The transfer of the boundary conditions has been accomplished by using the two-fold submodelling technique, the same as already introduced in Section 5.1. Namely, in the first step, a 3D solid submodel has been created at the location of interest (notch) with the aim to get there a precise displacement distribution. In the second step, the microstructural model (3D shell submodel) has been embedded in the 3D solid submodel.

The two-fold submodelling approach is shown in Figures 98 and 99. The global model has been loaded in a manner to act in the HCF regime. That is, the stresses in

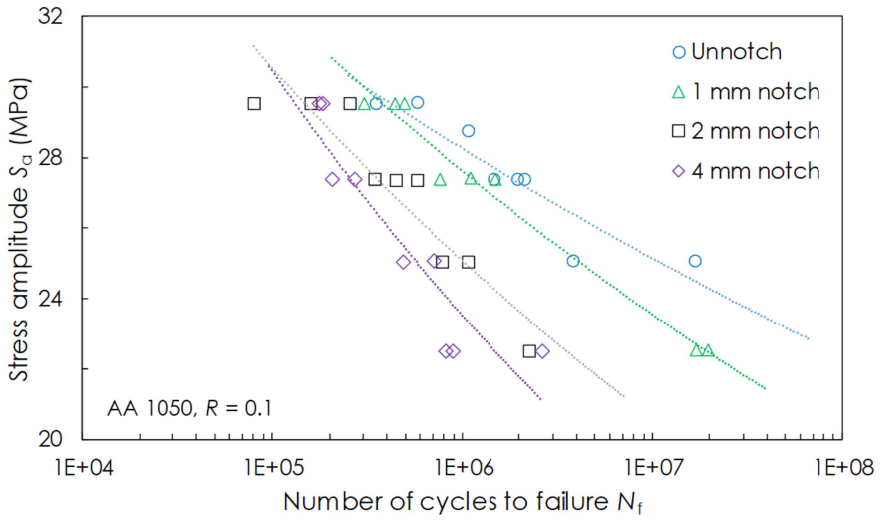

Figure 97: Experimental S-N curves of the 3.46 mm grain-sized aluminium alloy (AA) 1050 under the influence of different notch radii (flat specimen) [15L].

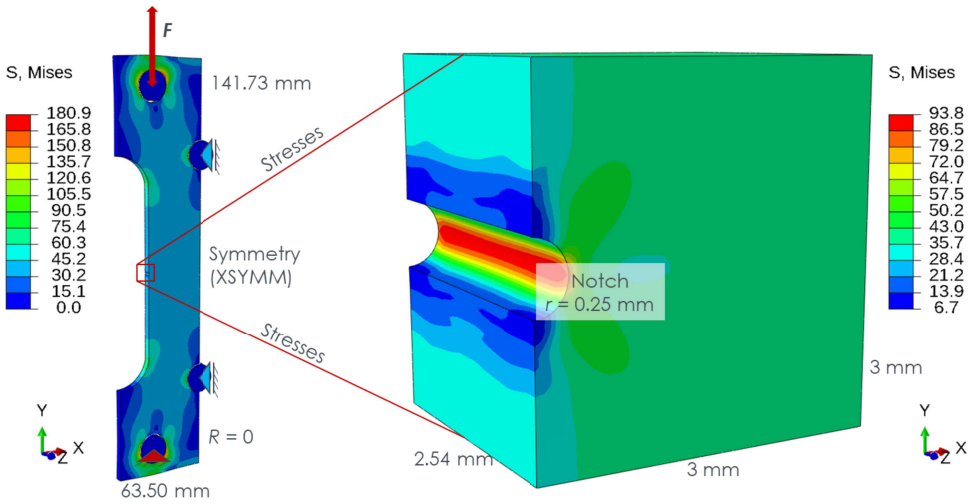

Figure 98: Left – 3D global model of the notched tensile specimen (half); Right – 3D submodel of the region at the notch ground.

the most critical regions are kept below the yield stress through the complete loading span (see y-axis of the *S-N* diagram in Figure 100). Namely, the transferred displacements from the 3D solid submodel to the microstructural one did not result in stresses that are higher than the yield stress (R_e = 95 MPa [15L]). This especially counts for the notch region where crack initiation is expected. Figure 99L shows shear stresses in a 3D deformable shell submodel, acting as a result of the transferred displacements to the boundary edges (denoted with numbers from 1 to 5) of the submodel.

After completing the estimation of fatigue life of the modified specimen, its *S-N* curve has been compared with the curve of the same specimen but with a 9.128 mm notch radius from Section 5.2.3. As visible from the comparison in Figure 100, there is evident qualitative agreement with the experimental results from [03M, 03R, 04F, 08M, 13C, 15L] and wiht Figure 97, i.e. the decrease of the notch size (from 9.128 to 0.25 mm) resulted in an evident increase in fatigue performance of the specimen

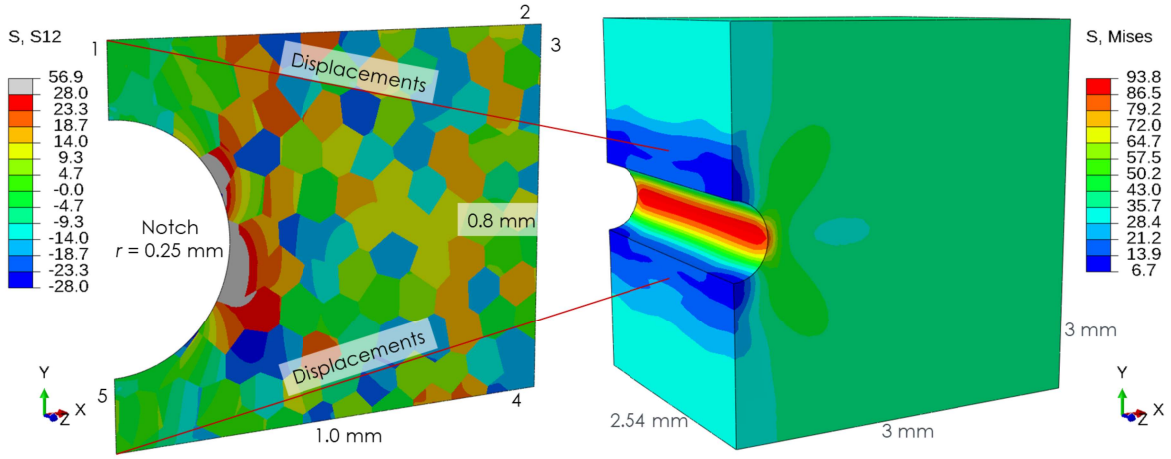

Figure 99: Left – Shear stress distribution in the 3D deformable shell submodel of aluminium AA 1050 under 25 MPa amplitude level; Right – 3D submodel.

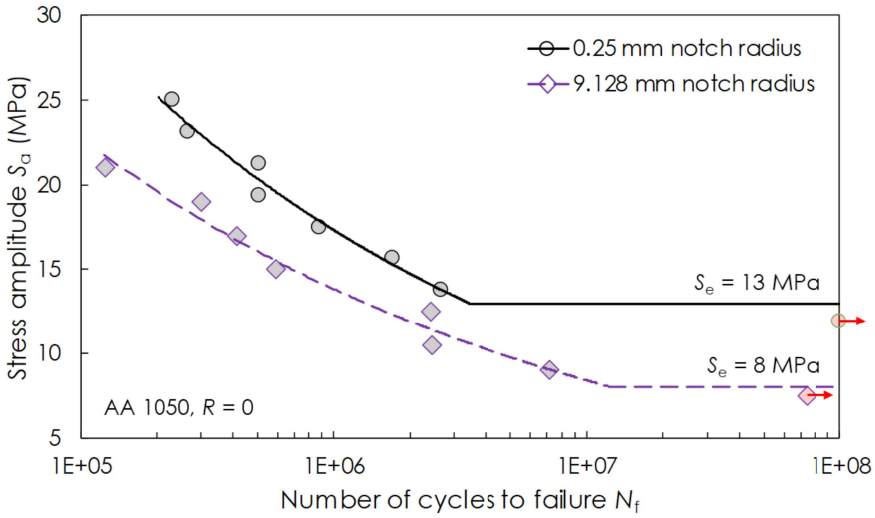

Figure 100: Calculated S-N curves showing the decrease in endurance limit when the size of the notch increases. (The validation for the 9.128 mm notch case is shown in Table 8)

made of the AA 1050 alloy. Namely, the endurance limit has been increased from 8 MPa (9.128 mm notch radius; see Section 5.2.3) to 13 MPa (0.25 mm notch radius).

In addition, Figure 101 shows the effect of different notch radii (r), i.e. different stress concentration factors (K_t), on the relation between S_e and CRSS values of the metals investigated in Section 5.2.3. The relation for the value K_t = 1 (r = 0 mm – un-notched, blue dot-dashed line) has been deduced from the relation for the value K_t = 2.36 (r = 9.128 mm [04F], red dotted line) – introduced in Section 5.2.3 (see Eq. 5.4) – by multiplying its S_e values by a factor K_{fat}, which is commonly called a fatigue stress concentration factor ($S_{e,Kt1}$ = $S_{e,Kt2.36}$ x K_{fat}) [15B]. The factor K_{fat} is determined from the factor K_t by using the expression: K_{fat} = 1 + q(K_t – 1); where q is the notch

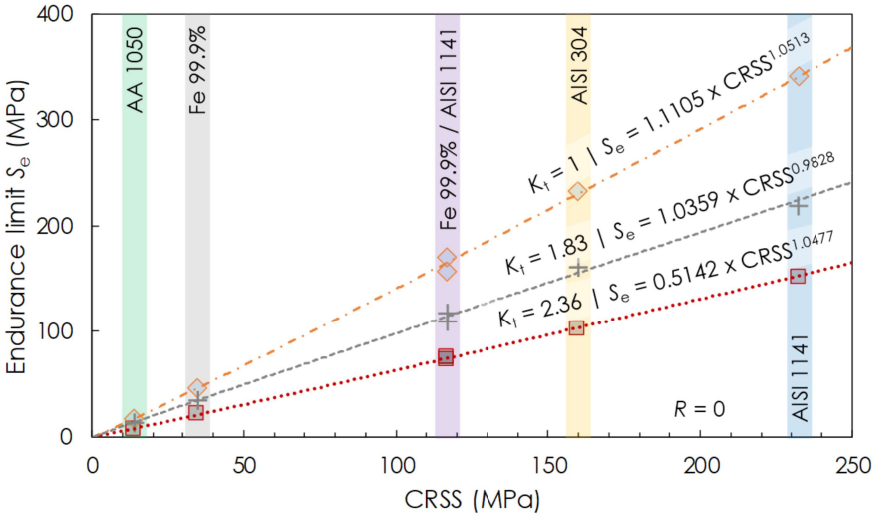

Figure 101: Relation between S_e ($S_{e,a}$) and CRSS values under the influence of different notch radii, i.e. different stress concentration factors: r = 9.128 mm (K_t = 2.36) [04F], r = 0.25 mm (K_t = 1.83) and r = 0 mm (K_t = 1), respectively. (Details for the 9.128 mm notch case are given in Section 5.2.3)

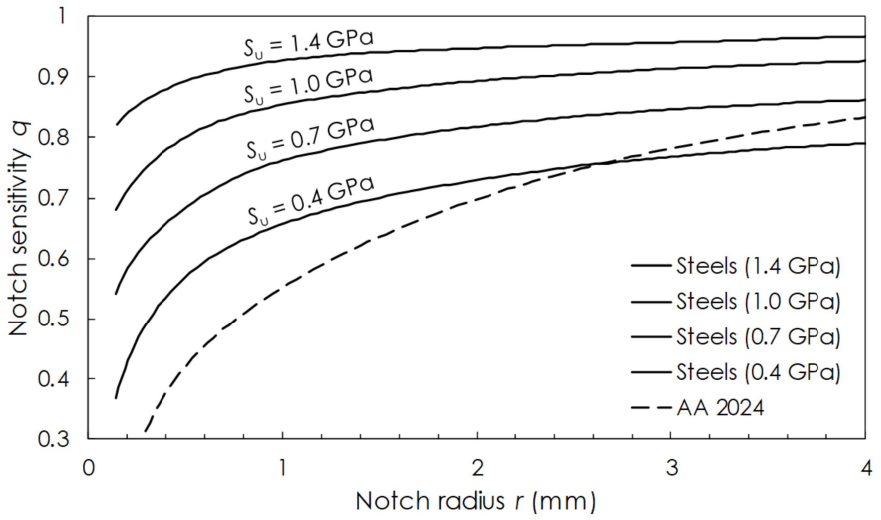

Figure 102: Notch sensitivity charts for steels with different ultimate strengths (S_U) and aluminium alloys AA 2024 subjected to reversed bending or reversed axial loads. For larger notch radii, it is recommended to use the values of q corresponding to the r = 4 mm [15B].

sensitivity and can be obtained for different types of metals from a diagram *q* versus *r*, as shown in Figure 102 [15B].

The relation between S_e and CRSS values for K_t = 1.83 (*r* = 0.25 mm, grey dashed line in Figure 101) has been inversely deduced from the relation for the unnotched case (K_t = 1) by using the expression: $S_{e,Kt1.83} = S_{e,Kt1} / K_{fat}$. It is noteworthy that the simulation-based S_e value calculated for the AA 1050 and for K_t = 1.83 in this section (see Figure 100) of 13 MPa is matching almost perfectly the value of 13.86 MPa, which can be calculated from the S_e-CRSS relation law for that specific K_t factor ($S_e = m_0$ x CRSS^s; $m_{0,Kt1.83}$ = 1.0359, $s_{Kt1.83}$ = 0.9828, see Figure 101; CRSS = 14 MPa [10J]). Aside of that, this study goes in line with a statement from Section 5.2.3 saying that the parameters m_0 and *s* of the Equation (5.4) are dependent on the notch radius, the loading ratio *R*, etc.

To conclude, this study shows that the multiscale fatigue simulation approach – supported by the existing knowledge on the notch sensitivity (see Figure 102) – can handle the notch radius effect with a high reliability, what promotes its application during the designing of structural components where notches play a predominant role.

5.7 Influence of Plasticity on the Fatigue Life Curve

Previously investigated materials in this work have been defined as purely elastic (global 3D models in macroscale simulations) and as orthotropically elastic (shell 3D microstructural models). The aim of this section is thus to show the influence of plastic properties, i.e. hardening, on the endurance limit. By adding the plastic aspect to the materials' constitutive laws, it can be imagined that certain effects on the endurance limit in the *S-N* diagram could be achieved.

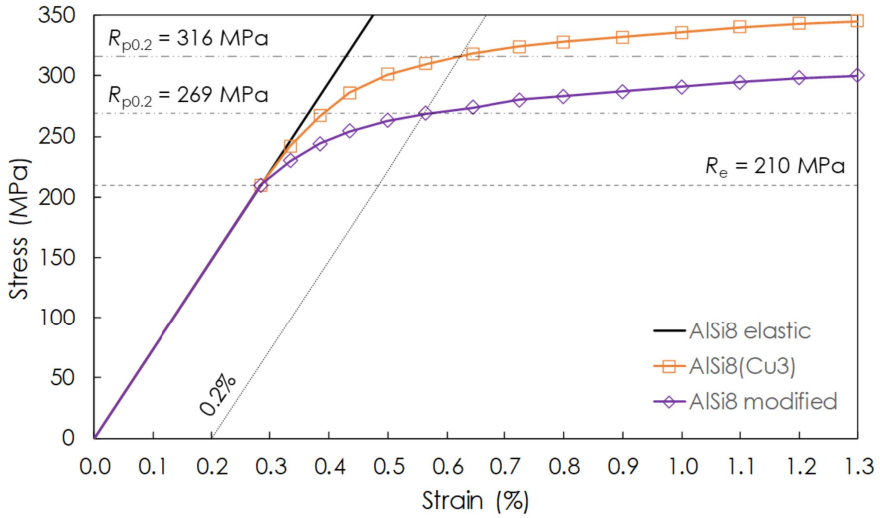

Figure 103: Applied hardening curves for the aluminium alloy AlSi8(Cu3) and its modification [19M].

Figure 103 shows the hardening law (curves) for the two considered materials, the aluminium alloy AA AlSi8(Cu3) and its modified variant. These initial hardening relations presumably play a role in the fatigue behaviour in the endurance limit region. The modification of the AlSi8 hardening law has been done arbitrarily in order to have a relative difference with respect to the original one. Additionally, AlSi8 defined just by the elastic mechanical properties has been analysed for comparison reasons. The original stress-strain curve has been taken from the internal database of IMWF [19M].

Among various metal plasticity models in Abaqus, isotropic hardening can be specified. Specification of this type of work hardening means that the yield surface changes its size uniformly in all directions such that the yield stress increases (or decreases) in all stress directions as plastic straining occurs. Although the model is referred to as a "hardening" model, strain softening or hardening followed by softening can be defined. If isotropic hardening is defined, the yield stress can be given in tabular function of plastic strain and, if required, of temperature and/or other predefined field variables. By having a look at Figure 103, symbols (squares and diamonds) defining hardening curves as well as representing one plastic stress-strain state are given in tabular form in Abaqus. The yield stress at a given state is simply interpolated from this table of data, and it remains constant for plastic strains exceeding the last value given as tabular data [ABQ].

On the other hand, the elastic response of all three materials is the same and is defined by using the components of the material stiffness matrix in the elastic orthotropic description, i.e. by the material elastic constants for cubic crystal symmetry: $C_{11} = C_{22} = C_{33} = 106{,}678$ MPa, $C_{12} = C_{13} = C_{23} = 52{,}543$ MPa and $C_{44} = C_{55} = C_{66} = 26{,}000$ MPa. Table 11 contains all the simulation-relevant mechanical properties, including the TM equation parameters, which are also the same for the three considered AlSi8 variants.

Table 11: Input data for AlSi8 and its modifications.

Material	E (GPa)	G (GPa)	υ -	R_e (MPa)	CRSS (MPa)	W_c (N/mm)	d (µm)
AlSi8	26	72	0.33	210	31	11	~50

After performing simulations by using the advanced fatigue modelling approach and with the aforementioned input data, the results have been plotted and presented in Figure 104 in the form of *S-N* curves. Simulation results in Figure 104 indicate that materials defined by using elastic-plastic constitutive laws show better fatigue durability than purely elastically defined materials. Namely, the modified AlSi8 alloy with the lowest hardening rate (purple dot-dashed line with diamonds in Figure 103) has the highest endurance limit of ~37 MPa, while the purely elastic alloy possesses the lowest endurance limit of ~35.4 MPa (black line with Xs). The original AlSi8 alloy has an intermediate endurance limit of ~36.6 MPa, which fits quite well to the experimental one of 35.6 MPa. According to the outcome of this study, the conclusion can be drawn that a lower hardening rate leads to a higher fatigue endurance limit, i.e. a higher fatigue resistance. A similar observation in the sense that the lower work hardening rates of BCC-based systems, aside of the higher CRSS, provides them higher endurance limits with respect to FCC systems as reported by Grosskreutz [71G] and Ferro et al. [65F]. On the other hand, as the loading level gets higher in the definite region of the fatigue life, the difference between the results of the three considered alloys becomes less pronounced.

To shed some light on the aforementioned observations, it is worthwhile to have a look at the stresses around microcracks that formed in the microstructural models of the three investigated materials under loading levels that are in the range of endurance limits. Figure 105 shows first the comparison of von Mises stresses between the microstructural models of the elastic material (left image) and the original material (right image) at the stress amplitude of 38.125 MPa. By using Abaqus visualization options, the stresses that are higher than the yield stress of the original AlSi8 alloy (R_e =

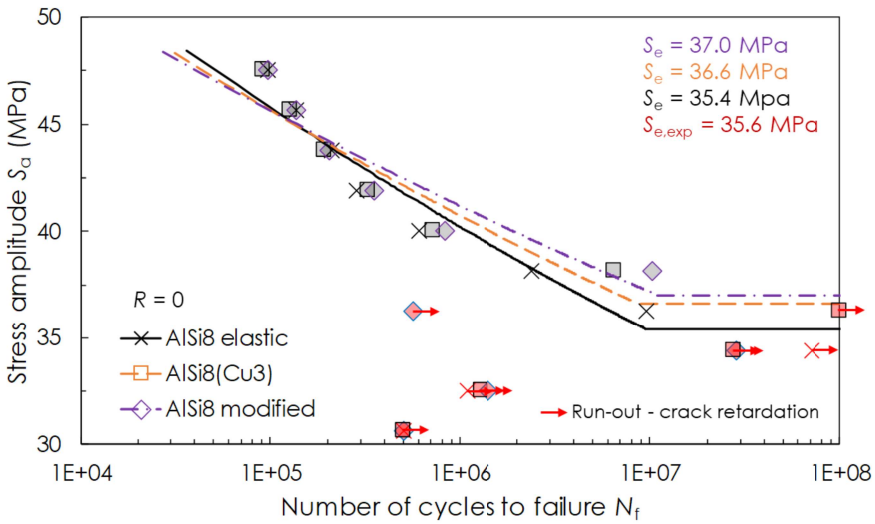

Figure 104: Simulation-based S-N curves showing the influence of hardening for AlSi8 [19M].

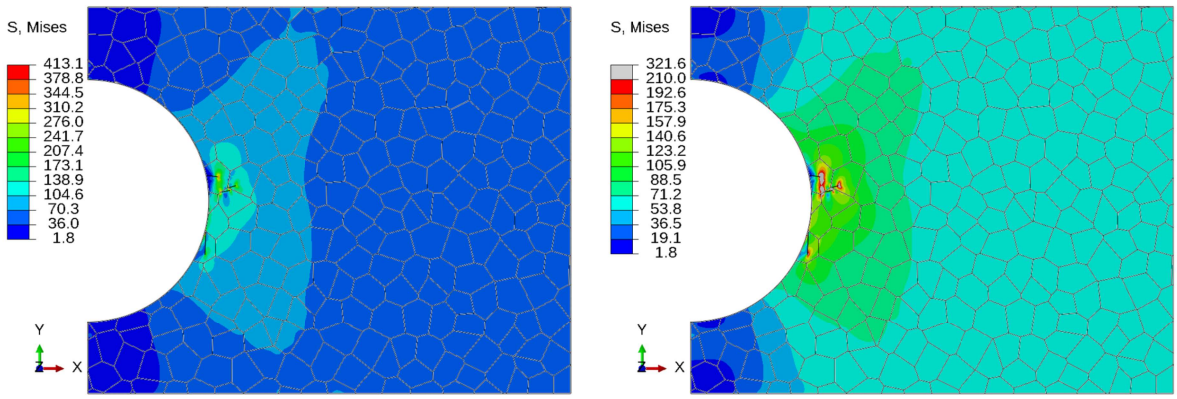

Figure 105: von Mises stresses at the end of the initiation stage in the microstructural model with: Left – Elastic properties; Right – Elastic-plastic properties of the original AlSi8 alloy. The applied stress amplitude is equal to 38.125 MPa.

210 MPa) have been coloured in grey Figure 105R. The grey-coloured stress representing plastic zones in Figure 105R are not present in Figure 105L as the elastic material is given there. Nevertheless, the highest stresses in both models can be compared: it is visible from the legends that the highest stresses at the tips of microcracks in the elastic materials reach 413 MPa, while in the original materials these stresses are equal to 322 MPa.

By further comparing the maximum stresses and plastic zones between the two elastic-plastically defined materials, it is apparent from Figure 106 that the modified AlSi8 alloy (right image), characterized with the lower hardening rate (see Figure 103), produces lower maximum stresses (286 MPa) in the microcrack tip regions. The original alloy produces maximum von Mises stresses of 322 MPa under the amplitude level of 38.125 MPa, as mentioned earlier. It can be concluded from the comparison of the stress fields that the plasticity is acting as means of relieving stresses. It is important to note that all the results in Figures 105, 106, but also 107 and 108 are plotted for the same loading level and at the end of the initiation stage; all three alloys exited the initiation stage after 9 broken segments at the aforementioned loading

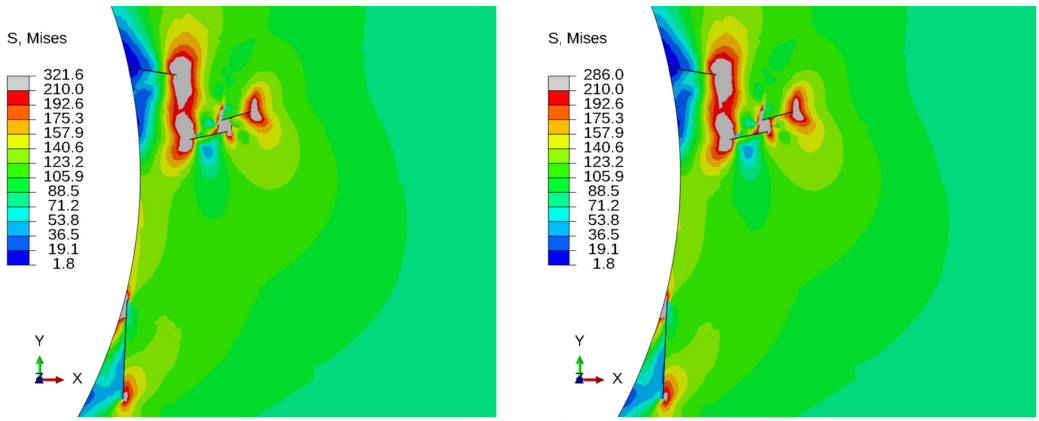

Figure 106: von Mises stresses at the end of the initiation stage in the microstructural model with elastic-plastic properties of the: Left – Original AlSi8 alloy; Right – Modified AlSi8 alloy [19M]; the applied stress amplitude is equal to 38.125 MPa. Zoomed views.

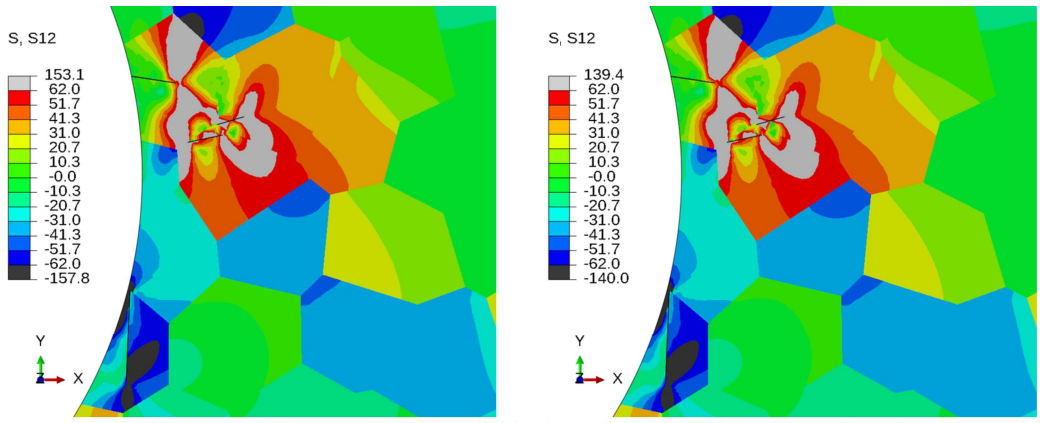

Figure 107: Shear stresses at the end of the initiation stage in the microstructural model with elastic-plastic properties of the: Left – Original AlSi8 alloy; Right – Modified AlSi8 alloy [19M]; the applied stress amplitude is equal to 38.125 MPa. Zoomed views.

level, what has been determined by using the RdM. The damage pattern was the same in all three cases, too.

A further interesting comparison between the modified and the original alloy is presented in Figure 107 where shear stresses are plotted. These stresses are again higher in the original alloy (153 MPa in Figure 107L versus 139 MPa in Figure 107R), what is in accordance with previous observations and what explains the difference in the fatigue life curves in Figure 104 as the higher shear stresses result in shorter fatigue initiation life according to the TM equation. In addition, Figure 108 shows the equivalent plastic strains (PEEQ [ABQ]) in the original (left image) and the modified AlSi8 alloy (right image). In contrast to the von Mises stresses, the PEEQ is higher in the materials with lower hardening rates, as expected.

The analysis brings new insight into the influence of plasticity on the fatigue life curves of metallic materials. According to the outcome of this study, the conclusion can be drawn that lower hardening rates lead to higher fatigue endurance limits, i.e. to higher fatigue resistance. Even though this influence is not excessive (e.g., decrease of around 13% in hardening rate in Figure 103 leads to an increase in the en-

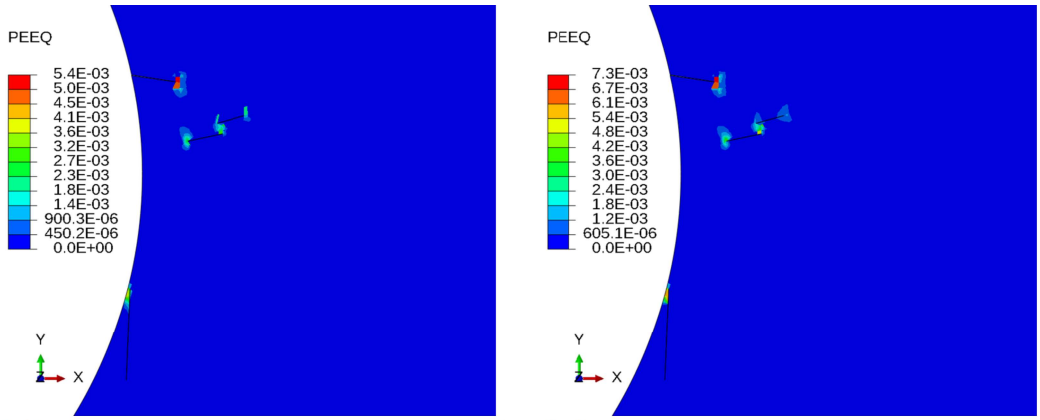

Figure 108: Equivalent plastic strains (PEEQ) at the end of the initiation stage in the microstructural model with elastic-plastic properties of the: Left – Original AlSi8 alloy; Right – Modified AlSi8 alloy [19M]; the applied stress amplitude is equal to 38.125 MPa. Zoomed views.

durance limit of 1%, 36.6 MPa versus 37 MPa in Figure 104), it can be detrimental in certain applications and thus provides a useful hint, which facilitates the selection of those types of materials with lower hardening rates, which are more fatigue resistant. These results are published in [19M].

It is suitable to indicate here that all the materials' constitutive laws in the previous studies have been defined as purely elastic, i.e. just by using the material elastic constants for cubic crystal symmetry C_{11}, C_{12} and C_{44}. Since these studies are done before the current one and since the here investigated influence of plasticity on, for example, the endurance limit is quantitatively not significant, their repetition with the plasticity model would qualitatively bring no difference and is thus avoided.

In addition, the microstructural model with the elastic-plastic properties of the original AlSi8 alloy has been analysed with the aim to compare its stress versus strain response when in the undamaged state (prior to the fatigue analysis) and when it contains cracks (e.g. at the end of the initiation stage, Figure 105R or Figure 108L). For this purpose, one displacement controlled forward loading and one reverse unloading have been applied to the top side of the model and the reaction forces have been measured accordingly. The desired stress-strain response of the two cases (damaged and undamaged microstructural 3D shell models) has been obtained by dividing the reaction forces by the area of the top side of the model (width of 1 mm multiplied with the shell thickness of 0.05 mm, which is also equal to the average grain size *d* of the alloy AlSi8, see Table 11) and by dividing the applied displacements by the height of the model (0.8 mm), respectively. Figure 109 shows that the damage introduced after the fatigue analysis influences the stress-strain response of the microstructural model. Namely, the microstructural model containing cracks (full red curve in Figure 109) lost some of its toughness (the area under the loading part of the curve) when compared to the undamaged model (dashed black curve). Aside of that, the results demonstrate that the difference between the two models is influenced by both the level of the damage and by the plasticity ef-

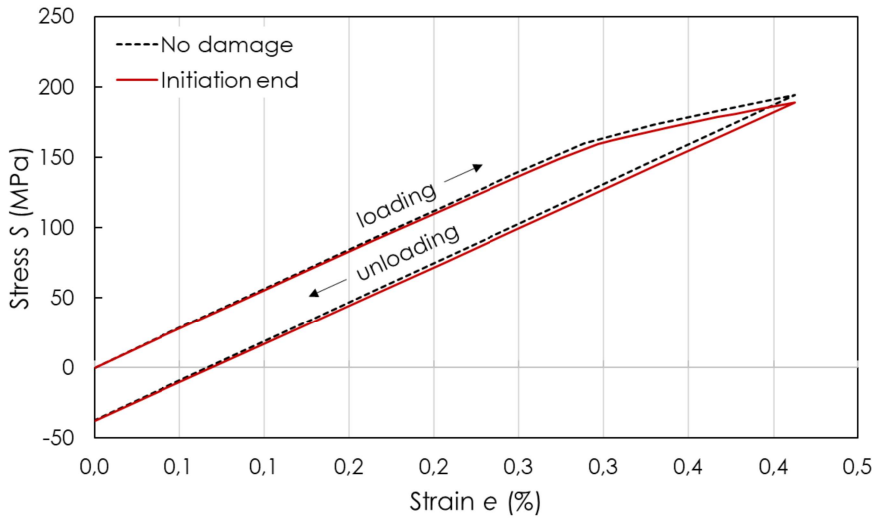

Figure 109: Different stress-strain response of the undamaged and the damaged (initiation end) microstructural model under one forward loading and reverse unloading.

fects. Namely, the models needed to be loaded to such an extend to enter the plastic regime, which can be perceived in Figure 109 by the changes of the slopes of the loading parts of the curves. Otherwise, no influence on the *S-e* response would be seen.

To conclude, the applied fatigue simulation approach is capable of analysing the influence of plasticity on the fatigue performance of metallic materials as well as the influence of the fatigue induced damage on their stress-strain response on the microstructural level.

5.8 Crack Initiation Energy and its Effect on the Fatigue Life Curve

Relevant properties of structural materials, regarding safety against failure, are strength and toughness. These two properties are primarily influenced by the microstructure of the material and are typically determined by means of mechanical tests, or in some cases by means of numerical models, as done in Section 5.5 where the fatigue strength of AISI 1141 steel has been determined under the influence of grain size. A significant aspect of FM used for characterising ductile materials is the *J*-integral, in particular the fracture toughness J_{Ic}, which is the value of the *J*-integral at the final fracture of a structure subjected to cyclic loading conditions. Another relevant value of the *J*-integral is the physical crack initiation J_i. [98D] The J_i value is also known as the crack initiation energy (W_c), which is a constituent of the TM model (Eq. 4.3, Section 4.3.1).

These two characteristic values of elastic-plastic (ductile) fracture mechanics (EPFM) are determined from the crack resistance *J-R* curve [88R]. Extensive investigations on tensile specimens of different kinds of steels, titanium, aluminium and cop-

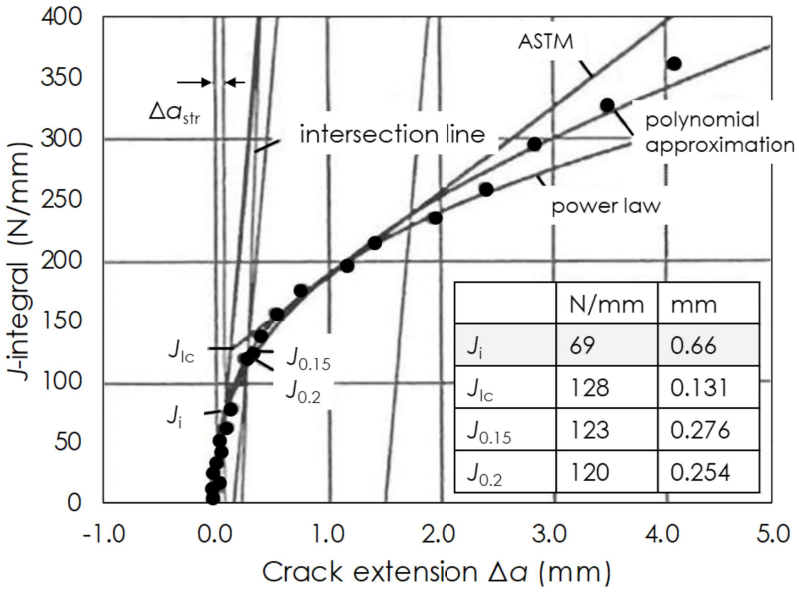

Figure 110: Determination of J_i values of 22 NiMoCr 3 7 specimen [88R].

per alloys, aiming to understand the microstructural deformation processes of ductile materials, have been performed in [85V, 90T, 98D]. In particular, the J_i value is determined from the *J-R* curves as the ordinate at the abscissa $\Delta a = \Delta a_{str}$, where Δa_{str} is the stretched zone (see Figure 110) measured on the fracture surface of the compact tension specimen. Some values of J_i for selected steels are listed together with the Δa_{str}-values in Table 12 [98D].

The stretched zone Δa_{str} represents the region of extreme plastic deformation of the crack tip prior to stable crack growth. Figure 110 gives an example of a *J-R* curve for 22 NiMoCr 3 7 steel. The J_i value determined from this curve is equal to 69 N/mm at Δa_{str} = 0.066 mm [88R]. The value is also tabulated in Table 12.

Table 12: Stretched zone Δa_{str} and experimental J_i-values determined for different materials.

Material	Δa_{str} (µm)	J_i (N/mm)
10 MnMo Ni 5 5	49	63 [98D]
20 MnMoNi 5 5	19	19 [98D]
22 NiMoCr 3 7	66	69 [88R]
X 20 CrMoV 12.1	46	54 [98D]

As aforementioned, the W_c (J_i) is an essential part of the TM equation (Eq. 4.3), in particular of its numerator. Based on that, it can be assumed that the W_c proportionally influences the number of cycles to nucleate a single crack segment in a microstructural model. To prove this mathematical assumption, a test simulation has been performed. The numerical model created for the AA AlSi8 from Section 5.7, together with the given material input data, has been used for the purpose of this parametric study. The only difference to the previous study, is the increased value of W_c, from 11 N/mm to the doubled value of 22 N/mm.

Table 13: Segmental cycles (N_s) of the AlSi8 alloy in dependence on the crack initiation energy (W_c) for an amplitude level of 40 MPa.

Iteration	Slip band length	W_c = 11 N/mm		W_c = 22 N/mm	
		N_s	Σ cycles	N_s	Σ cycles
1	0.04817	15,013	15,013	30,026	30,026
2	0.02568	23,992	39,005	47,985	78,011
3	0.06604	472	39,477	943	78,954
4	0.06604	36,232	75,709	72,464	151,418
5	0.02568	19,573	95,282	39,146	190,564
6	0.02568	10,891	106,173	21,782	212,346
7	0.06236	69,697	175,870	139,394	351,740
8	0.04817	21,428	197,298	42,856	394,596
9 (c1)	0.06604	54,121	251,419	108,242	502,838
10 (c2)	0.06488	927,685	1,179,104	1,855,370	2,358,208
11	0.06488	995,321	2,174,425	1,990,643	4,348,851
…	…	…	…	…	…

Table 13 contains results from the study, which has been performed at 40 MPa stress amplitude (see Figure 104). The results comprise cycles spent for the nucleation of each individual segmental crack at the two W_c magnitudes, 11 and 22 N/mm. By having a close look at these results, it is easy to notice that the segmental cycles (N_s)

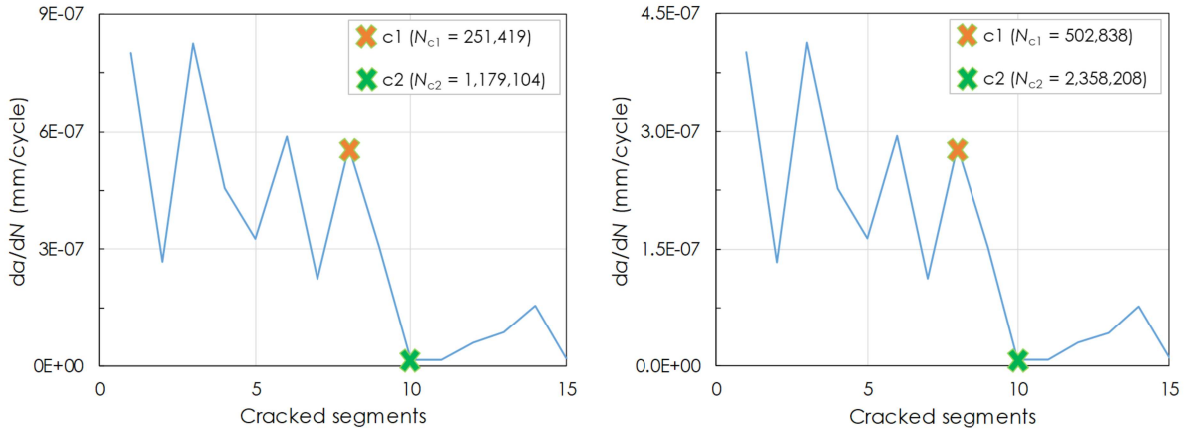

Figure 111: Crack growth rate for an AlSi8 alloy and for a crack initiation energy (W_c) of: Left – 11 N/mm; Right – 22 N/mm (da/dN two times lower). 40 MPa loading level in both cases.

are two times higher for the doubled W_c of 22 N/mm. Accordingly, the summed cycles are two times higher, too. These results prove the assumption that the W_c (J_i) proportionality alters the number of cycles to nucleate a single crack segment in a microstructural model. Aside of that, it also alters proportionally the complete (summed) number of cycles after each iteration of the fatigue crack initiation simulation.

Another interesting result to have a look at in Figure 111 is the one showing the d*a*/d*N* for the two W_c magnitudes. Again, as in the case of cycles, the higher magnitude of W_c proportionally increases the d*a*/d*N* (in this case also by the factor of two). This could be expected as cracks nucleating in both cases are the same in each iteration, having the same length, too (see second column of Table 13). The rates in Figure 111 are obtained simply by dividing the length of the iteration-specific segmental cracks (d_s, one fourth of the slip band length, see Section 4.3.1) by the iteration-specific segmental cycles (N_s). However, there is one exception and this study gives an opportunity to address another interesting aspect, which can be often encountered during the evaluation of the results coming out of fatigue crack initiation simulations.

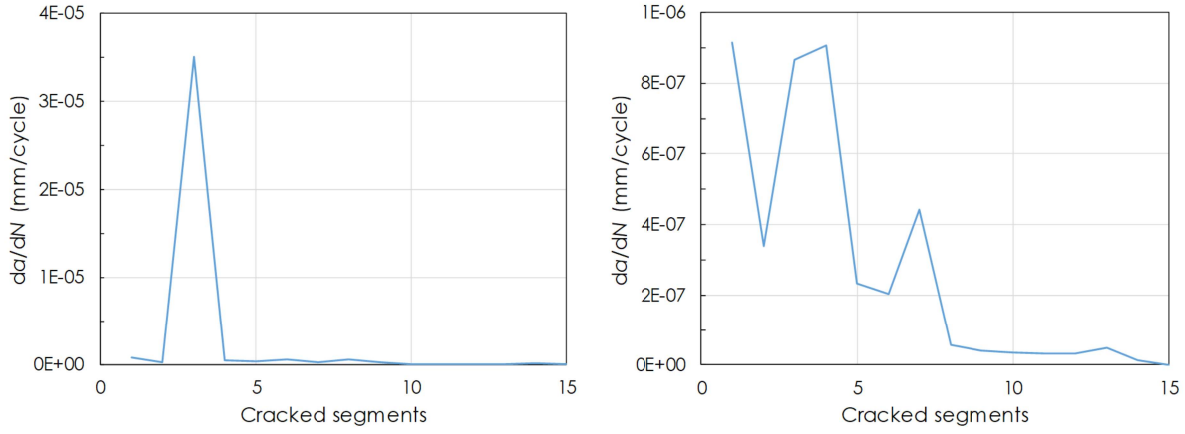

Figure 112: Fatigue crack growth rate of AlSi8 alloy (W_c = 11 N/mm) at 40 MPa loading level in: Left – Unmodified form (unrecognizable drop); Right – Averaged form (apparent drop).

Namely, by observing Table 13, iteration 3 comes into focus as its segmental cycles for both W_c magnitudes are considerably lower than all the other earlier and later segmental cycles (472 cycles for W_c of 11 N/mm and 943 cycles for 22 N/mm). When such relatively low segmental cycles are taken into account when plotting the d*a*/d*N*, extreme peaks are typically formed, as visible in Figure 112L.

Accordingly, the initiation completion is difficult to determine in such cases, as explained in Section 5.1, since other smaller peaks are visually not recognizable. This problem can be solved by modifying those problematic cycles, what in the end produces uniform d*a*/d*N* values as in the graphs from Figure 111. For the record, the 472 cycles obtained for the W_c of 11 N/mm has been modified to 20,000, and 943 cycles of 22 N/mm to 40,000 cycles. Modifying the extreme peak in Figure 112L leads to a significantly larger number of peaks becoming visible in the graph, as Figure 111 demonstrates. It is, however, important to indicate that the original segmental cycles (472 and 943, respectively) are used to calculate the overall number of cycles spent in the crack initiation stage. As mentioned earlier, the iteration after the first significant drop of d*a*/d*N* (see Rate-drop Method in Section 4.3.4) is used for determining the end of the initiation process (marked with a green cross) [17S].

On the other hand, Figure 112R shows the averaged d*a*/d*N*, which has been derived from the original segmental cycles (Table 13). It can be seen here that a considerably lower segmental number of cycles from iteration 3 does not lead to the appearance of the extreme peak from Figure 112L as it has been averaged by others. Averaging of the d*a*/d*N* and its role in determining the end of the initiation phase was discussed in details in Section 5.1.

Since the test simulation proved that the W_c alters proportionally the complete (summed) number of cycles after each iteration, and by that the cycles characterizing the initiation completion, the results for the other than 40 MPa stress amplitudes in the case of W_c being equal to 22 N/mm have been determined simply by multiply-

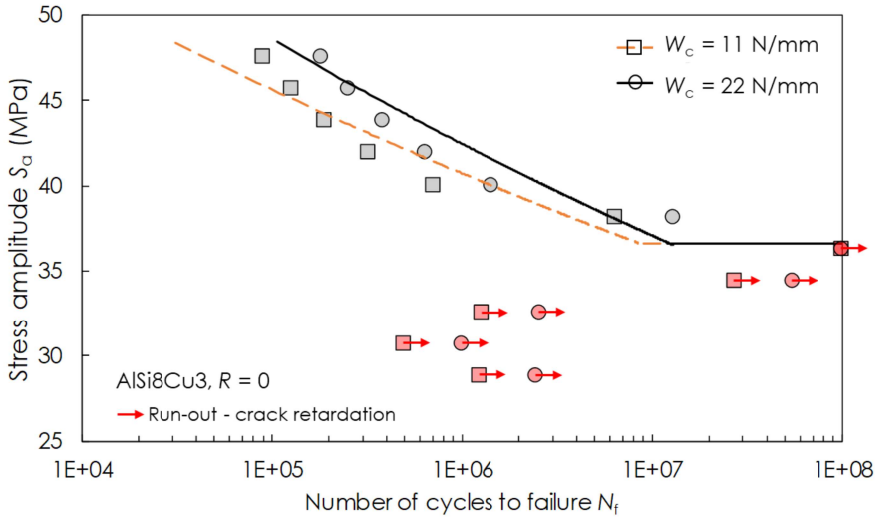

Figure 113: Numerical S-N curves comparing materials with different crack initiation energies; the "knee" shifts right with the increase in W_c. (The validation for the case W_c = 11 N/mm is discussed in Section 5.2.3)

ing the initiation cycles of W_c equal to 11 N/mm by the factor of two. Eventually, the results have been summarized in Figure 113 in the form of *S-N* curves.

By observing these curves, it is useful to conclude that the W_c shifts the definite parts of the fatigue life curves left and right depending on its magnitude, while the endurance limit (S_e = 36.6 MPa, see Section 5.7) stays unaltered. This observation can be used to understand a slight disagreement between experimental and simulation results in the slope (definite) regions of *S-N* curves in Section 5.1, where the steel AISI 1141 was analysed. Meaning that the application of a W_c lower than the used 19 N/mm would lead to a better agreement in the slope regions.

5.9 Crack Initiation inside a Replicated Microstructure

In contrast to the previous sections where the investigated microstructures have been created by using the Voronoi tessellation technique (see Section 4.3.2), in this section the microstructure has been modelled based on the real microstructure of a material. Namely, the left image in Figure 114 shows an etched microstructure of the high-purity AA 1050, which has been used to create a replicated model, shown in Figure 114R.

The replication process consists of drawing a sketch containing grain boundaries of the real microstructure by using the free software Acme TraceArt, importing the sketch into Abaqus software and creating the microstructural model where grains are separated from each other by the drawn grain boundaries, as depicted in Figure 114R. Additionally, local orientations have been prescribed to the grains. The created microstructural model has been used in a test simulation, with the purpose of showing the capability to simulate the crack initiation process inside such a replicated models. For this purpose, one amplitude level of 25 MPa has been selected. The model of the AA 1050 alloy, with the same material properties as the model in Section 5.2.3 and Section 5.6, has been placed at the notch tip of the global model, Figure 98. To illustrate this more precisely, a schematic representation in Figure 115 has been created with the purpose to put the replicated model in relation to the

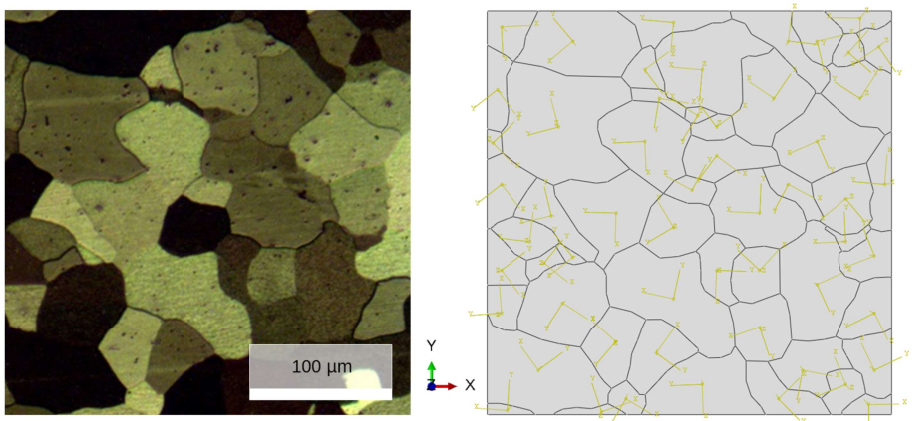

Figure 114: Left – Microstructure of AA 1050 alloy; Right – Microstructural model replicating the microstructure of the AA 1050 alloy.

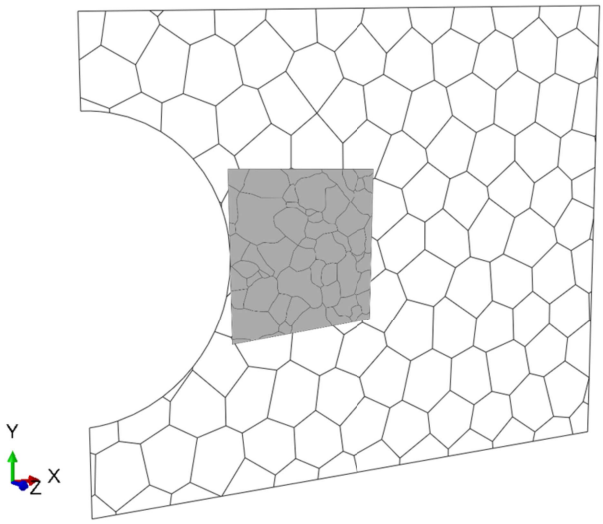

Figure 115: Comparison of the microstructural models of the AA 1050 alloy created by using the Voronoi tessellation (transparent) and by using the software Acme TraceArt (grey).

model of the AA 1050 alloy that has been created by using the Voronoi tessellation technique (see Section 5.6). The average grain size in the tessellated model is around 60 µm, and the largest grains of the replicated model are in that range, too. As visible in Figure 114R, every replicated grain has its own arbitrary coordinate system. Concerning the size of the model, a mismatch is evident due to the unavailability of a larger real microstructure of the AA 1050, which would allow the creation of a replicated model (currently 280 µm dimension in y-direction, Figure 115) in the size of tessellated model (currently 800 µm dimension in y-direction, Figure 115).

Figure 116 shows the results of the test simulation performed at 25 MPa amplitude level. The same loading level was applied to the tessellated model in Section 5.6 by using the submodelling technique. The left image presents the damaged replicated (microstructural) model (with the help of shear stresses) at the moment when the initiation process has been completed. The end of the initiation phase has been de-

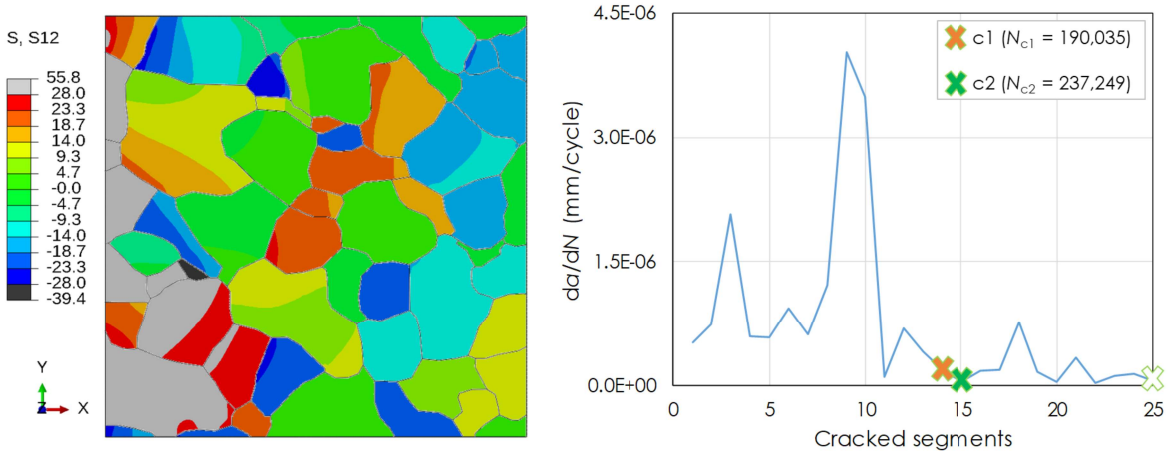

Figure 116: Left – Shear stress in the replicated microstructural model at the end of the initiation phase; Right – Fatigue crack growth rate derived for the replicated model at the 25 MPa amplitude level.

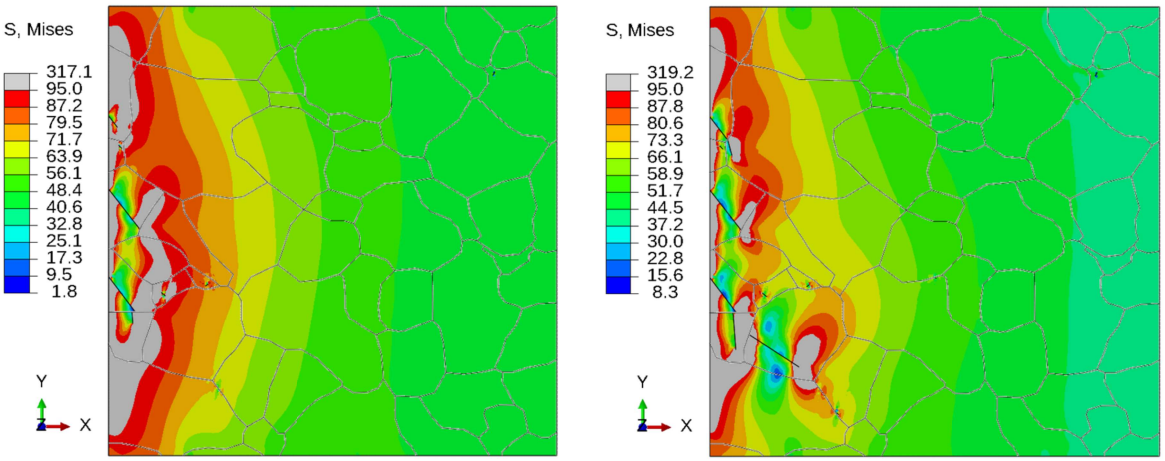

Figure 117: Left – Damaged model at the initiation end (213,642 cycles) at the 25 MPa loading level; Right – Model after 867,309 cycles at the same loading level. (Cycles are averaged between N_{c1} and N_{c2}, see e.g. Figure 116R)

termined by using the crack growth rate from the right image and by using the RdM, as explained in previous sections.

Even though the tessellated and the replicated models of the AA 1050 alloy (Figure 115) differ considerable in size and to a certain extend in the grain size, it is opportune to compare the resulting cycles, which have accumulated during the crack initiation at the same loading level. Despite the differences, those cycles match to each other relatively good. Namely, the tessellated model lasted 232,802 cycles until the initiation completion, while the replicated model took 213,642 cycles (averaged between N_{c1} and N_{c2}, Figure 116R).

For comparison reasons, Figure 117 shows von Mises stresses in the replicated model at the end of the initiation phase (left image; green cross in Figure 116R) and at the 25th simulation sequence belonging to the post-initiation phase (right image; white cross in Figure 116R, 867,309 cycles).

To conclude, this study shows that replicated microstructural models can be used in the crack initiation simulations as reliably as the tessellated models. However, it is opportune to indicate that numerical studies on artificial (random) microstructures allow much easier performance of parametric studies, while replicated microstructures make those studies much harder to perform due to increased temporal demand during their generation.

5.10 Determination of the Fatigue Life Curve for a Component

The topic of this study is the numerical determination of the complete fatigue lifetime of a dosing module flange made of austenitic stainless steel, by taking into account the influence of the material's microstructure in the stage of crack initiation. The number of cycles needed for crack initiation has been estimated on the basis of the TM equation as in all previously presented studies. The long crack growth duration has been estimated with the help of Paris law.

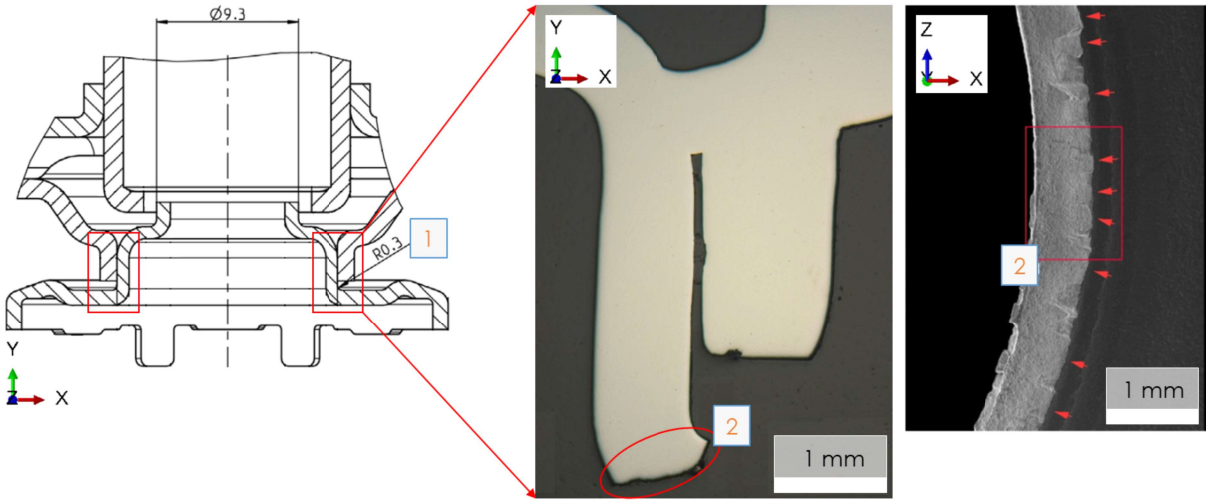

Figure 118: Left – Detail of the dosing module flange cut from the technical drawing, with the marked critical site (1); Right – Metallographic cut of the flange in the fracture region (2) [17O].

The dosing module flange analysed in this work is shown in Figure 118. The left image in Figure 118 gives the relevant dimensions of the flange together with the critical site – marked with red squares and number 1 – that becomes vulnerable under the cyclic loading. The right image shows, on the other hand, a cut of the already fractured flange, which failed at the location (Figure 118R, number 2) that is indicated in the left image. The flange failed under force-controlled cyclic loading conditions with the load ratio $R = -1$, i. e. under fully reversed fatigue loading or, in other words, under pure cyclic loading. The material of the flange is AISI 304 (X5CrNi18-10, 1.4301) austenitic stainless steel with a yield stress of 294 MPa, a Young's Modulus of 188 GPa and a Poisson's ratio of 0.26.

A numerical model of the dosing module flange has been set up and analysed by using the FEM-based software Abaqus. The model has been loaded under the same conditions as the flange in experiments and is shown in Figure 119L. This global model served in further studies for two purposes. The first one is to provide boundary conditions for microstructural, i.e. crack initiation, analyses and the second one to perform long crack growth analyses, similar as done in Section 5.1 where a specimen has been analysed. In order to perform the crack initiation analysis, where the microstructure plays a crucial role, the modelling scheme has been hierarchically split into multiple levels. The first level model has been already introduced and is shown in Figure 119L. In the following, the submodelling technique has been used for two lower levels. On the first sublevel, the critical site of the flange has been analysed by means of a 3D solid submodel (Figure 119R), with the purpose to obtain a more precise displacement and stress distribution than in the first level 3D solid model. This displacement distribution has been then applied to the second submodelling level where a detailed microstructural analysis has been performed. Namely, loading of the 3D shell-based microstructural model (Figure 120L) is applied by using

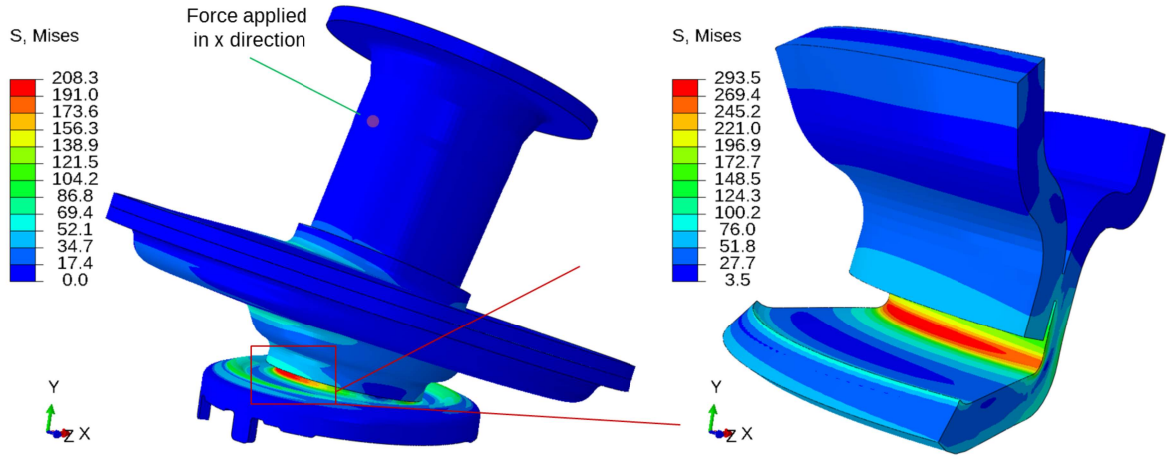

Figure 119: Left – Stressed macromodel of the dosing module component (austenitic stainless steel AISI 304), loaded by a force in the direction of the x-axis; Right – 3D submodel at the region of the notch ground.

local displacements transferred from the 3D solid submodel to the boundary edges of the microstructural model (marked with numbers from 1 to 4 in Figure 120L).

The microstructural model for crack initiation analysis is placed at the location where crack initiation is expected, i.e. at the location with the highest stresses. This location (see Figure 119R) corresponds to the failure location marked with number 2 in Figure 118. The size of the micromodel has been chosen arbitrarily to be 0.7 x 0.7 mm in size, by taking care that it is big enough to assess the crack initiation process. The model is generated by the Voronoi tessellation process [07G] and it contains a radius of 0.3 mm corresponding to the geometry of the flange at the critical site. Although looking like a 2D model in Figure 120L, it is a 3D deformable shell model meshed with membrane elements with reduced integration (M3D4R), from the Abaqus element library [ABQ]. Its microstructure has been created on the basis of etched a microstructure from an experimental study. The average grain size in the model is fixed as 26 µm, in accordance to the data from the experimental study.

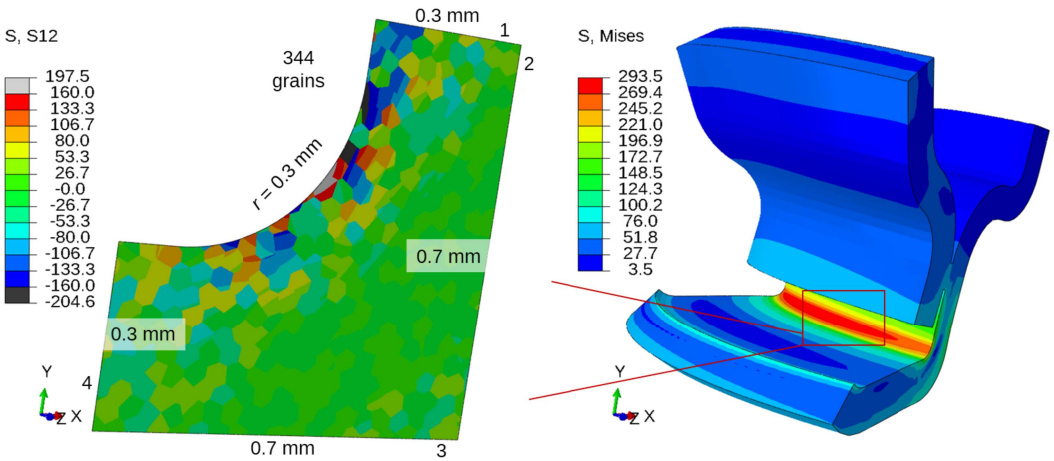

Figure 120: Left – Shear stresses in 3D deformable shell submodel, where loading is carried out by applying stress distributions of the 3D submodel to the boundary edges of the shell submodel (150 N loading level); Right – 3D submodel.

There are 344 grains in the model, which are meshed with 74,779 elements in total. Figure 120L presents the shear stress distribution obtained in the FEM analysis for the aforementioned alternating loading conditions (amplitude forces of 150, 300 and 450 N for $R = -1$), with the evident influence of the microstructure.

The elastic orthotropic material behaviour is assumed in the micromodel, while pure isotropic elasticity (E = 188 GPa and υ = 0.26) is adopted in the macromodel and in the 3D submodel of the micromodel, too. The components of the material stiffness matrix in an elastic orthotropic description, i.e. the elastic material constants for cubic crystal symmetry applied in the micromodel are: $C_{11} = C_{22} = C_{33}$ = 230,026 MPa, $C_{12} = C_{13} = C_{23}$ = 80,820 MPa, $C_{44} = C_{55} = C_{66}$ = 79,000 MPa.

The TM-based crack initiation model described in the previous sections is used to determine when a grain is likely to form a slip band and subsequently a crack. The driving force for crack nucleation depends on the orientation of the individual grains with respect to the applied loading. The material parameters of the TM model (Eq. 4.3, Section 4.3.1), used in this study are G = 79 GPa, υ = 0.26, and W_c = 69.0 kJ/m2 [88R]. The CRSS value of 160 MPa has been used, which was obtained for austenitic stainless steels by compression of pillars extracted from single grains by Monnet and Pouchon [13O].

The microstructural model (Figure 120L) has been loaded with three different amplitude forces, 150, 300 and 450 N, in accordance with the data available from the experimental study. The grains with highest stresses, i.e. the weakest grains in which first microcracks are expected to nucleate, are identified using the Abaqus plug-in enhanced with the TM model. It is visible from Figure 120L, which presents the undamaged micromodel, that the shear stresses differ from grain to grain as well as inside each individual grain.

Figure 121 presents results of the analysis for the 300 N loading level. The left image in Figure 121 depicts the micromodel containing nucleated microcracks, which can be easily perceived with the help of the von Mises stress distribution field. The other image on the right (Figure 121R) shows the accompanying crack growth rate

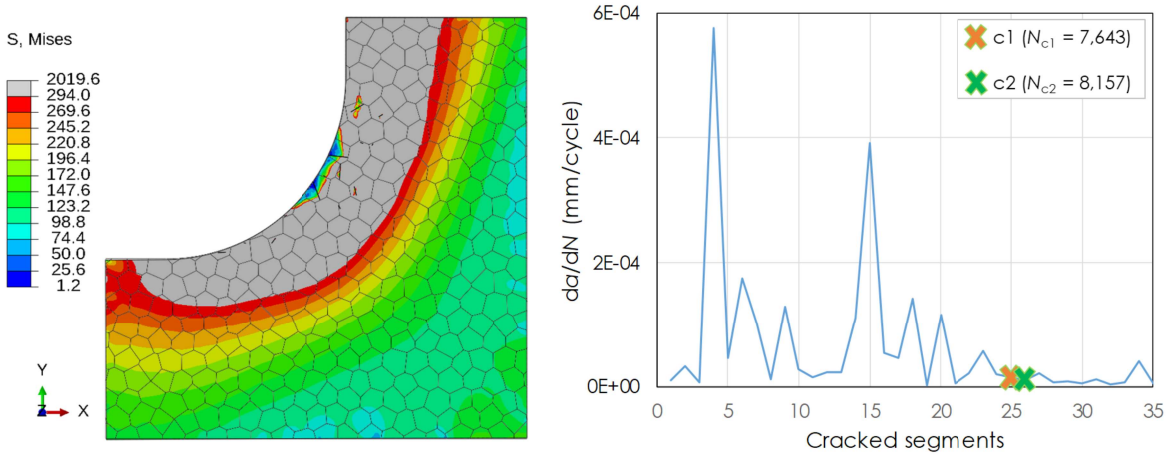

Figure 121: Left – Damaged microstructural model (shell submodel) at 300 N loading level; Right – Fatigue crack growth rate resulting from the 300 N loading level.

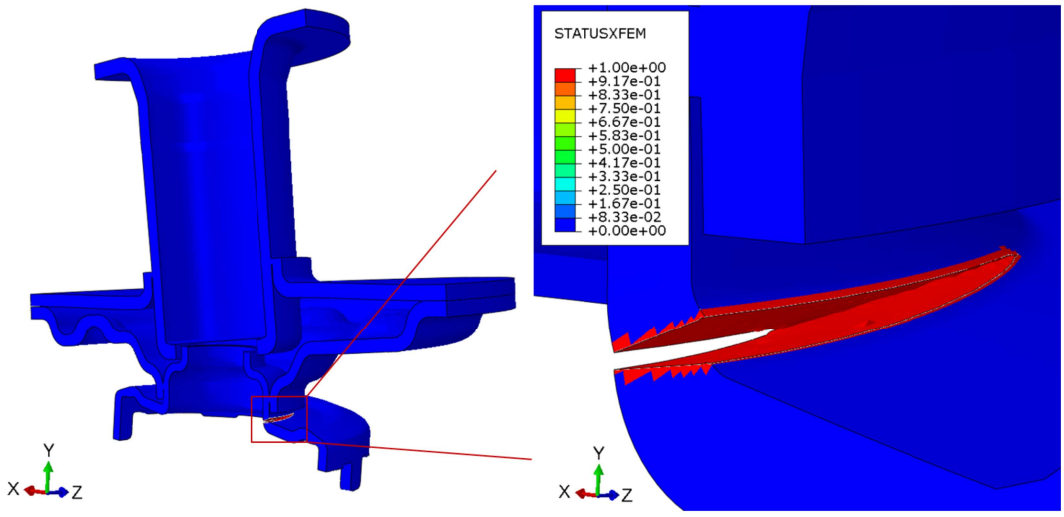

Figure 122: Left – 3D model with symmetrical boundary conditions used for the calculation of ΔK values; Right – Extended finite element method (XFEM) status variable STATUXFEM representing the crack (red area) [17O].

versus number of cracked slip band segments and the cycles for the initiation completion that have been estimated on the basis of the RdM; in this case the number of cycles equal to 8,157. For the 150 N case shown in Figure 120L, 188,480 cycles have been estimated.

The grey-coloured regions in Figure 121L represent stresses that surpass the yield stress (R_e = 294 MPa) of the investigated AISI 304 stainless steel. These regions are visualized by using a user-defined option for plotting output variable von Mises stress in the Abaqus/Visualization module. However, this does not mean that plasticity is introduced in the constitutive model; the material constitutive law is purely elastic, defined by the elastic constants for cubic crystal, as described earlier. Same as other regions of the microstructural model, the grey area behave elastically. As shown in Section 5.7, the influence of plasticity on the fatigue life curve is present but not significant and, therefore, it is not considered in this study.

Aside from different loading levels, 150, 300 and 450 N, the analysis has been performed for five different microstructures in the case of 150 N loading and three for the two other loading cases. All microstructures have been generated randomly in the same manner and have the same properties as the microstructure shown in Figure 120L.

The calculations of long crack growth are performed in accordance with LEFM principles: The crack driving force as a measure of the stresses and strains in the vicinity of the crack front is expressed using the effective stress intensity factor ΔK_{eff}, which needs to be considered under mixed-mode loading typically occurring in structural components (see Figure 122).

The values of ΔK_{eff} are calculated by using the following expression [13F]:

$$\Delta K_{eff} = \sqrt{\Delta K_I^2 + \Delta K_{II}^2 + \frac{1}{1-\upsilon}\Delta K_{III}^2} \tag{5.8}$$

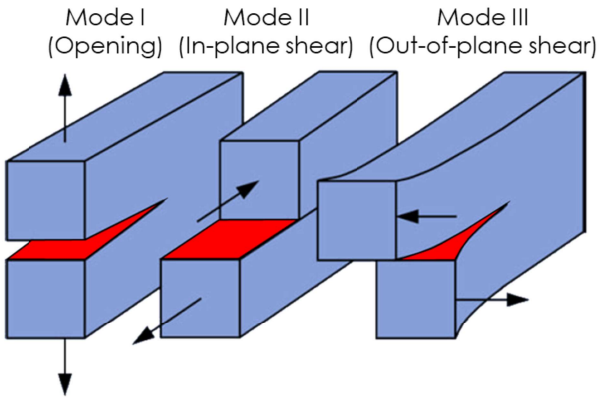

Figure 123: The three fracture modes that can occur in structural components [05A].

The component ΔK_I represents mode I (opening) stress intensity factor, ΔK_{II} represents mode II (in-plane shear) and ΔK_{III} mode III (out-of-plane or transverse shear) stress intensity factor. The three fracture modes that can occur in structural components are shown in Figure 123 [05A, 08S]. These components of the parameter ΔK have been calculated using the contour integral. For this purpose, the extended finite element method (XFEM) implemented into Abaqus [ABQ] has been applied for different stationary cracks (Figure 122).

Table 14 contains ΔK_{eff} values calculated for different crack lengths for the 150 N loading case.

Table 14: Calculated ΔK_{eff} values for different crack lengths at the 150 N loading level.

a (mm)	3.64	4.85	6.06	7.27	8.49	9.70	10.79	13.34	***14.55***
ΔK_{eff} (MPa√m)	17.80	20.96	22.65	27.28	38.51	40.89	45.93	67.36	***76.95***

Paris constants used for the AISI 304 steel are m = 3.59 and C = 1.42E-12, according to Krompholz and Ullrich [85K].

Crack front, crack angle and crack extension direction are on the other hand determined by the virtual crack extension technique, which is based on XFEM, too (Figure 124). The number of cycles needed to grow the crack to the size where final failure occurs has been estimated (as above in Section 5.1) by integrating Paris law (Eq.

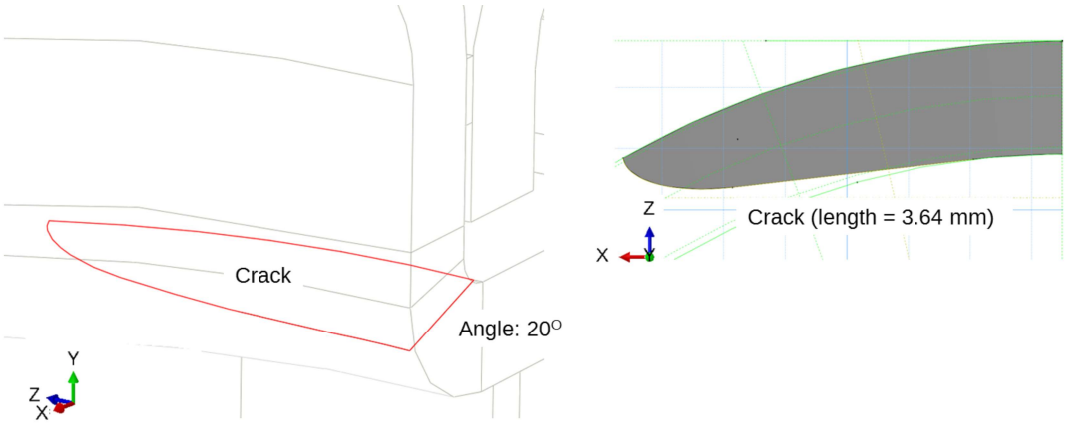

Figure 124: 3D crack front with the 20° angle in the dosing module determined by using an FEM-based crack extension technique (rendered view).

4.6, Section 4.3.5), which is based on ΔK (or in this case ΔK_{eff}) values, Table Table 14. The critical value of ΔK, K_{Ic} equal to 75 MPa$\sqrt{m}$ [85K], has been applied to determine when final failure should occur. Since K_{Ic} has been reached at a crack length of 14.55 mm for the loading level of 150 N, according to Table 14, the number of cycles N_f to propagate the crack up to failure can be easily obtained from the corresponding *a-N* diagram (see Figure Figure 125).

The initiation number of cycles N_{ini} for the 150 N loading level have been derived in previous microstructural analysis by averaging the values for five different microstructures, what resulted in 172,169 cycles (see the averaged value and scatter in Figure 126). This number of cycles is prescribed as the starting number for the long crack growth. For the present loading level of 150 N, final failure occurred after 222,000 cycles. The results are summarized in Figure 125, in the form of an *a-N* diagram.

The same procedure has been performed for the two other loading levels. Finally, the results for all investigated cases are presented in Figure 126 in the form of an *S-N* (Wöhler) diagram and, at the same place, compared with the experimental results. Figure 126 contains the lifetime results of both simulations, i.e. of short crack initiation and long crack growth that comprise the overall lifetime.

Besides the slope of the Wöhler curve, the modelling approach allowed to determine the endurance limit (F_e expressed in terms of force) as in Section 5.1. The final loading below which the infinite life has been reached is 93 N, Figure 126. Accordingly, the endurance force has been chosen to be that one, i.e. 94 N what is in relatively good agreement with the experimentally obtained endurance limit of 105 N [17O]. Based on conclusions from previous studies on the CRSS (Section 5.2) and W_c, even better agreement could be achieved by applying a higher CRSS value and a lower W_c.

Aside from that and as shown already in the case of specimen made of steel AISI 1141 (see Section 5.1), the results from Figure 126 confirm that the initiation phase

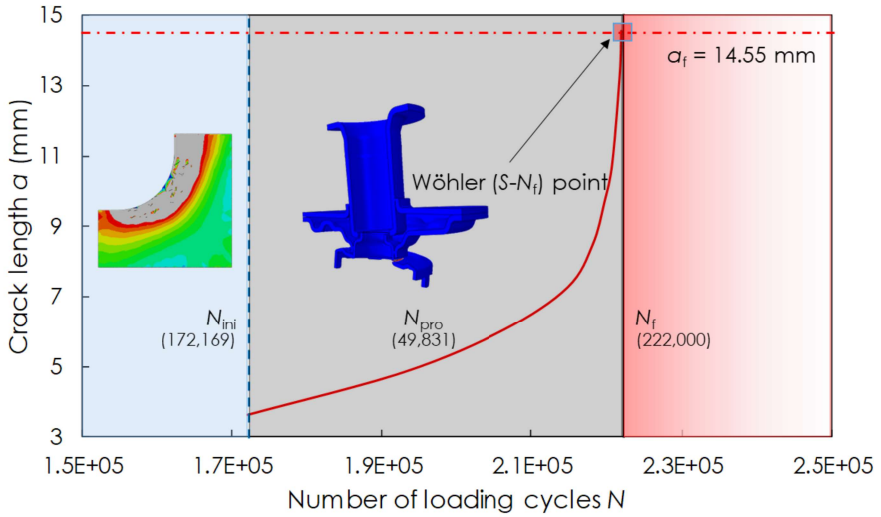

Figure 125: Dependence of the life cycles on the crack length for the 150 N loading case.

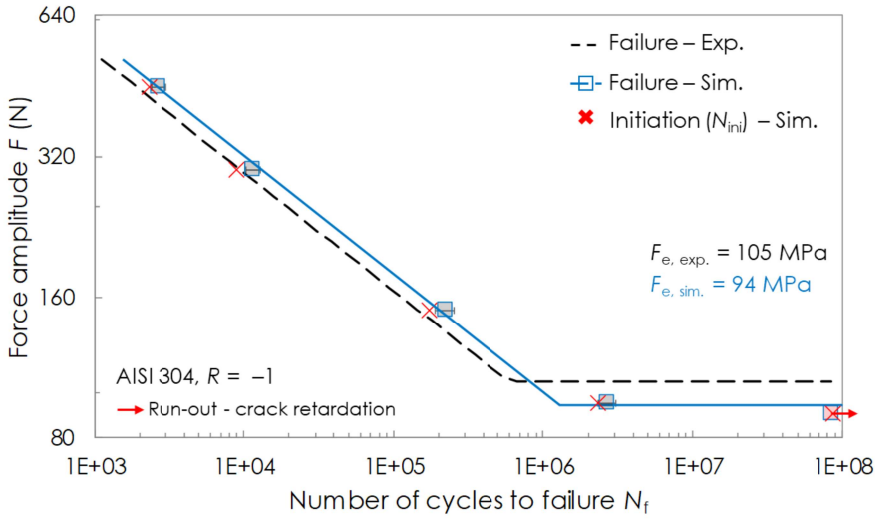

Figure 126: Numerically determined fatigue life curve for the dosing module flange (full blue line), compared with the experimentally obtained curve (dashed black line) [17O].

takes the majority of the fatigue life also in the case of the component.

Next to the study on the CRSS influence in Section 5.2.3, this was a second study where the steel AISI 304 was successfully analysed. Moreover, in these two studies different loading ratio values *R* were applied (*R* = 0 and *R* = -1, respectively), what proves the sensibility of the multiscale fatigue simulation approach to this high practically relevant influencing factor.

5.11 Determination of Paris law constants *C* and *m*

A very common and often used method for the characterization of the long crack growth is the Paris law (Eq. 5.9) which gives a relationship between the fatigue crack growth rate (FCGR) d*a*/d*N* and the stress intensity factor range Δ*K* at the crack tip during stable crack growth [04E]. A typical fatigue growth rate curve – also known as d*a*/d*N* versus Δ*K* curve – has been already shown earlier (Figure 36) and is shown again in Figure 127 due to its relevance for this study. The curve is defined by regions I, II and III. The Paris law relationship can be visualized as a straight line for the region of stable crack growth – region II [11B]. The accompanying mathematical equation contains two material parameters *C* and *m*, where *m* represents the slope of the line in Figure 127 and *C* the y-axis-intercept [88B]:

$$\frac{da}{dN} = C(\Delta K)^m \tag{5.9}$$

The crack growth rates in the region II are typically in the order of 10E-9 to 10E-6 m/cycle and correspond to stable crack growth. The constants *C* and *m* are usually determined in experiments [09N, 12C, 14A, 16U, 16N, 09Z] and depend on the material and various influencing factors such as temperature, environmental medium and *R* ratio [09N, 09Z]. The last is probably the most significant and usually results in closely

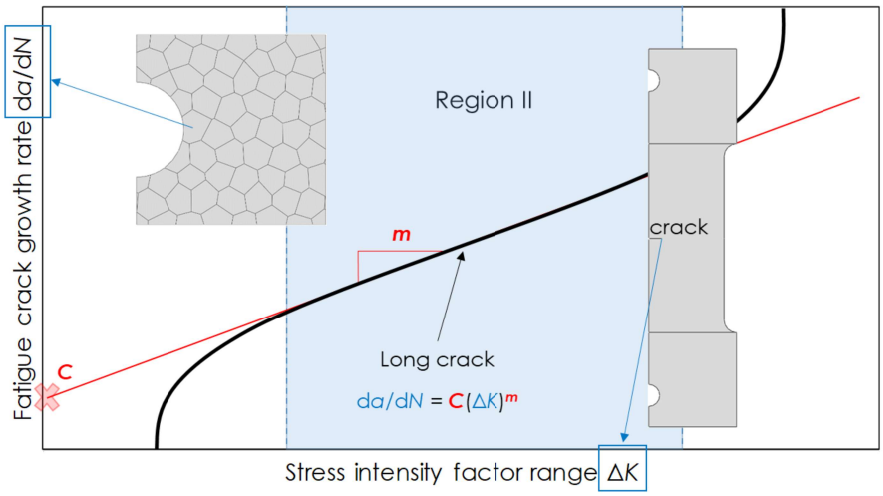

Figure 127: Typical growth behaviour of long fatigue cracks [11B] and schematic illustration of the two different approaches: a microstructure-based approach to determine the da/dN values and the fracture mechanics-based approach for the ΔK values determination.

spaced lines parallel to each other [88B]. For metals the slope *m* is typically of the order of 2 to 4 [09Z].

Since the experimental determination of the Paris law constants is typically tedious and time consuming, the objective of this study is to determine them numerically considering the influence of microstructure on the crack growth rate.

Simulations for the determination of the Paris law constants are performed by applying the same modelling framework as in previous sections. The framework contains the microstructural model that is used to calculate d*a*/d*N* at a crack tip on the basis of the Tanaka-Mura equation (Eq. 4.3, Section 4.3.1) and the macromodel that serves for the calculation of Δ*K* values on the basis of LEFM (see Section 5.1 for more details), as shown in Figure 127. In order to get the typical d*a*/d*N* versus Δ*K* diagram, d*a*/d*N* and Δ*K* parameters for six different crack lengths are determined. The constants can be then determined from the interpolated straight line, representing Region II in Figure 127 and defining the slope *m* and the y-axis-intercept *C*. The grain structure is assigned to the submodel to consider microcrack initiation processes in the vicinity of the crack tip.

Table 15: Considered structural crack lengths.

Crack designation	a_1	a_2	a_3	a_4	a_5	a_6
a (mm)	9.9	20.1	29.9	39.1	49.3	59.3

In order to accomplish the goal of the present study it was necessary to create two slightly different full-scale macromodels. Both models represent the same geometry, however, the ways of modelling the crack for determination of Δ*K* values on the one side and fatigue crack growth rate d*a*/d*N* on the other require certain adjustments at the regions of interest, i.e. on the crack-affected path. More specifically, the macromodel for the calculation of Δ*K* requires the usage of a special Abaqus technique to model the crack named as seam crack (Figure 128). A seam

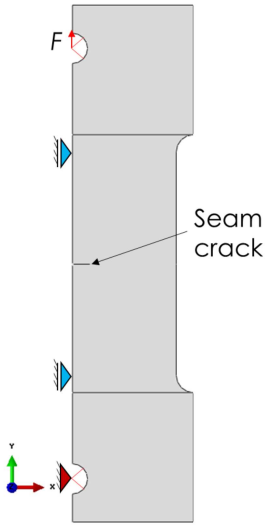

Figure 128: The half of full-scale model with applied boundary and loading conditions, and with the seam crack in the ΔK case.

defines an edge or a face in a model that is originally closed but can open as a crack during a numerical analysis [ABQ]. The macromodel (further: global model) for determination of d*a*/d*N* on the other hand needs to be geometrically adjusted to the submodel that is placed at the tip of the structural crack, as shown schematically in Figure 129. The considered structural crack lengths for the simulations are listed in Table 15.

The models were built on the basis of a specimen with a central pre-crack prepared for fatigue testing, shown in Figure 130, considered in the paper of Božić et al. [11B]. At the initial state the specimen has a notch of 0.2 mm and a pre-crack of 2*a* = 8 mm (Figure 130, A – Crack detail), which is considered in the creation of the microstructural model and accompanying global model (Figure 129).

Only half of the specimen was modelled due to symmetry with respect to the vertical y-axis. Symmetry boundary conditions fix the displacements in x-direction as

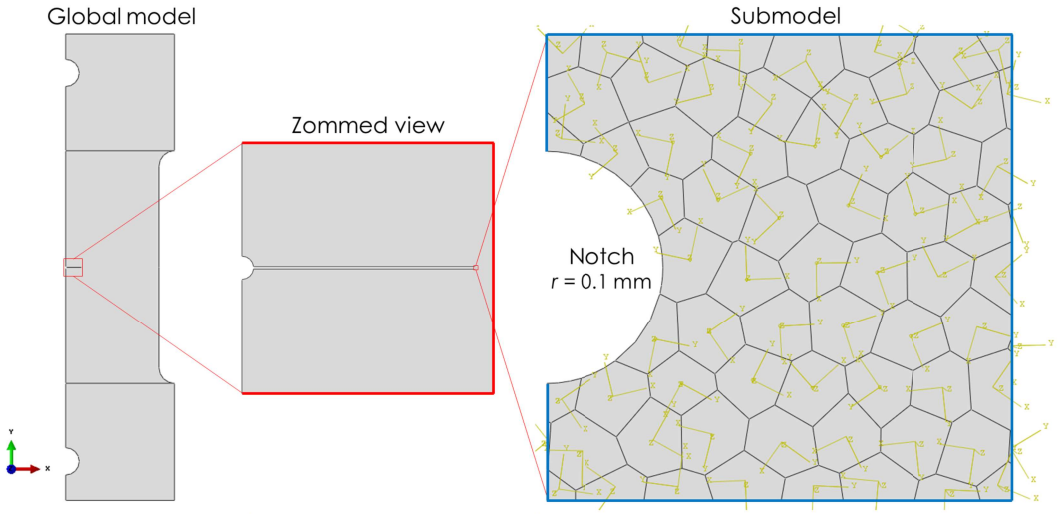

Figure 129: Geometry of the submodel containing a microstructure of the material and its location with respect to the global model.

well as rotations of any kind (Figure 128). The symmetry with respect to the x-axis is aligned with the crack and, therefore, cannot be used in either case. Namely, for ΔK determination, the applied seam cannot extend along the boundaries or edges of a part; it must be embedded within a face of a 2D part or within a cell of a solid part [ABQ]. In the other case, the used submodel (microstructural model) at the crack tip area requires the transfer of boundary conditions – in this case displacements – from both parts of the global model, as depicted by blue lines in Figure 129.

All models which are used here are built as 2D, in accordance to the geometry of the specimen and the fact that the main central part has a thickness of just 4 mm along the z-direction. The areas in the upper and lower part of the models with relatively higher thickness (54 mm) were also modelled as 2D. Those two parts are used to apply loading conditions and movement constraints, respectively, as shown in Figure 128. The thicknesses of the specimen in both regions, the central and outer, were considered by assigning plane stress thickness [ABQ] to their belonging sections.

The material behaviour is assumed to be purely linear elastic; only a small plastic zone at the crack tip is expected, therefore, no plastic material data are necessary to be used. The isotropic material data for the specimen made of conventional mild carbon steel were adopted from the study of Božić et al. [11B]. The material parameters applied to both models are: E = 206 GPa, υ = 0.3, R_e = 235 MPa and G = 80 GPa. Concerning the material description, the microstructural model requires orthotropic material data, i.e. elastic constants of cubic crystals. These constants are C_{11} = 277,307 MPa, C_{12} = 118,846 MPa and C_{44} = 80,000 MPa. Furthermore, the microstructural model enriched with the Tanaka-Mura equation requires two additional material properties, namely the critical resolved shear stress (CRSS) and the crack initiation energy (W_c). With respect to this, the following values were applied: CRSS = 117 MPa

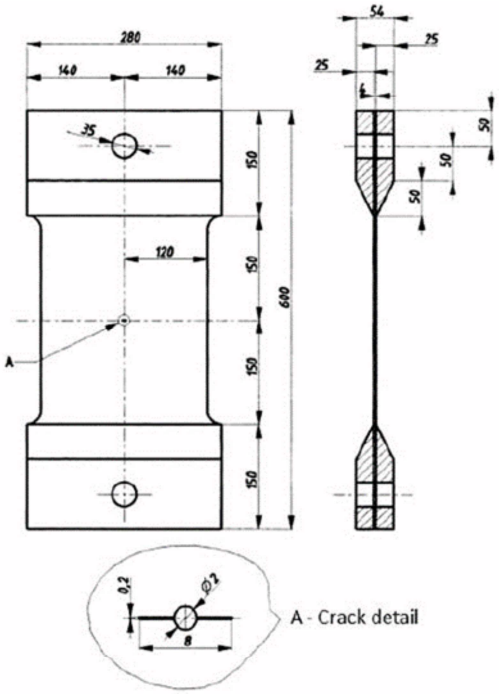

Figure 130: Geometry of the used specimen with a central pre-crack [3].

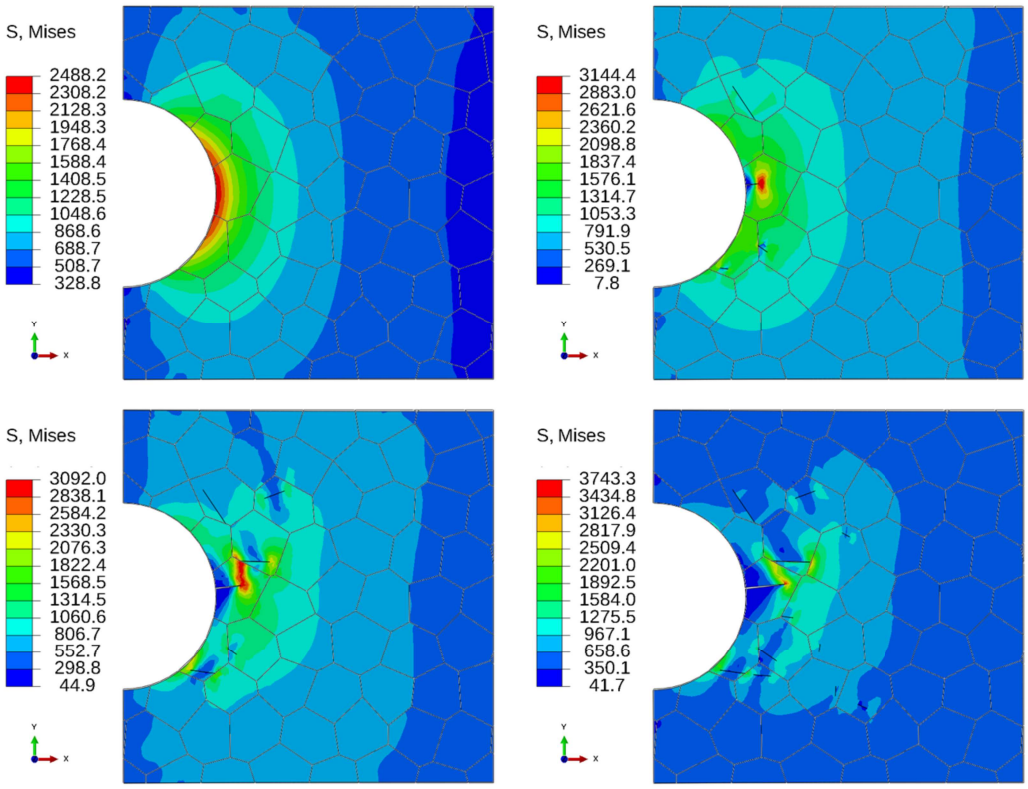

Figure 131: Image showing the microstructural model: Left (top) – In undamaged state (a = 20.1 mm); Right (top) – With 5 broken crack segments; Left (bottom) – With 15 broken crack segments; Right (bottom) – With 25 broken crack segments.

[14B] and W_c = 69 N/mm [88R]. It is opportune to introduce the experimentally obtained Paris law constants for the selected material in order to provide validation data for the numerical results that follow later; C = 1.43E-11 and m = 2.75 [11B].

As the material data, loading and boundary conditions were taken from [11B]. The testing specimen was exposed to constant amplitude cyclic tension load in a hydraulic fatigue testing machine. The load was applied to the pin which was placed in the hole in the upper part of the model while the pin in the lower hole was fixed (Figures 128 and 130). The force range and the stress ratio applied to the half-model were ΔF = 76,800 N and R = 0.0253, respectively [11B]. In contrast to the experiments, simulations on the global models were performed with static loading conditions, however, in combination with LEFM for the ΔK determination and with the Tanaka-Mura equation for the determination of da/dN.

For both models continuum plane stress 4-node bilinear elements with reduced integration and hourglass control (CPS4R) were used. In order to deal with the stress singularity at the crack tip in the case of ΔK calculation, special elements have to be used that are able to handle the infinite stresses properly. In Abaqus this is done by collapsing one side of an 8-node isoparametric element connected to the crack tip [ABQ], as already introduced in Figure 47 of Section 5.1. The submodel was very fine meshed (CPS4R elements); what in the end gave smooth stress distribution in the

undamaged as well as in the damaged submodel, as visible in Figure 131. To depict the mesh fineness, a single grain has 120 elements in average.

The submodel or microstructural model is placed right at the tip of the global model structural cracks (Table 15) where their extension is expected. The geometry of the submodel can be seen in Figure 129, as well as the location where it is placed with respect to the global model. As already mentioned, the Tanaka-Mura equation is typically used to estimate the duration of the short crack initiation stage. In this study, however, the equation is applied within the microstructural model with the aim to estimate the rate of the infinitesimal crack extension. Its size is selected to 0.4 mm x 0.4 mm including the tip of the structural crack of 0.1 mm radius, which can be identified as a notch. Moreover, the submodel takes into consideration the microstructure of the investigated material and its influence on the crack growth rate in the initial extension phase. The resulting average grain size, i.e. average slip band length is 50 µm, what is appropriate for the used material.

The von Mises stress state before the first formed crack segment is shown in Figure 131 as well as the stress states after 5, 15 and 25 broken crack segments. Those four figures show the simulation results for the crack length of 20.1 mm. Results for other considered structural cracks from Table 15 are principally similar and, therefore, not shown in the paper. Generally what happens for all considered structural cracks is that the formation of cracks in the submodel ceases after a certain number of steps – the number varies from one model setup to another. The reason for this is that grains that are favourable for cracking on the basis of the aforementioned condition fade out (see Section 4.3.2 for more details).

In order to determine the fatigue crack growth rate da/d*N*, both the cycles d*N* and the accompanying length *da* of each individual crack segment that formed in the microstructural model (Figure 131) have to be determined. The crack length d*a* can easily be quantified using the Abaqus graphical interface or can be rather gathered from output data. By taking the measured d*a* and the correlated d*N* from

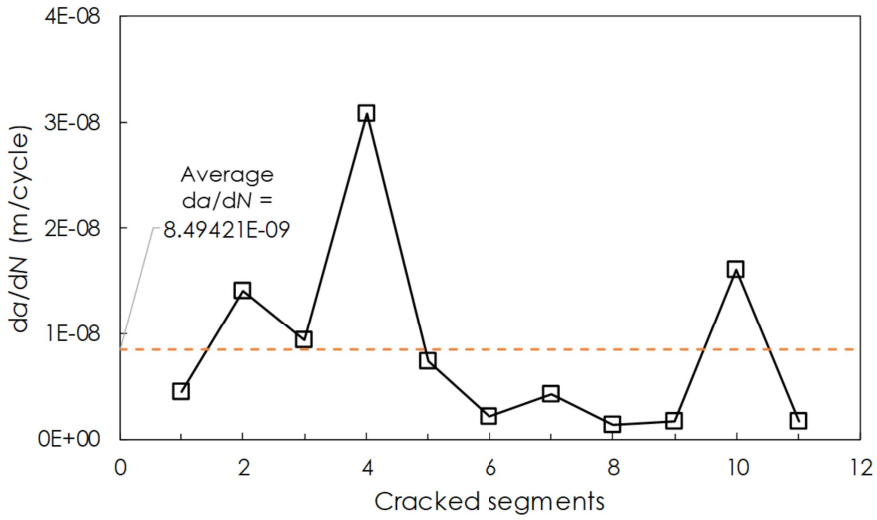

Figure 132: Crack growth rate in relation to the number of broken segments for the extension of the 20.1 mm long structural crack.

the Tanaka-Mura equation-based results, one can evaluate d*a*/d*N* for each simulation sequence. It is necessary to indicate that the common growth rate d*a*/d*N* is not a constant value, but it fluctuates as it can be seen in Figure 132 for the case of the 20.1 mm long structural crack. An assumption has been taken that the average d*a*/d*N* before the initiation stage ends or before the drop of d*a*/d*N* (see Section 4.3.4 for more details) represents the d*a*/d*N* value required for its plot versus accompanying Δ*K* values.

For the structural crack length of 20.1 mm this averaging results in d*a*/d*N* = 8.49421E-06 mm/cycle, which fits into the range of expected values according to literature [11B, 11C]. This averaged growth rate can be considered as extensional growth rate for the structural crack. The same procedure was applied for the remaining structural crack lengths from Table 15.

The Δ*K* as well as the *J*-Integral and other fracture mechanics characteristics, can be requested in Abaqus as history output data. In order to get Δ*K* values for each individual crack of six in total from Table 13, the same number of variations of the global model were modelled. By evaluating Δ*K* values for each crack length and putting the results into a common diagram the expected linear relationship between Δ*K* and the crack length *a* has been achieved (see Figure 133).

Finally, the results for d*a*/d*N* and for Δ*K* values are put into a common log-log diagram, Figure 134. The resulting six single points were interpolated with a straight line from which the material constants of Paris equation (Eq. 5.9) were determined; the slope of the line is *m* = 2.75 and the y-axis intercept *C* = 3.8E-12, agreeing quite well with the experimentally determined values of *m* = 2.75 and *C* = 1.43E-11 [11B].

To conclude, the aim of this part of the thesis was to numerically determine the Paris law material constants *C* and *m* and this was successfully accomplished by applying a two-scale modelling framework. Namely, Δ*K* values for six different structural cracks were calculated using the global model based on classical LEFM. In the second part, the fatigue crack growth rates at the tips of the same structural cracks

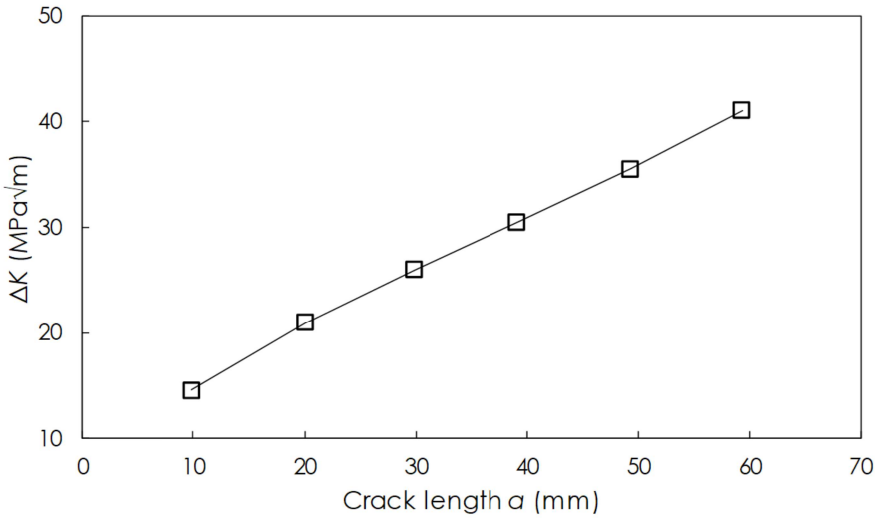

Figure 133: Calculated ΔK in dependence of the crack length (the width of the analysed specimen is 280 mm; see other dimensions in Figure 130).

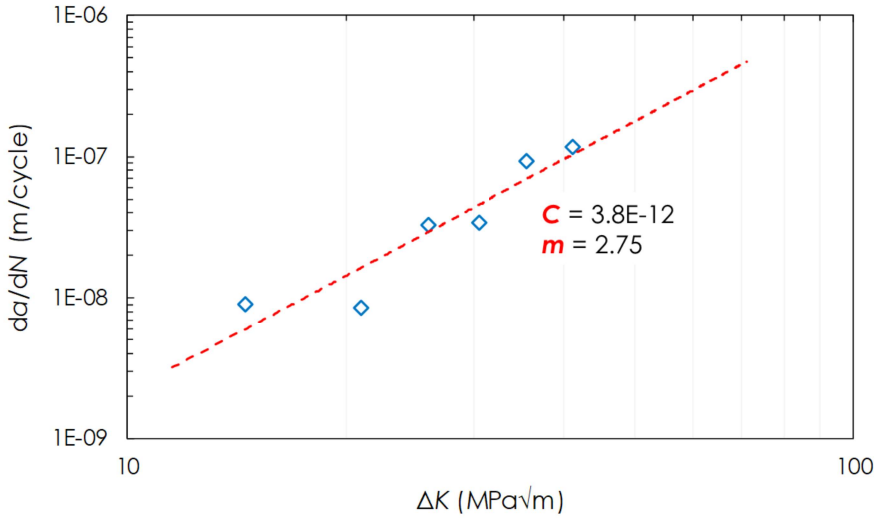

Figure 134: Extensional crack growth rate da/dN of different structural cracks vs. ΔK of the same cracks. Data are shown in log-log scale [17M].

were determined by using the microstructural model enriched by the Tanaka-Mura equation.

Since this study was the first, to the author's knowledge, attempt to determine the Paris constants in a numerical way by taking into account the microstructure of the material, and considering that the literature values of the investigated material match the numerically obtained ones quite good, the study and its working hypothesis seem to prove their worthiness. This study was part of a supervised master thesis [16S] (see Section 8.3) and was published in [17M].

6 Summary and Outlook

The work presents successful application of a multiscale materials modelling (MMM) approach developed with the aim to characterize the fatigue behaviour of metallic materials. The approach takes into account numerical analyses of the fatigue crack initiation and the fatigue crack growth stages in a sequential manner. The sequentiality means that upon determining the number of cycles needed for the fatigue crack to initiate by using the physically-based Tanaka-Mura model, the number of cycles needed for the long crack to propagate until the final failure are estimated by means of standard fracture mechanics. Another important part of this MMM approach is the determination of the critical resolved shear stress (CRSS) by using molecular dynamics (MD) or micropillar testing. The CRSS is an input parameter for the Tanaka-Mura model and among the other influencing parameters like the grain size or the crack initiation energy it proved to have the highest impact on the fatigue endurance limit. By sequentially combining the results from all the three scales it is possible to numerically predict the complete fatigue life of different specimens and components made of different metals on a physical basis, independent of empirical models.

In addition, it is now possible to investigate the material properties as well as different loading conditions in much greater depth and detail, as the multiscale model can be used to determine and quantify the influences of the nano, micro and macro levels on crack initiation and final fracture. The numerical determination of Paris law constants, and by that a reduction of the need for fatigue experiments, is one example showing importance and practical value of the multiscale fatigue modelling approach. Furthermore, the discovered relation between endurance limit and CRSS provides a facet of fatigue theory that is numerically predictive and which allows the selection of those types of materials, which are fatigue resistant. If proven with additional simulations as well as experimental studies, this relation can be used in future to estimate the endurance limits of various metallic materials just by knowing their CRSS values. The parameter studies can also serve to provide practical recommendations in terms of material optimization, e.g. covering the optimum number of grains in the thickness direction, the optimum grain orientations and/or shapes in critical areas, and even the minimum level of porosity in order to improve the fatigue strength of metallic specimens and components exposed to alternating stresses. Such findings, which aim to understand the fatigue behaviour of and, above all, to improve the life of the investigated structures, provide a basis to researchers and manufacturers for future development of new material structures.

The 3D shell model-based approach that is applied to simulate the crack initiation inside the microstructure leaves a lot of space for further development and numerous future studies. Even though these present simulations of the crack initiation phase deliver more than satisfactory results in its present state, a full 3D modelling is one of the important aspects that should be incorporated in the approach in the fu-

ture. Other aspects that should deserve a certain attention in future studies are, e.g., effects of more glide systems in grains, investigations of low-cycle fatigue, very high-cycle fatigue where grain refinement takes place before micro-cracks start nucleating, thermo-mechanical fatigue at elevated temperatures, the influence of varying loading amplitudes, consideration of plasticity by using crystal plasticity theory, an additional determination of stress-strain hysteresis loops and especially an extended study on the relation between the numerically determined endurance limits and the CRSS magnitudes of various metallic materials.

Furthermore, based on previous studies, different microstructures (with varying orientation, shape, size, etc. of the grains) yield different crack initiation lives at the same stress level, i.e., they result in scattering in the numerical fatigue life curves. Within the scope of a future work, these scattered results could be handled by means of statistical analyses. Additional mathematical models can be established, too, to evaluate the statistical analyses. This can be further used to set generally applicable rules for sizing of components or for the selection of suitable materials. Thus, engineers would be able to design components perfectly on target by selecting suitable setting levers with regard to crack initiation and fatigue fracture parameters.

7 Appendices

The appendix provides an introduction into the finite element method (FEM; Section 7.1) and theoretical background of the Tanaka-Mura (TM) model (Section 7.2), which both acted as a basis of this work.

7.1 Introduction into the FEM

The FEM is a numerical method for solving problems of engineering and mathematical physics. Typical problems of interest in these two areas that are solvable by use of the FEM include structural analysis, heat transfer, fluid flow, mass transfer, and electromagnetic analysis [12L].

The principal idea behind the FEM is the process of modelling a body by dividing it into an equivalent system of smaller bodies or units (finite elements) interconnected at points common to two or more elements (nodal points or nodes) and/or boundary lines and/or surfaces. This process is also named as discretization. Figure 135 shows an example of a mechanical part meshed by finite elements. The benefit of this approach is that instead of solving the problem for the entire body in one operation, the FEM formulates the equations for each finite element and combines them to obtain the solution of the whole body [12L].

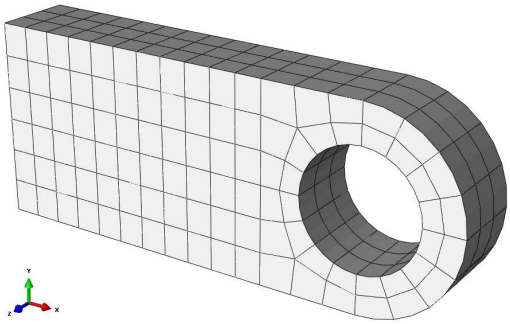

Figure 135: Connecting lug discretized with cubic finite elements.

For problems involving complicated geometries, loadings, and material properties, it is generally not possible to obtain analytical mathematical solutions. Analytical solutions are those given by a mathematical expression that yields the values of the desired unknown quantities at any location in a body (here the total structure or physical system of interest). These analytical solutions generally require the solution of ordinary or partial differential equations, which, because of the complicated geometries, loadings, and material properties, are not usually obtainable. Hence, numerical methods are necessary, such as the FEM, for acceptable solutions. The finite element formulation of the problem results in a system of simultaneous algebraic equations for the solution. These numerical methods yield approximate values of the unknowns at discrete numbers of points in the continuum. The FEM has been spe-

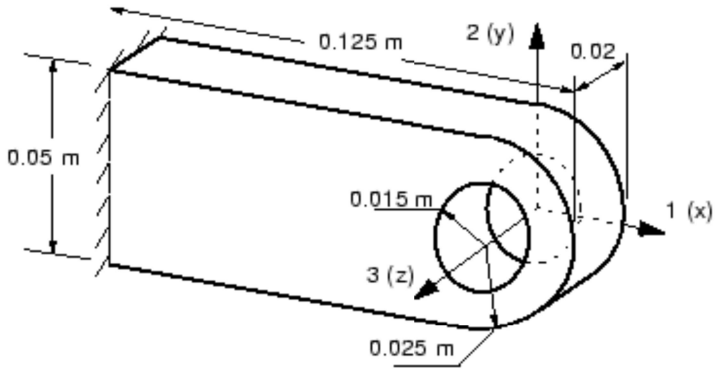

Figure 136: Geometry of the connecting lug [ABQ].

cifically applied to problems, where the governing differential equations are available [12L].

The method is illustrated with an example from the guide of FEM-based software Abaqus, shown in Figure 135. Details about the geometry of the investigated component are given in Figure 136. In this example, a connecting lug is welded firmly to a massive structure at one end. The other end contains a hole. When it is in service, a bolt is placed through the hole of the lug. An engineering problem could be in this case to determine, for example, the static deflection of the lug when a 30 kN load is applied to the bolt in the negative 2-direction [ABQ].

In order to perform such an analysis, the first step in creating the model is to define its geometry. In this case, a three-dimensional (3D) part is created, as shown in Figure 136. The next step involves defining and assigning material properties to the part. Here, for example, linear elastic properties of a steel can be prescribed by Young's modulus E = 200 GPa and Poisson's ratio υ = 0.3. Furthermore, the left-hand end of the connecting lug needs to be constrained in all three directions. This region is where the lug is attached to its parent structure. Rather than to include the complex bolt-lug interaction in the model, the user can simplify the loading boundary conditions and use a distributed pressure over the bottom half of the hole to load the connecting lug.

A further important step is the design of the finite element mesh for the lug. A possible mesh created by 3D continuum elements is shown in Figure 135 [ABQ]. The user needs to consider the type of elements that will be used before building the mesh for a particular problem. Elements that are commonly employed in practice are shown in Figure 137, including the type used in the above shown example (third element from left in the last bottom row; first order, or linear, cubic elements). The important decision regarding the mesh design is how many elements to use in the critical regions. For this example the critical region is around the circumference of the lug's hole. The influence of mesh density in a simulation result can be optionally investigated by performing a mesh convergence study.

When going from left to the right in Figure 137, shape function within each element set becomes more complex. This complexity is defined by the number of nodes on an edge of the element. As the complexity of the functions increases, the

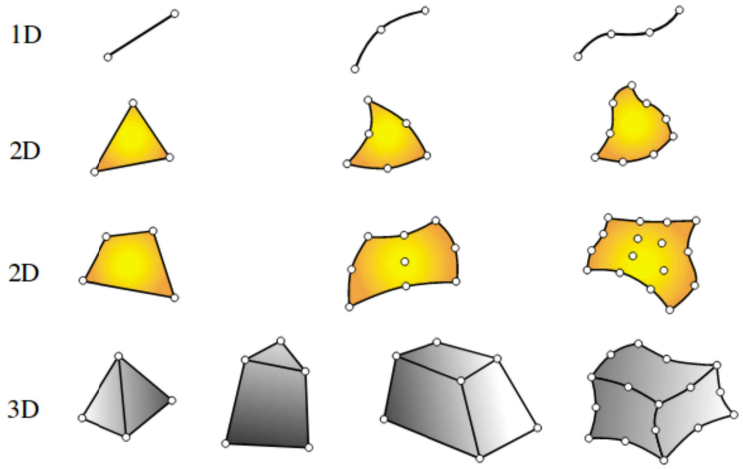

Figure 137: Typical types of finite elements [05F].

accuracy of the FEM-based analysis results increases, too. The purpose of these functions is to interpolate variables between nodes. Linear, quadratic, and cubic polynomials are frequently used functions because they are simple to work with in finite element formulations. However, trigonometric series can also be used. The FEM is one in which a continuous quantity, such as the displacements throughout the body, are approximated by a set of piecewise-continuous functions defined within each finite domain or finite element.

Another thing to consider during the FEM analysis are the output requests, i.e. the type of results required from the simulation. These can be displacements, stresses, reaction forces etc. The exemplary contour plot in Figure 138 displays the variation of an output variable, the von Mises stress, at the surface of the model. On the basis of such results, the engineer/analyst can decide whether to improve the structure in the sense of adjusting the geometry, material or some other aspect, or to leave it in the existing state. For the connecting lug example from Figure 138, 20-node hexahedral elements with reduced integration (C3D20R) are used [ABQ].

Typically, for the structural stress-analysis problem, the engineer seeks to determine displacements and stresses throughout the structure, which is subjected to ap-

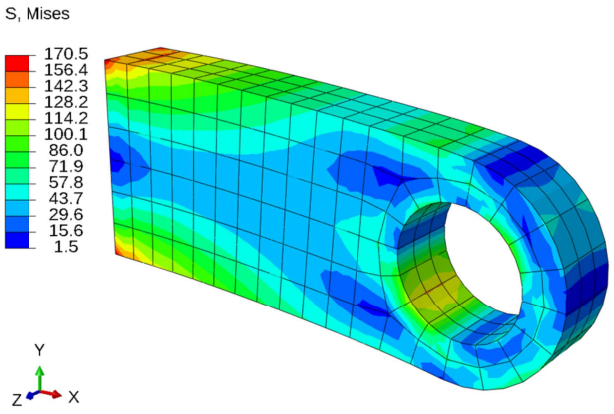

Figure 138: Stressed (von Mises) connecting lug.

plied loads. There are two general direct approaches traditionally associated with the FEM that are applied to describe equilibrium of such a structure. One approach, called the force, or flexibility, method, uses internal forces as the unknowns of the problem. The second approach, called the displacement, or stiffness, method, assumes the displacements of the nodes as the unknowns of the problem. It has been, however, shown in [74K] that, for computational purposes, the displacement (or stiffness) method is more desirable than the force method because its formulation is simpler for most structural analysis problems. Furthermore, a vast majority of general-purpose finite element programs have incorporated the displacement formulation for solving structural problems. There are other general methods available besides those two most common that can be used to develop the governing equations for both structural and non-structural problems [12L]. Further in text, only the displacement method will be explained.

As already hinted, the FEM involves modelling the structure using small interconnected elements called finite elements. A displacement function is associated with each finite element. Displacements are calculated at the nodes while all other displacements are interpolated from the shape functions. The strain (and resulting stress) is found by taking the derivative terms from the shape functions. Every interconnected element is linked, directly or indirectly, to every other element through common (or shared) interfaces, including nodes and/or boundary lines and/or surfaces. By using known stress/strain properties for the material making up the structure, e.g. Hooke's law for elastic materials (Eq. 7.1), one can determine the behaviour of a given node in terms of the properties of every other element in the structure.

$$S = Ee \tag{7.1}$$

where $\boldsymbol{S}$ is the stress, $\boldsymbol{e}$ the strain and E the Young's modulus of a material. It follows from Equation (7.1) that the stress computation procedure begins with strain computations, which are again derived from displacements. Computation of nodal displacements (and its derivative strains and stresses) and nodal forces in elements of a structure follows from the total set of algebraic equations describing the behaviour of each node, expressed in matrix notation.

$$Ku = f \tag{7.2}$$

where $\boldsymbol{K}$ is the global stiffness matrix, $\boldsymbol{u}$ the nodal displacements and f the nodal forces.

In the applications, the stress can be evaluated at the element nodal points (1, 2, 3 and 4 in Figure 139L located on the corners and possibly midpoints of the element by using the briefly explained procedure. These are called element nodal point stresses. It is, however, important to realize that the stresses computed at the same nodal point from adjacent elements will not generally be the same, since stresses are not required to be continuous in displacement-assumed finite elements. They are, therefore, in most software evaluated at the Gauss points, which are identified as 1', 2', 3' and 4' in Figure 139R, by passing their natural coordinates to the shape

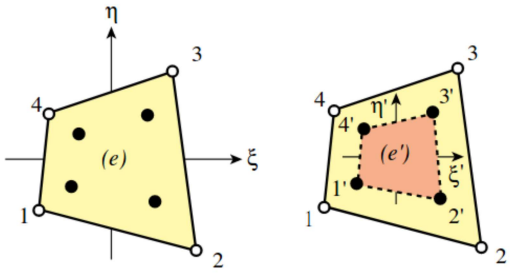

Figure 139: Gauss points inside a finite element [05F].

function of the element. Empirical evidence indicates that this approach generally delivers better stress values for quadrilateral elements whose geometry departs substantially from the rectangular shape [05F].

One significant aspect of applying the FEM is the analysis of structural integrity of a body, or in other words the analysis of damage, which reduces its integrity. To simulate damage, however, FEM solely is not able to serve the purpose. Namely, it has to be enhanced by a damage model. One such form is the extended finite element method (XFEM), which allows studying crack growth along an arbitrary, solution-dependent path without needing to remesh a model. Additionally, one can choose to study a crack that grows arbitrarily through the model or a stationary crack. Some more details about the method can be found in Section 5.10. Besides XFEM, there are other forms of introducing the damage in combination with the FEM, e.g. by applying the Roussilier model for void nucleation and growth or the TM model for fatigue crack nucleation and short crack growth (see Sections 4.3 and 5).

Concerning computer programs, or software, for the FEM, there are numerous options on the market. The interested user should carefully select a software that suits his/her needs the best. Below is a partial list of existing software for solving problems by using the FEM [12L]:

- Abaqus
- ADINA
- ANSYS
- COMSOL Multiphysics
- LS-DYNA
- MARC
- MSC NASTRAN
- HyperMesh

7.2 The Theory Behind the Tanaka-Mura Model

The slip band formed in a grain on the material surface is a preferential site for crack initiation during low strain fatigue of polycrystalline metals. The forward and reverse plastic flow within the slip band can be modeled according to the theory of Tanaka and Mura [81T, 82T] by dislocations with different signs moving on two neighboring atomic planes, and it is assumed that their movement is irreversible. Based on the model, the monotonic buildup of dislocation dipoles piled up at the grain boundary is systematically derived using the theory of continuously distributed dislocations. This buildup is associated with the progress of extrusions or intrusions. The number of stress cycles up to the nucleation of a crack of the grain size order is defined as the cycle when the stored strain energy of accumulated dislocations reaches a critical value. The relation between the nucleation life and the plastic strain range derived theoretically is in agreement with a Coffin-Manson type law [81T].

MODEL OF DAMAGE ACCUMULATION

In the fatigue of specimens of polycrystalline materials, a slip band crack is expected to nucleate in a grain (on or close to the surface) which has a high value of cyclic shear stress resolved from the applied stress on the slip plane in the slip direction. Under uniaxial stress, the resolved shear stress becomes maximum when the normal of the slip plane and the slip direction are inclined at 45° to the stress axis. Figure 140 and Figure 141 illustrate two extreme cases of the most favorably oriented grains located at the surface. Figure 140 is a section perpendicular to the specimen surface. The slip plane is perpendicular to the sheet face and the slip direction is in it. Figure 141 is a picture of the section parallel to the surface inside the specimen. The

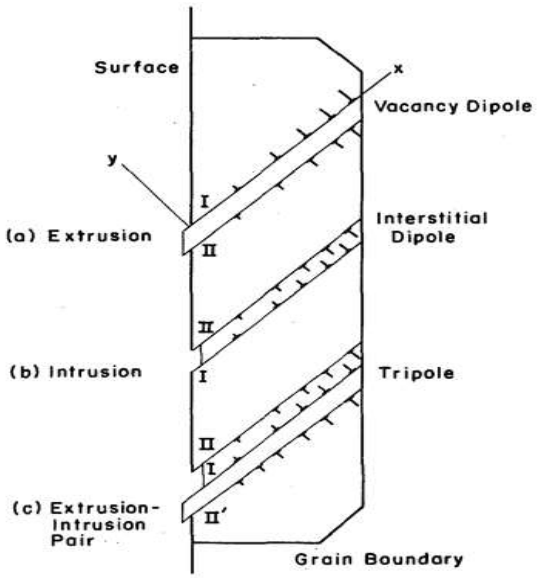

Figure 140: Dislocation motion in a most favourably oriented grain (Case A – surface grain perpendicular to the specimen surface) and the formation of extrusions and Intrusions by dislocation accumulation [81T].

slip plane is perpendicular to the specimen surface and the slip direction is at the specimen surface. In the following discussion, the former case is denoted as the case of orientation A and the latter one as that of orientation B [81T].

The dislocations generated in a most favourably oriented grain under a tensile stress are piled up against the grain boundary. As exemplarily shown in Figures 140 and 141, the dislocation pile-ups on plane I appear under such stress conditions. The difference is that the dislocations in Figure 140 are generated at the surface of the specimen and move to the interior of a grain, while those in Figure 141 are generated inside a grain and move to the grain boundary.

If the dislocations piled up on plane I would move in the opposite direction under reverse loading, there would be no accumulation of dislocations, so no fatigue fracture would take place. In the following model, it is assumed that the dislocations formed by previous forward loading are irreversible and that the reverse plastic flow is taken up by the motion of dislocations with the opposite sign on the other slip plane, which is located very close to the previous one. The dislocation pile-ups made under reverse loading are those on plane II shown in Figure 140 and Figure 141.

In the following sections, the progress of dislocation accumulation will be calculated by using the theory of continuously distributed dislocations. The calculation is carried out in two-dimensional (2D) cases and the material is assumed to be isotropic. By considering long-life fatigue, the slip band is isolated and the distance between two neighbouring planes is negligible compared with the length of pile-up planes.

The applied shear stress cycle is shown in Figure 142, where τ_1 is the maximum stress, τ_2 is the minimum stress and $\Delta\tau = \tau_1 - \tau_2$ is the applied shear stress range. The slip deformation localized within grains (crystals) under moderate and low stress levels is associated with the high-cycle fatigue (HCF) of polycrystalline metals such as low carbon steels. The localized slip band extended from $x = -a$ to a is shown in Figure 141. Points $-a$ and a are the grain boundary, where the dislocation motion is blocked. The first forward loading introduces the dislocation pile-up on plane I. The dislocation stress due to dislocation pile-up on plane I acts in the direction of the ap-

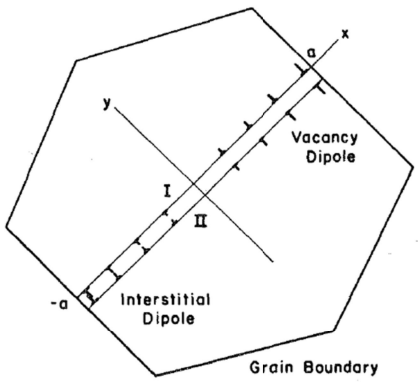

Figure 141: Dislocation motion in a most favourably oriented grain (Case B – surface grain parallel to the specimen surface) [81T].

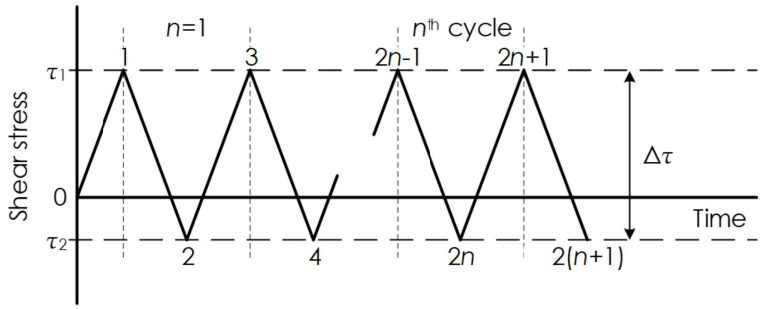

Figure 142: Applied shear stress pattern [81T].

plied forward loading and furthermore helps the negative pile-up of dislocations on plane II located very close to plane I during the following reverse loading. In the same manner, the dislocation stress due to dislocations on plane II helps the further dislocation pile-up on plane I during the following forward loading. Successive reversals of stress, therefore, give the ratcheting accumulation of plastic flow (dislocation dipoles). Although the macroscopic stress-strain hysteresis shows a saturated closed loop, the pile-up of dislocation dipoles increases monotonically by cyclic loading [82T].

DISLOCATION ACCUMULATION FOR THE CASE OF DOUBLE PILE-UP

The cyclic shear stress on the primary slip plane in a most favourably oriented grain (Figure 141) is shown in Figure 142, where τ_1 is the maximum stress and τ_2 is the minimum stress in one cycle. The Cartesian coordinates x, y are used as indicated in the figure. The grain size is 2*a* [81T].

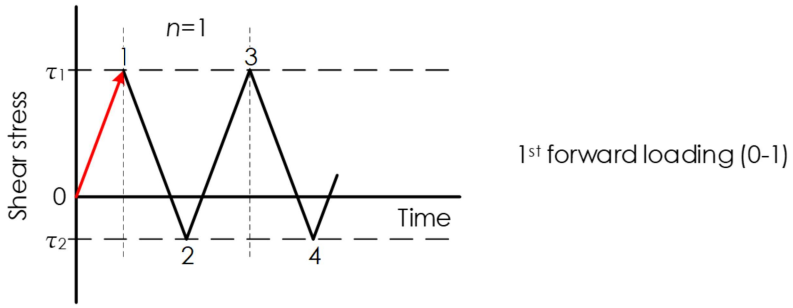

Figure 143: First forward loading.

Under the first loading of stress τ_1 (half cycle from 0 to 1 – Figure 143) greater than the critical resolved shear stress (CRSS), or in other words the frictional stress, the dislocation distribution (with density $D_I(x)$) is produced on plane I. By assuming the CRSS to be constant, the equilibrium condition of dislocations inside plane I is expressed as:

$$\tau_I^D + \tau_1 - CRSS = 0 \tag{7.3}$$

That is:

$$\tau_I^D = CRSS - \tau_1 = -(\tau_1 - CRSS) \tag{7.4}$$

where τ_I^D is the dislocation stress (back stress) which in this case acts in the direction of the applied shear stress τ_1. The CRSS acts reversely, i.e. in the direction opposite to τ_1.

According to the present model, the reverse loading from the stress τ_1 to τ_2 (e.g. from 1 to 2 – Figure 144) causes the dislocations with a negative sign piling up on plane II, instead of the dislocations moving in the reverse direction on plane I. By denoting the density of dislocations piled up on plane II as $D_{II}(x)$ and the dislocation stress due to $D_{II}(x)$ by τ_{II}^D, the equilibrium condition in plane II is expressed as:

$$\tau_{II}^D+\tau_I^D+\tau_2+CRSS=0 \tag{7.5}$$

where the dislocation stress τ_I^D due to dislocations on plane I from the previous forward loading enhances the negative pile-up of dislocations on plane II located very close to plane I during the current reverse loading. Since the distance between planes I and II is assumed to be very small compared with the pile-up length, τ_{II}^D on plane II can be regarded as the same as on plane I. Furthermore, the frictional stress CRSS is additionally acting on the motion of negative dislocations.

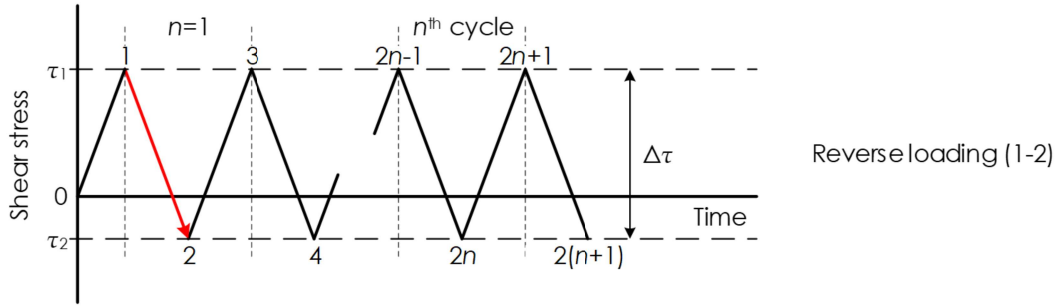

Figure 144: Reverse loading.

Substitution of Equations (7.4) into Eq. (7.5) yields the following:

$$\tau_{II}^D-(\Delta\tau-2CRSS)=0 \tag{7.6}$$

That is:

$$\tau_{II}^D=\Delta\tau-2CRSS \tag{7.7}$$

where $\Delta\tau = \tau_1 - \tau_2$. Only when $\Delta\tau$ is larger than 2CRSS the dislocations on plane II can be generated from x = 0 and pile up at $-a \le x \le a$.

The dislocation stress increment τ_i^D at the i^{th} step of forward and reverse loading processes is obtained in a similar manner:

$$\tau_i^D=(-)^i(\Delta\tau-2CRSS) \tag{7.8}$$

The index *i* takes 2*n* at the minimum stress after *n*-cycles and 2*n* + 1 at the maximum stress after *n*-cycles. This is explained graphically in Figure 145.

The stress field T_i after *n*-cycles can be given as the sum of three components: the applied stress and the internal stresses due to the dislocation pile-ups on planes I and II.

The stress field T_I due to the dislocation pile-up on plane I is given as:

$$T_I=\tau_1-CRSS+n(\Delta\tau-2CRSS) \tag{7.9}$$

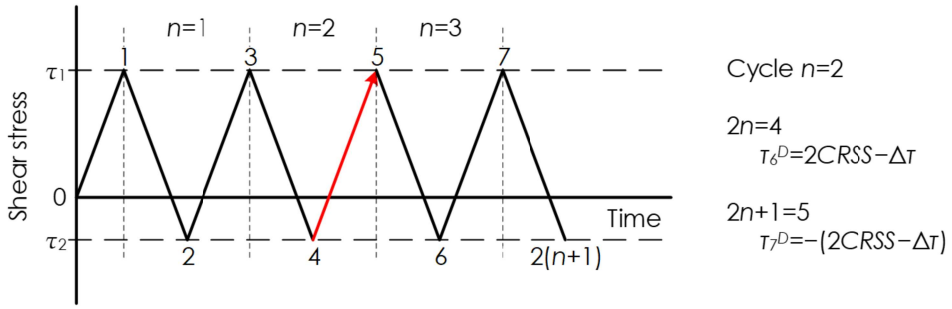

Figure 145: Forward loading.

The stress field T_{II} due to the dislocation pile-up on plane II is identical to that caused by a crack under the negative shear stress:

$$T_{II}=-n(\Delta\tau-2CRSS) \tag{7.10}$$

CRACK NUCLEATION

An embryonic crack forms in a dislocation pile-up accumulated under cyclic stress. A large tensile stress built up between two planes at the top of the pile-ups of vacancy dipoles shown in Figure 141 could become large enough to create the nucleus of a crack. The following growth of a crack embryo will take place along the slip bands. The condition of the growth of the crack embryo will be treated from the viewpoint of energy balance. If the stored strain energy due to dislocations accumulated after *n*-cycles becomes equal to the surface energy, the planes of dislocation dipoles can be transformed into a free surface.

The self-energy of dislocations introduced in the first loading (from 0 to 1 – Figure 143) [82T] can be expressed as follows:

$$U_1=\frac{\gamma_1(\tau_1-CRSS)}{2} \tag{7.11}$$

where the plastic displacement γ_1 in $-a \le x \le a$ is equal to:

$$\gamma_1=\frac{(\tau_1-CRSS)ba^2}{2A} \tag{7.12}$$

the domain of the dislocation distribution in the case B (Figure 141) between $-a < x < a$:

$$A=\frac{Gb}{2\pi(1-\upsilon)} \tag{7.13}$$

b is the Burgers vector, *G* the shear modulus, and υ the Poisson's ratio.

From Equations (7.11), (7.12) and (7.13), the following expression can be derived:

$$U_1 = \frac{(\tau_1 - CRSS)^2 \pi a^2 (1-\upsilon)}{2G} \tag{7.14}$$

which obeys the formulation of mechanics developed using energy that states that work, a function of energy, is force times distance.

The increment of the self-energy ΔU per half cycle (from e.g. 2 to 3 in Figure 144) has the same form in each load reversal and is given by substituting $\Delta\tau = \tau_1 - \tau_2$ and the 2CRSS in places of τ_1 and the CRSS in Equation (7.14), respectively [82T]:

$$\Delta U = \frac{(\Delta\tau - 2CRSS)^2 \pi a^2 (1-\upsilon)}{2G} \tag{7.15}$$

The total amount of the self-energy stored after n cycles is given as [82T]:

$$\sum_{i=1}^{2n} U_i = U_1 + 2n\Delta U \tag{7.16}$$

where U_i is the increment of the self-energy stored in the i^{th} stage of stress reversal.

For a long-life fatigue, the first term in the above equation is negligible compared with the second term. According to Tanaka and Mura [81T, 82T], the crack can nucleate on the slip band when the following energy condition is satisfied:

$$2n\Delta U = 2(2a)W_c = 4aW_c \tag{7.17}$$

The condition is valid for the case shown in Figure 141 with the pile-up length $2a$. The value of W_c is the specific fracture energy per a unit area along the slip band, or in other words the crack initiation energy.

From Equations (7.16) and (7.17), the following life law can be derived:

$$n = \frac{4GW_c}{\pi a(1-\upsilon)(\Delta\tau - 2CRSS)^2} \tag{7.18}$$

where n is defined as the number of stress cycles required for the crack nucleation.

By taking into account that the grain size is $d = 2a$ and by replacing n by N_g, the life law based on the theory of Tanaka and Mura takes its final form:

$$N_g = \frac{8GW_c}{\pi d(1-\upsilon)(\Delta\tau - 2CRSS)^2} \tag{7.19}$$

The above equation is of the Petch-type when the crack initiation life is fixed. It is also found that Equation (7.19) is equivalent to the Coffin-Manson law when $\Delta\tau$ is expressed in terms of the plastic strain range $\Delta\gamma$. More details on the derivation of the Tanaka-Mura model (Eq. 7.19), can be found in [81T] and in [82T].

8 List of Publications and Conference Contributions

8.1 Journal Publications

[11B [R]] Božić, Ž.; Mlikota, M. & Schmauder, S. (**2011**), 'Application of the ΔK, ΔJ and ΔCTOD parameters in fatigue crack growth modelling', *Technical Gazette* 18(3), 459-466.
http://hrcak.srce.hr/file/107024

[11C [R]] Božić, Ž.; Schmauder, S. & Mlikota, M. (**2011**), 'Fatigue growth models for multiple long cracks in plates under cyclic tension based on ΔK_I, ΔJ-integral and ΔCTOD parameter', *Key Engineering Materials* 488-489, 525-528.
http://www.scientific.net/KEM.488-489.525

[14B [R]] Božić, Ž.; Schmauder, S.; Mlikota, M. & Hummel, M. (**2014**), 'Multiscale fatigue crack growth modelling for welded stiffened panels', *Fatigue & Fracture of Engineering Materials & Structures* 37(9), 1043-1054.
https://onlinelibrary.wiley.com/doi/10.1111/ffe.12189

[15A] Claus, D.; Schumacher, P. M.; Wilke, M.; Mlikota, M.; Weber, U.; Schmauder, S.; Schierbaum, N.; Schäffer, T. E.; Wittmüß, P.; Teutsch, T.; Tarin, C.; Hoffmann, S.; Brucker, S.; Mischinger, J.; Schwentner, C.; Stenzl, A. & Osten, W. (**2015**), 'Intraoperative model based identification of tissue properties based on multimodal and multiscale measurements', *SPIE Conference Proceedings* 9328, 932805-932805-5.
http://proceedings.spiedigitallibrary.org/proceeding.aspx?articleid=2194741

[15B] Claus, D.; Schumacher, P. M.; Labitzke, T.; Mlikota, M.; Weber, U.; Schmauder, S.; Schierbaum, N.; Schäffer, T. E.; Wittmüß, P.; Teutsch, T.; Tarin, C.; Hoffmann, S.; Taran, F. A.; Brucker, S.; Mischinger, J.; Stenzel, A. & Osten, W. (**2015**), 'Intraoperative model based identification of tissue properties using a multimodal and multiscale elastographic measurement approach', *SPIE Conference Proceedings* 9540, 95400M-95400M-6.
http://proceedings.spiedigitallibrary.org/proceeding.aspx?articleid=2397360

[15D [R]] Mlikota, M.; Schmauder, S. & Weber, U. (**2015**), 'Multiscale simulation of overload effects on fatigue crack initiation in metallic materials', *DVM Report* / Bruchvorgänge und Bauteilsicherheit.

[15E] Mlikota, M.; Schmauder, S.; Weber, U.; Mitevski, B. & Weiß, S. (**2015**), Multiscale and multidisciplinary analysis of deformation and damage in the case of oligocrystalline structures, in Jiamei Deng & Qingjun Liu, ed., '*Proceedings of the 2015 International Conference on CSET & MSBE*', World Scientific, Hong Kong, pp. 113-118.
http://www.worldscientific.com/doi/abs/10.1142/9789814651011_0017

[R] Work-related publications and conference contributions (abbreviations in bold).

[16Z R] Zhang, Z.; Hu, Z.; Schmauder, S.; Mlikota, M. & Fan, K. (**2016**), 'Low-cycle fatigue properties of P92 ferritic-martensitic steel at elevated temperature', *Journal of Materials Engineering and Performance* 25(4), 1650-1662. http://link.springer.com/article/10.1007/s11665-016-1977-8

[17C] Claus, D.; Mlikota, M.; Geibel, J.; Reichenbach, T.; Pedrini, G.; Mischinger, J.; Schmauder, S. & Osten, W. (**2017**), 'Large-field-of-view optical elastography using digital image correlation for biological soft tissue investigation', *Journal of Medical Imaging* 4(1), 014505. https://doi.org/10.1117/1.JMI.4.1.014505

[17L R] Mlikota, M.; Schmauder, S.; Božić, Ž. & Hummel, M. (**2017**), 'Modelling of overload effects on fatigue crack initiation in case of carbon steel', *Fatigue & Fracture of Engineering Materials & Structures* 40(8), 1182-1190. http://onlinelibrary.wiley.com/doi/10.1111/ffe.12598/abstract

[17M R] Mlikota, M.; Staib, S.; Schmauder, S. & Božić, Ž. (**2017**), 'Numerical determination of Paris law constants for carbon steel using a two-scale model', *Journal of Physics*: *Conference Series* 843(1), 012042. https://doi.org/10.1088/1742-6596/843/1/012042

[17O R] Mlikota, M. & Schmauder, S. (**2017**), 'Numerical determination of component Wöhler curve', *DVM Report / Anwendungsspezifische Werkstoffgesetze für die Bauteilsimulation* 1684, 111-124.

[18B R] Božić, Ž.; Schmauder, S.; Mlikota, M. & Hummel, M. / Schmauder, S.; Chen, C.-S.; Chawla, K. K.; Chawla, N.; Chen, W. & Kagawa, Y., ed., (**2018**), Multiscale fatigue crack growth modeling for welded stiffened panels, Springer Singapore, pp. 1-21. https://doi.org/10.1007/978-981-10-6855-3_73-1

[18M R] Mlikota, M.; Schmauder, S. & Božić, Ž. (**2018**), 'Calculation of the Wöhler (*S-N*) curve using a two-scale model', *International Journal of Fatigue* 114, 289-297. https://doi.org/10.1016/j.ijfatigue.2018.03.018

[18L R] Mlikota, M.; Schmauder S. (**2018**), 'On the critical resolved shear stress and its importance in the fatigue performance of steels and other metals with different crystallographic structures', *Metals* 8(11), 883. https://doi.org/10.3390/met8110883

[19M R] Mlikota, M.; Schmauder S. (**2019**), 'Virtual testing of plasticity effects on fatigue crack initiation', *Advances in Engineering Materials, Structures and Systems: Innovations, Mechanics and Applications*, 587-592.

[20L R] Mlikota, M. & Schmauder, S. (**2020**), 'A newly discovered relation between the critical resolved shear stress and the fatigue endurance limit for metallic materials', *Metals* 10(6), 803.

8.2 Conference Talks and Poster Contributions

Numerical analysis of fatigue crack initiation and growth. DGM-Arbeitskreis Mikrostrukturmechanik: Skalenübergreifende Simulation der Materialermüdung, Osnabrück, Germany, 26 June **2013**.

Multiscale and multidisciplinary analysis of deformation and damage in the case of oligocrystalline structures. International Conference on Mechanical and Automation Engineering (MAEE2015), Hong Kong, China, 30-31 May **2015**.

Multiscale modelling of overload effects on fatigue crack initiation in case of carbon steel. 16th International Conference on New Trends in Fatigue and Fracture (NT2F16), Dubrovnik, Croatia, 24-27 May **2016**.

Numerical determination of Paris law constants for carbon steel using a two-scale model. 6th International Conference on Fracture Fatigue and Wear FFW 2017, Porto, Portugal, 26-27 July **2017**.

Fatigue life prediction of a flat steel specimen using a two-scale numerical model. IUTAM Symposium on Multi-scale Fatigue, Fracture & Damage of Materials in Harsh Environments, Galway, Ireland, 28 August – 1 September **2017**.

Advanced modelling of metal fatigue and its applications. DVM-Workshop: Numerische Simulation in der Betriebsfestigkeit, Bremerhaven, Germany, 24-25 January **2018**.

Numerical investigation of the difference in S-N-curves of FCC and BCC materials (Poster). 12th International Fatigue Congress: Fatigue 2018, Poitiers, France, 27 May – 1 June **2018**.

Advanced modelling of metal fatigue and its applications. International Conference on Fatigue Damage of Structural Materials, Hyannis, USA, 16-21 September **2018**.

Advanced multiscale modelling and simulation of metal fatigue and its applications. 11th International Conference on Structural Integrity and Failure, Perth, Australia, 03-06 December **2018**.

Influence of local residual stresses on fatigue crack initiation. 3rd International Conference on Structural Integrity and Durability (ICSID2019), Dubrovnik, Croatia, 03-07 June **2019**.

Simulation of the influence of microstructural effects and different stress conditions on fatigue crack initiation. 25th International Conference – Fracture and Structural Integrity, Catania, Italy, 09-14 June **2019**.

Advanced modelling and simulation of fatigue in the case of oligocrystalline. International Conference on Stents Materials, Mechanics and Manufacturing (ICS3M 2019), London, GB, 15-17 July **2019**.

8.3 Work-related Supervised Student Works

Master thesis: Regler, C. (**2015**), '*Einfluss verschiedener Elemente auf die Lebensdauer der Kokillengusslegierung AlCu4TiZr*', IMWF, University of Stuttgart / Volkswagen AG.

Master thesis: Rahman, M. M. (**2015**), '*Sensitivity analysis of solder fatigue for automotive cameras*', IMWF, University of Stuttgart / Robert Bosch GmbH.

Master thesis: Jamil, A. Y. (**2015**), '*Experimental and XFEM-based analysis of the fracture mechanical behaviour of materials for integrated circuit packaging*', IMWF, University of Stuttgart / Robert Bosch GmbH.

Internship: Sanghavi, C. Y. (**2016**), '*Fatigue crack propagation in dual phase steel*', IMWF, University of Stuttgart.

Master thesis: Nijagal, V. (**2016**), '*Fatigue simulation of plastic parts of Bosch diesel gasoline systems*', IMWF, University of Stuttgart / Robert Bosch GmbH.

Student research project: Staib, S. (**2016**), '*Determination of Paris Law constants C and m using the micromechanical coupled modelling approach*', IMWF, University of Stuttgart.

Master thesis: Schmiedt, M. (**2017**), '*Numerical modelling of the influence of mechanically and thermally induced residual stresses on the fatigue lifetime*', IMWF, University of Stuttgart.

9 List of Figures

10 List of Tables

11 Bibliography

[ABQ] Smith, M. (**2018**), *Abaqus Documentation*, Simulia.

[ATM] 'ASTM Standards', American Society for Testing and Materials (ASTM), Philadelphia.

[00K] Khireddine, D. & Khireddine, M.-H. (**2000**), 'Low cycle fatigue behaviour of an aluminium alloy with small shearable precipitates: Effect of surface coating', *International Journal of Fatigue* 22(7), 585-591.

[00Z] Zhai, T.; Wilkinson, A. & Martin, J. (**2000**), 'A crystallographic mechanism for fatigue crack propagation through grain boundaries ', *Acta Materialia* 48(20), 4917-4927.

[01K] Kujawski, D. (**2001**), 'Correlation of long- and physically short-cracks growth in aluminum alloys', *Engineering Fracture Mechanics* 68(12), 1357-1369.

[01Z] Zhuang, W. Z. & Halford, G. R. (**2001**), 'Investigation of residual stress relaxation under cyclic load', *International Journal of Fatigue* 23, 31-37.

[02T] Torres, M. & Voorwald, H. (**2002**), 'An evaluation of shot peening, residual stress and stress relaxation on the fatigue life of AISI 4340 steel', *International Journal of Fatigue* 24(8), 877-886.

[03C] Campos, M.; Bautista, A.; Caceres, D.; Abenojar, J. & Torralba, J. (**2003**), 'Study of the interfaces between austenite and ferrite grains in P/M duplex stainless steels', *Journal of the European Ceramic Society* 23(15), 2813-2819.

[03E] Ewing, J. A. & Humfrey, J. C. W. (**1903**), 'The fracture of metals under repeated alternations of stress', *Philosophical Transactions of the Royal Society of London. Series A, Containing Papers of a Mathematical or Physical Character* 200(321-330), 241-250.

[03F] Friak, M.; Sobll, M. & Vitek, V. (**2003**), 'Ab initio calculation of tensile strength in iron', *Philosophical Magazine* 83(31-34), 3529-3537.

[03H] Chapetti, M. D. (**2003**), 'Fatigue propagation threshold of short cracks under constant amplitude loading', *International Journal of Fatigue* 25(12), 1319-1326.

[03L] Ludwig, W.; Buffiere, J.-Y.; Savelli, S. & Cloetens, P. (**2003**), 'Study of the interaction of a short fatigue crack with grain boundaries in a cast Al alloy using X-ray microtomography ', *Acta Materialia* 51(3), 585-598.

[03M] Makkonen, M. (**2003**), 'Notch size effects in the fatigue limit of steel', *International Journal of Fatigue* 25(1), 17-26.

[03R] Maruno, Y.; Miyahara, H.; Noguchi, H. & Ogi, K. (**2003**), 'Notch size effects in the fatigue characteristics of Al-Si-Cu-Mg cast alloy', *Journal of the Japan Institute of Metals* 67(7), 331-335.

[03Q] Qiao, Y. & Argon, A. (**2003**), 'Cleavage cracking resistance of high angle grain boundaries in Fe-3%Si alloy', *Mechanics of Materials* 35(3-6), 313-331.

[03S] Schijve, J. (**2003**), 'Fatigue of structures and materials in the 20th century and the state of the art', *International Journal of Fatigue* 25(8), 679-702.

[04E] Esslinger, V.; Kieselbach, R.; Koller, R. & Weisse, B. (**2004**), 'The railway accident of Eschede - technical background', *Engineering Failure Analysis* 11(4), 515-535.

[04F] Fatemi, A.; Zeng, Z. & Plaseied, A. (**2004**), 'Fatigue behavior and life predictions of notched specimens made of QT and forged microalloyed steels', *International Journal of Fatigue* 26(6), 663-672.

[04T] Takaki, S.; Fujioka, M.; Aihara, S.; Nagataki, Y.; Yamashita, T.; Sano, N.; Adachi, Y.; Nomura, M. & Yaguchi, H. (2004), 'Effect of copper on tensile properties and grain-refinement of steel and its relation to precipitation behavior', *Materials Transactions* 45(7), 2239-2244.

[04U] Uchic, M. D.; Dimiduk, D. M.; Florando, J. N. & Nix, W. D. (**2004**), 'Sample dimensions influence strength and crystal plasticity', *Science* 305(5686), 986-989.

[05A] Anderson, T. L. (**2005**), *Fracture mechanics: Fundamentals and applications, Third edition*, Taylor & Francis Group, Boca Raton.

[05D] Dimiduk, D.; Uchic, M. & Parthasarathy, T. (**2005**), 'Size-affected single-slip behavior of pure nickel microcrystals', *Acta Materialia* 53(15), 4065-4077.

[05F] Felippa, C. (**2005**), FEM modeling: Introduction, 'Introduction to finite element methods', University of Colorado at Boulder.

[05G] Greer, J. R.; Oliver, W. C. & Nix, W. D. (**2005**), 'Size dependence of mechanical properties of gold at the micron scale in the absence of strain gradients', *Acta Materialia* 53(6), 1821-1830.

[05K] Kohler, C.; Kizler, P. & Schmauder, S. (**2005**), 'Atomistic simulation of precipitation hardening in α-iron: influence of precipitate shape and chemical composition', *Modelling and Simulation in Materials Science and Engineering* 13(1), 35-45.

[05O] Materials Engineering (**2005**), 'Bicycle crank failure II', The Open University, Online, Milton Keynes.
http://technology.open.ac.uk/materials/mem/mem_ccf4.htm

[05U] Uchic, M. D. & Dimiduk, D. M. (**2005**), 'A methodology to investigate size scale effects in crystalline plasticity using uniaxial compression testing', *Materials Science and Engineering: A* 400-401, 268-278.

[06B] Brückner-Foit, A. & Huang, X. (**2006**), 'Numerical simulation of micro-crack initiation of martensitic steel under fatigue loading', *International Journal of Fatigue* 28(9), 963-971.

[06D] Dimiduk, D. M.; Woodward, C.; LeSar, R. & Uchic, M. D. (**2006**), 'Scale-free intermittent flow in crystal plasticity', *Science* 312(5777), 1188-1190.

[06E] Düber, O.; Künkler, B.; Krupp, U.; Christ, H.-J. & Fritzen, C.-P. (**2006**), 'Experimental characterization and two-dimensional simulation of short-crack propagation in an austenitic–ferritic duplex steel', *International Journal of Fatigue* 28(9), 983-992.

[06G] Greer, J. R. & Nix, W. D. (**2006**), 'Nanoscale gold pillars strengthened through dislocation starvation', *Physical Review B* 73, 245410.

[06J] Johnston, S. R.; Potirniche, G. P.; Daniewicz, S. R. & Horstmeyer, M. F. (**2006**), 'Three-dimensional finite element simulations of microstructurally small fatigue crack growth in 7075 aluminium alloy', *Fatigue & Fracture of Engineering Materials & Structures* 29(8), 597-605.

[06K] Kiener, D.; Motz, C.; Schöberl, T.; Jenko, M. & Dehm, G. (**2006**), 'Determination of mechanical properties of copper at the micron scale', *Advanced Engineering Materials* 8(11), 1119-1125.

[06M] Mughrabi, H. (**2006**), 'Specific features and mechanisms of fatigue in the ultrahigh-cycle regime', *International Journal of Fatigue* 28(11), 1501-1508.

[07C] Csikor, F. F.; Motz, C.; Weygand, D.; Zaiser, M. & Zapperi, S. (**2007**), 'Dislocation avalanches, strain bursts, and the problem of plastic forming at the micrometer scale', *Science* 318(5848), 251-254.

[07F] Fajdiga, G.; Ren, Z. & Kramar, J. (**2007**), 'Comparison of virtual crack extension and strain energy density methods applied to contact surface crack growth', *Engineering Fracture Mechanics* 74(17), 2721-2734.

[07G] Huang, X.; Brueckner-Foit, A.; Besel, M. & Motoyashiki, Y. (**2007**), 'Simplified three-dimensional model for fatigue crack initiation', *Engineering Fracture Mechanics* 74(18), 2981-2991.

[07H] Hwang, C. & Ingraffea, A. (**2007**), 'Virtual crack extension method for calculating the second order derivatives of energy release rates for multiply cracked systems', *Engineering Fracture Mechanics* 74(9), 1468-1487.

[07J] Jiang, X.; Man, C.-S.; Shepard, M. & Zhai, T. (**2007**), 'Effects of shot-peening and re-shot-peening on four-point bend fatigue behavior of Ti-6Al-4V', *Materials Science and Engineering: A* 468-470, 137-143.

[07K] Kiener, D.; Motz, C.; Rester, M.; Jenko, M. & Dehm, G. (**2007**), 'FIB damage of Cu and possible consequences for miniaturized mechanical tests', *Materials Science and Engineering: A* 459(1), 262-272.

[07L] Li, J. X. (**2007**), 'The effect of microstructure and texture on high cycle fatigue properties of Al alloys', Doctoral thesis, University of Kentucky.

[07P] Parthasarathy, T. A.; Rao, S. I.; Dimiduk, D. M.; Uchic, M. D. & Trinkle, D. R. (**2007**), 'Contribution to size effect of yield strength from the stochastics of dislocation source lengths in finite samples', *Scripta Materialia* 56(4), 313-316.

[07R] Rao, S. I.; Dimiduk, D. M.; Tang, M.; Uchic, M. D.; Parthasarathy, T. A. & Woodward, C. (**2007**), 'Estimating the strength of single-ended dislocation sources in micron-sized single crystals', *Philosophical Magazine* 87(30), 4777-4794.

[08B] Bitzek, E.; Derlet, P.; Anderson, P. & Swygenhoven, H. V. (**2008**), 'The stress-strain response of nanocrystalline metals: A statistical analysis of atomistic simulations', *Acta Materialia* 56(17), 4846-4857.

[08C] Brinckmann, S.; Kim, J.-Y. & Greer, J. R. (**2008**), 'Fundamental differences in mechanical behavior between two types of crystals at the nanoscale', *Physical Review Letters* 100, 155502.

[08E] Etou, M.; Fukushima, S.; Sasaki, T.; Haraguchi, Y.; Miyata, K.; Wakita, M.; Tomida, T.; Imai, N.; Yoshida, M. & Okada, Y. (**2008**), 'Super short interval multi-pass rolling process for ultrafine-grained hot strip', *ISIJ International* 48(8), 1142-1147.

[08G] Greer, J. R.; Weinberger, C. R. & Cai, W. (**2008**), 'Comparing the strength of f.c.c. and b.c.c. sub-micrometer pillars: Compression experiments and dislocation dynamics simulations', *Materials Science and Engineering: A* 493(1), 21-25.

[08K] Kanemaru, T.; Kawagoishi, N.; Kondo, E.; Wang, Q. Y. & Ohzono, Y. (**2008**), Influence of grain size on notch sensitivities in fatigue of carbon steel, *in* 'Advances in Fracture and Damage Mechanics VII', Trans Tech Publications, 197-200.

[08M] McEvily, A. J.; Endo, M.; Yamashita, K.; Ishihara, S. & Matsunaga, H. (**2008**), 'Fatigue notch sensitivity and the notch size effect', *International Journal of Fatigue* 30(12), 2087-2093.

[08N] Norfleet, D.; Dimiduk, D.; Polasik, S.; Uchic, M. & Mills, M. (**2008**), 'Dislocation structures and their relationship to strength in deformed nickel microcrystals', *Acta Materialia* 56(13), 2988-3001.

[08S] Schijve, J. (**2008**), *Fatigue of structures and materials*, Springer Science+Business Media, Berlin.

[08W] Weinberger, C. R. & Cai, W. (**2008**), 'Surface-controlled dislocation multiplication in metal micropillars', *Proceedings of the National Academy of Sciences* 105(38), 14304-14307.

[09A] Santus, C. & Taylor, D. (**2009**), 'Physically short crack propagation in metals during high cycle fatigue', *International Journal of Fatigue* 31(8-9), 1356-1365.

[09B] Beden, S. M.; Abdullah, S. & Mohd Ihsan, A. K. A. (**2009**), 'Review of fatigue crack propagation models for metallic components', *European Journal of Scientific Research* 28(3), 364-397.

[09C] Schneider, A. S.; Kaufmann, D.; Clark, B. G.; Frick, C. P.; Gruber, P. A.; Mönig, R.; Kraft, O. & Arzt, E. (**2009**), 'Correlation between critical temperature and strength of small-scale bcc pillars', *Physical Review Letters* 103, 105501.

[09E] Besel, M. (**2009**), 'Mechanismenorientierte Lebensdauervorhersage für eine thermo-mechanisch hergestellte Flanschwelle mit gradiertem Gefüge', Doctoral thesis, University of Kassel.

[09G] Ghidini, T. & Donne, C. D. (**2009**), 'Fatigue life predictions using fracture mechanics methods', *Engineering Fracture Mechanics* 76(1), 134-148.

[09H] Shim, S.; Bei, H.; Miller, M.; Pharr, G. & George, E. (**2009**), 'Effects of focused ion beam milling on the compressive behavior of directionally solidified micropillars and the nanoindentation response of an electropolished surface', *Acta Materialia* 57(2), 503-510.

[09K] Kim, J.-Y. & Greer, J. R. (**2009**), 'Tensile and compressive behavior of gold and molybdenum single crystals at the nano-scale', *Acta Materialia* 57(17), 5245-5253.

[09M] Kim, J.-Y.; Jang, D. & Greer, J. R. (**2009**), 'Insight into the deformation behavior of niobium single crystals under uniaxial compression and tension at the nanoscale', *Scripta Materialia* 61(3), 300-303.

[09N] Branco, R.; Antunes, F. V.; Ferreira, J. A. M. & Silva, M. (**2009**), 'Determination of Paris law constants with a reverse engineering technique', *Engineering Failure Analysis* 16, 631-638.

[09R] Kumar, A.; Torbet, C. J.; Jones, J. W. & Pollock, T. M. (**2009**), 'Nonlinear ultrasonics for in situ damage detection during high frequency fatigue', *Journal of Applied Physics* 106(2), 024904.

[09S] Schneider, A.; Clark, B.; Frick, C.; Gruber, P. & Arzt, E. (**2009**), 'Effect of orientation and loading rate on compression behavior of small-scale Mo pillars', *Materials Science and Engineering: A* 508(1), 241-246.

[09T] Tschopp, M.; Bartha, B.; Porter, W.; Murray, P. & Fairchild, S. (**2009**), 'Microstructure-dependent local strain behavior in polycrystals through in-situ scanning electron microscope tensile experiments', *Metallurgical and Materials Transactions A* 40(10), 2363-2368.

[09Z] Szata, M. & Lesiuk, G. (**2009**), 'Algorithms for the estimation of fatigue crack growth using energy method', *Archives of Civil and Mechanical Engineering* 9(1), 119-134.

[10C] Chan, K. S. (**2010**), 'Roles of microstructure in fatigue crack initiation', *International Journal of Fatigue* 32(9), 1428-1447.

[10D] Daly, S. H. (**2010**), *Digital image correlation in experimental mechanics for aerospace materials and structures*, John Wiley & Sons, Ltd, Hoboken.

[10G] Glodez, S.; Jezernik, N.; Kramberger, J. & Lassen, T. (**2010**), 'Numerical modelling of fatigue crack initiation of martensitic steel', *Advances in Engineering Software* 41(5), 823-829.

[10J] Jennings, A. T.; Burek, M. J. & Greer, J. R. (**2010**), 'Microstructure versus size: Mechanical properties of electroplated single crystalline Cu nanopillars', *Physical Review Letter* 104, 135503.

[10K] Kraft, O.; Gruber, P. A.; Mönig, R. & Weygand, D. (**2010**), 'Plasticity in confined dimensions', *Annual Review of Materials Research* 40(1), 293-317.

[10L] Lowry, M.; Kiener, D.; LeBlanc, M.; Chisholm, C.; Florando, J.; Morris, J. & Minor, A. (**2010**), 'Achieving the ideal strength in annealed molybdenum nanopillars', *Acta Materialia* 58(15), 5160-5167.

[10M] McDowell, D. & Dunne, F. (**2010**), 'Microstructure-sensitive computational modeling of fatigue crack formation', *International Journal of Fatigue* 32(9), 1521-1542.

[10N] Jezernik, N.; Kramberger, J.; Lassen, T. & Glodez, S. (**2010**), 'Numerical modelling of fatigue crack initiation and growth of martensitic steels', *Fatigue and Fracture of Engineering Materials and Structures* 33(11), 714-723.

[10O] Mlikota, M. (**2010**), 'Numerical simulation of fatigue crack growth in plates subjected to cyclic tension load', Master thesis, University of Zagreb.

[10P] Prskalo, A.-P.; Schmauder, S.; Ziebert, C.; Ye, J. & Ulrich, S. (**2010**), 'Molecular dynamics simulations of the sputtering of SiC and Si_3N_4', *Surface and Coatings Technology* 204(12-13), 2081-2084.

[10S] Schneider, A.; Clark, B.; Frick, C.; Gruber, P. & Arzt, E. (**2010**), 'Effect of prestraining on the size effect in molybdenum pillars', *Philosophical Magazine Letters* 90(11), 841-849.

[11A] Atzori, B.; Meneghetti, G. & Ricotta, M. (**2011**), 'Analysis of the fatigue strength under two load levels of a stainless steel based on energy dissipation', *Frattura ed Integrita Strutturale* 17, 15-22.

[11B] Božić, Ž.; Mlikota, M. & Schmauder, S. (**2011**), 'Application of the ΔK, ΔJ and ΔCTOD parameters in fatigue crack growth modelling', *Technical Gazette* 18(3), 459-466.

[11C] Božić, Ž.; Schmauder, S. & Mlikota, M. (**2011**), 'Fatigue growth models for multiple long cracks in plates under cyclic tension based on ΔK_I, ΔJ-integral and ΔCTOD parameter', *Key Engineering Materials* 488-489, 525-528.

[11D] Keil, B. & Devletian, J. (**2011**), 'Comparison of the mechanical properties of steel and ductile iron pipe materials', *Pipelines 2011: A Sound Conduit for Sharing Solutions*, 1301-1312.

[11F] Clair, A.; Foucault, M.; Calonne, O.; Lacroute, Y.; Markey, L.; Salazar, M.; Vignal, V. & Finot, E. (**2011**), 'Strain mapping near a triple junction in strained Ni-based alloy using and biaxial nanogauges', *Acta Materialia* 59(8), 3116-3123.

[11G] Greer, J. R. & Hosson, J. T. D. (**2011**), 'Plasticity in small-sized metallic systems: Intrinsic versus extrinsic size effect', *Progress in Materials Science* 56(6), 654-724.

[11K] Kiener, D. & Minor, A. M. (**2011**), 'Source truncation and exhaustion: Insights from quantitative in situ TEM tensile testing', *Nano Letters* 11(9), 3816-3820.

[11L] Islam, M. A.; Sato, N. & Tomota, Y. (**2011**), 'Tensile and plane bending fatigue properties of pure iron and iron-phosphorus alloys at room temperature in the air', *Transactions of the Indian Institute of Metals* 64(3), 315-320.

[11N] Kunz, A.; Pathak, S. & Greer, J. R. (**2011**), 'Size effects in Al nanopillars: Single crystalline vs. bicrystalline', *Acta Materialia* 59(11), 4416-4424.

[11P] Prskalo, A.-P.; Schmauder, S.; Ziebert, C.; Ye, J. & Ulrich, S. (**2011**), 'Molecular dynamics simulations of the sputtering process of silicon and the homoepitaxial growth of a Si coating on silicon', *Computational Materials Science* 50(4), 1320-1325.

[11Q] Quey, R.; Dawson, P. & Barbe, F. (**2011**), 'Large-scale 3D random polycrystals for the finite element method: Generation, meshing and remeshing', *Computer Methods in Applied Mechanics and Engineering* 200(17-20), 1729-1745.

[11R] Schaef, W.; Marx, M.; Vehoff, H.; Heckl, A. & Randelzhofer, P. (**2011**), 'A 3-D view on the mechanisms of short fatigue cracks interacting with grain boundaries', *Acta Materialia* 59(5), 1849-1861.

[11S] Schmauder, S. & Kohler, C. (**2011**), 'Atomistic simulations of solid solution strengthening of α-iron', *Computational Materials Science* 50(4), 1238-1243.

[11T] Schneider, A.; Frick, C.; Clark, B.; Gruber, P. & Arzt, E. (**2011**), 'Influence of orientation on the size effect in bcc pillars with different critical temperatures', *Materials Science and Engineering: A* 528(3), 1540-1547.

[12A] Abuzaid, W. Z.; Sangid, M. D.; Carroll, J. D.; Sehitoglu, H. & Lambros, J. (**2012**), 'Slip transfer and plastic strain accumulation across grain boundaries in Hastelloy X', *Journal of the Mechanics and Physics of Solids* 60(6), 1201-1220.

[12B] Baldissera, P. & Delprete, C. (**2012**), 'The formal analogy between Tanaka-Mura and Weibull models for high-cycle fatigue', *Fatigue & Fracture of Engineering Materials & Structures* 35(2), 114-121.

[12C] Branco, R.; Antunes, F. V.; Costa, D.; Yang, F. P. & Kuang, Z. B. (**2012**), 'Determination of the Paris law constants in round bars from beach marks on fracture surfaces', *Engineering Fracture Mechanics* 96, 96-106.

[12E] Ersland, C. H. (**2012**), 'Atomistic modeling of failure in iron', Doctoral thesis, Norwegian University of Science and Technology.

[12H] Hradecky, S. (**2012**), 'Incident: Qantas B744 near Singapore on May 9th 2011, engine shut down in flight', The Aviation Herald, Online. http://avherald.com/h?article=43c55d38/0000

[12L] Logan, D. L. (**2012**), *A first course in the finite element method, 5th edition*, Global Engineering, Stamford.

[12M] Miao, J.; Pollock, T. M. & Jones, J. W. (**2012**), 'Microstructural extremes and the transition from fatigue crack initiation to small crack growth in a polycrystalline nickel-base superalloy', *Acta Materialia* 60(6-7), 2840-2854.

[12N] Mikkola, E.; Marquis, G. & Solin, J. (**2012**), 'Mesoscale modelling of crack nucleation from defects in steel', *International Journal of Fatigue* 41(0), 64-71.

[12P] Mirzazadeh, M. M. & Plumtree, A. (**2012**), 'High cycle fatigue behavior of shot-peened steels', *Metallurgical and Materials Transactions A* 43(8), 2777-2784.

[12R] Ramazani, A.; Mukherjee, K.; Prahl, U. & Bleck, W. (**2012**), 'Modelling the effect of microstructural banding on the flow curve behaviour of dual-phase (DP) steels', *Computational Materials Science* 52(1), 46-54.

[12S] Shade, P.; Uchic, M.; Dimiduk, D.; Viswanathan, G.; Wheeler, R. & Fraser, H. (**2012**), 'Size-affected single-slip behavior of Rene N5 microcrystals', *Materials Science and Engineering: A* 535, 53-61.

[12W] Wang, Q.; Khan, M. K. & Bathias, C. (**2012**), 'Current understanding of ultra-high cycle fatigue', *Theoretical and Applied Mechanics Letters* 2(3), 031002.

[13B] Bruesewitz, C.; Knorr, I.; Hofsaess, H.; Barsoum, M. W. & Volkert, C. A. (**2013**), 'Single crystal pillar microcompression tests of the MAX phases Ti_2InC and Ti_4AlN_3', *Scripta Materialia* 69(4), 303-306.

[13C] Chapetti, M. D. & Guerrero, A. O. (**2013**), 'Estimation of notch sensitivity and size effect on fatigue resistance', *Procedia Engineering* 66, 323-333.

[13F] Fett, T. & Munz, D. (**2013**), Chapter 9.5 – Fracture Mechanics, in *Handbook of Advanced Ceramics (Second edition)*, Somiya, S., ed., Academic Press, Oxford, 681-715.

[13G] Glodez, S.; Sori, M. & Kramberger, J. (**2013**), 'A statistical evaluation of micro-crack initiation in thermally cut structural elements', *Fatigue & Fracture of Engineering Materials & Structures* 36(12), 1298-1305.

[13K] Glodez, S.; Sori, M. & Kramberger, J. (**2013**), 'Prediction of micro-crack initiation in high strength steels using Weibull distribution', *Engineering Fracture Mechanics* 108, 263-274.

[13L] Lorenzino, P. & Navarro, A. (**2013**), 'Initiation and growth behavior of very-long microstructurally short fatigue cracks', *Frattura ed Integrità Strutturale* 25, 138-144.

[13M] Mayer, H.; Schuller, R. & Fitzka, M. (**2013**), 'Fatigue of AA 2024-T351 aluminium alloy at different load ratios up to 10^{10} cycles', *International Journal of Fatigue* 57(0), 113-119.

[13N] Lorenzino, P.; Navarro, A. & Krupp, U. (**2013**), 'Naked eye observations of microstructurally short fatigue cracks', *International Journal of Fatigue* 56(0), 8-16.

[13O] Monnet, G. & Pouchon, M. A. (**2013**), 'Determination of the critical resolved shear stress and the friction stress in austenitic stainless steels by compression of pillars extracted from single grains', *Materials Letters* 98, 128-130.

[13R] Morgeneyer, T.; Helfen, L.; Mubarak, H. & Hild, F. (**2013**), '3D digital volume correlation of synchrotron radiation laminography images of ductile crack initiation: An initial feasibility study', *Experimental Mechanics* 53(4), 543-556.

[13S] Sangid, M. D. (**2013**), 'The physics of fatigue crack initiation', *International Journal of Fatigue* 57(0), 58-72.

[13T] Schneider, A.; Kiener, D.; Yakacki, C.; Maier, H.; Gruber, P.; Tamura, N.; Kunz, M.; Minor, A. & Frick, C. (**2013**), 'Influence of bulk pre-straining on the size effect in nickel compression pillars', *Materials Science and Engineering: A* 559, 147-158.

[14A] Carrascal, I.; Casado, J. A.; Diego, S.; Lacalle, R.; Cicero, S. & Alvarez, J. A. (**2014**), 'Determination of the Paris' law constants by means of infrared thermographic techniques', *Polymer Testing* 40, 39-45.

[14B] Božić, Ž.; Schmauder, S.; Mlikota, M. & Hummel, M. (**2014**), 'Multiscale fatigue crack growth modelling for welded stiffened panels', *Fatigue and Fracture of Engineering Materials and Structures* 37(9), 1043-1054.

[14C] Castelluccio, G. M.; Musinski, W. D. & McDowell, D. L. (**2014**), 'Recent developments in assessing microstructure-sensitive early stage fatigue of polycrystals', *Current Opinion in Solid State and Materials Science* 18(4), 180-187.

[14D] Christ, H.-J.; Fritzen, C.-P. & Köster, P. (**2014**), 'Micromechanical modeling of short fatigue cracks', *Current Opinion in Solid State and Materials Science* 18(4), 205-211.

[14E] Davis, B.; Wawrzynek, P. & Ingraffea, A. (**2014**), '3-D simulation of arbitrary crack growth using an energy-based formulation – Part I: Planar growth', *Engineering Fracture Mechanics* 115(0), 204-220.

[14G] Guo, E.-Y.; Xie, H.-X.; Singh, S. S.; Kirubanandham, A.; Jing, T. & Chawla, N. (**2014**), 'Mechanical characterization of microconstituents in a cast duplex stainless steel by micropillar compression', *Materials Science and Engineering: A* 598(C), 98-105.

[14H] Healy, C. (**2014**), 'Plasticity of metallic nanostructures – Molecular dynamics simulations', Doctoral thesis, The University of Edinburgh.

[14J] Goodman, J. (**1899**), *Mechanics applied to engineering*, Longmans, Green and co., London.

[14K] Hocker, S.; Schmauder, S.; Bakulin, A. & Kulkova, S. (**2014**), 'Ab initio investigation of tensile strengths of metal(1 1 1)/a-Al_2O_3(0001) interfaces', *Philosophical Magazine* 94(3), 265-284.

[14L] Krupp, U. & Alvarez-Armas, I. (**2014**), 'Short fatigue crack propagation during low-cycle, high cycle and very-high-cycle fatigue of duplex steel – An unified approach', *International Journal of Fatigue* 65, 78-85.

[14M] Morgeneyer, T. F.; Taillandier-Thomas, T.; Helfen, L.; Baumbach, T.; Sinclair, I.; Roux, S. & Hild, F. (**2014**), 'In situ 3-D observation of early strain localization during failure of thin Al alloy (2198) sheet', *Acta Materialia* 69(0), 78-91.

[14O] Okamoto, N. L.; Inomoto, M.; Adachi, H.; Takebayashi, H. & Inui, H. (**2014**), 'Micropillar compression deformation of single crystals of the intermetallic compound ζ-$FeZn_{13}$', *Acta Materialia* 65, 229-239.

[14P] Perez-Jimenez, M. J. (**2014**), A bioinspired computing approach to model complex systems, *in* Marian Gheorghe; Grzegorz Rozenberg; Arto Salomaa; Petr Sosik & Claudio Zandron, ed., 'Membrane Computing', Springer International Publishing, Cham, 20-34.

[14R] Polak, J. & Man, J. (**2014**), 'Fatigue crack initiation – The role of point defects', *International Journal of Fatigue* 65(0), 18-27.

[14S] Sharifi, H.; Salehi, M. & Saeri, M. (**2014**), 'The effect of ferrite grain size on the fatigue behavior of ferrite-martensite dual-phase steels', *International Journal of Iron & Steel Society of Iran* 2, 11-16.

[14T] Sistaninia, M. & Niffenegger, M. (**2014**), 'Prediction of damage-growth based fatigue life of polycrystalline materials using a microstructural modeling approach', *International Journal of Fatigue* 66, 118-126.

[15B] Budynas, R. G. & Nisbett, J. K. (**2015**), *Shigley's mechanical engineering design, Tenth edition*, McGraw-Hill Education, New York, chapter: Fatigue failure resulting from variable loading, pp. 273-349.

[15C] Cruzado, A.; Gan, B.; Jimenez, M.; Barba, D.; Ostolaza, K.; Linaza, A.; Molina-Aldareguia, J.; Llorca, J. & Segurado, J. (**2015**), 'Multiscale modeling of the mechanical behavior of IN718 superalloy based on micropillar compression and computational homogenization', *Acta Materialia* 98, 242-253.

[15K] Kulkova, S. E.; Bakulin, A. V.; Kulkov, S. S.; Hocker, S. & Schmauder, S. (**2015**), 'Influence of interstitial impurities on the Griffith work in Ti-based alloys', *Physica Scripta* 90(9), 094010.

[15L] Lorenzino, P. & Navarro, A. (**2015**), 'Grain size effects on notch sensitivity', *International Journal of Fatigue* 70, 205-215.

[15M] Mughrabi, H. (**2015**), 'Microstructural mechanisms of cyclic deformation, fatigue crack initiation and early crack growth', *Philosophical Transactions of the Royal Society of London A: Mathematical, Physical and Engineering Sciences* 373(2038), 1-20.

[15N] Lorenzino, P. & Navarro, A. (**2015**), 'Growth of very long "short cracks" initiated at holes', *International Journal of Fatigue* 71(Supplement C), 64-74.

[15O] Lorenzino, P. & Navarro, A. (**2015**), 'The variation of resonance frequency in fatigue tests as a tool for in-situ identification of crack initiation and propagation, and for the determination of cracked areas', *International Journal of Fatigue* 70, 374-382.

[15R] Rogne, B. & Thaulow, C. (**2015**), 'Strengthening mechanisms of iron micropillars', *Philosophical Magazine* 95(16-18), 1814-1828.

[15S] Signetti, S. & Pugno, N. M. (**2015**), 'Frontiers in modeling and design of bio-inspired armors', *Frontiers in Materials* 2(17), 1.

[16A] Hagen, A. & Thaulow, C. (**2016**), 'Low temperature in-situ micro-compression testing of iron pillars', *Materials Science and Engineering: A* 678, 355-364.

[16B] Bakulin, A.; Spiridonova, T.; Kulkova, S.; Hocker, S. & Schmauder, S. (**2016**), 'Hydrogen diffusion in doped and undoped a-Ti: An ab-initio investigation', *International Journal of Hydrogen Energy* 41(21), 9108-9116.

[16C] Chen, Z. M.; Okamoto, N. L.; Demura, M. & Inui, H. (**2016**), 'Micropillar compression deformation of single crystals of $Co_3(Al,W)$ with the $L1_2$ structure', *Scripta Materialia* 121, 28-31.

[16D] Chowdhury, P. & Sehitoglu, H. (**2016**), 'Mechanisms of fatigue crack growth – a critical digest of theoretical developments', *Fatigue & Fracture of Engineering Materials & Structures* 39(6), 652-674.

[16H] Hiatt, J. (**2016**), 'What is a SN-Curve?', Technical report, Siemens PLM Community.

[16I] Hui, W.; Zhang, Y.; Zhao, X.; Xiao, N. & Hu, F. (**2016**), 'High cycle fatigue behavior of V-microalloyed medium carbon steels: A comparison between bainitic and ferritic-pearlitic microstructures', *International Journal of Fatigue* 91(Part 1), 232-241.

[16J] Jin, H.-H.; Ko, E.; Kwon, J.; Hwang, S. S. & Shin, C. (**2016**), 'Evaluation of critical resolved shear strength and deformation mode in proton-irradiated austenitic stainless steel using micro-compression tests', *Journal of Nuclear Materials* 470, 155-163.

[16N] Ancona, F.; Palumbo, D.; Finis, R. D.; Demelio, G. P. & Galietti, U. (**2016**), 'Automatic procedure for evaluating the Paris Law of martensitic and austenitic stainless steels by means of thermal methods', *Engineering Fracture Mechanics* 163, 206-219.

[16O] Okamoto, N. L.; Fujimoto, S.; Kambara, Y.; Kawamura, M.; Chen, Z. M. T.; Matsunoshita, H.; Tanaka, K.; Inui, H. & George, E. P. (**2016**), 'Size effect, critical re-

solved shear stress, stacking fault energy, and solid solution strengthening in the CrMnFeCoNi high-entropy alloy', *Scientific Reports* 6, 35863.

[16R] Rösler, J.; Harders, H. & Bäker, M. (**2016**), *Mechanisches Verhalten der Werkstoffe*, Springer Vieweg, Wiesbaden, chapter: Elastisches Verhalten, 31-62.

[16S] Staib, S. (**2016**), 'Determination of Paris law constants *C* and *m* using a micromechanical based modelling approach', Student research project, IMWF, University of Stuttgart.

[16T] Tofique, M. W.; Bergström, J. & Burman, C. (**2016**), 'Very high cycle fatigue crack initiation mechanisms in different engineering alloys', *Procedia Structural Integrity* 2, 1181-1190.

[16U] Chauhan, S.; Pawar, A. K.; Chattopadhyay, J. & Dutta, B. K. (**2016**), 'Determination of fatigue properties using miniaturized specimens', *Transactions of the Indian Institute of Metals* 69(2), 609-615.

[16Y] Zhang, J.; Yang, S. & Lin, J. (**2016**), 'A nonlinear continuous damage model based on short-crack concept under variable amplitude loading', *Fatigue & Fracture of Engineering Materials & Structures* 39, 79-94.

[16Z] Zhang, Z.; Hu, Z.; Schmauder, S.; Mlikota, M. & Fan, K. (**2016**), 'Low-cycle fatigue properties of P92 ferritic-martensitic steel at elevated temperature', *Journal of Materials Engineering and Performance* 25(4), 1650-1662.

[17G] Gillner, K. & Muenstermann, S. (**2017**), 'Numerically predicted high cycle fatigue properties through representative volume elements of the microstructure', *International Journal of Fatigue* 105, 219-234.

[17K] Kositski, R. & Mordehai, D. (**2017**), 'Role of dislocation pile-ups in nucleation-controlled size-dependent strength of Fe nanowires', *Acta Materialia* 136, 190-201.

[17L] Mlikota, M.; Schmauder, S.; Božić, Ž. & Hummel, M. (**2017**), 'Modelling of overload effects on fatigue crack initiation in case of carbon steel', *Fatigue and Fracture of Engineering Materials and Structures* 40(8), 1182-1190.

[17M] Mlikota, M.; Staib, S.; Schmauder, S. & Božić, Ž. (**2017**), 'Numerical determination of Paris law constants for carbon steel using a two-scale model', *Journal of Physics: Conference Series* 843(1), 012042.

[17O] Mlikota, M. & Schmauder, S. (**2017**), 'Numerical determination of component Wöhler curve', *DVM Bericht / Anwendungsspezifische Werkstoffgesetze für die Bauteilsimulation* 1684, 111-124.

[17P] Palomares-Garcia, A. J.; Perez-Prado, M. T. & Molina-Aldareguia, J. M. (**2017**), 'Effect of lamellar orientation on the strength and operating deformation mechanisms of fully lamellar TiAl alloys determined by micropillar compression', *Acta Materialia* 123, 102-114.

[17S] Schmiedt, M. (**2017**), 'Numerical modelling of a specimen fatigue lifetime under the influence of temperature and mechanically induced residual stresses', Master thesis, University of Stuttgart.

[17W] Wang, Z.-Y.; Wang, Q.-Y. & Cao, M. (**2017**), 'Experimental study on fatigue behaviour of shot-peened open-hole steel plates', *Materials* 10(9), 996.

[18A] Bhaduri, A. (**2018**), *Mechanical properties and working of metals and alloys*, Springer, Singapore.

[18B] Božić, Ž.; Schmauder, S.; Mlikota, M. & Hummel, M. / Schmauder, S.; Chen, C.-S.; Chawla, K. K.; Chawla, N.; Chen, W. & Kagawa, Y., ed., (**2018**), *Handbook of Mechanics of Materials*, Springer Singapore, chapter Multiscale fatigue crack growth modeling for welded stiffened panels, 1-21.

[18H] Bruder, T.; Hanselka, H.; Heim, R.; Kaufmann, H.; Kieninger, M.; Nuffer, J. & Sonsino C. M. / Mastinu, G. & Ploechl, M., ed., (**2018**), *Road and Off-Road Vehicle System Dynamics Handbook*, CRC Press, chapter: Fatigue and Structural Durability of Automotive Components, 263-306.

[18M] Mlikota, M.; Schmauder, S. & Božić, Ž. (**2018**), 'Calculation of the Wöhler (*S-N*) curve using a two-scale model', *International Journal of Fatigue* 114, 289-297.

[18L] Mlikota, M. & Schmauder, S. (**2018**), 'On the critical resolved shear stress and its importance in the fatigue performance of steels and other metals with different crystallographic structures', *Metals* 8(11), 883.

[18T] LSP Technologies (**2018**), 'Shot peening', LSP Technologies, Online, Dublin. https://www.lsptechnologies.com/shot-peening/

[18W] Wu, X. (**2018**), 'On Tanaka-Mura's fatigue crack nucleation model and validation', *Fatigue and Fracture of Engineering Materials and Structures* 41, 894-899.

[18Y] Tanaka, Y.; Takaki, S.; Tsuchiyama, T. & Uemori, R. (2018), 'Effect of grain size on the yield stress of cold worked iron', *ISIJ International* 58(10), 1927-1933.

[19M] Mlikota, M. & Schmauder, S. (**2019**), 'Virtual testing of plasticity effects on fatigue crack initiation', *Advances in Engineering Materials, Structures and Systems: Innovations, Mechanics and Applications*, 587-592.

[19P] Deveci, M. (**2019**), 'Shot peening residual stresses', Stresstech, Online. https://www.stresstech.com/en-fi/know-how/articles/stresstech-bulletin-14-shot-peening-residual-stresses/

[19S] Schmauder, S. (**2019**), 'Einführung in die Festigkeitslehre', Teaching manuscript, University of Stuttgart.

[20L] Mlikota, M. & Schmauder, S. (**2020**), 'A newly discovered relation between the critical resolved shear stress and the fatigue endurance limit for metallic materials', *Metals* 10(6), 803.

[20M] MatWeb, Material property data (**2020**), Online. http://www.matweb.com/

[33F] French, H. J. (**1933**), 'Fatigue and the hardening of steels', *Transactions of the American Society for Steel Treating* 21(10), 899-946.

[42C] Cleaves, H. E. & Hiegel, J. M. (**1942**), 'Properties of high-purity iron', *Journal of Research of the National Bureau of Standards* 28, 643-667.

[59A] Alder, B. J. & Wainwright, T. E. (**1959**), 'Studies in molecular dynamics. I. General method', *The Journal of Chemical Physics* 31(2), 459-466.

[60W] Wöhler, A. (**1860**), 'Versuche zur Ermittlung der auf die Eisenbahnwagen-Achsen einwirkenden Kräfte und der Widerstandsfähigkeit der Wagen-Achsen', *Zeitschrift für Bauwesen* 10, 584-616.

[63F] Fuchs, H. O. (**1963**), 'Forecasting fatigue life of peened parts', *Metal Progress* 83-84, 75-78.

[63P] Paris, P. & Erdogan, F. (**1963**), 'A critical analysis of crack propagation laws', *Journal of Basic Engineering* 85(4), 528-533.

[63S] Stein, D.; Low, J. & Seybolt, A. (**1963**), 'The mechanical properties of iron single crystals containing less than $5x10^{-3}$ ppm carbon', *Acta Metallurgica* 11(11), 1253-1262.

[64F] Ferro, A. & Montalenti, G. (**1964**), 'On the effect of the crystalline structure on the form of fatigue curves', *Philosophical Magazine* 10, 1043.

[64R] Rahman, A. (**1964**), 'Correlations in the motion of atoms in liquid argon', *Physical Review* 136, A405-A411.

[65F] Ferro, A.; Mazzetti, P. & Montalenti, G. (**1965**), 'On the effect of the crystalline structure on fatigue: Comparison between body-centred metals (Ta, Nb, Mo and W) and face-centred and hexagonal metals', *The Philosophical Magazine: A Journal of Theoretical Experimental and Applied Physics* 12(118), 867-875.

[65K] Klesnil, M.; Holzmann, M.; Lukáš, P. & Ryš, P. (**1965**), 'Some aspects of the fatigue process in low-carbon steel', *Journal of Iron & Steel Institute* 203, 1043-1048.

[65Y] Yoshikawa, A. & Sugeno, T. (**1965**), 'Factors responsible for the sharp fatigue limit in iron and steel', *Transactions of the Metallurgical Society of AIME* 233, 1314-1317.

[66S] Stein, D. & Low, J. (**1966**), 'Effects of orientation and carbon on the mechanical properties of iron single crystals', *Acta Metallurgica* 14(10), 1183-1194.

[67B] Buck, A. (**1967**), 'Fatigue properties of pure metals', *International Journal of Fracture Mechanics* 3(2), 145-152.

[70W] Wöhler, A. (**1870**), 'Über die Festigkeits-Versuche mit Eisen und Stahl', *Zeitschrift für Bauwesen* 20, 74-106.

[71G] Grosskreutz, J. C. (**1971**), 'Fatigue mechanisms in the sub-creep range', *American Society for Testing and Materials* 495, 5-60.

[74K] Kardestuncer, H. (**1974**), *Elementary matrix analysis of structures*, McGraw-Hill, New York.

[76K] Kitagawa, H. & Takahashi, S. (**1976**), Applicability of fracture mechanics to very small cracks or the cracks in the early stage, *in* 'Proceedings of the 2nd International Conference on Mechanical Behaviour of Materials (ICM2)', ASM, 627-631.

[79C] Clemens, D.; Galante, J. & Rostoker, W. (**1979**), 'The influence of grain size on the fatigue behavior of annealed 316 LVM stainless steel', *Journal of Biomedical Materials Research* 13, 437-441.

[79H] Haddad, M. E.; Topper, T. & Smith, K. (**1979**), 'Prediction of non propagating cracks', *Engineering Fracture Mechanics* 11(3), 573-584.

[79I] Ibrahim, M. F. E. & Miller, K. J. (**1979**), 'Determination of fatigue crack initiation life', *Fatigue & Fracture of Engineering Materials & Structures* 2, 351-360.

[79R] Ritchie, R. O. (**1979**), 'Near-threshold fatigue-crack propagation in steels', *International Metals Reviews* 24(1), 205-230.

[80K] Klesnil, M. & Lukáš, P. (**1980**), *Fatigue of metallic materials*, Elsevier Scientific, Amsterdam.

[81S] Tsach, U. (**1981**), 'Locking of thin plate/shell elements', *International Journal for Numerical Methods in Engineering* 17(4), 633-644.

[81T] Tanaka, K. & Mura, T. (**1981**), 'A dislocation model for fatigue crack initiation', *Journal of Applied Mechanics* 48(1), 97-103.

[81Y] Taylor, D. & Knott, J. F. (**1981**), 'Fatigue crack propagation behaviour of short cracks; The effect of microstructure', *Fatigue & Fracture of Engineering Materials & Structures* 4(2), 147-155.

[82T] Tanaka, K. & Mura, T. (**1982**), 'A theory of fatigue crack initiation at inclusions', *Metallurgical Transactions A* 13(1), 117-123.

[83F] Feller-Kniepmeier, M. & Hundt, M. (**1983**), 'Deformation properties of high purity α-Fe single crystals', *Scripta Metallurgica* 17(7), 905-908.

[83R] Robin, C.; Louah, M. & Pluvinage, G. (**1983**), 'Influence of an overload on the fatigue crack growth in steels', *Fatigue & Fracture of Engineering Materials & Structures* 6(1), 1-13.

[83Z] Zheng, X. & Hirt, M. A. (**1983**), 'Fatigue crack propagation in steels', *Engineering Fracture Mechanics* 18(5), 965-973.

[84S] Suresh, S. & Ritchie, R. O. (**1984**), 'Propagation of short fatigue cracks', *International Metals Reviews* 29(1), 445-475.

[85B] Boyer, H. & Metals, A. (**1985**), *Atlas of fatigue curves*, American Society for Metals, Ohio.

[85K] Krompholz, K. & Ullrich, G. (**1985**), 'Investigations into the fatigue crack initiation and propagation behaviour in austenitic stainless steel X5CrNi18-9 (1.4301)', *Materialwissenschaft und Werkstofftechnik* 16(8), 270-276.

[85V] Van Stone, R. H.; Cox, T.; Low Jr, J. R. & Psioda, J. A. (**1985**), 'Microstructural aspects of fracture by dimpled rupture', *International Materials Reviews* 30, 157.

[86M] Murakami, Y. & Endo, M. (**1986**), 'Effects of hardness and crack geometry on ΔK_{th} of Small Cracks', *Journal of the Society of Materials Science, Japan* 35(395), 911-917.

[88B] Broek, D. (**1988**), *The practical use of fracture mechanics*, Kluwer Academic Publishers, Dordrecht.

[88R] Roos, E. & Eisele, U. (**1988**), 'Determination of material characteristic values in elastic-plastic fracture mechanics by means of J-integral crack resistance curves', *Journal of Testing and Evaluation* 16(1), 1-11.

[90T] Thomason, P. F. (**1990**), *Ductile fracture of metals*, Pergamon Press, Oxford, New York, Beijing, Frankfurt, Sao Paulo, Sydney, Tokyo, Toronto.

[92D] Dietmann, H. (**1991**), *Einführung in die Elastizitäts- und Festigkeitslehre*, Alfred Kröner Verlag, Stuttgart.

[95F] Farrahi, G. H.; Lebrijn, J. L. & Couratin, D. (**1995**), 'Effect of shot peening on residual stress and fatigue life of a spring steel', *Fatigue & Fracture of Engineering Materials & Structures* 18, 211-220.

[95R] de los Rios, E.; Walley, A.; Milan, M. & Hammersley, G. (**1995**), 'Fatigue crack initiation and propagation on shot-peened surfaces in A316 stainless steel', *International Journal of Fatigue* 17(7), 493-499.

[96L] Lukáš, P. (**1996**), *ASM handbook, vol. 19, fatigue and fracture*, ASM International, Materials Park, chapter: Fatigue crack nucleation and microstructure, 96-109.

[96S] Socie, D. F. & Furman, S. (**1996**), Fatigue damage simulation models for multiaxial loading, *in* G. Lutjering & H. Nowack, ed., 'Fatigue '96, Proceedings of the Sixth International Fatigue Congress', Pergamon Press, New York, 967-976.

[96W] Wu, X. (**1996**), *Handbook of mechanical properties of aircraft structural metals, Vol. 2 Damage tolerance*, Aviation Industry Press, Beijing.

[96Y] Yang, L. & Fatemi, A. (**1996**), 'Impact resistance and fracture toughness of vanadium-based microalloyed forging steel in the as-forged and Q&T conditions', *Journal of Engineering Materials and Technology* 118, 71-79.

[97E] Ellyin, F. (**1997**), *Fatigue damage, crack growth and life prediction*, Springer, Dordrecht.

[98B] Bramfitt, B. L. (**1998**), Structure/property relationships in irons and steels, in *Metals Handbook Desk Edition (Second edition)*, Davis, J. R., ed., ASM International, 153-173.

[98D] Deimel, P. & Sattler, E. (**1998**), 'Non-metallic inclusions and their relation to the *J*-integral, $J_{i,phys}$, at physical crack initiation for different steels and weld metals', *Journal of Materials Science* 33(7), 1723-1736.

[98H] Hoshide, T. & Kusuura, K. (**1998**), 'Life prediction by simulation of crack growth in notched components with different microstructures and under multiaxial fatigue', *Fatigue & Fracture of Engineering Materials & Structures* 21(2), 201-213.

[98S] Suresh, S. (**1998**), *Fatigue of materials*, Cambridge University Press, Cambridge.

[99N] Newman, J.; Phillips, E. & Swain, M. (**1999**), 'Fatigue-life prediction methodology using small-crack theory', *International Journal of Fatigue* 21(2), 109-119.

12 Acknowledgement

Firstly, I need to express my very profound gratitude to my parents Tomislav and Ivanka for providing me with unfailing emotional and moral support through the process of researching and writing this doctoral thesis, throughout my years of study and in my life in general. Without them, I would not be the person I am today and this accomplishment would not have been possible. For these reasons, I dedicate this work to them.

I am also grateful to my sister Mirela and my brothers Branko and Darijo for being there for me whenever it is needed. I am also grateful to my other family members and friends who have supported me along the way.

A very special gratitude goes out to Prof. Siegfried Schmauder for supervising and guiding me through the preparation of this work. The door to Prof. Schmauder's office was always open whenever I had an inquiry about my research or writing. He was consistently armed with immense patience, motivation, great ideas and knowledge and as well guided me in the right direction whenever he thought I needed it. I am gratefully indebted for his valuable comments on this thesis, too.

I would like to mention my master thesis supervisor Prof. Željko Božić and ex-colleague Dr. Alen-Pilip Prskalo. I am thankful to Prof. Božić for introducing me into the field of metal fatigue and to Dr. Prskalo for being of extreme help during my first days in Germany in general. Thanks to Prof. Božić go also for being the second reader of this thesis. I am grateful to all my ex- and current colleagues and especially to the institute staff: Kerstin Hilscher and Iris Weber for their invaluable support and assistance.

Finally, I am grateful to God for his presence in my life, for the good health and well-being that were necessary to complete this work.

13 Biography

Marijo Mlikota was born in Konjic in 1986. He grew up in Zagreb, where he graduated at the age of 24 in Mechanical Engineering from the University of Zagreb. From 2011 to 2020, he was scientific researcher and a doctoral candidate at the Institute for Materials Testing, Materials Science and Strength of Materials (IMWF), University of Stuttgart. Aside of fatigue of metallic materials, he was involved in the research fields of metal erosion, soft tissue behaviour etc.